

Self-assembling Peptides as Biofunctional Component in Medical Fabrics

Reem Saeed Alazragi

Submitted in accordance with the requirements for the degree of
Doctor of Philosophy

The University of Leeds

School of Chemistry

May 2014

The candidate confirms that the work submitted is her own and that appropriate credit has been given where reference has been made to the work of others.

This copy has been supplied on the understanding that it is copyright material and that no quotation from the thesis may be published without proper acknowledgement.

©2014 The University of Leeds and R S Alazragi

Acknowledgments

It would not have been possible to conduct the research and write this thesis without the help and support of many kind and helpful people around me, to only some of whom it is possible to give particular thanks.

I would like to express my deep gratitude and thanks to my supervisor, Dr. Amalia Aggeli for the opportunity to research this work under her supervision. I would like to thank her for the guidance, encouragement and teachings. I would very much like to thank everyone who helped me throughout this project, especially Professor Stephen Russell from the School of Design at University of Leeds. Also, I would like to extend my wonderful thanks to Dr. Julie fisher for her support, and Dr Stacy Wilshaw for the training in the Faculty of biological Science.

I would like to thank all in CMNS that have made my time in and out of the lab enjoyable. I'm particularly grateful to the peptide group that made me feel welcome from day one and took the time to show me what I needed to know in the early stages of this work, in particular Dr Phil Davies, Dr Steven Maude and Dr Danielle Miles.

I could not have completed this study without the financial support from the Ministry of Education -The kingdom of Saudi Arabia.

I will be forever thankful to my parents who have been a rock to me, offering help, advice and support. I would like to thank the rest of my family for always believing in me, especially my brother Dr. Marwan Special thanks to my husband for his generous support. I would finally like to thank my friends who have constantly reminded me to have a life outside work.

Abstract

The importance of medical fabrics is reflected by increased clinical need and consumption over the past decade in the health and medical sectors. Medical fabric products, including wound dressings, are currently defined as ‘medical devices’ by European legislation. To ensure effectiveness as a wound dressing, these fabrics should assist the repair process by providing sufficient protection against bacterial spread in the wound bed. Chronic wounds are an increasingly urgent health problem, owing to the rising population of elderly, obese and diabetic patients. When treating such wounds with drug releasing dressings, the immediate release of the drug is a common limitation. Thus, the development of smart drug delivery dressings that release antibacterial agents into the wound bed when required would be a useful aid in medicine. The overall aim of this study was to develop a wound dressing that was able to release the antibacterial agents only in the presence of bacteria.

Medical dressings were treated with pH-responsive, self-assembling peptides as antibacterial carriers that were able to release the loaded drug when stimulated by the bacterial pH. A methodology developed for potential future medical application is presented. The preliminary design consisted of three stages. First, the self-assembled peptide candidates were studied and selected as drug carriers. Second, fabrics were treated with the selected self-assembled peptides using two different methods: (1) coating with the peptides from the outer surface by impregnating in peptide solution and (2) incorporating the self-assembled peptides within the structure by electrospinning. The treatment success of the dressing was investigated using a series of complementary techniques such as FTIR, TEM, SEM and CLSM. Third, potential effectiveness of the dressings was assessed *in vitro* using two antibiotics model, vancomycin and levofloxacin separately, against a *Staphylococcus epidermidis* bacterial strain, a species commonly found in infected wounds. The study findings clearly demonstrated the *in vitro* potential of self-assembling peptide technology in improving the function of medical fabrics.

Table of Contents

Acknowledgments.....	ii
Abstract	iii
Table of Contents	iv
List of Figures	xii
List of Tables.....	xxiv
List of Abbreviations.....	xxvi
Chapter 1	1
1 Introduction	1
1.1 Introduction to medical fabrics	1
1.1.1 Healthcare and hygiene products.....	1
1.1.2 Extracorporeal devices	2
1.1.3 Implantable materials	2
1.1.3.1 Implantable materials for hard tissue engineering.....	3
1.1.3.2 Implantable materials for soft tissue engineering.....	3
1.1.4 Non-Implantable materials	5
1.1.4.1 Drug-releasing textiles.....	5
1.1.4.2 Wound care dressings	8
1.2 Advantages and limitations of current drug-releasing textiles.....	14
1.3 Introduction to peptides.....	15
1.3.1 Primary structure of peptide	15
1.3.2 Secondary structure of peptide	18
1.3.2.1 α - Helix	18
1.3.2.2 β -Sheet	19
1.4 Molecular self-assembly of peptides.....	20

1.4.1 Examples of self-assembling peptide nanostructures and their potential as drug carriers	20
1.4.1.1 Cyclic peptide nanotube	20
1.4.1.2 Amyloid peptide	22
1.4.1.3 β - Hairpin peptide	23
1.4.1.4 Amphiphilic peptide	25
1.4.1.5 Ionic Complementary Peptide	28
1.4.1.6 P ₁₁ series of peptides	30
1.5 Advantages and limitations of peptide-based drug-delivery systems	34
1.6 Aims and Objectives	35
Chapter 2	36
2 Experimental procedures and techniques	36
2.1 Materials	36
2.1.1 Chemicals	36
2.1.2 Peptides	36
2.2 General methods	36
2.2.2 pH measurement	36
2.2.3 Peptide solution preparation	37
2.3 Characterization techniques	37
2.3.1 Transmission electron microscopy, TEM	37
2.3.1.1 Background	37
2.3.1.2 Method	38
2.3.2 Scanning electron microscopy, SEM	39
2.3.2.1 Background	39

2.3.2.2 Method	40
2.3.3 Energy-dispersive X-ray spectroscopy, EDX	40
2.3.4 Fourier transform infra-red spectroscopy, FT-IR.....	41
2.3.4.1 Background.....	41
2.3.4.2 Method.....	43
2.3.5 Attenuated total reflectance spectroscopy, ATR-IR.....	44
2.3.5.1 Background.....	44
2.3.5.2 Method.....	45
2.3.6 Confocal laser scanning microscope, CLSM	45
2.3.6.1 Background.....	45
2.3.6.2 Method	46
Chapter 3	48
3 Self-assembly and morphology of peptide nanostructures and their gelation properties	48
3.1 Introduction	48
3.1.1 Peptide self-assembly in water	48
3.1.2 Peptide self-assembly under physiological conditions.....	49
3.2 Materials and methods	50
3.2.1 Materials	50
3.2.2 Methods	51
3.2.2.1 Preparation of P ₁₁ -2 solutions in 100% D ₂ O	51
3.2.2.2 Preparation of P ₁₁ -2 solution in 90% D ₂ O and 10% HFIP	51
3.2.2.3 Preparation of P ₁₁ -2 solutions at different pH levels	52
3.2.2.4 Preparation of peptide solutions under physiological conditions	52
3.3 Results	54

3.3.1 Self-assembly of P ₁₁ -2 in 100% D ₂ O	54
3.3.1.1 Transmission electron microscopy, TEM	55
3.3.1.2 Fourier transform infrared spectroscopy, FTIR	58
3.3.2 Self-assembly of P ₁₁ -2 in 90% D ₂ O and HFIP	59
3.3.2.1 Transmission electron microscopy, TEM	60
3.3.2.2 Fourier transform infrared spectroscopy, FTIR	64
3.3.3 Self-assembly of P ₁₁ -2 as a function of pH	66
3.3.3.1 Transmission electron microscopy, TEM	66
3.3.3.2 Fourier transform infra-red Spectroscopy, FTIR	66
3.3.4 Peptide self-assembly in physiological-like solution	68
3.3.4.1 P ₁₁ -9	68
3.3.4.2 P ₁₁ -12	71
3.4 Discussion	74
3.4.1 Self-assembly of P ₁₁ -2 in 100% D ₂ O	74
3.4.2 Self-assembly of P ₁₁ -2 in 90% D ₂ O and 10% HFIP	75
3.4.3 Self-assembly of P ₁₁ -2 as a function of pD	76
3.4.4 Peptide self-assembly under physiological-like solutions	78
3.5 Conclusions	79
Chapter 4	80
4 Preparation and characterization of self-assembled peptide coated cellulosic fabric ..	80
4.1 Introduction	80
4.1.1 Modified coated dressing for wound care applications	81
4.2 Materials and methods	84
4.2.1 Materials	84

4.2.2 Methods	84
4.2.2.1 Coating of cellulose fabric with P ₁₁ -4.....	84
4.2.2.2 Coating of cellulose fabric with P ₁₁ -8.....	85
4.3. Results.....	85
4.3.1 Coating of cellulose fabric with self-assembling peptides	85
4.3.2 Transmission Electron Microscopy, TEM	87
4.3.3 Scanning Electron Microscopy, SEM	87
4.3.3.1 Cellulose fabric coated with P ₁₁ -4 (10 mg/ml).....	87
4.3.3.2 Cellulose fabric coated with P ₁₁ -4 (2 mg/ml).....	91
4.3.3.3 Cellulose fabric coated with P ₁₁ -8 (10 mg/ml).....	94
4.3.3.4 Cellulose fabric coated with P ₁₁ -8 (2 mg/ml).....	97
4.3.4 Confocal Laser scanning microscopy, CLSM.....	100
4.3.4.1 Cellulose fabric coated with P ₁₁ -4	100
4.3.4.2 Cellulose fabric coated with P ₁₁ -8	100
4.3.5 Attenuated Total Reflectance spectroscopy, ATR	105
4.3.5.1 Cellulose fabric coated with P ₁₁ -4 (10 mg/ml).....	105
4.3.5.2 Cellulose fabric coated with P ₁₁ -4 (2 mg/ml).....	106
4.3.5.3 Cellulose fabric coated with P ₁₁ -8 (10 mg/ml).....	108
4.3.5.4 Cellulose fabric coated with P ₁₁ -8 (2 mg/ml).....	109
4.4 Discussion	112
4.4.1 Fabrics coated with P ₁₁ -4	112
4.4.2 Fabrics coated with P ₁₁ -8	114
4.4.3 Characterization of samples coated with self-assembled peptides.....	115

4.5 Conclusions	116
Chapter 5	117
5 Antimicrobial activity of self-assembled peptide-coated cellulosic fabric against <i>Staphylococcus epidermidis</i>	117
5.1 Introduction	117
5.1.1 Bacterial resistance to antibiotic	119
5.2 Materials and method	121
5.2.1 Materials	121
5.2.2 Methods	122
5.2.2.1 Development of an antimicrobial dressing	122
5.3 Results	124
5.3.1 Effect of antibiotics on peptide self-assembly	124
5.3.1.1 Transmission electron microscopy, TEM	124
5.3.2 Coating cellulosic fabrics with fibril-encapsulated antibiotics	125
5.3.2.1 Scanning electron microscopy, SEM	127
5.3.2.2 Confocal laser scanning microscopy, CLSM	127
5.3.2.3 Attenuated total reflectance spectroscopy, ATR-IR	129
5.3.3 Antimicrobial activity of the coated fabrics	130
5.3.3.1 Identification of <i>SE</i>	131
5.3.3.2 Effect of bacterial pH on peptide self-assembly	132
5.3.3.3 Drug release study	138
5.4 Discussion	146
5.5 Conclusions	150
Chapter 6	151
6 Fabrication and characterization of polycaprolactone peptide-enriched fabrics	151

6.1 Introduction	151
6.1.1 Introduction to electrospinning	151
6.2 Materials and methods	158
6.2.1 Materials	158
6.2.2 Methods	158
6.2.2.1 Solutions for electrospinning	158
6.2.2.2 Electrospinning process	158
6.3 Results	159
6.3.1 Scanning electron microscope, SEM.....	159
6.3.1.1 100% PCL.....	160
6.3.1.2 PCL/P ₁₁ -4.....	162
6.3.1.3 PCL/P ₁₁ -8.....	166
6.3.2 Confocal laser scanning microscope, CLSM	169
6.3.3 Energy-dispersive X-ray spectroscopy, EDX	170
6.3.4 X-ray photoelectron spectrometer, XPS.....	172
6.3.5 Attenuated total reflectance spectroscopy, ATR.....	174
6.3.6 The effect of the electrode charge on fabric morphology	174
6.3.7 The effect of peptide concentration on fabric morphology	176
6.3.7.1 Transmission electron microscopy, TEM.....	176
6.4 Discussion	179
Chapter 7	181
7 Conclusions and future work	181
7.1 Conclusions	181
7.2 Future work	182

8. References	184
Appendix	197

List of Figures

Figure 1.1: Different release mechanisms in drug delivery systems [17].....	7
Figure 1.2: The general structure of an alpha amino acid.....	16
Figure 1.3: The condensation of two amino acids forming the peptide bond.....	16
Figure 1.4: Chemical structures of amino acids [39].	17
Figure 1.5: The torsion angles phi Φ and psi ψ	18
Figure 1.6: Structure of an α -helix [40].	18
Figure 1.7: Structure of β -sheet. (A) Parallel and (B) antiparallel arrangement [41].....	19
Figure 1.8: Schematic of the formation of cyclic peptide nanotubes (right) from the flat ring-shaped conformation (left). Partially taken from Ghaderi <i>et al</i> [47].....	21
Figure 1.9: Complex of cyclic (Ala) ₁₂ containing gentamycin [51].	22
Figure 1.10: Model of self-assembly of amyloid peptide. (a) Flat bilayers. (b) Bilayers twist to form nanotubes. Partially taken from Scanlon, S. and A. Aggeli [56].....	23
Figure 1.11: Lanreotide peptide nanotubes in water. Color code: green, hydrophilic; red, aromatic hydrophobic; and blue, aliphatic hydrophobic surface of the peptide [56].....	24
Figure 1.12: (A) Schematic of folding and subsequent self-assembly when MAX1 and	24
Figure 1.13: Mechanism of self-assembly of surfactant-like peptide V ₆ D into a bilayer and then into rings that stack into a peptide nanotube [69].....	26
Figure 1.14: The Structure of the peptide amphiphile designed by Stupp <i>et al</i> . (A) Five key structural features of the molecule: 1- hydrophobic alkyl tail, 2- four cysteine residues, 3- three glycine residues, 4- serine residues to interact with calcium, 5-cell adhesion ligand. (B) Conical shape of the molecule. (C) Schematic showing the cylindrical micelle formed from the amphiphilic peptide [72].	27
Figure 1.15: Bolaamphiphilic peptides forming the nanotube. Blue= hydrophilic head, white= hydrophobic [68].....	27
Figure 1.16: Self -assembly of peptides as mediated by complementary charges [53]. .	28
Figure 1.17: (A) Structure of the ionic-complementary peptide EAK16-II. (B) Three-dimensional molecular model of EAK16s. The top, middle and bottom schemes	

represent the EAK16-I, EAK16II and EAK16-IV structures with charge distribution of - + - + - + - + , - - + + - - + +.....	29
Figure 1.18: Hierarchical β -sheet tape self-assembly [44].....	30
Figure 1.19: Behaviour of peptides as a function of pH P ₁₁ -5 [45].	32
Figure 1.20: Phase behaviour of P ₁₁ -9 as a function of pD. (a) In D ₂ O. (b) In D ₂ O containing 130 mM NaCl, I: nematic gel, II: flocculate, III: nematic fluid, IV: isotropic fluid [86].....	33
Figure 2.1: Schematic representation of transmission electron microscopy [98].	39
Figure 2.2: Schematic representation of scanning electron microscopy [103].	41
Figure 2.3: Schematic showing FT-IR components [109].	42
Figure 2.4: A multiple reflection ATR system [114].	45
Figure 2.5: Schematic diagram of the optical pathway and principal components in a laser scanning confocal microscope [119].	47
Figure 3.1: Molecular structure of P ₁₁ -2.	49
Figure 3.2: Molecular structures of peptides P ₁₁ -9 (top) and P ₁₁ -12 (bottom).....	50
Figure 3.3: Photographs of P ₁₁ -2 samples in D ₂ O (left-hand side) and their optical micrographs through cross-polar lenses (right-hand side). (A) 1, (B) 5, (C) 10, (D) 20, (E) 40.....	55
Figure 3.4: TEM image of 1 mg/ml P ₁₁ -2 in D ₂ O, one week old. Scale bar =100 nm. ..	56
Figure 3.5: TEM image of 5 mg/ml P ₁₁ -2 in D ₂ O, one week old. Scale bar =100 nm. .	56
Figure 3.6: TEM image of 10 mg/ml in D ₂ O, one week old. Scale bar =100 nm.....	56
Figure 3.7: TEM image of 20 mg/ml P ₁₁ -2 in D ₂ O, one week old. Scale bar =100.	57
Figure 3.8: TEM image of 40 mg/ml in D ₂ O, one week old. Scale bar =100.....	57
Figure 3.9: TEM image of 60 mg/ml P ₁₁ -2 in D ₂ O, one week old. Scale bar =100 nm. .	57
Figure 3.10: Fitted IR amide I' band of 20 mg/ml P ₁₁ -2 in D ₂ O showing β -sheet conformation.	58
Figure 3.11: Overlaid amide I bands for different concentrations of P ₁₁ -2 in D ₂ O.	59

Figure 3.12: Photographs of P ₁₁₋₂ samples in 90% D ₂ O and 10% HFIP (left-hand side) and their optical micrographs through cross-polar lenses (right-hand side). (A) 1, (B) 5, (C) 10, (D) 20, (E) 40 and (F) 60 mg/ml.....	60
Figure 3.13: TEM image of 1 mg/ml P ₁₁₋₂ in 90% D ₂ O and 10% HFIP, one week old. Scale bar = 100 nm.	
Figure 3.14: TEM image of 5 mg/ml P ₁₁₋₂ in 90% D ₂ O and 10% HFIP, one week old Scale bar =100 one week old.....	61
Figure 3.15: TEM image of 10 mg/ml P ₁₁₋₂ in 90% D ₂ O and 10% HFIP, one week old. Scale bar =100 nm.....	61
Figure 3.16: TEM image of 20 mg/ml P ₁₁₋₂ in 90% D ₂ O and 10% HFIP, one week old.	62
Figure 3.17: TEM image of 40 mg/ml P ₁₁₋₂ in 90% D ₂ O and 10% HFIP, after one week.	62
Figure 3.18: TEM image of 40 mg/ml P ₁₁₋₂ in 90% D ₂ O and 10% HFIP, 17 days old.	63
Figure 3.19: TEM image of 60 mg/ml P ₁₁₋₂ in 90% D ₂ O and 10% HFIP, 17 days old.	63
Figure 3.20: Fitted IR amide I band of 20 mg/ml P ₁₁₋₂ in D ₂ O and 10% HFIP showing β -sheet conformation.....	64
Figure 3.21: Overlaid IR amide I bands for different concentrations of P ₁₁₋₂ in 90% D ₂ O and %10 HFIP.....	65
Figure 3.22: P ₁₁₋₂ solutions at different levels of pD: (A) pD = 2.8, (B) pD = 5.2, (C) pD = 7.3 and (D) pD = 9.	66
Figure 3.23: TEM images of 20 mg/ml P ₁₁₋₂ in 90% D ₂ O and 10% HFIP at different pD levels. (A) pD = 2.8, (B) pD = 5.2, (C) pD = 7.3 and (D) pD = 9. All samples were one-week old. Scale bar = 100 nm.	67
Figure 3.24: Overload IR amide I' regions of 20 mg/ml P ₁₁₋₂ in 90% D ₂ O and 10% HFIP as a function of pD.	67
Figure 3.25: Photographs of peptide gels of 20 mg/ml P ₁₁₋₉ under different physiological conditions: (A) in DPBS, (B) in DMEM, (C) in physiological-like buffer and (D) in Tris buffer.	68

Figure 3.26: TEM images of 20 mg/ml P ₁₁ -9 under different physiological-like conditions: (A) in DPBS, (B) in DMEM, (C) in physiological-like buffer and (D) in Tris buffer.....	69
Figure 3.27: Fitted IR amide I' band of 20 mg/ml P ₁₁ -9 in D ₂ O containing 130 mM NaCl.....	69
Figure 3.28: Fitted IR amid I' band of 20 mg/ml P ₁₁ -9 in D ₂ O containing 130 mM NaCl and 30 mM of Tris-HCl.....	70
Figure 3.29: Photographs of peptide gels of 20 mg/ml P ₁₁ -12 under different physiological-like conditions. (A) in DPBS, (B) in DMEM, (C) in physiological-like buffer, (D) in Tris buffer.....	71
Figure 3.30: TEM images of 20 mg/ml P ₁₁ -12 under different physiological-like conditions: (A) in DPBS, (B) in DMEM, (C) in physiological-like buffer and (D) in Tris buffer.....	72
Figure 3.31: Fitted IR amide I' band for 20 mg/ml P ₁₁ -12 in D ₂ O containing 130 mM NaCl.....	72
Figure 3.32: Fitted IR amide I' band of 20 mg/ml P ₁₁ -12 in 130 mM NaCl and 30 mM of Tris-HCl in D ₂ O.....	73
Figure 3.33: Behaviour of P ₁₁ -2 in water as a function of increasing peptide concentration [44].	75
Figure 3.34: Schematic of proposed self-assembly pathways for formation of fibrils and nanotubes starting from ribbons [123].	76
Figure 3.35: Schematic of phase behaviour of P ₁₁ amino acid residue peptides in aqueous solution as functions of pH. P ₁₁ -2, P ₁₁ -3 and P ₁₁ -4 at c = 6.3 mM, P ₁₁ -5 at c = 13.1 mM [122].	77
Figure 3.36: Charge distributions on P ₁₁ -2 dimers in an antiparallel β -sheet tapelike substructure: (A) pH < 5 and (B) pH > 5. The repulsion between molecules is indicated by arrows.....	77
Figure 4.1: Molecular structures of peptide P ₁₁ -4 (top) and peptide P ₁₁ -8 (bottom).	81
Figure 4.2: Cellulose strand showing hydrogen bonding between chains [138].	83

Figure 4.3: Schematic of the dipping method for preparing regenerated cellulose fabric coated with self-assembled peptides. Green = peptide	84
Figure 4.4: Photograph of cellulose fabrics dipped in P ₁₁ -4 at 10 mg/ml.....	86
Figure 4.5: Photograph of cellulose fabrics dipped in P ₁₁ -8 at 10 mg/ml.....	86
Figure 4.6: Photograph of cellulose fabrics dipped in P ₁₁ -4 at 2 mg/ml.....	86
Figure 4.7: Photograph of cellulose fabrics dipped in P ₁₁ -8 at 2 mg/ml.....	86
Figure 4.8: TEM micrographs of peptide fibrils. (A) P ₁₁ -4 in water (10 mg/ml) at pH 2.9. (B) P ₁₁ -8 in water (10 mg/ml) at pH 10.	87
Figure 4.9: SEM micrographs of cellulose fabrics at relatively low magnification. (A) Uncoated cellulose fabric. (B) Cellulose fabric treated with HCl. (C) Cellulose fabric coated with P ₁₁ -4 (10 mg/ml).....	88
Figure 4.10: SEM micrographs of cellulose fabrics at relatively moderate magnification. (A) Uncoated cellulose fabric. (B) Cellulose fabric treated with HCl. (C) Cellulose fabric coated with P ₁₁ -4 (10 mg/ml).....	89
Figure 4.11: SEM micrographs of cellulose fabrics at relatively high magnification. (A) Uncoated cellulose fabric. (B) Cellulose fabric treated with HCl. (C) Cellulose fabric coated with P ₁₁ -4 (10 mg/ml).....	90
Figure 4.12: SEM micrographs of cellulose fabrics at relatively low magnification. (A) Uncoated cellulose fabric. (B) Cellulose fabric treated with HCl. (C) Cellulose fabric coated with P ₁₁ -4 (2 mg/ml).....	91
Figure 4.13: SEM micrographs of cellulose fabrics at relatively moderate magnification. (A) Uncoated cellulose fabric. (B) Cellulose fabric treated with HCl. (C) Cellulose fabric coated with P ₁₁ -4 (2 mg/ml).....	92
Figure 4.14: SEM micrographs of cellulose fabrics at relatively high magnification. (A) Uncoated cellulose fabric. (B) Cellulose sample treated with HCl. (C) Cellulose sample coated with P ₁₁ -4 (2 mg/ml).....	93
Figure 4.15: SEM micrographs of cellulose fabrics at relatively low magnification . (A) Uncoated cellulose fabric. (B) Cellulose fabric treated with NaOH. (C) Cellulose fabric coated with P ₁₁ -8 (10 mg/ml).....	94

Figure 4.16: SEM micrographs of cellulose fabrics at relatively moderate magnification. (A) Uncoated cellulose fabric. (B) Cellulose fabric treated with NaOH. (C) Cellulose fabric coated with P ₁₁₋₈ (10 mg/ml).....	95
Figure 4.17: SEM micrographs of cellulose fabrics at relatively high magnification. (A) Uncoated cellulose fabric. (B) Cellulose fabric treated with NaOH. (C) Cellulose fabric coated with P ₁₁₋₈ (10 mg/ml).....	96
Figure 4.18: SEM micrographs of cellulose fabrics at relatively low magnification. (A) Uncoated cellulose fabric. (B) Cellulose fabric treated with NaOH. (C) Cellulose fabric coated with P ₁₁₋₈ (2 mg/ml).....	97
Figure 4.19: SEM micrographs of cellulose fabrics at relatively moderate magnification. (A) Uncoated cellulose fabric. (B) Cellulose fabric treated with NaOH. (C) Cellulose fabric coated.....	98
Figure 4.20: SEM micrographs of cellulose fabrics at relatively high. (A) Uncoated cellulose fabric. (B) Cellulose fabric treated with NaOH. (C) Cellulose fabric coated with P ₁₁₋₈ (2 mg/ml).	99
Figure 4.21: CLSM images of cellulose fabrics. (A) Uncoated cellulose fabric. (B) Fluorescently tagged P ₁₁₋₄ peptide gel at 10 mg/ml. (C) Fabric coated with fluorescently tagged peptide P ₁₁₋₄ (10 mg/ml) at 10 X magnification. (D) Same as (C) but at 20 X magnification.....	101
Figure 4.22: CLSM images of cellulose fabrics. (A) Uncoated cellulose fabric. (B) Fluorescently tagged P ₁₁₋₄ peptide gel at 2 mg/ml. (C) Fabric coated with fluorescently tagged peptide P ₁₁₋₄ (2 mg/ml) at 10 X magnification. (D) Same as (C) but at 20 X magnification.....	102
Figure 4.23: CLSM images of cellulose fabrics. (A) Uncoated cellulose fabric. (B) Fluorescently tagged P ₁₁₋₈ peptide gel at 10 mg/ml. (C) Fabric coated with fluorescently tagged peptide P ₁₁₋₈ (10 mg/ml) at 10 X magnification. (D) Same as (C) but at 20 X magnification.....	103
Figure 4.24: CLSM images of cellulose fabrics. (A) Uncoated cellulose fabric. (B) Fluorescently tagged P ₁₁₋₈ peptide gel at 2 mg/ml. (C) Fabric coated with fluorescently tagged peptide P ₁₁₋₈ (2 mg/ml) at 10 X magnification. (D) Same as (C) but at 20 X magnification.....	104

Figure 4.25: IR spectra of a blank cellulose sample (red) and cellulose sample coated with P ₁₁ -4 (10 mg/ml) (black).	105
Figure 4.26: Band-fitted IR amide I' band of cellulose fabric coated with P ₁₁ -4 (10 mg/ml) showing β -sheet conformation.	106
Figure 4.27: IR spectrum of blank cellulose sample (red) and cellulose sample coated with P ₁₁ -4 (2 mg/ml) (black).	107
Figure 4.28: Fitted IR amide I' band of cellulose fabric coated with P ₁₁ -4 (2 mg/ml) with the β -sheet conformation.	108
Figure 4.29: IR spectra of blank cellulose sample (red) and cellulose sample coated with P ₁₁ -8 (10 mg/ml) (black).	109
Figure 4.30: Fitted IR amide I' band of cellulose coated with P ₁₁ -8 (10 mg/ml) showing β -sheet conformation.	110
Figure 4.31: IR spectra of blank cellulose sample and cellulose sample coated with P ₁₁ -8 (2 mg/ml).	111
Figure 4.32: Fitted IR amide I' band of cellulose/P ₁₁ -8 (2 mg/ml) showing β -sheet conformation.	111
Figure 4.33: Structural changes in P ₁₁ -4 nanotapes in response to changes in pH.	113
Figure 4.34: pH-dependant behaviour of P ₁₁ -4 nanotapes ● is the percentage of β -sheet by FTIR and ▲ by NMR. Adopted from Aggeli 2007 [86].	113
Figure 4.35: Structural changes in P ₁₁ -8 nanotapes in response to changes in pH.	114
Figure 4.36: pH-dependant behaviour of P ₁₁ -8 nanotapes ● is the percentage of β -sheet by FTIR and ▲ by NMR. Adopted from Aggeli 2007 [86].	115
Figure 5.1: Structures of antibiotics: (A) Vancomycin [151], (B) Levofloxacin [152].	118
Figure 5.2: Development of cellulosic fabrics coated with peptide fibril-encapsulated	120
Figure 5.3: Switchable drug release from the pH-responsive dressing stimulated by bacterial-induced changes of pH. Red is bacteria. Green is peptide. Blue is antibiotic.	121
Figure 5.4: Streaking pattern.	123

Figure 5.5: TEM images of peptides fibrils encapsulating antibiotics (A) Control P ₁₁ -4, (B) control P ₁₁ -8 (C) P ₁₁ -4/vancomycin (D) P ₁₁ -4/levofloxacin (E) P ₁₁ -8/vancomycin (F) P ₁₁ -8/levofloxacin.	125
Figure 5.6: Development of fabric coated with P ₁₁ -4 encapsulated antibiotics. (A) P ₁₁ -4 fluid solution containing vancomycin. (B) P ₁₁ -4 gel containing vancomycin. (C) P ₁₁ -4 fluid solution containing levofloxacin. (D) P ₁₁ -4 gel containing levofloxacin.....	126
Figure 5.7: Development of fabric coated with P ₁₁ -8 encapsulated antibiotics. (A) P ₁₁ -8 fluid solution containing vancomycin, (B) P ₁₁ -8 gel containing vancomycin, (C) P ₁₁ -8 fluid solution containing levofloxacin, (D) P ₁₁ -8 gel containing levofloxacin.....	126
Figure 5.8: SEM images of dressings coated with peptide fibrils containing antibiotics. (A) Control sample of cellulose fabric with vancomycin, (B) cellulose and levofloxacin, (C) cellulose fabric coated with P ₁₁ -4/vancomycin, (D) cellulosic fabric coated with P ₁₁ -4/levofloxacin, (E) cellulose fabric coated with P ₁₁ -8/vancomycin, (F) cellulose and P ₁₁ -8/levofloxacin.....	128
Figure 5.9: CLSM images of dressings coated with peptide fibrils and antibiotics. (A) Control, (B) P ₁₁ -4/vancomycin, (C) P ₁₁ -4/levofloxacin, (D) control, (E) P ₁₁ -8/vancomycin, (F) P ₁₁ -8/levofloxacin.....	129
Figure 5.10: IR spectra of a cellulose sample coated with P ₁₁ -4 peptide fibrils, cellulosic fabric coated with P ₁₁ -4/vancomycin and fabric coated with P ₁₁ -4/levofloxacin.....	130
Figure 5.11: IR spectra of a cellulose sample coated with P ₁₁ -8 peptide fibrils, cellulosic fabric coated with P ₁₁ -8/vancomycin and fabric coated with P ₁₁ -8/levofloxacin.....	130
Figure 5.12: Identification of <i>SE</i> . (A) MHA plate displaying typical colony morphology, the creamy colour of <i>SE</i> . (B) Gram stain of a single colony, grape-like clusters of Gram-positive cocci.....	131
Figure 5.13: Measurement of the pH of an <i>SE</i> culture.....	131
Figure 5.14: Effect of bacteria on the 30 mg/ml P ₁₁ -4gel. (A) Blank agar immediately after applying the P ₁₁ -4 gel, (B) blank agar one day after applying the P ₁₁ -4 gel, (C) agar with the <i>SE</i> culture immediately after applying the P ₁₁ -4 gel, (D) agar with the P ₁₁ -4 and <i>SE</i> culture after one day.	133
Figure 5.15: Effect of bacteria on the 20 mg/ml the P ₁₁ -4 gel. (A) Blank agar immediately after applying the P ₁₁ -4 gel on agar, (B) blank agar one day after applying	

the P ₁₁₋₄ gel, (C) agar with the <i>SE</i> culture immediately after applying the P ₁₁₋₄ gel, (D) agar with the P ₁₁₋₄ gel with the <i>SE</i> culture after one day	134
Figure 5.16: The effect of bacteria on the 10 mg/ml P ₁₁₋₄ gel. (A) Blank agar immediately after applying the P ₁₁₋₄ gel, (B) blank agar with the P ₁₁₋₄ gel after one day, (C) agar with the <i>SE</i> culture immediately after applying the P ₁₁₋₄ gel, (D) agar with the P ₁₁₋₄ gel and the <i>SE</i> culture after one day.....	135
Figure 5.17: Effect of bacteria on the 30 mg/ml P ₁₁₋₈ gel. (A) Blank agar immediately after applying the P ₁₁₋₈ gel, (B) blank agar with the P ₁₁₋₈ gel after one day, (C) agar with the <i>SE</i> culture immediately after applying the P ₁₁₋₈ gel, (D) agar with the <i>SE</i> culture and the P ₁₁₋₄ gel after one day.....	136
Figure 5.18: Effect of bacteria on the 20 mg/ml P ₁₁₋₈ gel at (A) blank agar immediately after applying the P ₁₁₋₈ gel, (B) blank agar with the P ₁₁₋₈ gel after one day, (C) agar with the <i>SE</i> culture immediately after applying the P ₁₁₋₈ gel, (D) agar with the <i>SE</i> culture with the P ₁₁₋₈ gel after one day.....	137
Figure 5.19: Effect of bacteria on the 10 mg/ml P ₁₁₋₈ gel. (A) Blank agar immediately after applying the P ₁₁₋₈ gel, (B) blank agar with the P ₁₁₋₈ gel after one day, (C) agar with the <i>SE</i> culture immediately after applying the P ₁₁₋₈ gel, (D) agar with the <i>SE</i> culture and P ₁₁₋₈ gel after one day.....	138
Figure 5.20: Disk diffusion test of control samples. (A) Control P ₁₁₋₄ , (B) Control P ₁₁₋₈	139
Figure 5.21: Disk diffusion test of vancomycin (16 µg/ml) released from peptide fibrils. (A) Fabric containing vancomycin, (B) fabric containing P ₁₁₋₄ -encapsulated vancomycin, (C) fabric containing P ₁₁₋₈ -encapsulated vancomycin.....	140
Figure 5.22: Disk diffusion test of the release of vancomycin (32 µg/ml) from peptide fibrils. (A) Fabric containing vancomycin, (B) fabric containingP ₁₁₋₄ -encapsulated vancocymcin, (C) fabric containingP ₁₁₋₈ -encapsulated vancomycin.....	141
Figure 5.23: Disk diffusion test of the release of vancomycin (64 µg/ml) from peptide fibrils. (A) Fabric containing vancomycin, (B) fabric containingP ₁₁₋₄ -encapsulated vancomycin, (C) fabric containingP ₁₁₋₈ -encapsulated vancocymcin.....	142
Figure 5.24: Average of inhibition zones diameters in the disk diffusion assay of vancomycin. Data is expressed as the mean (n=3) ± 95% confidence intervals. Data was analysed by one way ANOVA followed by calculation of the minimum significant	

difference by the post-hoc T test ($p < 0.05$). * = significant difference compared to the control sample.	142
Figure 5.25: Disk diffusion test for the release of levofloxacin (16 $\mu\text{g/ml}$) from peptide fibrils. (A) Fabric containing levofloxacin, (B) fabric containing levofloxacin encapsulated into P ₁₁₋₄ , (C) fabric containing levofloxacin encapsulated into P ₁₁₋₈ ...	143
Figure 5.26: Disk diffusion assay of the release of levofloxacin (32 $\mu\text{g/ml}$) from peptide fibrils. (A) Fabric containing levofloxacin, (B) fabric containing levofloxacin encapsulated into P ₁₁₋₄ , (C) fabric containing levofloxacin encapsulated into P ₁₁₋₈ ...	144
Figure 5.27: Disc diffusion assay of the release of levofloxacin (64 mg/ml) from peptide fibrils. (A) Fabric containing levofloxacin, (B) fabric containing levofloxacin encapsulated into P ₁₁₋₄ , (C) fabric containing levofloxacin encapsulated into P ₁₁₋₈ ...	145
Figure 5.28: Average of inhibition zones diameters in the disk diffusion assay of levofloxacin. Data is expressed as the mean ($n=3$) \pm 95% confidence intervals. Data was analysed by one way ANOVA followed by calculation of the minimum significant difference by the post-hoc T test ($p < 0.05$). * = significant difference compared to the control sample.	145
Figure 5.29: β -Sheet percentage of P ₁₁₋₄ ● as determined by FTIR and ▲ by NMR. I: nematic gel, II: flocculate, III: nematic fluid, IV: isotropic fluid [86].....	148
Figure 5.30: β -Sheet percentage of P ₁₁₋₈ ● as determined by FTIR and ▲ by NMR. I:isotropic fluid, II: biphasic solution, III: nematic gel [86].	148
Figure 5.31: The hypothesis of the therapeutic release from P ₁₁₋₄ fibrils. Green is peptide, blue is antibiotic.	149
Figure 5.32: The hypothesis of the therapeutic release from P ₁₁₋₈ fibrils. Green is peptide, blue is antibiotic.	149
Figure 6.1: Publications on electrospinning [159].	152
Figure 6.2: Electrospinning equipment [162].	152
Figure 6.3: An electrospun PCL membrane made by Bolgen et al. A) SEM micrograph. B) an optical micrograph [167].	154
Figure 6.4: ESEM photographs of BCNU/PEG–PLLA fibres containing 10% wt of BCNU [169].	155

Figure 6.5: SEM images of electrospun scaffolds. (A) PCL scaffold; (B) PCL-EAK scaffold [171].	156
Figure 6.6: SEM images SEM images of electrospun scaffolds (A) PEO scaffold; (B) PEO with 0.059% (w/v) EAK [172].	157
Figure 6.7: Schematic illustrates the hypothesis of the PCL/peptide fibres preparation. Gray; PCL. Blue; P ₁₁ -4. Red P ₁₁ -8.	157
Figure 6.8: Effect of distance on 100% PCL fibre' diameters. (A) tip to collector = 18 cm; Mag 2.36 KX. (B) tip to collector =18 cm; Mag 49.14 KX. (C) tip to collector = 20 cm; Mag 2.9 KX .(D) tip to collector = 20 cm; Mag 63.63 KX (voltage= 25 kV; at room Temp).	161
Figure 6.9: Effect of temperature on 100% PCL fibre' diameters. (A) room temp; Mag 4.5 KX. (B) room temp; Mag 27.14 KX. (C) 50 °C; Mag 3.8 KX . (D) 50 °C; Mag 83.63 KX (voltage = 25 kV; distance =16).	161
Figure 6.10: Effect of voltage on 100% PCL fibre' diameters. (A) V=15 kV; Mag 2.36 KX. (B) V =15 kV; Mag 49.14 KX. (C) V = 20 kV; Mag 2.9 KX. (D) V = 20 kV; Mag 63.63 KX (room temp; distance=18).	162
Figure 6.11: Effect of distance on PCL/P ₁₁ -4 fibbers' diameters. (A) tip to collector =16 cm; Mag 2.02 KX. (B) tip to collector = 16 cm; Mag 100.00 KX. (C) tip to collector = 18 cm; Mag 3.06 KX. (D) tip to collector = 18 cm; Mag 40.32 KX (V =15 kV; room temp).	163
Figure 6.12: : Effect of temperature on PCL/P ₁₁ -4 fibres' diameters. (A) room temp; Mag 6.61 KX. A2) at room temp; Mag 111.71 KX. (C) at 50 °C; Mag 3.8 KX. B2) 50 °C; Mag 83.63 KX (voltage = 20 kV; tip to collector distance = 20).	164
Figure 6.13: Effect of voltage on PCL/P ₁₁ -4 fibre' diameters. (A) 15 kV; Mag 2.36 KX. (B) 15 kV; Mag (C) 20 kV; Mag 1.9 KX . (D) 20 kV; Mag 57.63. (E) 25 kV; Mag 43.82. (F) 25 kV;	165
Figure 6.14: Effect of distance on PCL/P ₁₁ -8 fibbers' diameters. (A) tip to collector = 16 cm; Mag 3.55 KX. (B) tip to collector =16 cm; Mag 43.14 KX. (C) tip to collector = 18 cm; Mag 6.36 KX. (D) tip to collector = 18 cm; Mag 73.63 KX. (E) tip to collector = 20 cm; Mag 8.75 KX. (F) tip to collector = 20 cm; Mag 143 KX (voltage= 25 kV; at room Temp).	167

Figure 6.151: Effect of temperature on PCL/P ₁₁ -8 fibres' diameters. (A) room temp; Mag 6.61 KX. (B) at room temp; Mag 111.71 KX. (C) at 50 °C; Mag 3.8 KX . (D) 50 °C; Mag 83.63 KX (voltage = 20 kV; tip to collector distance = 18 cm).	168
Figure 6.16: Effect of voltage on PCL/P ₁₁ -8 fibre' diameters. (A) 15 kV; Mag 2.36 KX. (A) 15 kV; Mag 57.14 KX. (C) 20 kV; Mag 1.9 KX . (D) 20 kV; Mag 57.63 KX. (E) 25 kV; Mag . (F) 25 kV; Mag (Temp= 50 °C; distance = 16).	169
Figure 6.17: Visualization of fluorescence-labelled P ₁₁ -4 in PCL fibres.....	170
Figure 6.18: EDX spectra of electrospun fibres. (A) Control PCL. (B) PCL/P ₁₁ -4.....	171
Figure 6.19: XPS spectra of the electrospun samples of 100% PCL.	172
Figure 6.20: XPS spectra of the electrospun samples (B) PCL/P ₁₁ -4. (C) PCL/P ₁₁ -8.	173
Figure 6.21: IR spectra of electrospun fabric. (A) before electrospinning. (B) after electrospinning. (C) overlaid band fitted of amide I for PCL/P ₁₁ -8 and PCL/P ₁₁ -4.	175
Figure 6.22: SEM images of electrospun fibres. (A) and (B) low and high magnification of PCL/P ₁₁ -4. (C) and (D) low and high magnification of PCL/P ₁₁ -8.	176
Figure 6.23: SEM images of PCL/P ₁₁ -8 with high concentration of P ₁₁ -8.	177
Figure 6. 24: TEM image of PCL/P ₁₁ -8 showing thick and thin fibres.	178
Figure 6.25: The EDX spectrum of PCL/P ₁₁ -8. (A) thick. (B) thin fibre.	178

List of Tables

Table 2.1: Infrared bands of the peptide [111].....	43
Table 2.2: The amide I' region component bands [111, 112].....	44
Table 2.3: Infrared bands of amino acids side chains [111].	44
Table 3.1: Preparation methods for P ₁₁ -2 solutions in D ₂ O.....	51
Table 3.2: Preparation methods for P ₁₁ -2 solutions in 90% D ₂ O and 10% HFIP.....	52
Table 3.3: Conditions for preparation of P ₁₁ -9 gels.	53
Table 3.4: Conditions for preparation of P ₁₁ -12 gels.	53
Table 3.5: Identification of peaks in the fitted IR amide I' band of 20 mg/ml P ₁₁ -2 in D ₂ O.....	59
Table 3.6: Identifications of peaks in the IR amide I' band of 20 mg/ml P ₁₁ -2 in 90% D ₂ O and 10% HFIP.....	65
Table 3.7: Identifications of peaks in the fitted IR amide I' band of 20 mg/ml P ₁₁ -9 in D ₂ O containing 130 mM NaCl.....	70
Table 3.8: Identification of peaks in the IR fitted amide I' band of 20 mg/ml P ₁₁ -9 in D ₂ O containing 130 mM NaCl and 30 mM Tris-HCl.....	71
Table 3.9: Identification of peaks in fitted IR amide I' band of 20 mg/ml P ₁₁ -12 in D ₂ O containing 130 mM NaCl.....	73
Table 3.10: Identification of peaks in fitted amide I' band for 20 mg/ml P ₁₁ -12 in 130 mM NaCl and 30 mM of Tris-HCl in D ₂ O.	74
Table 4.1: Identifications of peaks in the fitted amide I' band of cellulose coated with P ₁₁ -4 (10 mg/ml).	106
Table 4.2: Identifications of peaks found in fitted amide I' band of cellulose coated with P ₁₁ -4 (2 mg/ml).	108
Table 4.3: Identification of peaks found in fitted amide I' band of cellulose coated with P ₁₁ -8 (10 mg/ml).	110
Table 4.4: Identification of peaks found in fitted amide I' band of cellulose coated with P ₁₁ -8 (2 mg/ml).	112

Table 6.1: Electrospinning parameters.....	159
Table 6.2: The chemical elements in the elctrospun fibres by SEM/EDX.	172
Table 6.3: The chemical elements in the elctrospun fibres by XPS.....	173

List of Abbreviations

A β	Amyloid β -sheet
ATR	Attenuated total reflectance
C*	Critical aggregation concentration
DOX	Doxorubicin
DMEM	Dulbecco's Modified Eagle Medium
DNA	Deoxyribonucleic acid
EDX	Energy-dispersive X-ray spectroscopy
ECM	Extra cellular matrix
FTIR	Fourier transform infra-red spectroscopy
FDA	Food and Drug administration
GnRH	Gonadotropin-releasing hormones
HA	Hydroxyapatite
HFIP	Hexafluoroisopropanol
IRS	Internal reflection spectroscopy
MMPs	Matrix metalloproteinases
MIR	Multiple internal reflectance
MRSA	Methicillin-resistant Staphylococcus aureus
n/w	Narrow width
PET	Polyethylene terephthalate
PEVA	Polyethylene-co-vinyl acetate
PGA	Polyglycolic acid
PTFE	Polytetrafluoroethylene
PHB	Poly(3-hydroxybutyrate)
PHBV	Poly(3-hydroxybutyrate-co-3-hydroxyvalerate)
PDLLA	Poly(D,L-lactide)

PLA	Poly(lactic acid)
PLLA	Poly(L-lactic acid)
PCL	Polycaprolactone
SEM	Scanning electron microscopy
SE	Staphylococcus epidermidis
TFA	Trifluoroacetic acid
TG	Tegaderm polyurethane
w/w	Wide width

Chapter 1

1 Introduction

1.1 Introduction to medical fabrics

The word fabric is broadly defined as a flexible sheet consisting of a network of natural or artificial fibres. Medical fabrics are used in medical applications and play a major role in every stage of human health from detecting symptoms and diagnosis to curing diseases [1]. The technology of medical fabrics has developed significantly to meet human needs. Large varieties of medical materials are being produced, ranging from simple bandages to permanent body implants. In the United States alone, the revenue from medical textile product sales was estimated at about \$11.3 billion in 1980. This number rose to \$32.1 billion in 1990 and further increased to \$76 billion in 2000. In Europe, medical textile sales comprise about 10% of the textile market, with an annual growth rate of about 4% [2]. Medical fabrics can be categorized into four areas of applications:

- Healthcare and hygiene products.
- Extracorporeal devices.
- Non-implantable materials.
- Implantable materials [3].

1.1.1 Healthcare and hygiene products

The term ‘healthcare and hygiene products’ refers to a wide range of disposable or non-disposable materials used for human healthcare in everyday life, such as clothes, wipes, blankets, pillowcases, feminine products, baby care as well as hospital staff apparel including surgical masks, gloves and surgical head wear [4].

In hospitals, spread of infectious material is a common problem in operating theatres; thus, a clean environment is required. Disposable surgical materials and surgical gowns have been developed to act as textile barriers against microorganisms. Several synthetic and natural antimicrobial agents are widely used in hospital textiles, such as antibiotics, phenols, iodophors, silver, aloe vera and tea tree oil [3]. Vego *et al.* performed several studies on the development of antimicrobial finished fabrics to serve as advanced antimicrobial barriers for hospital use. Antibacterial polyester is one example of their products that was enhanced by the addition of polyethylene glycol to polyester fabrics. They found that the treated fabric was resistant to *Staphylococcus epidermidis*, *Candida albicans* and *Aspergillus fumigatus* [1].

1.1.2 Extracorporeal devices

Extracorporeal devices are medical devices used to purify blood outside the body. Examples include the artificial kidney, artificial liver and mechanical lung. Artificial kidneys are used in haemodialysis to filter waste products, such as urea and creatinine from blood. It is usually used when kidneys are in renal failure. The process is performed by circulating the blood through semi-permeable membranes to remove waste materials. The membranes can be either flat sheets or a bundle of hollow fibres. Similar to an artificial kidney, an artificial liver is an extracorporeal device that supports patients with acute liver failure. The artificial liver also utilizes ultrafiltration membranes to purify a patient's blood. An artificial lung is a microporous membrane that is permeable to gas but not liquid; hence, it provides a patient's blood with oxygen and removes carbon dioxide. Medical textiles used for producing these devices are made from materials such as regenerative cellulose, polyester, polypropylene and silicon [2].

1.1.3 Implantable materials

Fabrics are widely used as implanted material for soft and hard tissue engineering applications owing to their strength, flexibility and porosity. Their porosity can be adjusted to be produced with different diameters and shapes as the porosity determines the rate of human tissue growth. The fibres diameters also can be controlled to produce either large or small fibres depending on the application they are applied for and the

defected organ to be repaired. They can be made from either degradable or non degradable polymer, also depending on the application they are used for. For example, heart valve implants must be made from non-degradable material, while hernia repair requires biodegradable polymers in physiological conditions. Finally, for successful implantation, fabrics should be made from non-toxic material and must be free from contamination [2, 5].

Examples of clinical applications of fibrous materials for reconstructing hard and soft tissues are briefly described below.

1.1.3.1 Implantable materials for hard tissue engineering

Hard tissue engineering uses scaffolds in combination with living cells to restore hard tissue, such as bones and joints. Natural polymers such as calcium alginate, collagen type I and hyaluronan have been used for osteoconductivity. Collagen type I is a natural material used for 3D scaffolds for bone regeneration. It is the major component of the extracellular matrix. However, collagen has some limitations. It dissolves in living tissues, and it has poor mechanical strength. To improve collagen scaffold properties, researchers have developed hybrid scaffolds of collagen with inorganic materials or synthetic polymers [6]. For example, the combination of polyglycolic acid (PGA) and collagen sponges with basic fibroblast growth factor and dexamethasone was found to be more effective for bone regeneration than conventional materials [7]. PGA with poly (D, L-lactide urethane) is another example of scaffolding material widely used for bone tissue engineering. This hybrid has shown excellent physical properties and can be formed into shapes at 60 °C, which allows surgeons to shape it during surgery [2].

1.1.3.2 Implantable materials for soft tissue engineering

i. Vascular grafts

Vascular engineering involves the use of artificial grafting materials to replace damaged arterial vessels. Grafting materials act as temporary substrates for cell growth and are absorbed by surrounding tissues; the end result is a biological vascular graft. Ideal

vascular graft materials should be non-thrombogenic, elastic, able to maintain long-term tensile strength and highly porous to allow cell ingrowth [8].

For the first half of the twentieth century, grafting materials were made from glass, silver and rubber; however, these were not entirely successful because they were rejected by the body. In 1953, after years of research, Voorhees et al. found that tubes made from plastic were accepted by the body [3, 8]. This finding was followed by the development of various grafting materials made from synthetic polymers, such as polytetrafluoroethylene (PTFE), which was patented by DuPont in 1944 [9], and polyethylene terephthalate (PET), which was first implanted by Julian in 1957 [3, 8, 10, 11].

Several modifications meant to improve graft properties, such as coating them with different biofunctional polymers, have been made. Biologically derived substances such as collagen, chitosan, elastin and albumin are also used to coat grafts. For example, Dacron grafts are coated with protein (collagen/albumin) and antibiotics to reduce blood loss and prevent infection [8]. Despite the progress made in textile graft technology, improvements are still required. Researchers are currently focusing on developing high-performance grafts using appropriate materials and technologies, such as using electrospinning to produce advanced nanografting materials, see chapter 6 [8, 12].

ii. Hernia repair

Although hernias can occur in different places in the body, they occur most often at weak spots or scars in the abdominal wall. Hernia repair mesh is usually made from porous fabrics. At the implanted site, the mesh is absorbed, and a new biological membrane is formed. Varieties of modified composite meshes with enhanced properties have been developed, such as meshes with antibacterial activity. For example, Dualmesh[®] Plus is a hernia repair product containing silver carbonate and chlorhexidine diacetate, which inhibits microbial colonization at the implanted site [13]. Another example of a modified mesh is a polypropylene mesh coated with bioabsorbable omega-3 fatty acids, which helps repair ventral hernias. This coated mesh has been shown to be more effective than uncoated ones. Although hernia meshes perform well, the ideal graft for hernia repair has not yet been developed [14].

iii. Nerve tissue regeneration

The most common way to repair peripheral nerve injury is to reconnect ends of the damaged nerve stumps. However, in some cases, this cannot be done, so nerve grafts are used to regenerate peripheral nerves. Fibrous scaffolds are promising materials for regenerating axons because they serve as a growth substrate for neural cells. For example, a blend of poly (3-hydroxybutyrate) (PHB) and poly(3-hydroxybutyrate-co-3-hydroxyvalerate) (PHBV) was studied by Mesaeli et al. They found that the addition of collagen type I to the scaffold blend provided a more favourable environment for Schwann cell growth and myelin sheath regeneration compared to scaffold without collagen [15, 16].

1.1.4 Non-Implantable materials

Non-implantable materials are used for external applications, such as bandages, gauzes, wound care products, antimicrobial barriers, cosmetic materials and drug-releasing textiles such as transdermal patches [3].

1.1.4.1 Drug-releasing textiles

Common medication methods, such as oral tablets or venous injections, may result in drug deficiencies. For example, oral drugs may metabolize in the intestinal tract and lose their activity before fulfilling their purpose. To cure this problem, high drug doses are required, which may, in turn, be toxic. Thus, it would be advantageous to have a more advanced delivery system that increases drug bioavailability at a specific site with limited side effects. Textiles are an attractive choice for drug-delivery applications. Depending on the clinical application, they can be applied as non-implantable or implantable textiles such as anti-adhesive patches for surgical application [17, 18].

1.1.4.1.1 Fabrication methods for drug-releasing textiles

Drug-releasing textiles can be fabricated by different methods, including coating, encapsulation, bioconjugation and ion-exchange [3, 17]. Each method is briefly described below.

i. Coating

Coating is a simple method in which the drug is directly loaded onto the fabric surface by dipping the fabric in a drug solution. Drugs may also be encapsulated in micro- or nanomaterials before coating [3]. This method is described in more detail in Chapter 4.

ii. Encapsulation

Encapsulation refers to any process in which the drug is loaded within the textile structure. To encapsulate drugs within a textile, a homogeneous mixture of the drug and the dissolved textile polymer is prepared. Electrospinning is one of the most efficient techniques for fabricating drug encapsulated textiles for various biomedical applications, including tissue engineering and drug delivery [3]. This technique is described in detail in Chapter 6.

iii. Ion-complexes

In ion complexing, the drug is associated to the fabric via charges on the fabric surface and on drug molecules. In these complexes, drugs are the mobile counter ions that are released by an ion-exchange process in physiological systems [3].

iv. Bioconjugation

Bioconjugation refers to the coupling of two biomolecules with a stable covalent link. In drug-releasing textiles, bioconjugation is used to covalently couple drug molecules to a fabric surface when fabric surfaces are modified by attached biofunctional groups. Functional groups can be synthetically created by different methods, including wet chemistry and plasma treatment [3].

v. Inclusion compounds

An inclusion compound is a complex in which a small molecule resides within the molecular cavity of a larger molecule. Cyclodextrin, which has a hydrophobic core and a hydrophilic outer surface, is most commonly used as a large molecule for inclusion compounds in drug-releasing textiles [3].

1.1.4.1.2 Drug- release mechanisms

When working to develop advanced drug-releasing textiles, it is important to consider how drugs are released in or on the body. For optimal performance, a drug must be released in a controlled manner. Controlled drug release is defined as delivering a required amount of a drug over a defined period of time. Drug-delivery systems can be adjusted to release the drug in three different ways: immediate release, extended release or triggered release (see Figure 1.1) [17]. The choice from these three mechanisms should be made in accordance with the pharmaceutical requirements. The mechanisms of release are briefly discussed below.

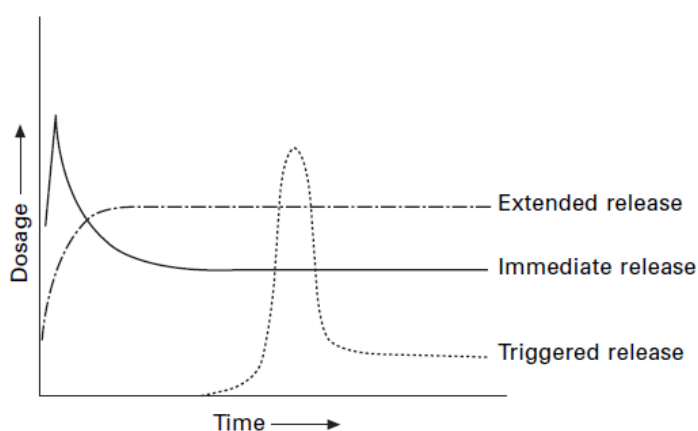


Figure 1.1: Different release mechanisms in drug delivery systems [17].

i. Immediate release

With immediate release, the drug is released in a short time. The release is controlled by factors, such as digestive juices in the stomach and intestinal tract. To maintain effective action, this type of release requires a high dosage of the drug. At the beginning of treatment, the drug concentration rapidly increases, followed by a sharp decline (Figure 1.1). This type of release is usually prescribed when immediate action is required [17].

ii. Extended release

In extended release, also called prolonged or sustained drug release, the drug is applied in a low effective dose and is delivered at a constant rate of release over a prolonged period, which can range from hours to days to years. Therefore, dosing frequency is reduced. Different principles such as diffusion and dissolution are used to control the

drug release rate from drug-releasing textiles. In the diffusion-controlled system, the drug release rate is determined by the diffusion coefficient of the drug released from the textile polymer. In the dissolution-controlled system, the rate of drug release is determined by the dissolution rate of the polymer used to fabricate the drug-encapsulating textile [17, 18].

iii. Triggered release

In a triggered release, also called a delayed release, the drug is released when the delivery system is stimulated by an external trigger such as pH, temperature or ionic strength [17]. Once triggered, the release rate of the triggered drug can be modified either to immediately release the whole drug content or to follow a slow extended release protocol. An ion-exchange system is an example of a triggered release. The release rate of the triggered drug is controlled by ionic properties of mobile ions in the fabric together with the ionic strength of the surrounding area [17].

1.1.4.2 Wound care dressings

1.1.4.2.1 Wounds

According to the Wound Healing Society, a wound is defined as damage to or a break in the skin. This damage can obstruct the anatomical structure and protective function of the skin [19].

Wounds have many causes such as external factors resulting from physical or chemical injury and may be exacerbated by the underlying physiological condition of the patient. Physical causes include abrasion, knives, gun shots, and surgical instruments. obstruct chemicals also cause wounds as well as radiation and electricity [19].

Based on healing time, wounds are frequently classified as either acute or chronic. Acute wounds usually heal completely within 8–12 weeks. Chronic wounds persist beyond a twelve-week period. Chronic wounds are often hard to heal or, in the worst case, never heal. Such wounds are characterized by the loss of skin or underlying soft tissue, such as pressure sores and venous or diabetic ulcers [19, 20]. Since they do not respond to conventional treatments, chronic wounds are a major burden on healthcare

providers because of the long healing time and large nursing costs associated with managing patients [21].

1.1.4.2.2 Wound exudates

Wound exudate is a fluid produced by damaged blood vessels in a wound and contains electrolytes, nutrients, proteins, inflammatory mediators, protein digesting enzymes, such as matrix metalloproteinases (MMPs), growth factors and waste products, as well as various types of cells (e.g. neutrophils, macrophages and platelets). Exudates play an important role in wound healing. In healthy patients, exudates promote cell proliferation, provide nutrients for cell metabolism and aid the autolysis of necrotic tissue. However, in chronic wounds, exudates can interfere with the viability of the growth factor and slow cell proliferation. Elevated levels of MMPs in chronic wounds have been associated with poor wound healing because neotissue may be enzymatically degraded. In this situation, exudates have been described as having ‘corrosive’ effects on wounds; in such situations, the wound becomes locked in the inflammatory stage of healing and does not progress to granulation and epithelialisation [22].

1.1.4.2.3 Wound healing

Wound healing can be simply defined as a skin reparation process. It is a biological process required to re-establish the integrity of damaged tissue. This process appears to be simple, but in fact, three overlapping phases occur during the repair of damaged tissue: the haemostasis/inflammatory phase, proliferative phase and maturation phase [20, 23-26].

A detailed discussion of the mechanisms of wound healing is outside the scope of this study; however, to provide relevant context for the experimental study that follows in later chapters, it is instructive to briefly review the main stages.

i. Haemostasis/ Inflammatory phase

Haemostasis is achieved within a few minutes of injury, commonly up to a period of 24 h. It is the process in which the flow of blood from injured vessels is prevented. It is initiated by clotting factors that convert blood from liquid to solid. One important

clotting factor is fibrinogen, which stimulates the clotting mechanism to form a network of fibrin in the wound, thereby preventing bleeding [20].

ii. Proliferative phase

In the proliferative phase, granulation tissue is formed, which is a soft rudimentary tissue containing fibroblasts, inflammatory cells, hyaluronic acid, endothelial cells, new blood vessels and collagen [20].

iii. Maturation and the remodelling phase

Maturation is the final stage that can take a long time, usually, several months to years after injury. It involves the formation of the connective tissue and strengthening of new connective tissue and strengthening of the new epithelium, which determine the final scar [20].

1.1.4.2.4 Wound infection complications

The term “wound infection” is clinically defined as the development of a microorganism colony in the wound site. Microorganisms are classified as fungi, viruses, and bacteria. Bacteria are classified as Gram-negative and Gram-positive bacteria depending on their structure. Gram-negative bacteria include *Escherichia coli* and *Pseudomonas aeruginosa*. Gram-positive bacteria include *Staphylococcus aureus* and *staphylococcus epidermidis* [8]. When the skin is injured, subcutaneous tissues are vulnerable to microorganism colonisation. The removal and replacement of dressings also exposes the wound site to potential contamination by microorganisms. The three main sources of microorganism contamination of wounds are: (i) exogenous sources such as microorganisms suspended in air or present on the implement causing the injury, (ii) the surrounding skin microflora such as *Staphylococcus epidermidis*, (iii) endogenous sources such as gut and oral flora. Both acute and chronic wounds are susceptible to be contaminated by any one of these sources of infection. Such contamination causes wound inflammation, pain, and a reduction in the speed on the healing process [27, 28]. Extended healing times are particularly likely if the bacterium

is able to develop from its planktonic state to biofilm form. Once established biofilms are responsible for poor healing outcomes and they are common in chronic wound sites.

1.1.4.2.5 Wound dressings

Open wounds can be readily infected by microorganism colonization unless a protective layer is provided in the form of a suitably designed dressing [29]. Moist wound healing is critical to good healing outcomes and requires exudates to be effectively managed by the dressing. Dressings should also be capable of gas exchange as well as permitting the permeation of moisture vapour from the wound and diffusion of oxygen into the wound site. All required properties of a wound dressing are rather difficult to generalize because of the large variety of wound types that must be managed and because the state of a wound changes with time. Clearly, it is important to select the most suitable dressing from those that are clinically approved. For example, heavily exuding wounds require absorbent dressings to prevent the maceration of the surrounding tissue; these dressings must be capable of removing fluid at a rate that prevents the wound site from drying out.

Wound dressings may be classified on the basis of their polymer composition (e.g. natural or synthetic), form (e.g. non-woven, foam, hydrogel) or function (low adherent, antimicrobial, absorbent, occlusive). The classification may also refer to either traditional or modern dressings [19].

(1) Traditional dressings

Traditional dressings can be thought of as passive products, such as bandage, tulle, gauze and cotton wool. These dressings can be made from either natural or synthetic polymers or combinations of the two. Their primary function is to cover the wound and absorb exudates; however, they are becoming increasingly less common because of their functional limitations:

- Limited ability to prevent infection
- Disruption of the wound bed during removal
- Limited or no oxygen permeability
- Require frequent dressing changes

- Promote a dry environment that is unfavourable for healing [30].

Despite these limitations, traditional dressings are still used for the debridement or cleaning of minor wounds [30].

(2) Modern dressings

A range of modern dressings has been developed to address the performance requirements for an optimal wound healing environment. These dressings are designed to address one or more of the following needs:

- Provide a moist wound healing environment and protect the wound from dehydration.
- Allow effective oxygen exchange between the wound and the external environment, providing circulation to aid tissue regeneration.
- Biocompatible, nontoxic and non-immunogenic.
- Ease of application to the wound surface and removal without pain to the patient.
- Facilitate delivery of bioactive agents to accelerate wound healing [19].

Some of the major commercially successful dressings are classified according to their material form, as described below.

i. Hydrocolloid dressings

Hydrocolloid dressings are used for moderately exuding wounds such as minor burns and traumatic injuries. They are made from colloidal materials combined with an outer adhesive layer. Colloidal materials include gel forming agents such as gelatine and pectin. Hydrocolloid materials interact with the wound exudate to form a gel, which enhances the formation of granulation tissue. One disadvantage of this type of dressing is that it can produce an unpleasant odour. Commercial examples of hydrocolloid dressings include TegisorbTM (3M Healthcare, Loughborough, UK) and Comfeel (Coloplast, Peterborough, UK) [31].

ii. Hydrogels

Hydrogels are swellable hydrophilic materials that are intended to improve reepithelisation of wounds. They can be made from synthetic polymers such as poly(methacrylates) and poly(vinylpyrrolidone). They are composed of approximately 70% water which allows them to promote rehydration [32]. Due to the high water content, they are unable to treat wounds that are highly exuding. Thus, they are suitable for moderately exuding wounds by swelling and storing water within their structure [19]. They need to be frequently changed since once the absorbent capacity has been reached there is a risk of leakage. Examples of hydrogel dressings include Nu-gelTM (Johnson & Johnson, Acost, UK) and PurilonTM (Coloplast) [19, 31, 33].

iii. Foam dressings

Foam dressings are usually made of polyurethane. The void structure within the dressing provides volume for fluid absorption so that, depending upon their surface wetting characteristics, they can be used for heavily exuding wounds. Examples of foam dressings include Lyofoam[®] (Conva Tec) and Allevyn[®] (Smith and Nephew) [19].

iv. Alginate dressings

Alginate dressings are commonly based on calcium alginate and are derived from alginic acid extracted from seaweed [34, 35]. They are highly absorbent and biodegradable. When applied to the wound, calcium ions present in the alginate fibres exchange with sodium ions present in the wound exudate forming sodium alginate gel, which provides a moist wound healing environment and low adherence to the wound site. Alginate dressings are normally delivered as fibrous assemblies known as nonwovens and are popular because they can stimulate epithelial proliferation and improve some cellular process in wound healing. Examples of alginate dressings include KaltostatTM (ConvaTec) and SorbsanTM (3M Healthcare) [31].

vi. Film dressings

Film dressings are made from nylon derivatives. They are usually supported by an adhesive polyethylene layer to make them adhesive. They are unable to absorb large

volumes of exudates and need to be frequently changed to avoid the accumulation of excess exudate and resultant bacterial proliferation. Available products include Opsite™ (Smith and Nephew) [19, 31].

vii. Biological dressings

Biological dressings, sometimes called bioactive dressings, can play an active part in wound healing and new tissue formation. Such dressings can also play a role in tissue engineering applications. These dressings incorporate bioactive agents, such as antibiotics and growth factors. One example is the use of hyaluronic-acid-modified liposomes produced as drug carriers to deliver growth factors to wound sites [19].

1.2 Advantages and limitations of current drug-releasing textiles

Textiles have advantageous properties such as strength, flexibility, porosity and the ability to design them with desired criteria. Thus, textile technology has a number of diverse applications in the medical and healthcare sectors, ranging from disposable wipes to artificial organs to drug-releasing applications. This project is an attempt to contribute to the development of smart medical textiles, in particular, to development of controlled drug-release textiles for wound care.

The delivery of therapeutic drugs into wounds is a developing area. Most of modern dressings are not designed to deliver bioactive agents to a wound in a control manner. They are rarely reported to control the drug release. The release of a drug into a wound in an uncontrolled manner is a common limitation of drug releasing dressings. If the release rate is too high, the drug can be unloaded from the dressing before infection is arrested. Furthermore, a 'burst release' within the first few hours may lead to overdose cytotoxicity, which can give rise to delayed wound healing, or to the development of antibiotic resistance [36]. Inversely, if the release rate is too low, the drug delivery may be below the effective therapeutic dose that is required to be effective. Another limitation caused by uncontrolled drug release from wound dressings is that it leads to the need for frequent changes. When the dressing is removed, the newly formed

epithelium can be damaged, so limiting dressing changes is usually considered to be beneficial [36, 37].

To overcome these limitations, attention has been paid to develop materials that provide potential for controlled drug delivery. Controlled drug delivery to wounds normally means the delivery of an active agent to the wound site in a sustained manner. The ideal bioactive dressing should release the drug at the optimum therapeutic concentration followed by a sustained constant delivery [37]. These criteria can limit the frequency of dressing changes. Under these circumstances patient compliance can be improved, especially in those suffering from chronic wounds, where the patient needs to undergo extended periods of treatment [19]. In light of such considerations, there is a need for a more conservative approach for smart wound-care materials that are more effective and more functional than traditional materials. Optimistically, the addition of self-assembling peptides as a biofunctional component to medical fabrics could have the potential to combine the advantages of triggered release with slow kinetic release.

1.3 Introduction to peptides

Before discussing self-assembling peptides, it is worthwhile reviewing peptide composition and structure.

1.3.1 Primary structure of peptide

Peptides are linear chains synthesized from the polymerization of amino acid building blocks. Amino acids are very small biomolecules with an average molecular weight of 135 Dalton. Amino acid molecules have a central carbon atom ($C\alpha$) that is attached to an amine group (NH_2), a carboxyl group ($COOH$) and a side chain (R) (Figure 1.2). When a carboxyl group on one amino acid reacts with an amine group on an adjacent amino acid, one water molecule is released; this process is known as a condensation reaction (Figure 1.3).

There are 20 natural amino acids used as building blocks for peptides (Figure 1.4). They are classified in four ways according to their side chains: (1) non-polar and neutral (hydrophobic), (2) polar and neutral, (3) acidic and polar, (4) basic and polar [38]. All amino acids, except glycine, are chiral as they can form two stereoisomer around the central carbon; they are called L and D. L is for left-handed form and D is for right handed form.

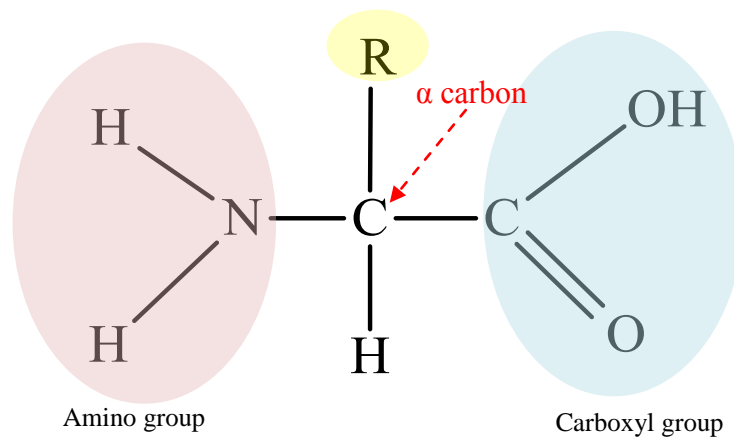


Figure 1.2: The general structure of an alpha amino acid.

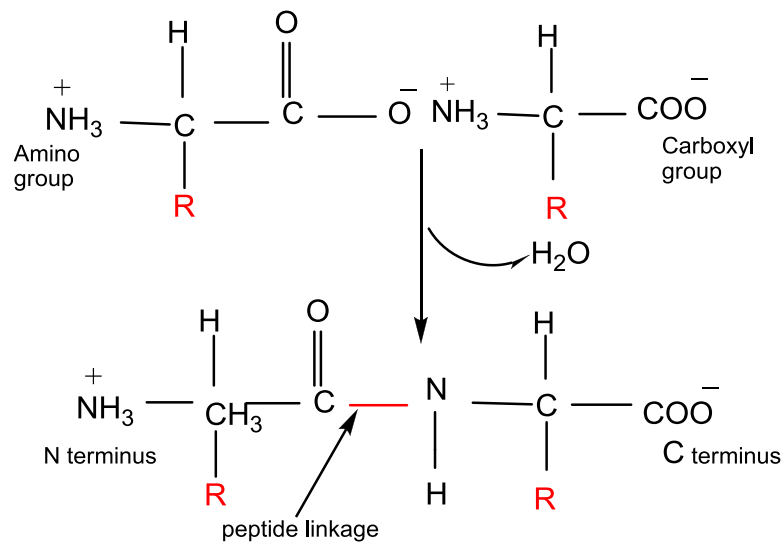


Figure 1.3: The condensation of two amino acids forming the peptide bond.

Twenty standard Amino Acids

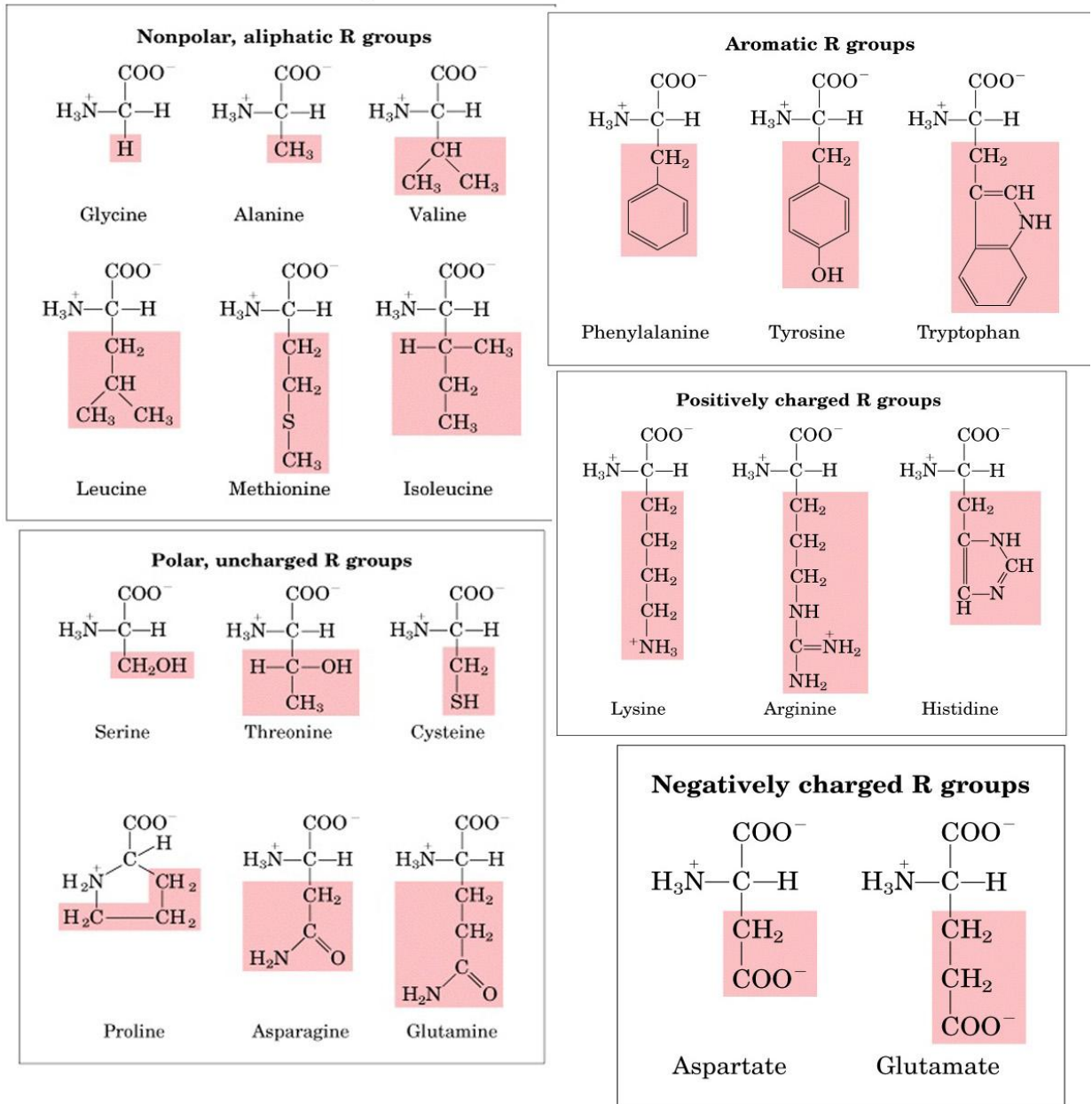


Figure 1.4: Chemical structures of amino acids [39].

1.3.2 Secondary structure of peptide

Secondary structure refers to certain repetitive conformations of the peptide backbone. The conformation of the backbone is determined by the torsion angles Φ and ψ (Figure 1.5). Based on these angles, there are two common peptide conformations: the α -helix and β -sheet [38].

1.3.2.1 α - Helix

The α -helix is a right-handed coil resulting when a series of residues that have ϕ and ψ angles of around 60° and 50° respectively. It is stabilized by hydrogen bonding between N-H and C=O groups of residues which are four positions apart (i and $i+4$). There are about 3.6 residues per turn of the helix (Figure 1.6) [38].

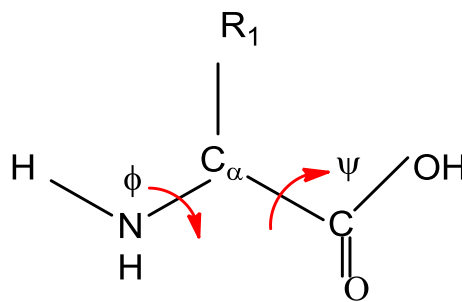


Figure 1.5: The torsion angles phi Φ and psi ψ .

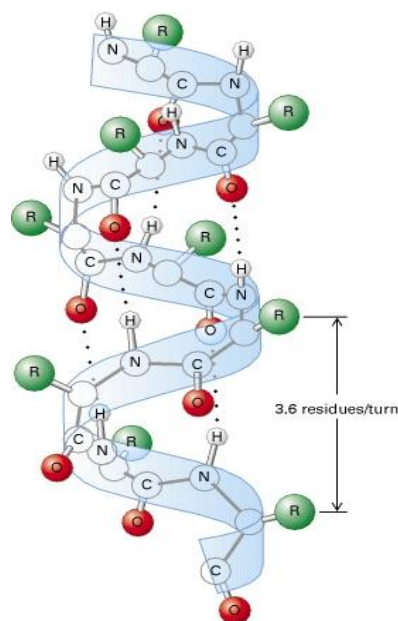


Figure 1.6: Structure of an α -helix [40].

1.3.2.2 β -Sheet

β -Sheet is formed from two or more β -strands. A β -strand is an extended stretch of polypeptide molecule appeared in a zig-zag manner. The β -sheet is stabilised by hydrogen bonds between C=O groups of amino acids in one β -strand and the N-H groups of the amino acids in another adjacent β -strand [38].

β -Sheet can exist in one of two ways, either parallel or anti-parallel (Figure 1.7). Anti-parallel β -sheets are more stable than parallel, as they have a more stable geometry of hydrogen bonds. Antiparallel β -sheets have hydrogen bonds that are perpendicular to the strand axis, while parallel β -sheets have hydrogen bonds at an angle between the β -strands [38].

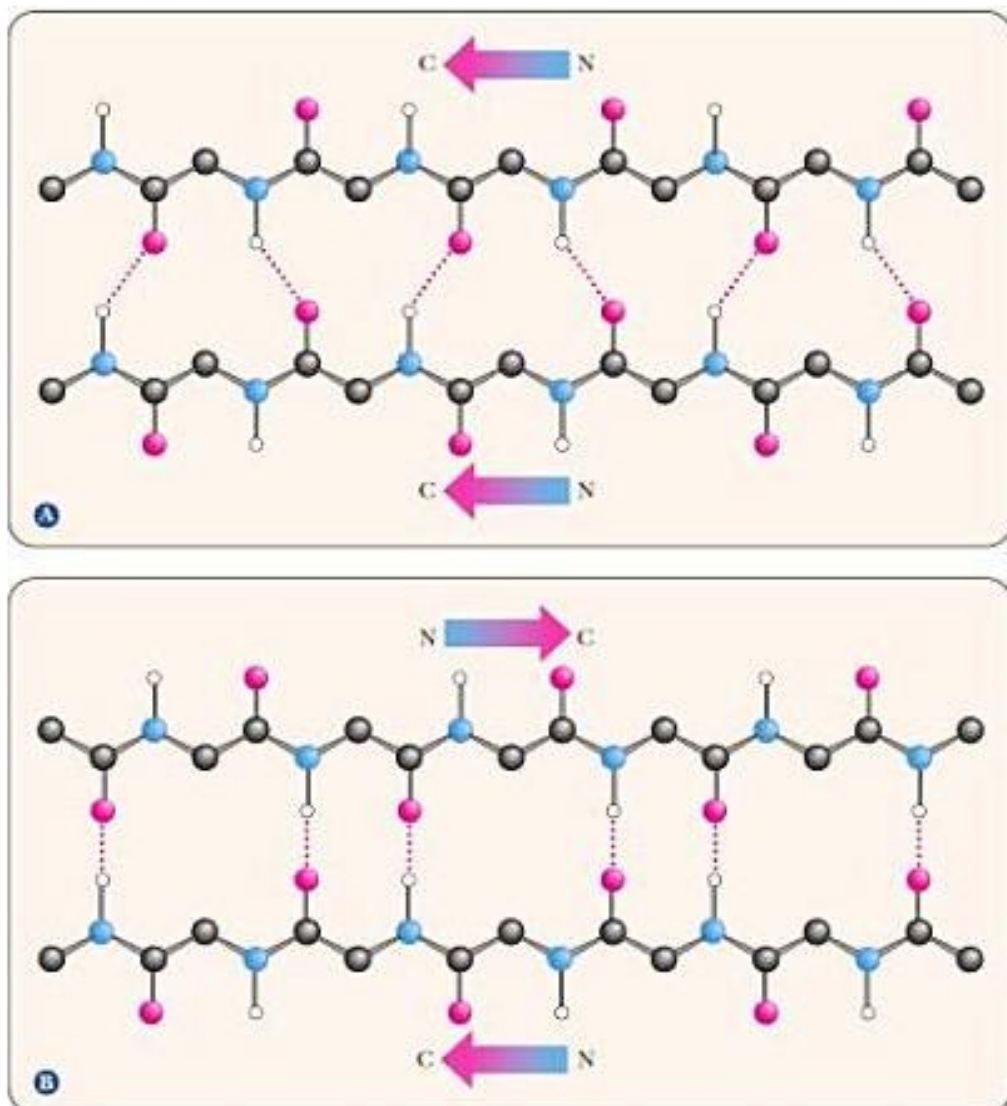


Figure 1.7: Structure of β -sheet. (A) Parallel and (B) antiparallel arrangement [41].

1.4 Molecular self-assembly of peptides

Molecular self-assembly is a major field in nanotechnology research which is based on bottom-up approaches. It is defined as the spontaneous organization of individual components through non-covalent forces such as hydrogen bonds, hydrophobic attractions, electrostatic interactions and van der Waals interactions [42].

Molecular self-assembly can be either nucleated or non-nucleated (classical). Non-nucleated self-assembly continuously occurs at any molecular concentration, and the process involves only one energetic parameter, the free-energy change for the formation of one dimer. In nucleated self-assembly, a critical concentration (c^*) is required before the first aggregate forms (nucleus); in this case, two energetic parameters are involved: nucleation energy and growth energy. A wide range of biological polymers follow the nucleated self-assembly mechanism, including lipids, DNA and peptides. As the self-assembly of peptides follows a nucleated mechanism, it only occurs when peptide concentration is above c^* . Below this concentration, the molecules are monomeric with random conformations. When the concentration is greater than c^* , stable aggregate nuclei are formed. Then followed by the nucleus growth, where the aggregates grow and elongate in gradual manner with an increase in concentration resulting in an increase in chain length and number [43-46].

1.4.1 Examples of self-assembling peptide nanostructures and their potential as drug carriers

Peptides can self-assemble into a wide range of different well-defined soluble aggregates that form peptide hydrogels and respond to chemical triggers. Some examples are briefly described here along with their selected applications as drug carriers.

1.4.1.1 Cyclic peptide nanotube

In 1974, De Santis et al. developed a theory that peptides containing an even number of alternating D- and L- amino acid residues can form closed flat-shaped rings that would be arranged in the antiparallel stack model through backbone-backbone hydrogen

bonding [47]. Based on this theory, in 1993 Ghaderi *et al.* developed the first member of such a peptide structure at the nanoscale; this structure has an internal pore diameter of about 7 Å formed from a sequence of eight residues of amino acids, cyclo[(L-Gln-D-Ala-L-Glu-D-Ala)₂], (Figure 1.8). Their investigation was extended by using 12 residues, cyclo[-L-(Gln-D-Ala-L-Glu-D-Ala)₃], to design a larger tube having a pore diameter of 13 Å [47-50]. Thus, it is deduced that the diameter of the pore can be controlled by varying the number of amino acids [48].

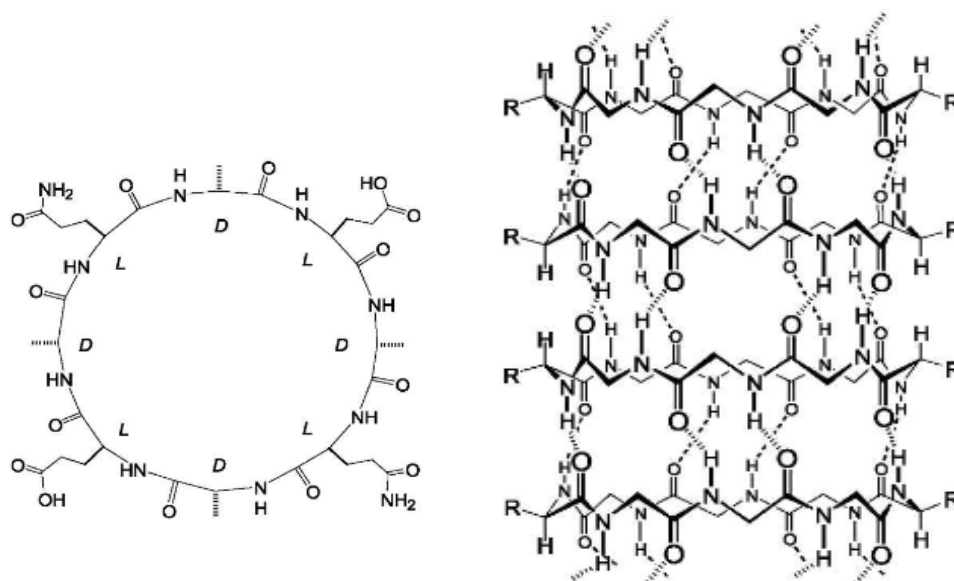


Figure 1.8: Schematic of the formation of cyclic peptide nanotubes (right) from the flat ring-shaped conformation (left). Partially taken from Ghaderi *et al* [47].

Many researchers have studied the use of Ghaderi cyclic peptide nanotubes as drug carriers. For example, in the study by Banerjee and Yadav, the peptide (Ala)₁₂ was used as a carrier for gentamycin (Figure 1.9). They did several experiments to understand the interactions between gentamycin and the carrier. Their overall finding was that the interaction energy is sufficient for holding gentamycin until delivery to the target, thus avoiding the premature expulsion of drug. Thus, this carrier is expected to be a promising material for decreasing side effects from gentamycin and increasing its bioavailability [51].

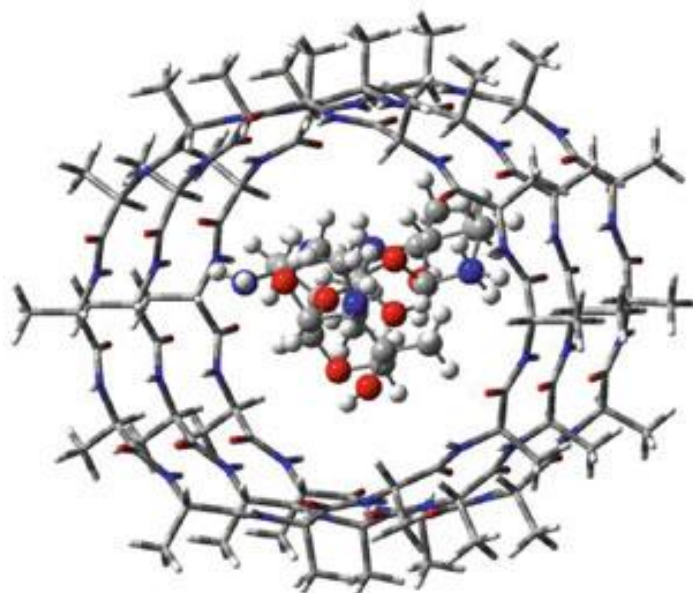


Figure 1.9: Complex of cyclic (Ala)₁₂ containing gentamycin [51].

1.4.1.2 Amyloid peptide

Significant attention has been focused on understanding of the formation of amyloid fibrils. Several undesirable diseases occur from the accumulation of amyloid fibrils, including Alzheimer's diseases, prion disease, Type II diabetes and Parkinson's disease [52-54]. The amyloid fibre is considered to be a generic structure and a key example of a natural peptide for forming rigid nanostructures to be employed for different applications, such as scaffolding that supports physical structures and vehicles to carry drugs. The amyloid β -sheet ($A\beta$) is the core recognition motif for Alzheimer's β -amyloid. It is usually formed by 30–40 amino acids. These amino acids self-assemble into β -sheets at low pH (Figure 1.10a) [55]. These β -sheets stack on top of each other to form the final nanotubes (Figure 1.10b). Each tube has an outer diameter of 52 nm, a wall thickness of 4 nm and a length of several microns [56]. Recently, laboratory studies have suggested that amyloid peptides could be used as biofunctional materials for drug-delivery applications since they are stable against harsh physical, chemical and biochemical conditions. Thus, active drugs could be released from amyloid termini over extended periods ranging from days to weeks. This was tested using a family of gonadotropin-releasing hormones GnRH; the results showed that amyloid peptides could be adopted as a sustained release system to promote the long action of GnRH [57, 58].

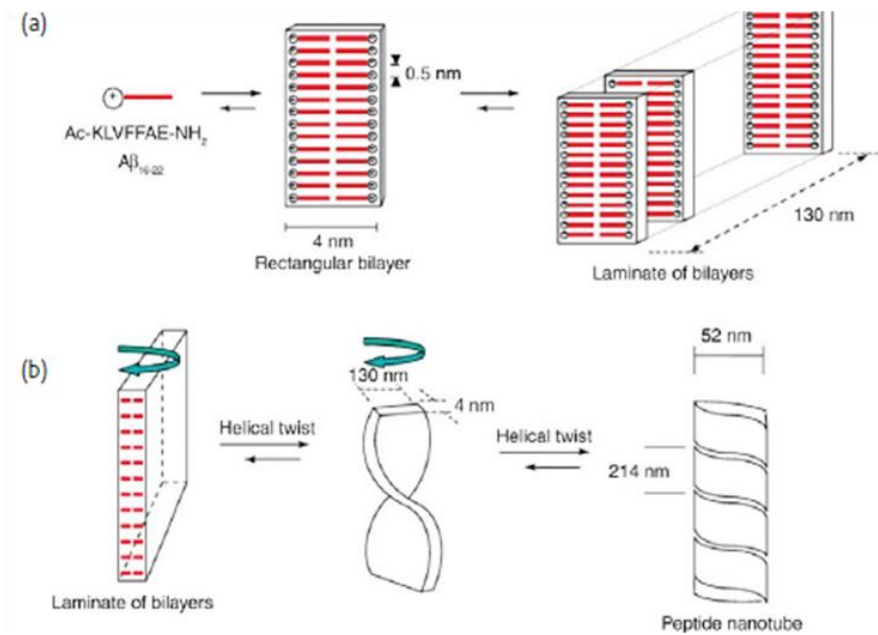


Figure 1.10: Model of self-assembly of amyloid peptide. (a) Flat bilayers. (b) Bilayers twist to form nanotubes. Partially taken from Scanlon, S. and A. Aggeli [56].

1.4.1.3 β- Hairpin peptide

Nanotubes arising from self-assembled β-hairpin peptides have been reported. Lanreotide growth hormone inhibitor peptide is a natural example of an assembled nanotube made from such conformation (Figure 1.11). In water, the peptides assemble into bilayers consisting of amphiphilic β-sheets with aliphatic and aromatic residues. The hairpin conformation of the building block is stabilized by disulphide bonds. Hydrogen bonding drives the peptides to assemble into long ribbons. About 26 ribbons associate laterally due to hydrophobic effect to form nanotubes with diameters of 24 nm, resulting in hydrogel formation [56].

The Schneider and Pochan groups have demonstrated hydrogels made from β-hairpin building blocks of MAX1 and MAX8 peptides (Figure 1.12). MAX1 and MAX8 are peptides containing 20 amino acids and are built from alternative residues of lysine and valine with one lysine replaced by glutamic acid in MAX8. These molecules have a high propensity for folding into β-hairpin structures. Figure 1.12 shows that the self-assembly process of MAX peptides is driven by external stimuli [59-63].

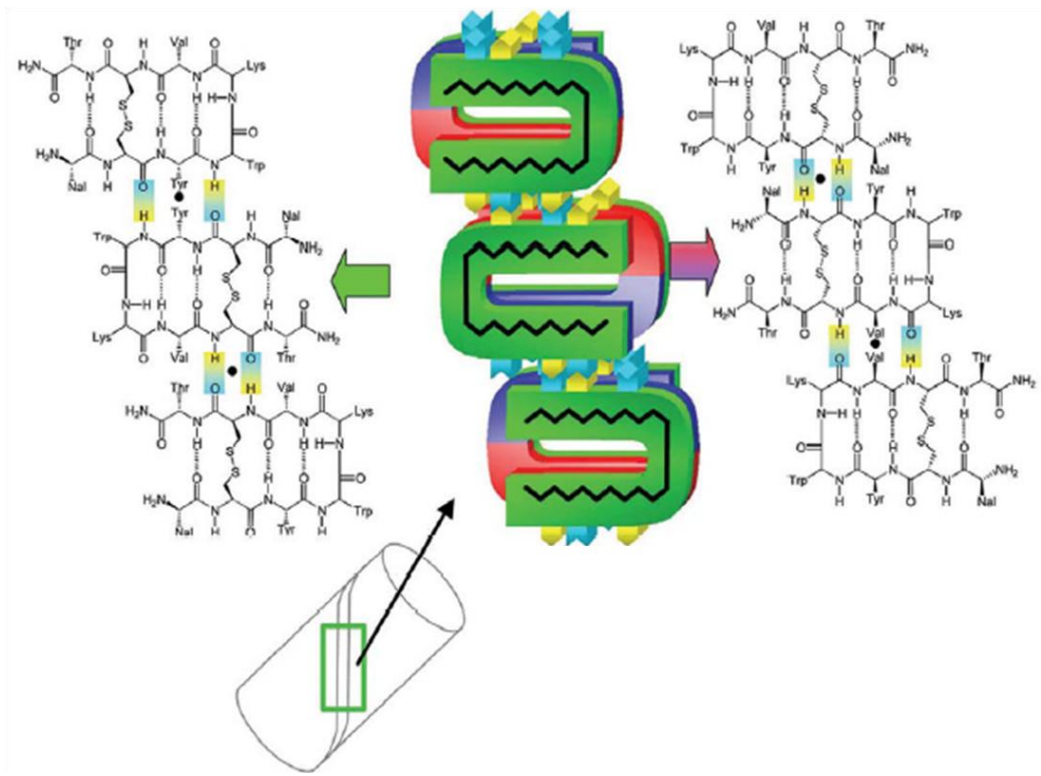


Figure 1.11: Lanreotide peptide nanotubes in water. Color code: green, hydrophilic; red, aromatic hydrophobic; and blue, aliphatic hydrophobic surface of the peptide [56].

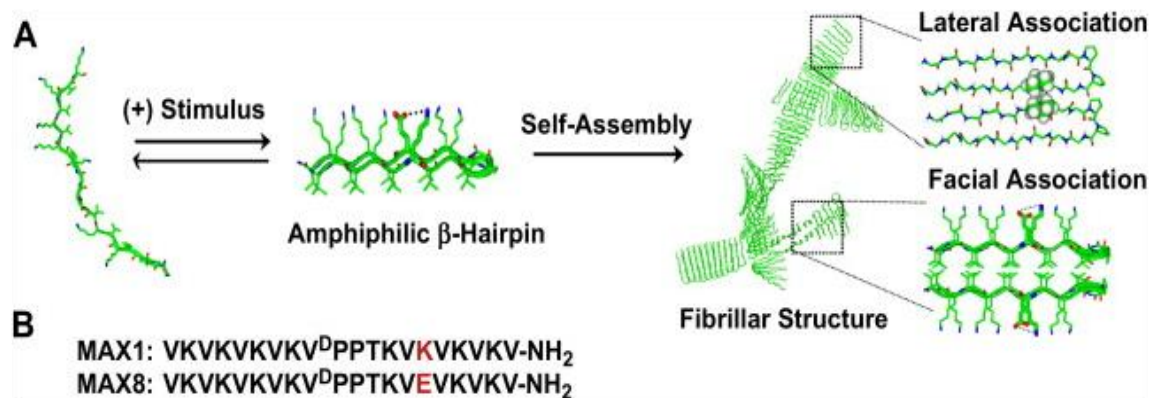


Figure 1.12: (A) Schematic of folding and subsequent self-assembly when MAX1 and MAX8 peptides are placed in DMEM. (B) Peptide sequences of MAX1 and MAX8 [64].

The inflammatory response to MAX1 and MAX8 hydrogel was assessed. The data showed that they do not provoke an inflammatory immune response when implanted into animals; therefore, they are suitable candidates for biomedical applications. For example, curcumin molecules were incorporated into the gel matrix of MAX8 to induce

programmed cell death (apoptosis) in medulloblastoma cancer [65]. Curcumin is water insoluble and has relatively low bioavailability. The encapsulation of curcumin into MAX8 as a hydrogel vehicle increased bioavailability and effectiveness in the tumour.

1.4.1.4 Amphiphilic peptide

Amphiphilic peptides are molecules with both hydrophilic and hydrophobic parts. The hydrophilic part is usually peptide and the hydrophobic part is usually non-peptide [66]. Different amphiphilic peptide structures exist including surfactants-like peptides, peptide-conjugated amphiphiles and bolaamphiphile. Surfactant-like peptides are molecular mimics of membrane phospholipids. They are composed of consecutive hydrophobic amino acids as a tail and one or more hydrophilic amino acids as a head group. It is believed that in water, the hydrophobic effect drives the nonpolar regions of peptide molecules towards each other and away from water-forming bilayer rings. These rings stack on top of each other to form peptide nanotubes [67-70]. Shuguang Zhang *et al.* presented the pathway of peptide nanotube formation through the molecular modelling of the surfactant peptide V₆D (Figure 1.13). Many other surfactant-like peptides have been designed with different charges, based on their amino acid sequences, such as negatively charged A₆D and V₆D₂ and positively charged A₆K and V₆K. Another example of an artificial surfactant-like peptide was designed by Shuguang Zhang *et al.* by mimicking the structure of phospholipids. Phosphoserine was added to the molecule as a hydrophilic head, and alanine or valine was added as a hydrophobic tail to design surfactant-like peptides, such as pSA₆ and pSV₆ [68, 71].

Conjugated-peptide amphiphile combines the structural features of surfactant-like peptide with the functions of bioactive peptides. In this type of structure, a peptidic recognition motif is added to the peptide molecule to mediate cell attachment and guidance for tissue engineering applications. An example for peptide-conjugated amphiphile was designed by Stupp *et al.* [72, 73]. The Stupp complex self-assembles, in water, into fibres to direct the mineralization of hydroxyapatite HA. The designed peptide has an alkyl tail containing 16 carbon atoms attached to an ionic peptide (Figure 1.14). To promote cell-adhesion, RGD (arginine–glycine–aspartic acid) was added to the C-terminus. Four cysteine residues were incorporated into the peptide region to form disulphide bonds between adjacent peptide molecules and enhance peptide cross-linking

[50, 72-74]. This complex structure tends to concentrate inorganic cations, such as calcium, for mineralization applications.

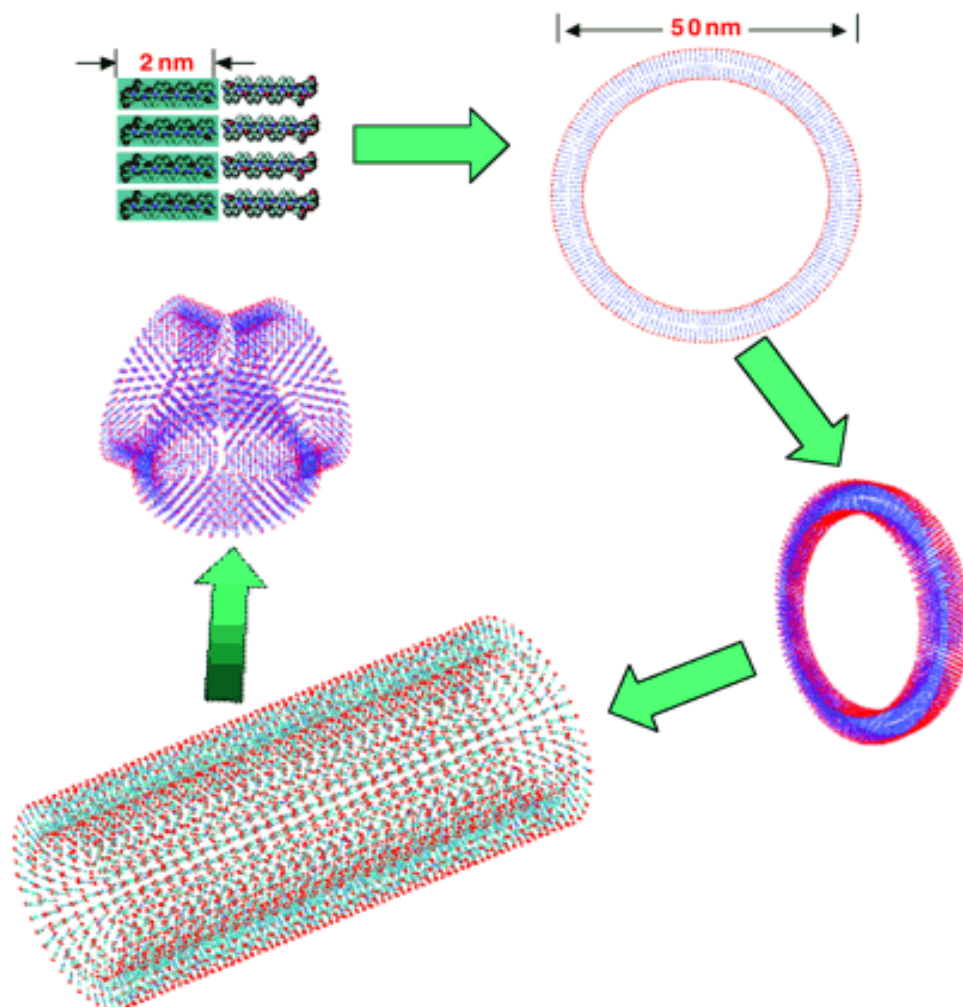


Figure 1.13: Mechanism of self-assembly of surfactant-like peptide V₆D into a bilayer and then into rings that stack into a peptide nanotube [69].

Bolaamphiphilic peptides differ from traditional surfactants by having two head groups of hydrophilic peptides connected by a hydrophobic alkyl chain (Figure 1.15). Xiaojun Zhao designed several bolaamphiphilic peptides in water composed of natural amino acids; these, in turn, self-assemble into nanotubes with hydrophilic cores and hydrophilic outer surfaces.

Compared with nanotubes formed by surfactant-like peptides, bolaamphiphilic peptide nanotubes are smaller with inner diameters of less than 10 nm. It has been reported that their structure and size make them excellent carriers for encapsulating and transferring hydrophilic compounds into target cells [68].

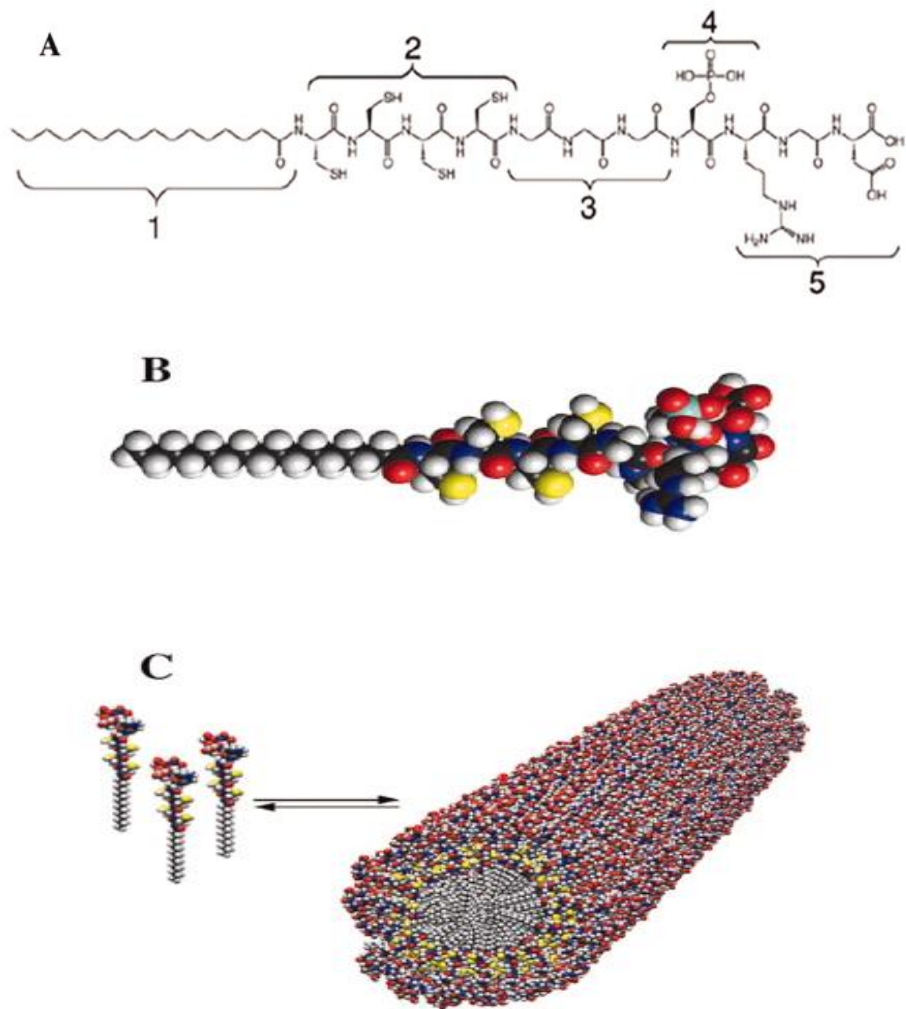


Figure 1.14: The Structure of the peptide amphiphile designed by Stupp *et al.* (A) Five key structural features of the molecule: 1- hydrophobic alkyl tail, 2- four cysteine residues, 3- three glycine residues, 4- serine residues to interact with calcium, 5- cell adhesion ligand. (B) Conical shape of the molecule. (C) Schematic showing the cylindrical micelle formed from the amphiphilic peptide [72].

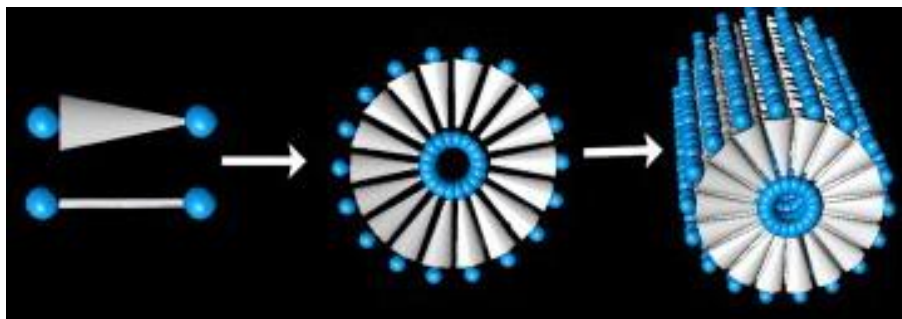


Figure 1.15: Bolaamphiphilic peptides forming the nanotube. Blue= hydrophilic head, white= hydrophobic [68].

It is possible that surfactant-like peptides with hydrophobic fatty tails have immense potential for delivering hydrophobic drugs. A surfactant-like tetraail peptide, [(C₁₈)₂K]₂KR₈GRGDS], was designed and synthesized for hydrophobic drug delivery. The molecule is composed of four hydrophobic aliphatic tails and a hydrophilic peptide head group. Ibuprofen and doxorubicin (DOX) were loaded into the amphiphilic design. The loaded drugs released in sustain manner and showed high phototoxicity against cancer cells indicating their potential for photodynamic therapy [75, 76].

1.4.1.5 Ionic Complementary Peptide

In the early 1990s, the potential importance of ionic complementary peptides was first demonstrated by Shuguang Zhang et al. The formation of such charged peptides occurs through electrostatic interactions between positively and negatively charged building blocks within the peptide, in addition to hydrogen bonding and van der Waals forces (Figure 1.16) [77-79]. Ionic complementary peptides can adopt two different secondary structures, which result from different types of charge distributions along the sequence: β -structures and helical structures. When the charges are arranged in the alternating distribution of $\bullet\text{---}\text{---}\bullet\text{+++}$ (\bullet is the hydrophobic residue), the peptide will assemble into the helical structure. However, if they arranged as $\bullet\text{---}\text{+}$, they will assemble into the β -structure [80, 81].

The first ionic complementary peptide EAK 16 was designed by Zhang et al. and is composed of 16 peptide residues. Based on differences in charge distributions, EAK16 is classified into EAK16-I, EAK16-II and EAK16-IV (Figure 1.17) [78, 82].

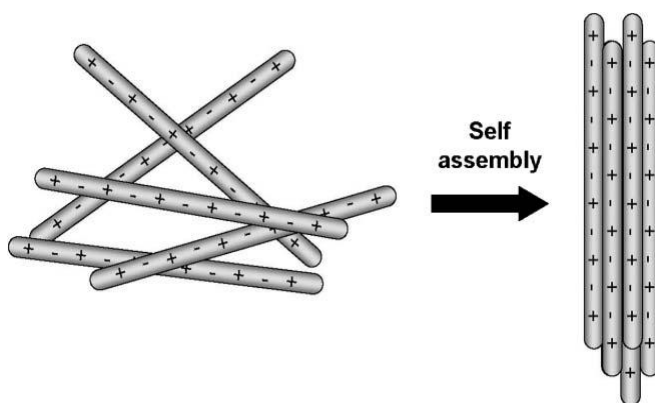


Figure 1.16: Self -assembly of peptides as mediated by complementary charges [53].

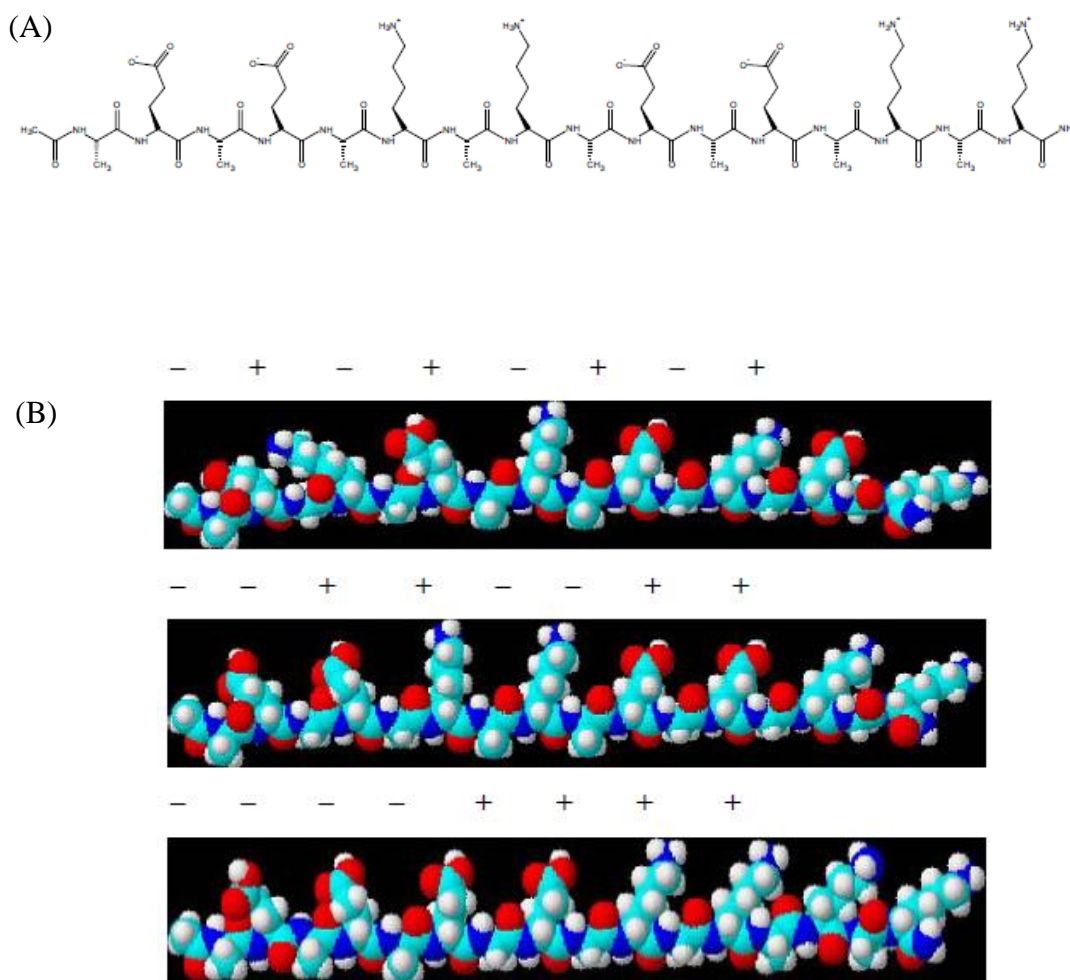


Figure 1.17: (A) Structure of the ionic-complementary peptide EAK16-II. (B) Three-dimensional molecular model of EAK16s. The top, middle and bottom schemes represent the EAK16-I, EAK16II and EAK16-IV structures with charge distribution of $- + - + - + - +$, $- - + + - - + +$ and $- - - - + + + +$, respectively [79].

In water, EAK16-II forms β -sheets having a hydrophobic face on one side and a hydrophilic face on the other [53]. These β -sheets stack on top of each other to form EAK16-II fibrils. This peptide self-assembles in aqueous solution to form peptide gels. Applications of these complementary peptides have been demonstrated in drug delivery fields. They have been used to encapsulate hydrophobic compounds and increase their solubility in aqueous environments. For example, EAK16-II has been used to increase the solubility of pyrene in aqueous solution. Pyrene is a weakly water-soluble material with a solubility of $\sim 7.0 \times 10^{-7}$ M. EAK16-II was shown to form a stable complex with pyrene in aqueous solutions with a solubility of 5×10^{-3} M [79].

1.4.1.6 P₁₁ series of peptides

At the University of Leeds, a new class of peptides (P₁₁) has been designed, synthesized and studied by Aggeli *et al* [44]. These peptides are 11 amino acids in length and self-assemble by the nucleated mechanism. All amino acids used to design P₁₁ series of peptides are L amino acids. They form β -strand conformations and self-assemble into long β -sheet tapes and higher-order aggregates. Solutions of the aggregates have been found to become gels if peptide is used at sufficiently high concentrations [44].

A theoretical model has been built to quantitatively describe this peptide self-assembly process, and the model has also been used to fit experimental data [44]. A model tape-forming peptide is P₁₁-2 (CH₃CO-Q-Q-R-F-Q-W-Q-F-E-Q-Q-NH₂), which self-assembles into tapes and higher-order aggregates in water and forms hydrogels (Figure 1.18).

The self-assembly of P₁₁ peptides only occurs at peptide concentrations greater than a certain value known as the critical concentration (c^*) [44]. At concentrations lower than c^* , the peptides exist as random-coil monomers. In this case, monomeric peptides can have any values for the torsion angles Φ and ψ [44].

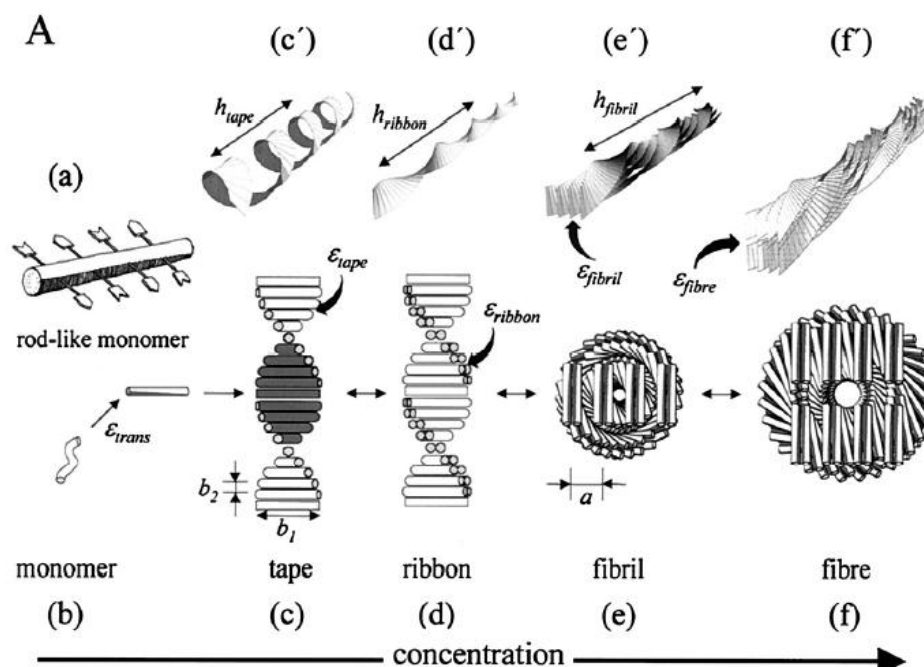


Figure 1.18: Hierarchical β -sheet tape self-assembly [44].

When the concentration is sufficiently high to start self-assembly, the monomeric peptides undergo a straightening process to form rod-like β -strand monomers with complementary donor and acceptor groups on opposing sides. For the peptides to self-assemble, the loss of entropy must be balanced by the gain in enthalpy. The main entropy loss is associated with straightening the peptide chain from its random coil into its β -strand conformation. Enthalpy is gained from interactions between the hydrophilic charged and uncharged residues, which can be involved in hydrogen bonding and electrostatic interactions. This process is mainly entropic in nature and is expressed by the energetic parameter $\varepsilon_{\text{trans}}K_bT$ which is the free-energy change per molecule [44].

To form a tape, the rod-like β -strand monomers interact via complementary recognition between donor and acceptor groups and form hydrogen bonds. This process is mainly driven by an enthalpic gain and is described by the term $\varepsilon_{\text{tape}}K_bT$, which is the free-energy change owing to the association of two peptides. The tape is the simplest form of a hierarchical structure in peptide self-assembly. At equilibrium, tapes are twisted and bent. The intrinsic twist within the peptide tapes arises from the chirality of amino acid residues, while bending originates from differences between upper and lower sides of the tapes [44].

When the peptide concentration is increased, two neighbouring tapes stack together through the hydrophobic faces and the hydrophilic faces are in contact with water thus giving rise to form ribbons. This process is stabilized by $\varepsilon_{\text{ribbon}}K_bT$, which is the free energy change per pair of stacked tapes and is mainly enthalpic in nature. For two tapes to stack together both must decrease their bend and twist to facilitate the presence of one another. The resultant ribbon has more of a saddle curvature rather than the helical twist that is observed for the tapes [44].

At still higher concentrations, several ribbons can stack together to form a fibril. Fibrils are more rigid and longer than ribbons and are stabilized by $\varepsilon_{\text{fibril}}K_bT$, which again is mainly enthalpic in nature. There is an energy cost that restricts fibril formation; this is the elastic penalty associated with the untwisting of the ribbons upon stacking. If the energy of the fibril formation is greater than the untwisting energy of the fibril, then the self-assembly of fibrils will occur [44]. With further increases in concentration, a pair of fibrils can stack together side by side and entwine to produce fibres. These fibres are formed from mutual attractions between the C and N termini of each peptide pair. Fibres are stabilized by $\varepsilon_{\text{fibre}}K_bT$ [44].

1.4.2 Factors influencing peptide self-assembly

Peptide self-assembly can be influenced by several factors, including peptide concentration, pH and the presence of salt [38-40].

Peptide concentration strongly affects peptide self-assembly. A critical peptide concentration is needed to start the self-assembly process. Generally, at concentrations below the critical peptide concentration, peptides are in monomer states. At the critical concentration, peptides start to self-assemble into β -sheet aggregates. For example, Aggeli et al. demonstrated that, in water, P₁₁-1 is predominantly in a monomeric random coil conformation at $c \leq 0.1$ mM. However, at higher concentrations, it forms peptide aggregates [44].

pH Charged amino acids have an important role in the stabilization of peptide assembled structures through electrostatic interactions and hydrogen bonding. Variation in pH can change the peptide conformation. For example, polylysine chains can be converted from α -helix to β -sheet when the pH is above 10. At this pH, 95% of lysine residues are protonated. This process is reversible. When pH is lower than 10, the α -helix is converted to a β -sheet [83].

The gelation behaviour of P₁₁ series peptide is influenced by pH. For example, P₁₁-5 (CH₃CO-Q-Q-O-F-O-W-O-F-Q-Q-Q-NH₂) was designed to form fibrils at basic pH and to be as monomers at lower pH (Figure 1.19) [84].

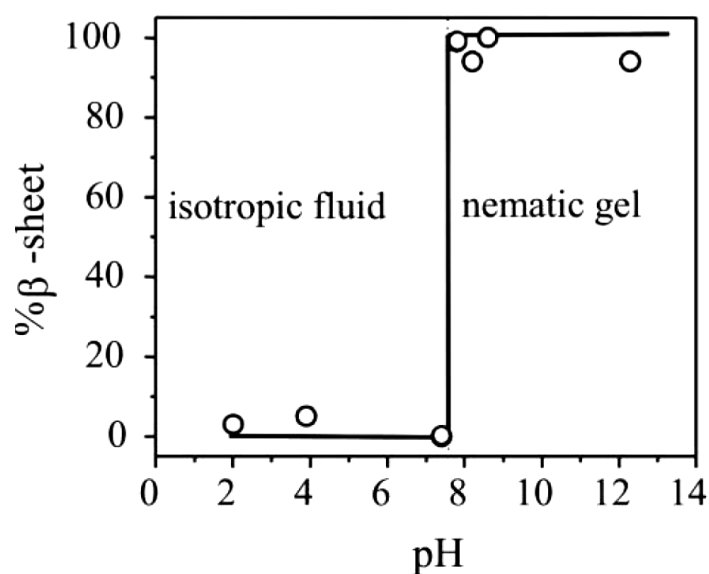


Figure 1.19: Behaviour of peptides as a function of pH P₁₁-5 [45].

The presence of salt can affect the critical concentration of peptides. Chen *et al* have investigated the effects of salt on the assembly of EAK 16-I (AEAKAEAKAEAKAEAK). In water, the critical concentration of EAK16-I is around 0.3 mg/ml. At the presence of 20 mM of NaCl, the critical concentration of the peptide increased to 0.8 mg/ml [79, 85].

In a study carried by Aggeli *et al*, the effect of salt presence on P₁₁-9 self-assembly, for example, was studied. In the absence of salt, a sharp transition from flocculation to nematic fluid is observed at pD < 6.5. In the presence of 130 mM NaCl, a broader transition from flocculation to nematic gel is observed (Figure 1.20).

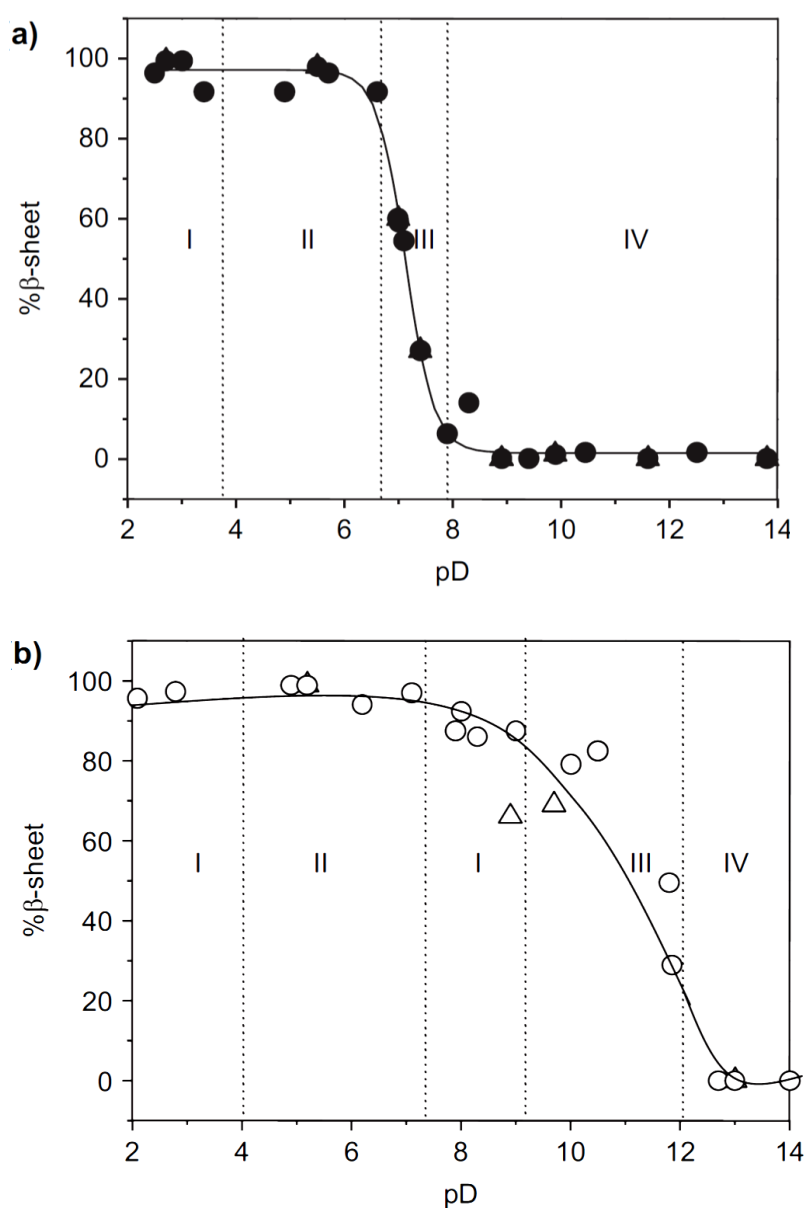


Figure 1.20: Phase behaviour of P₁₁-9 as a function of pD. (a) In D₂O. (b) In D₂O containing 130 mM NaCl, I: nematic gel, II: flocculate, III: nematic fluid, IV: isotropic fluid [86].

1.5 Advantages and limitations of peptide-based drug-delivery systems

Applications of self-assembled peptides are very diverse. They have been applied as nanowires [87], biosensors [88], selective transport channels [89], antibacterial agents [90], and as a scaffold for wide range of tissue engineering applications [91]. In term of drug delivery applications, carriers at the nanoscale have unique potential in the pharmacokinetic behaviour [92, 93]. Because of their enhanced permeation and retention effects, they can reach a disease site. Therefore, they are able to detect, image and treat diseases. Many nano-drug carriers are under extensive investigation worldwide, including liposomes, polymer micelles and dendrimers. They are biocompatible, biodegradable and non-immunogenic biomaterials. By using natural amino acids, maximum biocompatibility is expected. Further, if it is found that there are types of amino acids or certain sizes of peptides that cause an immune response, they can be modified. In addition, peptides are chemically and thermally stable at high temperatures in the presence of organic solvents and at extreme values of pH. They can be rapidly synthesized chemically, and novel amino acid residues can be readily incorporated.

Amyloid peptides are attractive for their mechanical strength; however, they are historically associated with human diseases. *In vivo*, they can accumulate either outside cells or inside cells causing cytotoxicity. β -Hairpin peptides, such as MAX1 and MAX8, are attractive in biomedical applications, particularly in applications with post-operative infections because they have antibacterial properties. However, because of their large size, they require substantial amounts of raw materials and are cost-inefficient. Some self-assembling peptides, such as ionic complementary peptides, are formed by classical non-nucleated processes; in such cases, controlling aggregate growth is challenging. The P₁₁ series of β -sheet tape-forming peptides are more advantageous than other equivalent families since they are based on shorter amino acid sequences. Thus, they are easier to design and more cost-effective. The ability to change uncharged polar groups gives them versatility in chemical and mechanical properties. As they undergo 1D hierarchical β -sheet self-assembly, they can be controlled by triggers such as pH, temperature and ionic strength. They have highly specific recognition capabilities. Thus, they can form very precisely ordered building blocks for specific applications. Therefore, because of these advantages, they are considered to be very good candidates for different applications in medicine [38, 52, 94].

1.6 Aims and Objectives

The aim of this study is to determine the feasibility of combining P₁₁ sequence self-assembling peptides with fibrous media for biofunctional application. Fabrics were treated with pH-responsive self-assembling peptides to release therapeutic agents when stimulated by pH. Optimistically, this project could lead to the design of a smart material for biomedical applications with particular emphasis on the control of infections in chronic wounds.

The specific objectives of the project are as follows:

- 1) Investigate the self-assembly of different peptides to determine the optimum preparation conditions for designing peptide nanotubes and to compare the mechanism of tube formation with that of fibrillar structure analogues. The investigation includes testing those factors that affect peptide behaviour, such as peptide concentration and pH.
- 2) Treat medical fabrics with selected self-assembled peptides. The fabrics will be treated with self-assembled peptides by two different methods. (1) Fabrics will be coated with self-assembled peptides from the outer surface by dipping. (2) Self-assembled peptides will be incorporated into the structure of the fabric by electrospinning. Complementary characterization techniques will be applied to investigate the developed materials.
- 3) Investigate the feasibility of encapsulating antibiotics into self-assembled peptides.
- 4) Evaluate the bioactivity against bacteria of the fabrics treated with antibiotics encapsulated into self-assembled peptides.

Chapter 2

2 Experimental procedures and techniques

2.1 Materials

2.1.1 Chemicals

1, 1, 1, 3, 3, 3-hexafluoro-2-propanol (HFIP \geq 99% purity), deuterium oxide, deionized water, sodium hydroxide pellets, sodium chloride, concentrated hydrochloric acid, deuterated sodium hydroxide, deuterated hydrochloric acid and sodium azide, were purchased from Sigma Aldrich Ltd, Gillingham, Dorset, UK.

2.1.2 Peptides

P₁₁-2 (MW 1,593 Da), P₁₁-4 (MW 1,565 Da), P₁₁-8 (MW 1,565 Da), P₁₁-9 (MW 1,432 Da) and P₁₁-12 (MW 1,593 Da) were purchased from the Polypeptide Group (Strasbourg, France). All peptides were tested in house for purity on arrival using HPLC, UV spectroscopy and elemental analysis (Appendix A).

2.2 General methods

2.2.2 pH measurement

All samples were adjusted to the desired pH or pD (pD values are meter reading plus 0.4). Sample pH was determined using either a WPA CD720 meter and a CMW711 semi-micro single junction probe, or a Sartorius Docu-pH meter and a VWR sympHony semi-micro combination double junction probe. Both probes were filled with, and stored in, 3.5 M KCl solution.

2.2.3 Peptide solution preparation

Peptides were weighed to the desired weights using a Mettler AE240 balance. The desired amount of the needed solvents were added to the weighed peptide vials using Gilson micropipet. Vials were sealed with barafilm and vortexed for 30 s with Scientific Industries Vortex Genie 2 vortexer. Then, the samples were sonicated for 20 mins using a Bandelin Sonorex RK52H sonicator.

2.3 Characterization techniques

2.3.1 Transmission electron microscopy, TEM

2.3.1.1 Background

TEM is widely used by researchers in physics, chemistry and biology. It has a principle of work similar to that of the light microscope but essentially differs through the utilization of high- energy-electron-beam to form images rather than visible light. The wavelength of the electrons is much smaller than the wavelength of the visible light; therefore, the resolution in TEM is higher than the resolution of light microscopes. It can reveal fine details, which are a thousand times smaller than the smallest resolvable object in light microscopes such as a single column of atoms [95].

TEM consists of a vertical column containing a series of electromagnetic lenses, condenser lenses, and objective lenses. A specimen chamber is located between the condenser lenses and the objective lenses. The microscope is provided by an electron gun which creates a beam of electrons, and a suitable electron detector [95]. The main components of TEM are illustrated below in Figure 2.1. The electron gun generates the primary electrons beam which travels through the vacuum in the column of the microscope. Then, the beam is accelerated by an electric potential and focussed by the electromagnetic lenses to pass into the sample. The electron beam interacts with the sample in a vacuum chamber and undergoes elastic or inelastic scattering or otherwise produces different signals such as X-rays, Auger electrons, or light. The image is formed from the electrons transmitted through the specimen with small scattering angles and are collected by the detector to record an image [96].

The electron scattering pattern differs from sample to sample according to its density. Biological samples that composed of elements with low atomic number such as bacteria, biological membrane structures, and proteins have low electron-scattering powers resulting in unclear images. Therefore, such samples have to be stained prior to imaging with negative stains to enhance the image contrast. Negative stains are heavy metal compounds with high atomic number, which can penetrate between the sample projections and reveal its fine details. Many negative stains can be used such as osmium tetroxide, ammonium molybdate, uranyl formate and uranyl acetate [97].

2.3.1.2 Method

Pieces of mica were cleaved and coated with a carbon film. The coated mica was then left overnight to dry. Then, hexagonal mesh size 400 copper grids were coated with the carbon film by immersing the mica in a water surface with an angle about 45° to allow the carbon coat to float on the water surface. The water was slowly removed from the beaker in order to allow the film to lie on the surface of the grids. After the film deposited on the grids, they were kept overnight to dry. The coated grids were discharged to form static charges on the grid surface using Edwards 306 a high vacuum coating system. The peptide samples were diluted in pure water. A droplet of the diluted sample was placed onto a clean discharged surface of the grid and left for one minute; the excess was removed using filter paper. Then the grids were introduced on top of a droplet of uranyl acetate (UA, 0.4%) in order to be negatively stained. The excess is removed and left to go dry. The samples were imaged with a Philips CM10 electron microscope at an accelerating voltage of 80 kV or imaged with FEGTEM an Oxford instruments 80 mm² SDD EDX detector.

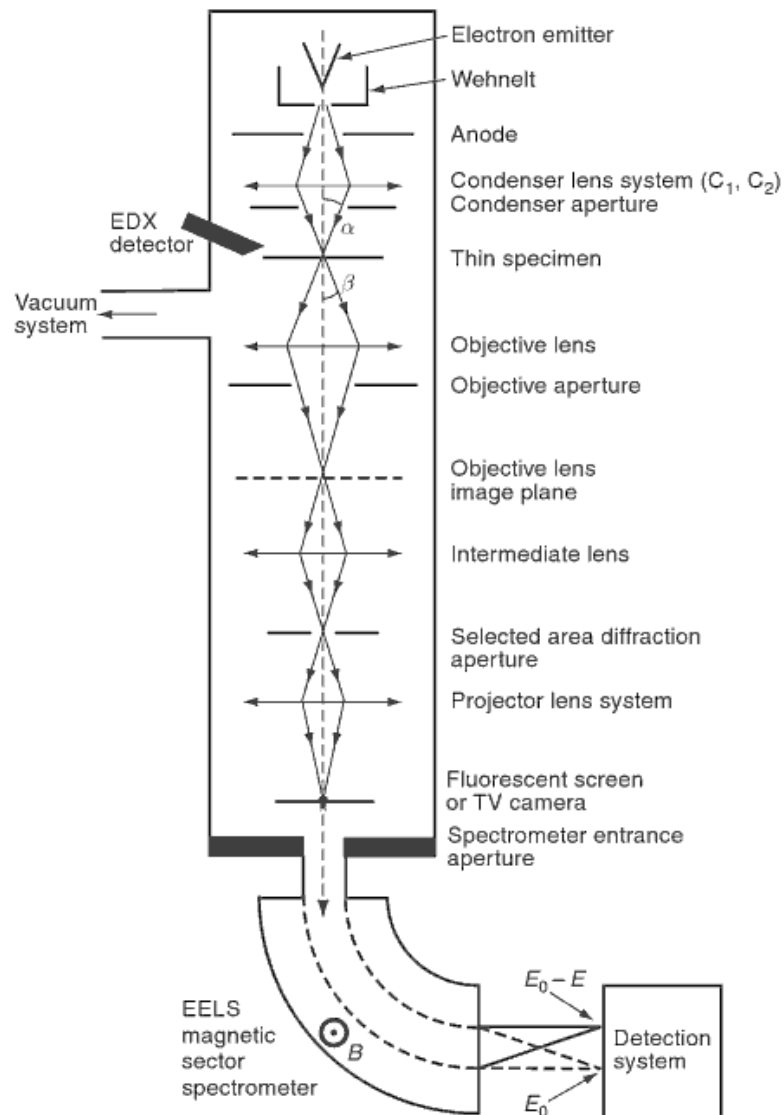


Figure 2.1: Schematic representation of transmission electron microscopy [98].

2.3.2 Scanning electron microscopy, SEM

2.3.2.1 Background

SEM is one of the most important instruments for the analysis and examination of samples morphology. Similar to TEM, the basic principle of imaging using SEM is based on the interaction under high-vacuum conditions (10^{-5} - 10^{-7} Torr) between the point of interest on the specimen surface and the high-energy electron beam. In the area in which the interaction occurs between the beam and the specimen surface, various electronic particles will be produced: 1) secondary electron SE; 2) backscattered electrons BSE; 3) Auger electrons; 4) X-rays; and 5) cathodoluminescence [99]. The secondary electron released from the interaction spot is characteristic of the surface at

that point; then, the secondary electrons are detected by the Everhart-Thornley-Detector. The detector conveys the electron signals to a visual signal displayed on a Cathode Ray Tube (CRT) [100, 101]. SEM components are illustrated in Figure 2.2.

Conductive materials, such as metals can be viewed by directly putting them in the specimen chamber without prior preparation. On the other hand, some non-conductive materials, such as biological samples require several processing steps to prevent the sample from vacuum-related damage and electrical charging. They can be coated with any conductive materials such as gold, palladium, platinum and graphite [100, 101].

2.3.2.2 Method

The samples were attached to SEM stubs using carbon pads using double sided stick carbon pads. They were sputter coated with Pt/Pd Ager sputter coater model 208HR (coat in 80% Pt and 20% Pd) with about 5 nm layer of platinum and palladium (50:50) using a Cressington 108 sputter coater. Then, the samples were imaged using a Gemini LEO 1530 FEGSEM made by Carl Zeiss. The images were taken at different magnification with an accelerating voltage of 10 kV. The diameters ranges of the fabricated nanofibers were measured using image analysis software ImageJ.

2.3.3 Energy-dispersive X-ray spectroscopy, EDX

EDX is an analytical technique used in conjunction with electron microscopy. It is used to provide near surface elemental identification and quantitative compositional information. The electron beam strikes the surface of a sample. This leads to the emission of the X-rays from the material. X-rays are generated from about 2 microns in depth and finally result in a set of peaks. Each peak corresponds to a specific element in the examined region, based on the fundamental that each element has a unique atomic structure [102].

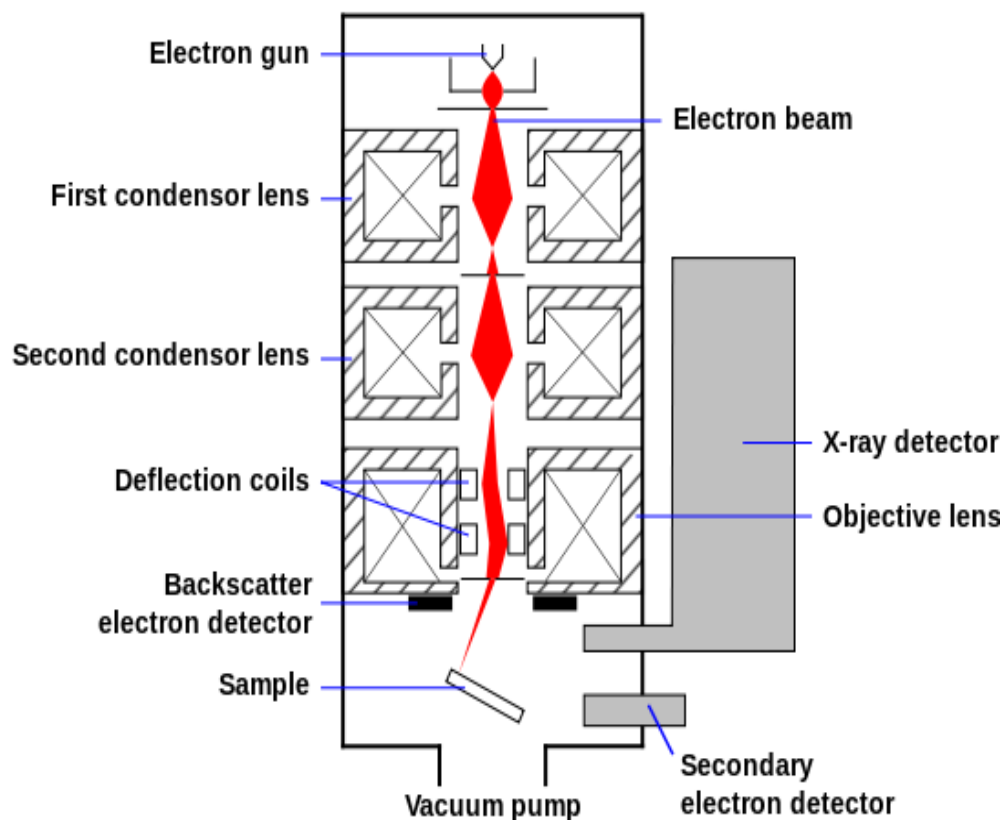


Figure 2.2: Schematic representation of scanning electron microscopy [103].

2.3.4 Fourier transform infra-red spectroscopy, FT-IR

2.3.4.1 Background

Fourier transform infrared spectroscopy, FTIR, is a technique which has been adopted in analytical laboratories for over seventy years. It is a useful tool for identifying any unknown materials using a source of IR light. IR is a radiation with frequencies and energies lower than those associated with visible light. When the IR light passes through the sample, it will be absorbed by the sample molecules giving spectra. These spectra are corresponding to the frequencies of vibrations of the bonds between atoms. Each different material has a unique combination of atoms; thus, FTIR can present a unique fingerprint for every type of material [104-108].

The FTIR basic components are; the infrared source, interferometer, detector, the sample compartment, and computer. The unique part in the FTIR is the interferometer. The interferometer has a beamsplitter and two types of mirror; fixed and moving mirror (Figure 2.3). The beamsplitter splits the incoming infrared beam into two optical beams,

whilst one beam reflects off the flat mirror, the other beam reflects off the moving mirror [107, 108].

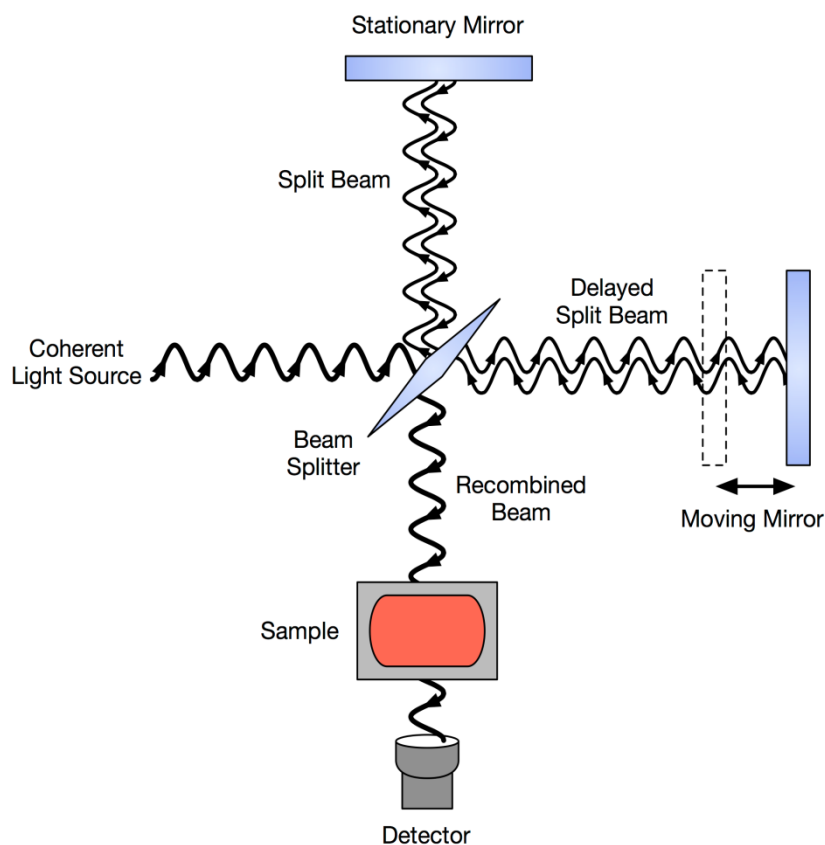


Figure 2.3: Schematic showing FT-IR components [109].

After reflecting off the beams from their respective mirrors, the two lights recombine again at the beamsplitter. The recombined signal results from the interfering between each other with the resulting signal known as “interferogram”. The interferogram has a unique prosperity into which every infrared frequency is encoded into it. Following, the interferogram is then transmitted through the sample surface, and reflected off with the specific characteristics of the sample owing to the function of the molecule vibration. The reflected beam arrives at the detector for final measurement. Finally, the measured signals is digitized and sent to the computer to be displayed for the user [107, 108].

FTIR has been used in the examination of peptide conformation. Nine absorption bands can be used to study peptide secondary structure (amide A, B, I, II, III, IV, V, VI, VII) (Table 2.1). The frequencies of amide I band are the most useful indicator for particular peptide secondary structures and appeared as a peak at $1600\text{-}1700\text{ cm}^{-1}$ [110]. The frequencies of vibration in the amide I band arises from the hydrogen bonding involving

the C=O and NH groups in the secondary structure of peptide. In order to obtain a semi-quantitative analysis for an examined peptide, the amide I band at the region 1600-1700 cm^{-1} should be fitted to ascertain the number and positions of individual component bands in Table 2.2 [110]. The individual amino acids that affect the amide I region are listed Table 2.3. The Trifluoroacetic acid, TFA, mostly interferes with the synthetic peptides infrared spectrum, located at 1673 cm^{-1} . It is a strong acid used in the synthesis and purification of peptides and other organic compounds. TFA is a negatively charged compound bounded to positively charged residues. The amount of TFA present in a peptide solution depends on the number of positively charged residues in the peptide [110]. The peptide bands can also be overlapped with the H₂O bending vibration at 1640 cm^{-1} , therefore, FTIR studies of peptides samples will be run in deuterated solvents [110].

2.3.4.2 Method

FTIR spectra were recorded using a Thermo Scientific Nicolet 6700 FTIR spectrophotometer using OMNIC 7.3 (Thermo Scientific, UK) software. The samples were then placed between CaF₂ crystals separated by lead spacer. All spectra are collected after subtraction of the component peaks of the peptide amide I band were obtained through second derivative analysis. OMNIC Peak Analysis tool were used to fit the amide I band.

Table 2.1: Infrared bands of the peptide [111].

Amide Band	Wavenumber / cm^{-1}	Origin
A	~3300	NH stretching
B	~3100	NH stretching
I	1600-1690	C=O stretching
II	1480-1575	CN stretching, NH bending,
III	1229-1301	CN stretching, NH bending,
IV	625-767	OCN bending mixed with other nodes
V	640-800	Out-of plane NH bending
VI	537-606	Out-of plane C=O bending
VII	~200	Skeletal torsion

Table 2.2: The amide I' region component bands [111, 112].

Amide I' band (cm ⁻¹)	Secondary structure assignment
1613-1630	β-sheet
1642-1649	Random coil
1650-1655	α-helix
1658-1674	Turn
1673	TFA
1682-1690	β-sheet
1694-1697	Turn

Table 2.3: Infrared bands of amino acids side chains [111].

Amino Acid	Wavenumber cm ⁻¹	Origin
Aspartic acid	1715	C=O stretch
Glutamic acid	1585	COO ⁻ asymmetric stretch
	1710	C=O stretch
Glutamine	1565	COO ⁻ asymmetric stretch
	1620-1640	ND ₂ stretch
Arginine	1670	C=O stretch
	1580	CN stretch
Histidine	1610	CN asymmetric stretch
	1600, 1625	ionised ring
Phenylalanine	1620	non-ionised ring
	1596,1607	Ring
Tyrosine	1500,1575	ionised ring
	1517,1590,1615	non-ionised ring
Tryptophan	1545	Ring

2.3.5 Attenuated total reflectance spectroscopy, ATR-IR

2.3.5.1 Background

Attenuated total reflectance (ATR) is also known as internal reflection spectroscopy (IRS) or multiple internal reflectance (MIR) [113]. This technique has become popular

tool for biological studies. It is a direct, flexible, simple and sensitive infrared technique. It can give qualitative and semi-quantitative analysis of compositional changes, conformation, orientation, and molecular interactions for samples either too thick or too strongly absorbing material [113]. In this technique, the changes that occur in an internally reflected infrared beam when the beam comes into contact with a sample are measured (Figure 2.4). The critical angle is defined as a function of the refractive indices of the two surfaces. The outcome attenuated radiation is measured by the spectrometer and gives the spectral characteristic of the sample. The ATR crystal is usually made of materials with high refractive index such as silicon, germanium, zinc selenide and diamond.

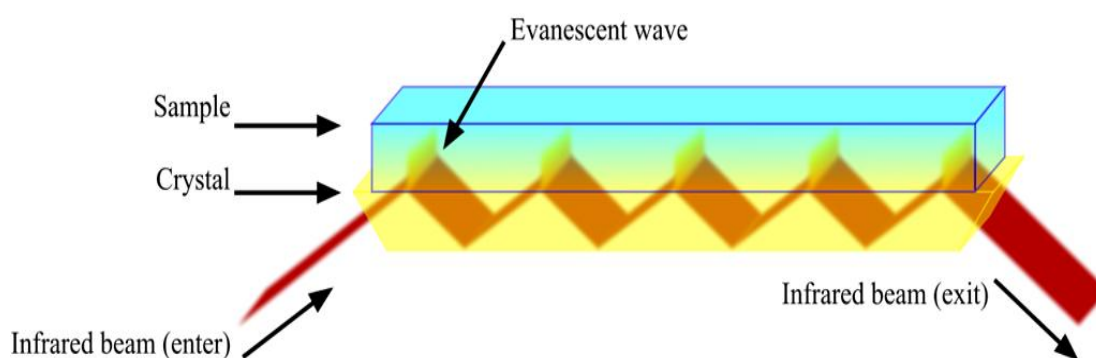


Figure 2.4: A multiple reflection ATR system [114].

2.3.5.2 Method

Golden Gate single reflection diamond ATR spectrometer from Specac Company was used to investigate the samples. A background air spectrum was recorded just before a sample was analysed. After the background collection, the sample was directly placed on a diamond crystal. Spectra were collected at room temperature. The spectra were processed with OMNIC 32 software.

2.3.6 Confocal laser scanning microscope, CLSM

2.3.6.1 Background

All fluorescence microscopes use fluorescence to create an image. The term of fluorescence is described as the emission of light from molecules that have absorbed light with a particular wavelength from an outside source of energy. The re-emitted light usually has a longer wavelength and lower energy than the absorbed radiation.

This reflected light is used to study the properties of organic or inorganic materials [115].

Laser scanning confocal microscope is an essential tool which uses the phenomena of fluorescence. This technique has an advantage of generating three dimensional images for a sample with excellent resolution, about 0.1 to 0.2 μm . Also, it is capable to reveal the presence of a single fluorescent molecule [116]. It has the ability to create optical sections within thick cells and tissue samples by rejecting the out-of-focus information from the image by the use of a suitably positioned pinhole [117, 118].

The basic component of the confocal microscopy was developed by Marvin Minsky in the mid-1950s. The first commercial instruments became available to the biological research in the late 1980s [116]. The main components of any laser scanning confocal microscope are: 1) laser excitation source; 2) dichromatic mirror; 3) objective lens; 4) pinhole aperture detectors and 5) specimen stage (Figure 2.5). To generate an image, first, a laser beam is passed through a light source aperture. Then, it is focused by an objective lens into a small volume within or on the surface of the sample. Scattered and reflected laser light as well as fluorescent light emitted from the sample are re-collected by the objective lens. The unwanted reflected light is separated by the use of suitable reflecting dichromatic mirrors. The in-focus light, after passing the pinhole, is collected by a very high sensitive detector called a photomultiplier. The signal comes from the photomultiplier is converted to a digital form containing the sample information. These informations are displayed on a computer screen where the sample can be adjusted to be presented [116].

2.3.6.2 Method

The CLSM images were taken by using the confocal upright zeiss LSM510 in the faculty of biological science at Leeds University. The specimens were directly placed on the sample stage. The LSCM images were taken by using the confocal upright Zeiss LSM510 in the faculty of biological science at Leeds University. The samples were directly placed on the sample stage. A laser light was applied on the sample surface. The images were adjusted and imported using zeiss LSM image browser software.

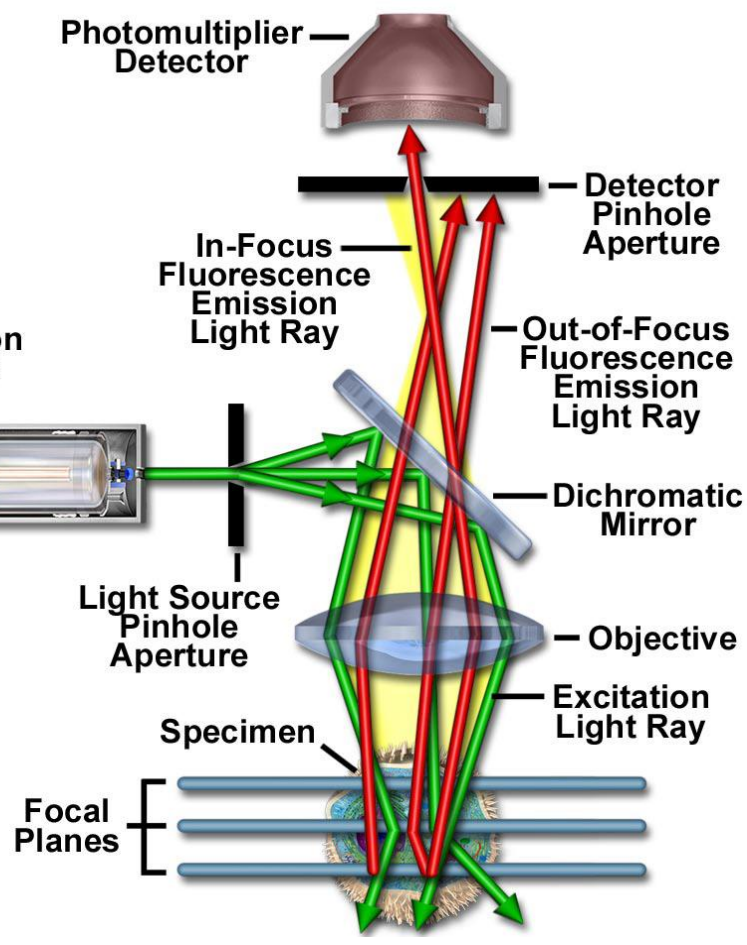


Figure 2.5: Schematic diagram of the optical pathway and principal components in a laser scanning confocal microscope [119].

Chapter 3

3 Self-assembly and morphology of peptide nanostructures and their gelation properties

3.1 Introduction

The purpose of the work described in this chapter is to study the mechanisms of nanotube formation and to determine the optimum conditions for their preparation. Applying nanotubes as drug carriers is of interest because their hollow cylindrical structures can permit the loading of large amounts of therapeutic agents. Moreover, their structures can protect entrapped drug molecules from denaturation and degradation throughout the delivery process [120, 121]. In previous studies within The Centre for Molecular Nanoscience, CMNS, at the University of Leeds, peptide nanotubes formed when P₁₁-2 was mixed with water and hexafluoroisopropanol (HFIP). Also, they were viewed when P₁₁-12 was prepared under physiological conditions. Therefore, in this chapter, peptide self-assembly is investigated in water and under physiological conditions where the formation of nanotubes is expected. The peptide nanotubes investigated here are compared with peptide fibre analogues. The study also includes the investigation of factors that affect peptide behaviour such as peptide concentration and pH.

3.1.1 Peptide self-assembly in water

The peptide P₁₁-2 (CH₃CO-Q-Q-R-F-Q-W-Q-F-E-Q-Q-NH₂) was selected to test the self-assembly of peptides in water. In aqueous solution at low pH and a concentration of 6.3 mM, P₁₁-2 forms fibril structures with a left-hand twist; at high pH, it forms a monomeric solution. As shown in Figure. 3.1, P₁₁-2 has hydrophobic phenylalanine residues at positions 4 and 8 and hydrophobic tryptophan at position 6; these groups provide intermolecular side-chain recognitions via π - π interactions. Charged arginine

and glutamic acid in the molecule promote antiparallel recognition through Coulombic attractions. These attractions, as well as hydrogen bonds, guide peptide molecules to self-assemble one-dimensionally, resulting in a hydrophilic antiparallel β -sheet arrangement [122]. In the presence of HFIP in the peptide solution, peptide nanotubes are formed [123]. In this chapter, P₁₁-2 is investigated for the formation of fibrils in pure water and of tubes in aqueous solutions of HFIP.

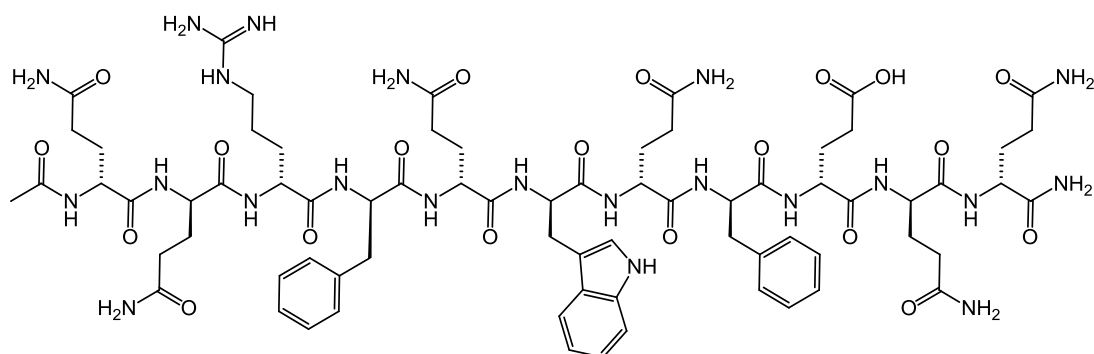


Figure 3.1: Molecular structure of P₁₁-2.

3.1.2 Peptide self-assembly under physiological conditions

By designing suitable self-assembled nanostructures under appropriate physiological conditions, novel nanostructures may be developed. This could open opportunities for applying self-assembled peptides in biological and medical applications. In our laboratory, P₁₁ peptide variants were designed to self-assemble into tapes and higher-order aggregates in the complex milieu of the physiological conditions as opposed to pure water. In a study first conducted by Sue Felton (at CMNS, School of Chemistry, University of Leeds) P₁₁ peptide variants, e.g. P₁₁-4 and P₁₁-8, were designed to self-assemble into fibrils of stacked tapes and gelled physiological media; these gels are currently being explored as scaffolds for tissue engineering applications [124]. More recently, in a work carried out in the same group by Dr Danielle Miles, gels based on peptide nanotubes (rather than fibrils) formed when 20 mg/ml of P₁₁-12 self-assembled in a phosphate-buffered saline solution [129]. In this study, the self-assembly and gelation of P₁₁-9 (CH₃CO-S-S-R-F-E-W-E-F-E-S-S-NH₂) and P₁₁-12 (CH₃CO-S-S-R-F-O-W-O-F-E-S-S-NH₂) were investigated in different physiological environments for preparing peptide nanotubes and for determining appropriate preparation conditions. P₁₁-9 has ionisable arginine residues at position 3, glutamic acid at positions 5, 7 and 9,

and four serine residues at positions 1, 2, 10 and 11. P₁₁₋₁₂ has serine residues at positions 1, 2, 10 and 11 and has ornithine side chains at positions 5 and 7. Figure 3.2 illustrates the molecular structures of P₁₁₋₉ and P₁₁₋₁₂.

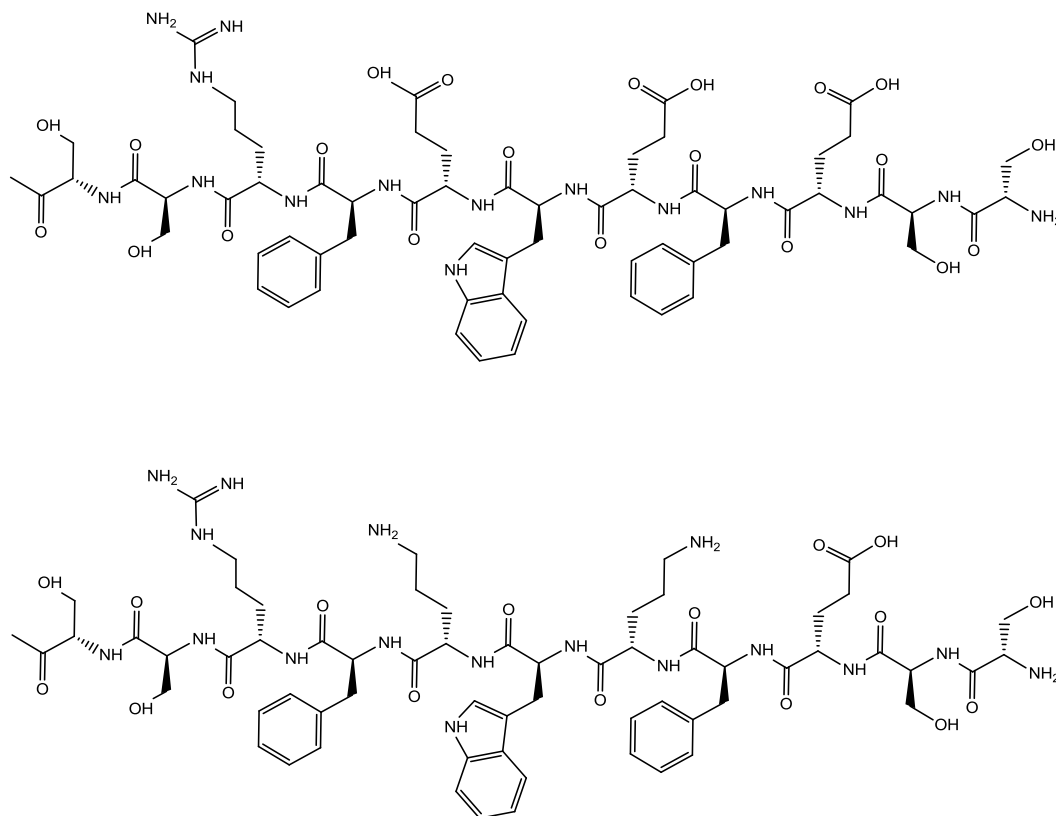


Figure 3.2: Molecular structures of peptides P₁₁₋₉ (top) and P₁₁₋₁₂ (bottom).

3.2 Materials and methods

3.2.1 Materials

Dulbecco's phosphate buffered saline (DPBS) without calcium and magnesium was purchased from Sigma Aldrich Ltd., Gillingham, Dorset, UK. Dulbecco's modified Eagle's medium (DMEM) was purchased from Fisher Scientific, Loughborough, Leicestershire UK.

3.2.2 Methods

3.2.2.1 Preparation of P₁₁₋₂ solutions in 100% D₂O

Solutions of varying concentrations were made by adding 0.5 ml of D₂O to the required weight of peptide. The resulting peptide concentrations are given in Table 3.1. Each sample was individually vortexed for approximately 30 s. Then, the samples were sonicated for around 20 min. The solutions were acidic between pH ~ 2.7 and 4.17; all were prepared at constant room temperature.

Table 3.1: Preparation methods for P₁₁₋₂ solutions in D₂O.

Peptide concentration	Details of preparation
1 mg/ml	0.5 mg P ₁₁₋₂ + 0.5 ml D ₂ O
5 mg/ml	2.5 mg P ₁₁₋₂ + 0.5 ml D ₂ O
10 mg/ml	5 mg P ₁₁₋₂ + 0.5 ml D ₂ O
20 mg/ml	10 mg P ₁₁₋₂ + 0.5 ml D ₂ O
40 mg/ml	20 mg P ₁₁₋₂ + 0.5 ml D ₂ O
60 mg/ml	30 mg P ₁₁₋₂ + 0.5 ml D ₂ O

3.2.2.2 Preparation of P₁₁₋₂ solution in 90% D₂O and 10% HFIP

Solutions of P₁₁₋₂ were prepared by weighing the required amounts of peptide. Then, 0.05 ml of HFIP was added to the dry peptide. The solutions were vortexed until they were clear and then 0.45 ml of D₂O was added to each sample. All samples were vortexed again for about 30 s and sonicated for 20 min. Preparation details are given in Table 3.2. All samples were acidic between pH 2.7 and 3.8; these processes were conducted at constant room temperature.

Table 3.2: Preparation methods for P₁₁₋₂ solutions in 90% D₂O and 10% HFIP.

Peptide concentration	Details of preparation
1 mg/ml	0.5 mg P ₁₁₋₂ + 0.05 ml HFIP + 0.45 ml D ₂ O
5 mg/ml	2.5 mg P ₁₁₋₂ + 0.05 ml HFIP + 0.45 ml D ₂ O
10 mg/ml	5 mg P ₁₁₋₂ + 0.05 ml HFIP + 0.45 ml D ₂ O
20 mg/ml	10 mg P ₁₁₋₂ +0.05 ml HFIP + 0.45 ml D ₂ O
40 mg/ml	20 mg P ₁₁₋₂ + 0.05 ml HFIP + 0.45 ml D ₂ O
60 mg/ml	30 mg P ₁₁₋₂ + 0.05 ml HFIP + 0.45 ml D ₂ O

3.2.2.3 Preparation of P₁₁₋₂ solutions at different pH levels

To study the behaviour of P₁₁₋₂ in response to pD, four solutions of P₁₁₋₂ were prepared. A volume of 0.05 ml of HFIP was added to 10 mg of P₁₁₋₂ and left to become clear. Then, 0.045 ml of D₂O was added to the mixture. The solutions were vortexed to be completely mixed. The samples were then adjusted to have different pD (2.8, 5.2, 7.3 and 9). Microlitre aliquots of 0.5 M NaOD were added to the solutions to alter their pD levels. Values of solution pD were obtained by $pD = pH \text{ metre reading} + 0.4$ [125, 126].

3.2.2.4 Preparation of peptide solutions under physiological conditions

Solutions of P₁₁₋₉ and P₁₁₋₁₂ were prepared under different physiological conditions, as shown in Tables 3.3 and 3.4, respectively. All samples were prepared at room temperature around 20°C. The samples were vortexed for 20 s and sonicated for 20 min. Then, to maximize peptide solubility, they were warmed to approximately 80°C for around 5 min.

Table 3.3: Conditions for preparation of P₁₁₋₉ gels.

Preparation conditions	pH/pD before adjustment	pH/pD	pH/pD after adjustment
10 mg of P ₁₁₋₉ + 0.5 ml DPBS containing 0.04% of NaN ₃	pH 5.4	0.4 μL of 0.5 M NaOH	pH 7.5
10 mg of P ₁₁₋₉ + 0.5 ml DMEM containing 0.04% of NaN ₃	pH 5.7	0.3 μL of 0.5 M NaOH	pH 7.2
10 mg of P ₁₁₋₉ + 0.5 ml of the physiological-like buffer solution (130 mM NaCl in D ₂ O)	pD 5.9	0.4 μL of 0.5 M NaOD	pD 7.3
10 mg of P ₁₁₋₉ + 0.5 ml of Triss-buffer (130 mM NaCl and 30 mM Tris-HCl in D ₂ O)	pD 9	0.5 μL of 0.5 M DCl	pD 7.1

Table 3.4: Conditions for preparation of P₁₁₋₁₂ gels.

Preparation conditions	pH/pD before adjustment	pH/pD	pH/pD after adjustment
10 mg of P ₁₁₋₁₂ + 0.5 ml DPBS containing 0.04% of NaN ₃	pH 3.8	0.6 μL of 0.5M NaOH	pH 7.4
10 mg of P ₁₁₋₁₂ + 0.5 ml DMEM containing 0.04% of NaN ₃	pH 5.2	0.7 μL of 0.5M NaOH	pH 7.3
10 mg of P ₁₁₋₁₂ + 0.5 ml of the physiological- like buffer solution (130 mM NaCl in D ₂ O)	pD 3.3	0.7 μL of 0.5M NaOD	pD 7.2
10 mg of P ₁₁₋₁₂ + 0.5 ml of Triss-buffer (130 mM NaCl and 30 mM Triss-HCl in D ₂ O)	pD 8.8	0.4 μL of 0.5M DCl	pD 7.2

3.3 Results

3.3.1 Self-assembly of P₁₁₋₂ in 100% D₂O

The peptide solutions described in Table 3.1 are shown in Figure 3.3. Figure 3.3(A) shows that, at a concentration of 1 mg/ml (0.6 mM), the solution forms a clear isotropic fluid with weak birefringence. At this concentration, which is above the critical concentration of P₁₁₋₂ ribbons, the solution contains both flexible ribbons and some monomeric peptides. According to the Aggeli group, the critical concentration for P₁₁₋₂ β -sheet ribbons is ≥ 0.1 mM [127].

Figure 3.3(B) shows that, at a concentration of 5 mg/ml (3.1 mM), a slightly viscous birefringent solution formed because of the increased peptide concentration. At this concentration (above c^*_{IN}), rigid fibrils are present, forming a nematic solution and showing optical birefringence. The c^*_{IN} represents the concentration at which the isotropic phase converts to the nematic phase. Birefringence is a property of the nematic phase; it is identified by the many colours visible when exposed to cross-polarised light [44, 127]. c^*_{IN} of P₁₁₋₂ is approximately 1.4 mg/ml (0.9 mM).

Figure 3.3(C) shows that, at a concentration of 10 mg/ml (6.2 mM), the solution shows strong birefringence and is more viscous when compared to the solution having a concentration of 5 mg/ml. When the peptide concentration was further increased to 20 mg/ml (12.5 mM), the sample forms a gel, as shown in Figure 3.3(D). At this concentration, which is above c^*_{gel} for P₁₁₋₂, rigid fibrils are connected to create fibre-like junctions, and a nematic gel forms. c^*_{gel} represents the concentration at which a solution changes from a nematic viscoelastic fluid to a nematic elastomeric-like gel [44]. c^*_{gel} for P₁₁₋₂ is estimated to be about 15 mg/ml (10 mM).

At concentrations of 40 mg/ml (25 mM) and 60 mg/ml (37 mM), Figures 3.3(E) and 3.3(F) show that the solutions are cloudy self-supported nematic gels. These hydrogel samples were observed over a period of five months after their preparation. After that time, they retain their original appearance, implying that they are stable.

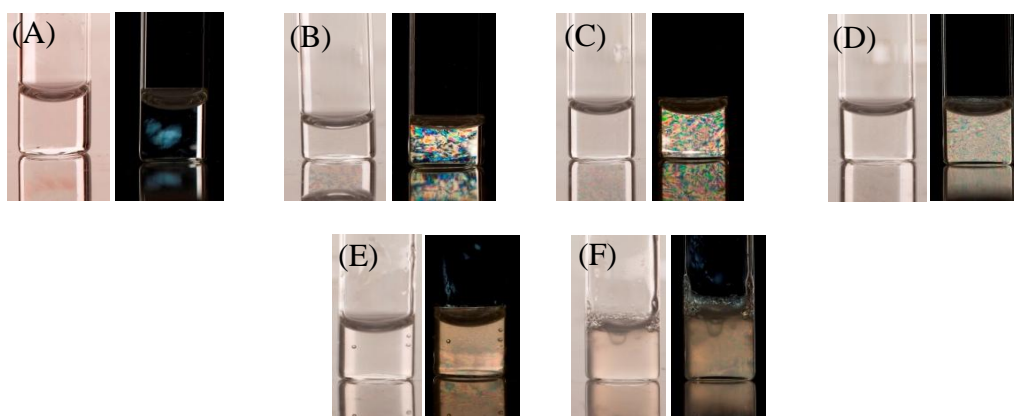


Figure 3.3: Photographs of P₁₁₋₂ samples in D₂O (left-hand side) and their optical micrographs through cross-polar lenses (right-hand side). (A) 1, (B) 5, (C) 10, (D) 20, (E) 40 and (F) 60 mg/ml.

3.3.1.1 Transmission electron microscopy, TEM

TEM was employed to study the morphology of P₁₁₋₂ aggregates as a function of peptide concentration. Figures 3.4–3.9 show the morphology of self-assembled P₁₁₋₂ in D₂O at different concentrations. In general, the majority of the aggregates are homogenous fibrils. The width and the rigidity of the fibrils increase with increasing peptide concentration.

Figure 3.4 shows a TEM image of peptide aggregates formed at a concentration of 1 mg/ml. A background of flexible ribbons is covering the grid with width about 4 nm. There are also flexible fibrils having wide width (w/w) of about 8–10 nm and narrow width (n/w) of about 2–3 nm and persistence lengths from 150 to 180 nm. At 5 mg/ml (Figure 3.5), most structures are fibrils with an approximate w/w of 8–13 nm and persistence length around 160 to 200 nm. There are also ribbons having widths of approximately 2–4 nm. At 10 mg/ml (Figure 3.6), the structures are rigid fibrils with longer persistence length, about 300–350 nm, covering the background of the grid and having w/w of about 10–14 nm and n/w of about 4–5 nm. The fibrils have twist pitches from 130 to 200 nm.

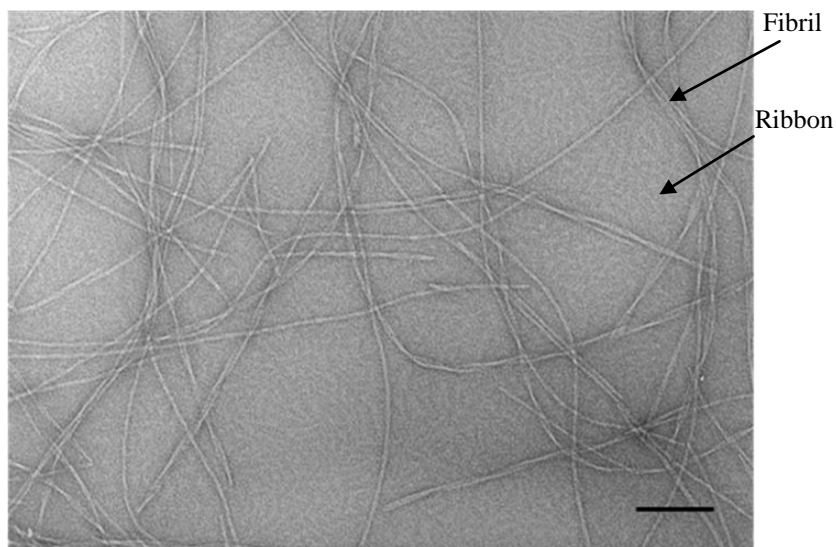


Figure 3.4: TEM image of 1 mg/ml P₁₁-2 in D₂O, one week old. Scale bar =100 nm.

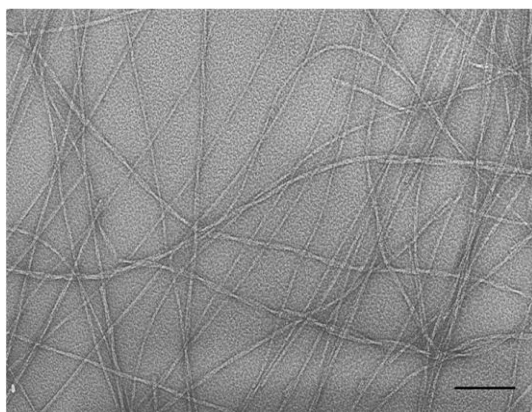


Figure 3.5: TEM image of 5 mg/ml P₁₁-2 in D₂O, one week old. Scale bar =100 nm.

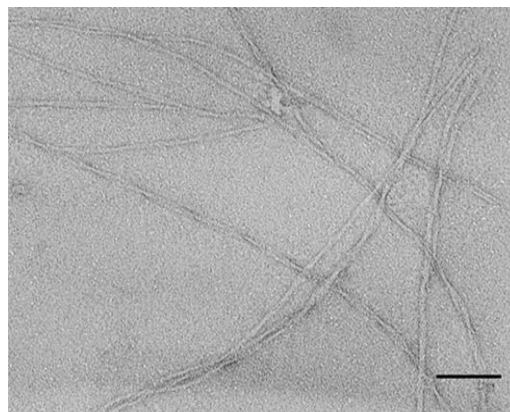


Figure 3.6: TEM image of 10 mg/ml in D₂O, one week old. Scale bar =100 nm

At 20 mg/ml (Figure 3.7), the aggregates are rigid fibrils covering the grid with w/w of about 10–15 nm and n/w of about 2–4 nm; these comprise about 90% of the aggregates. Few thin ribbons also form with widths of approximately 2–3 nm. At 40 mg/ml (Figure 3.8), the aggregates are fibrils having w/w of about 6–10 nm and n/w of about 2–3 nm.

At 60 mg/ml (Figure 3.9), highly twisted fibres form with fibre-like junctions. The fibres have w/w of approximately 15–24 nm, n/w of 4–5 nm and twist pitch of about 100–130 nm.

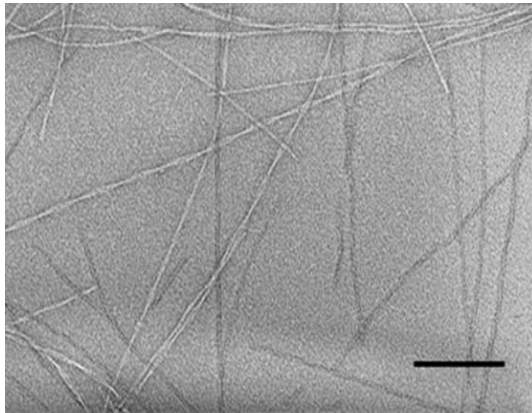


Figure 3.7: TEM image of 20 mg/ml P₁₁-2 in D₂O, one week old. Scale bar =100.

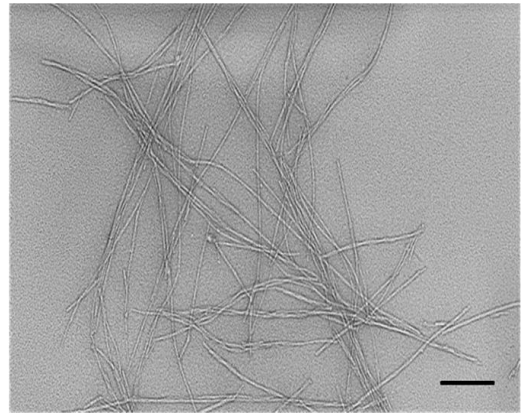


Figure 3.8: TEM image of 40 mg/ml in D₂O, one week old. Scale bar =100.

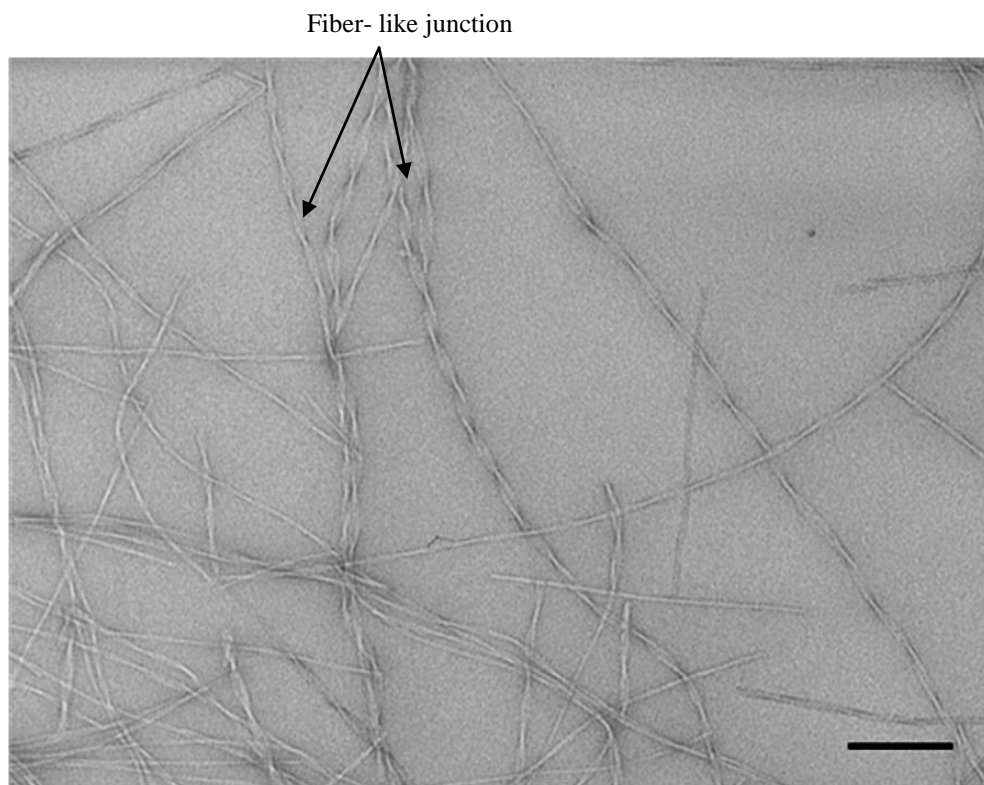


Figure 3.9: TEM image of 60 mg/ml P₁₁-2 in D₂O, one week old. Scale bar =100 nm.

3.3.1.2 Fourier transform infrared spectroscopy, FTIR

FTIR spectra were analysed for all peptide samples, and the amide I band region was band-fitted to determine the proportion of peptides in β -sheets. Figure 3.10 shows a representative spectrum of P₁₁-2 at a concentration of 20 mg/ml in D₂O; the spectrum was taken one week after sample preparation. The spectrum has a large absorption band at 1616 cm⁻¹, attributed to β -sheet aggregates, and another one at 1630 cm⁻¹. The spectrum shows a peak at 1649 cm⁻¹, corresponding to the random coil conformation. A peak is present at 1675 cm⁻¹, which corresponds to TFA molecules. The individual components of P₁₁-2 in the fitted amide I region are listed in Table 3.5. The table shows that about 89% of the peptide molecules are in β -sheets, while about 10% are in the random coil conformation.

Figure 3.11 presents overlaid spectra of amide I bands of P₁₁-2 in D₂O at concentrations of 60, 40, 20 and 10 mg/ml. All spectra are dominated with peaks located at β -sheet area.

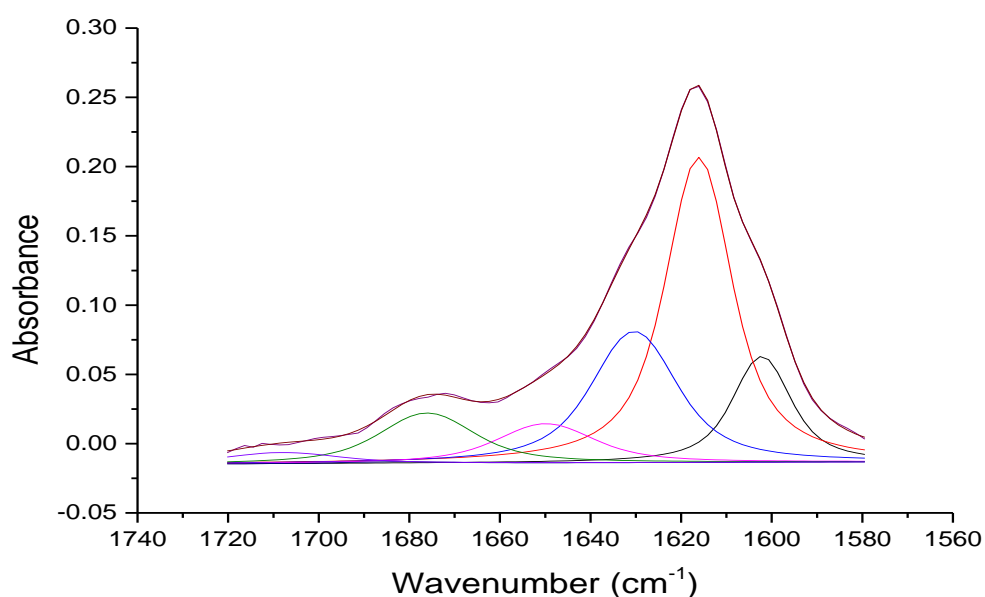


Figure 3.10: Fitted IR amide I' band of 20 mg/ml P₁₁-2 in D₂O showing β -sheet conformation.

Table 3.5: Identification of peaks in the fitted IR amide I' band of 20 mg/ml P₁₁-2 in D₂O.

Peak Centre cm ⁻¹	Area	Assignment
1601.212	1.6429	Arginine side chain
1616.118	5.5546	β-sheet
1630.343	2.9417	β-sheet
1649.900	0.9931	Random coil
1675.100	1.1897	TFA
1697.147	0.0493	Turn

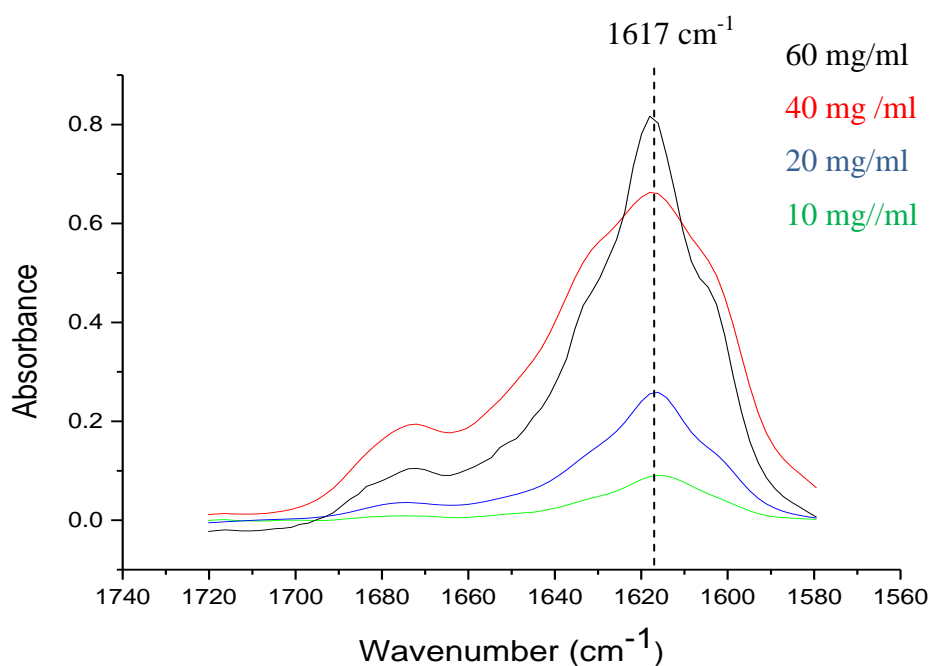


Figure 3.11: Overlaid amide I bands for different concentrations of P₁₁-2 in D₂O.

3.3.2 Self-assembly of P₁₁-2 in 90% D₂O and HFIP

Figure 3.12 shows solutions of P₁₁-2 in 90% D₂O and 10% HFIP. The solutions exhibit gelation behaviour and birefringence similar to those for solutions of P₁₁-2 in 100% D₂O. At the low concentration of 1 mg/ml, P₁₁-2 forms an isotropic liquid with weak

birefringence. At the higher concentrations of 5 and 10 mg/ml, P₁₁₋₂ is arranged into nematic domains forming nematic viscoelastic fluids. At concentrations of 20, 40 and 60 mg/ml, P₁₁₋₂ forms strong self-supported gels.

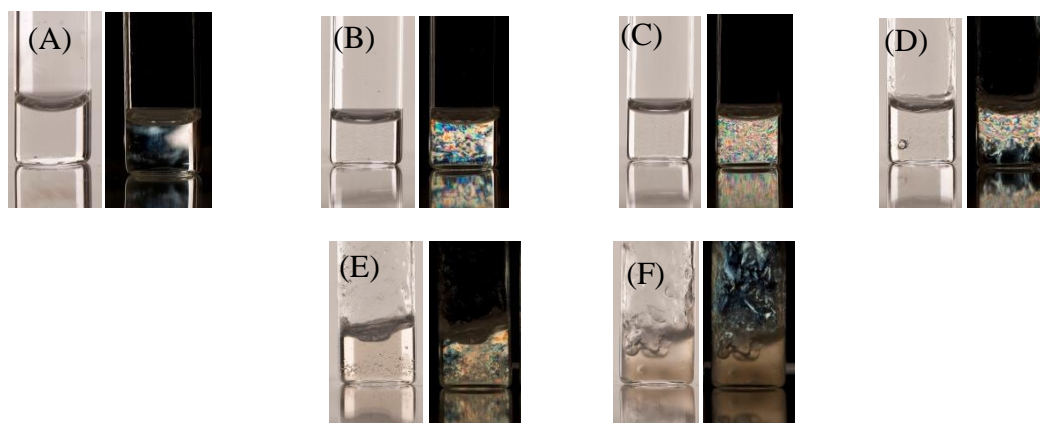


Figure 3.12: Photographs of P₁₁₋₂ samples in 90% D₂O and 10% HFIP (left-hand side) and their optical micrographs through cross-polar lenses (right-hand side). (A) 1, (B) 5, (C) 10, (D) 20, (E) 40 and (F) 60 mg/ml.

3.3.2.1 Transmission electron microscopy, TEM

TEM was employed to investigate P₁₁₋₂ self-assembly as a function of peptide concentration in the presence of 10% HFIP in D₂O. In general, two different types of peptide aggregates were observed: fibrils and tubes. At 1 mg/ml of peptide (Figure 3.13), approximately 60% of the structures are still in the initial stage and appeared as circular amorphous aggregates with diameters around 12 to 23 nm. Fibrils appear with w/w of 10–15 nm and n/w of about 2–3 nm. Their persistence length is 95–130 nm, and the twist pitch is about 60–68 nm. At 5 mg/ml (Figure 3.14), short fibril aggregates appear with w/w of about 10–13 nm, n/w of about 2–3 and total lengths of around 164 nm. At 10 mg/ml (Figure 3.15), helical structures, which are intermediate structures for nanotubes, appear with widths of about 23–25 nm.

Amorphous aggregates

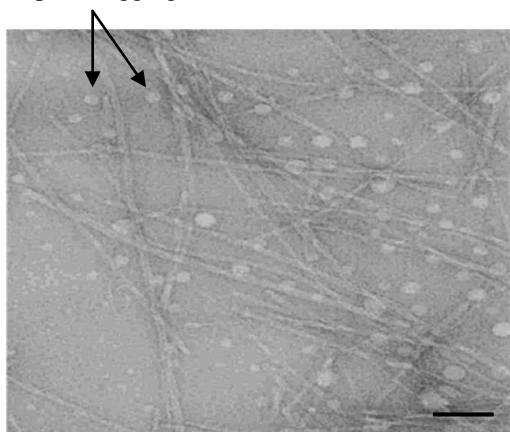


Figure 3.13: TEM image of 1 mg/ml P₁₁-2 in 90% D₂O and 10% HFIP, one week old. Scale bar = 100 nm.

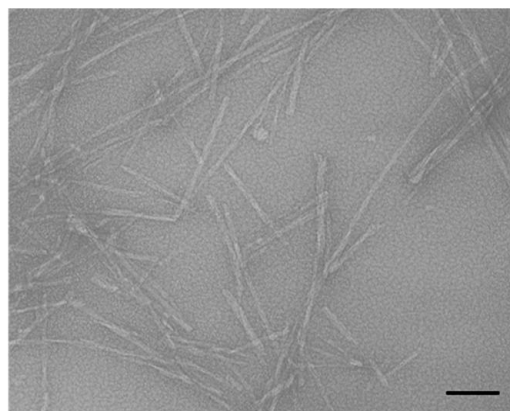


Figure 3.14: TEM image of 5 mg/ml P₁₁-2 in 90% D₂O and 10% HFIP, one week old. Scale bar = 100 nm.

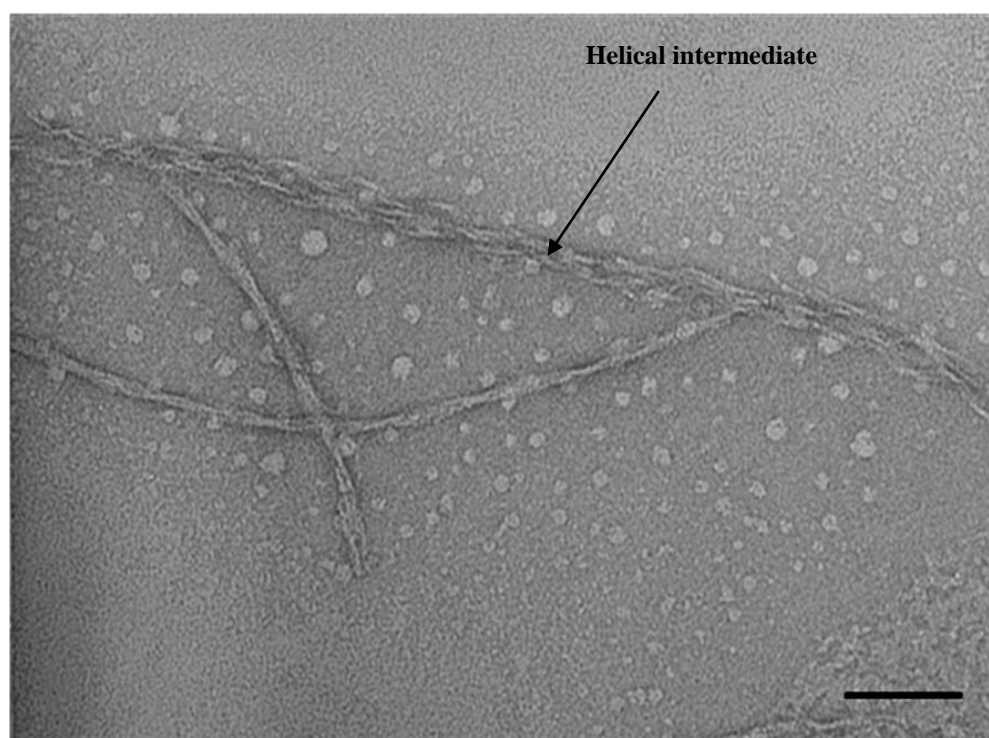
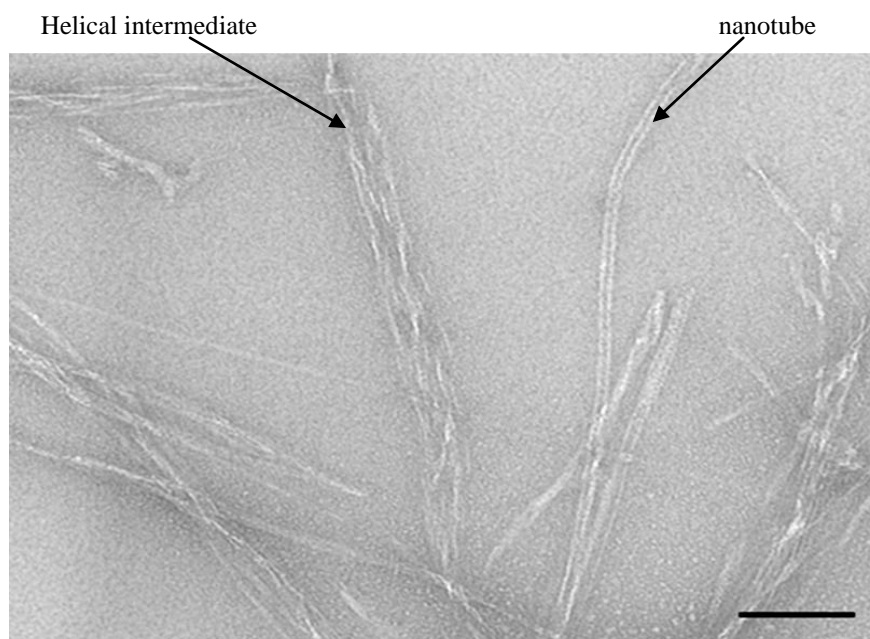


Figure 3.15: TEM image of 10 mg/ml P₁₁-2 in 90% D₂O and 10% HFIP, one week old. Scale bar = 100 nm.

For 20 mg/ml, Figure 3.16 shows intermediate helices and a peptide nanotube with an inner pore of about 5–6 nm and an outer pore of about 11–13 nm. In Figure 3.17, at 40 mg/ml, P₁₁-2 favours the formation of nanotubes rather than fibrils. About 70% of the aggregates are tubes having inner pore diameters of approximately 5–7 nm and outer diameters of around 12–14 nm. Approximately 30% of the aggregates are helical

intermediates for nanotube formation. After 17 days, Figure 3.18 shows that the majority of aggregates are nanotubes with inner pore diameters of about 5–8 nm and outer pore diameters of about 13–18 nm.



**Figure 3.16: TEM image of 20 mg/ml P₁₁-2 in 90% D₂O and 10% HFIP, one week old.
Scale bar =100 nm.**

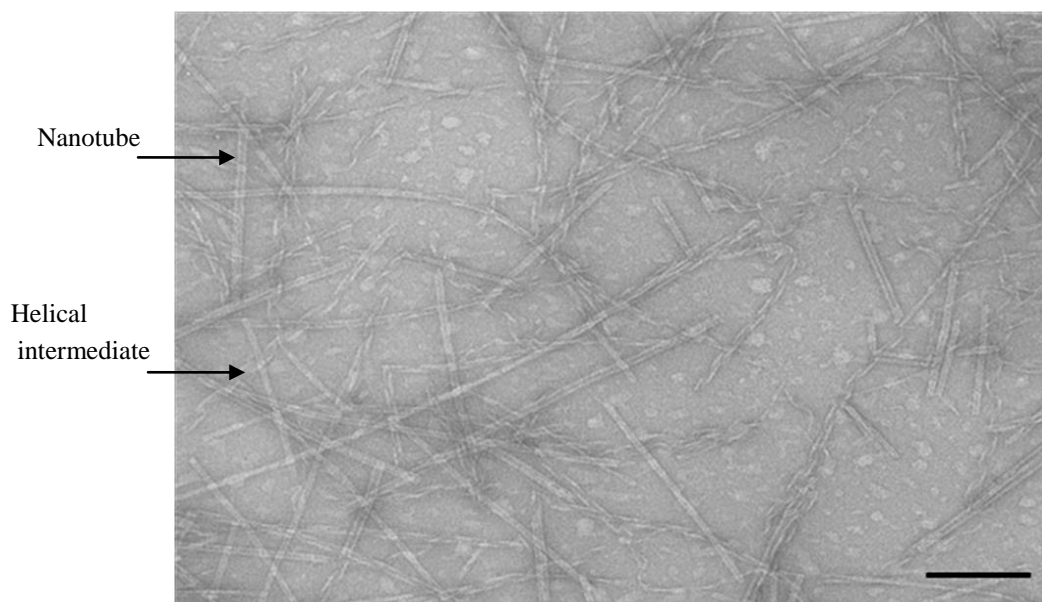


**Figure 3.17: TEM image of 40 mg/ml P₁₁-2 in 90% D₂O and 10% HFIP, after one week.
Scale bar =100 nm.**

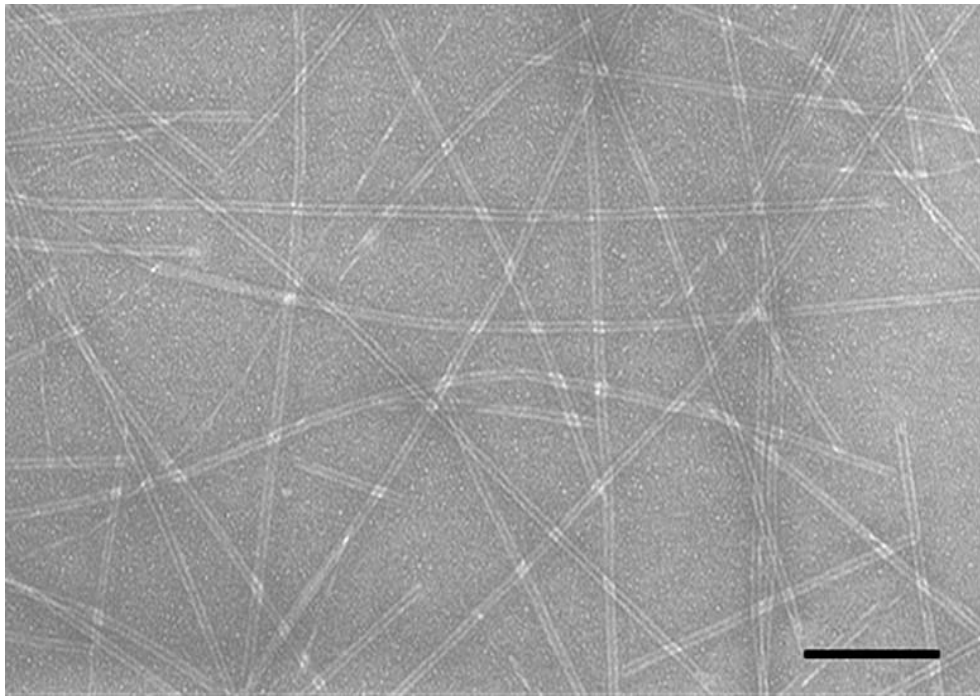


**Figure 3.18: TEM image of 40 mg/ml P₁₁-2 in 90% D₂O and 10% HFIP, 17 days old.
Scale bar =100 nm.**

At 60 mg/ml (Figure 3.19), peptide nanotubes do not occur; instead, the aggregates are highly twisted fibrils having w/w of about 7–10, n/w of 3–5 nm.

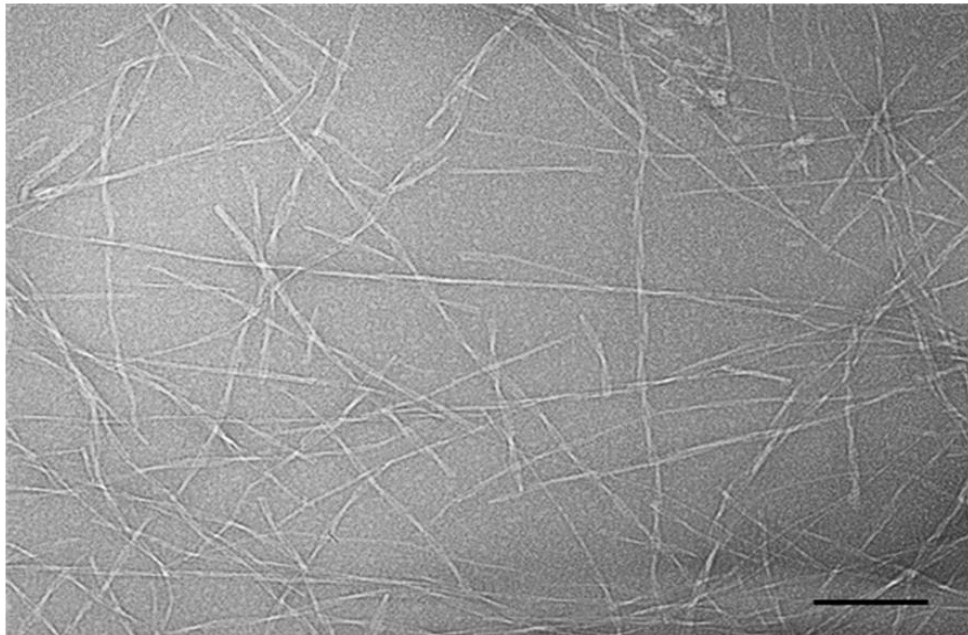


**Figure 3.19: TEM image of 60 mg/ml P₁₁-2 in 90% D₂O and 10% HFIP, 17 days old.
Scale bar =100 nm.**

3.3.2.2 Fourier transform infrared spectroscopy, FTIR

FTIR spectra were taken for P₁₁-2 as a function of peptide concentration in the presence of 10% HFIP in D₂O. Figure 3.20 shows representative spectra of P₁₁-2 at a concentration of 20 mg/ml at one week after sample preparation. The band-fitted spectrum shows a large peak at 1618 cm⁻¹, which corresponds to β -sheet conformation and another one at 1636 cm⁻¹. A weak peak appears at 1682 cm⁻¹, which corresponds to the antiparallel β -sheet. Identifications of individual components are listed in Table 3.6. The table indicates that 92% of the P₁₁-2 spectrum has the β -sheet conformation, which is relatively similar to the portion of β -sheet in pure water in section 3.3.1.2.

Figure 3.21 presents overlaid spectra in amide I regions of P₁₁-2 in D₂O in the presence of 10% HFIP at peptide concentrations of 60, 20, 40 and 10 mg/ml. Each spectrum has a peak indicating the β -sheet conformation.

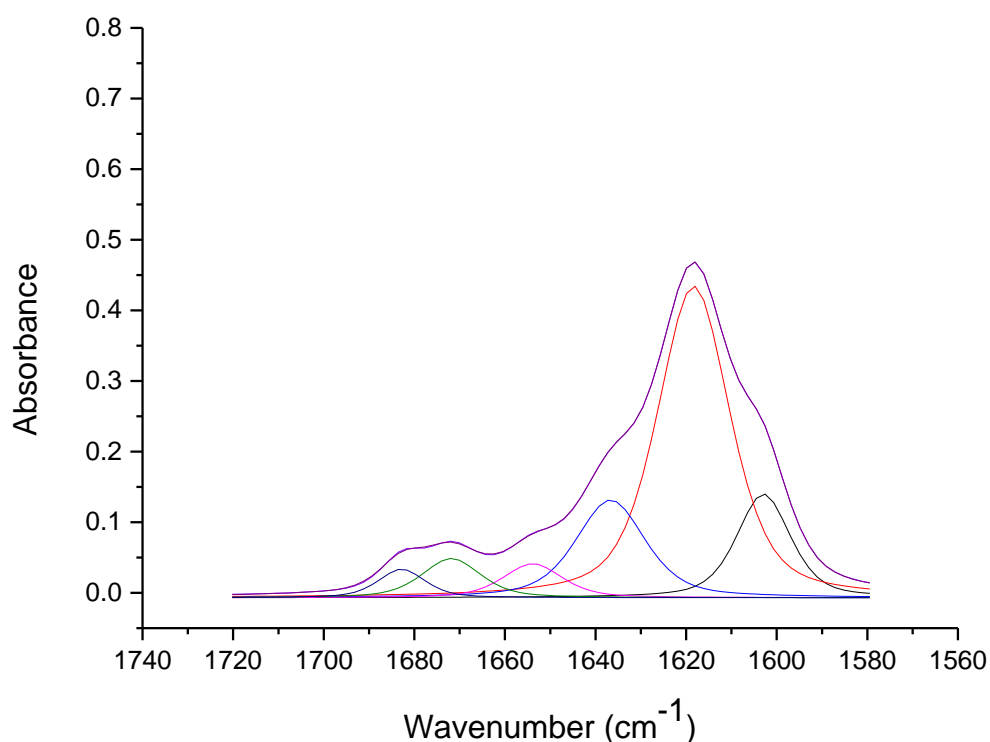


Figure 3.20: Fitted IR amide I band of 20 mg/ml P₁₁-2 in D₂O and 10% HFIP showing β -sheet conformation.

Table 3.6: Identifications of peaks in the IR amide I' band of 20 mg/ml P₁₁-2 in 90% D₂O and 10% HFIP.

Peak Centre cm ⁻¹	Area	Assignment
1602.916	2.7140	Arginine side chain
1618.328	10.9779	β-sheet
1636.679	3.2807	β-sheet
1653.875	0.9778	α-helix
1671.849	1.1144	TFA
1682.786	0.6489	β-sheet

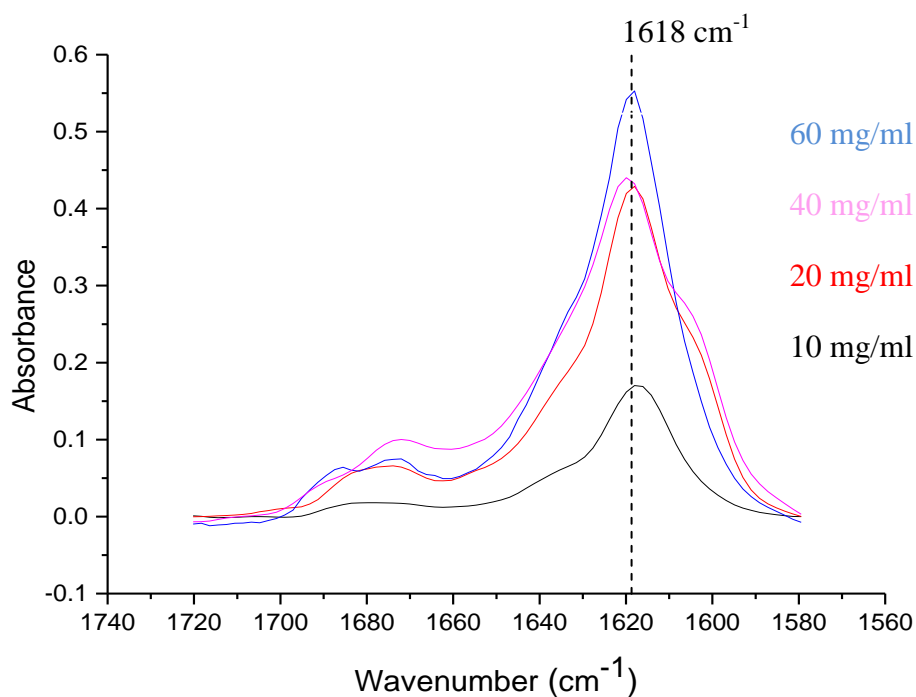


Figure 3.21: Overlaid IR amide I' bands for different concentrations of P₁₁-2 in 90% D₂O and %10 HFIP.

3.3.3 Self-assembly of P₁₁₋₂ as a function of pH

The self-assembly process depends on a number of external triggers, such as peptide concentration, ionic strength and pH/pD [122]. In this section, preliminary data are presented on the responsiveness of P₁₁₋₂ self-assembly to changes in pH. The behaviour of P₁₁₋₂ at different pD levels was tested in 90% D₂O and 10% HFIP.

Solutions of P₁₁₋₂ in D₂O and HFIP were prepared at different levels of pD, as described in Section 3.2.2.3. The results are shown in Figure 3.22. The solution of P₁₁₋₂ at pD = 2.8 forms a clear nematic gel, while solutions at pD levels of 5.2, 7.3 and 9 form cloudy liquids with many gel-like precipitates. This phenomenon is called solution flocculation; it occurs when P₁₁₋₂ solutions have pH > 5 [122].

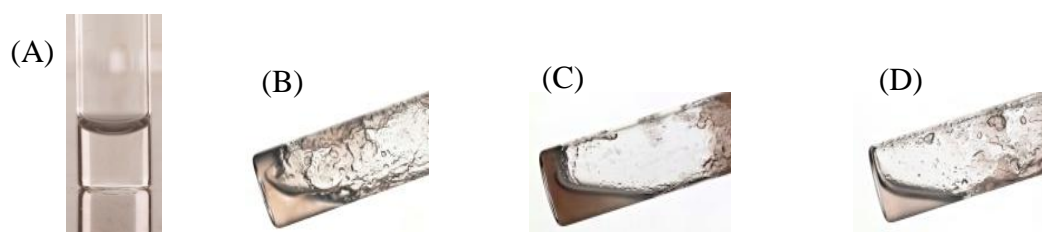


Figure 3.22: P₁₁₋₂ solutions at different levels of pD: (A) pD = 2.8, (B) pD = 5.2, (C) pD = 7.3 and (D) pD = 9.

3.3.3.1 Transmission electron microscopy, TEM

TEM was used to investigate morphologies of the peptide aggregates as a function of pD. Figure 3.23(A) shows that, at pD = 2.8, P₁₁₋₂ aggregates are well distributed. At pD = 5.2, Figure 3.23(B) shows that P₁₁₋₂ starts to form bundles of aggregates. For pD = 7.3 and pD = 9, Figures 3.23(C) and 3.23(D) show that P₁₁₋₂ forms large bundles of peptide aggregates.

3.3.3.2 Fourier transform infra-red Spectroscopy, FTIR

Figure 3.23 shows spectra of P₁₁₋₂ samples at different pD levels. The figure shows that P₁₁₋₂ at pD levels of 2.8, 5.2, 7.3 and 9 have large absorption bands centred at 1618 cm⁻¹, which correspond to the β -sheet conformation.

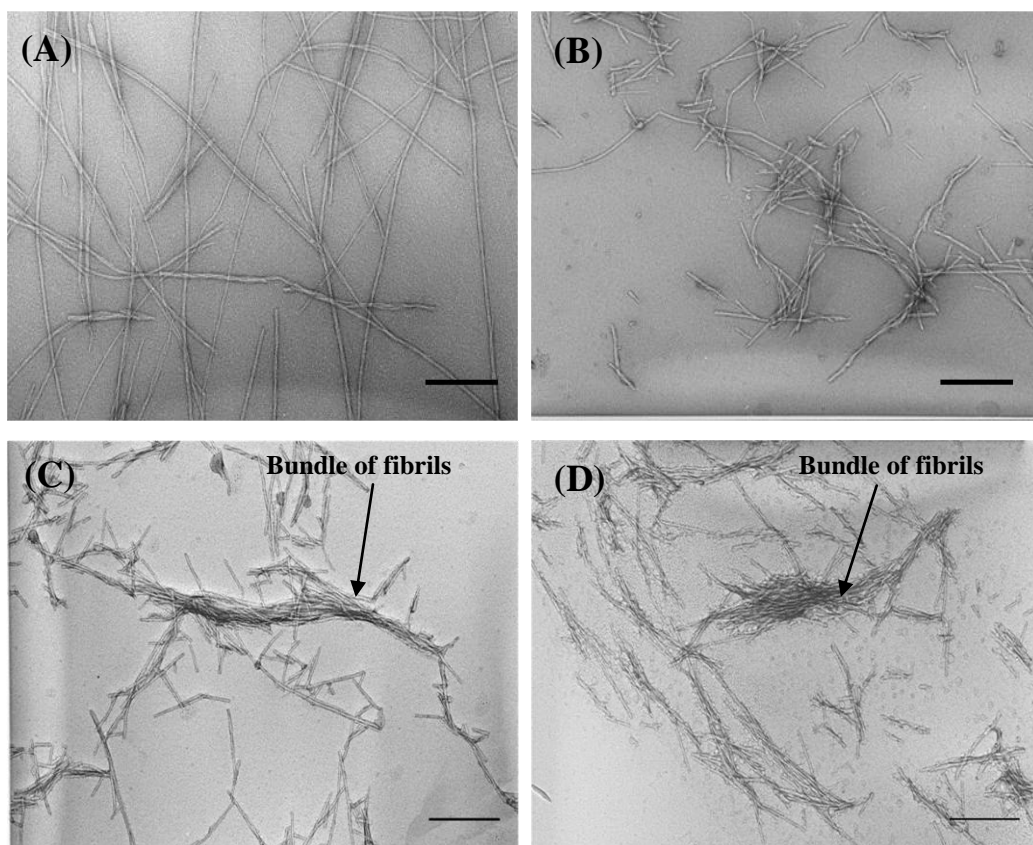


Figure 3.23: TEM images of 20 mg/ml P₁₁₋₂ in 90% D₂O and 10% HFIP at different pD levels. (A) pD = 2.8, (B) pD = 5.2, (C) pD = 7.3 and (D) pD = 9. All samples were one-week old. Scale bar = 100 nm.

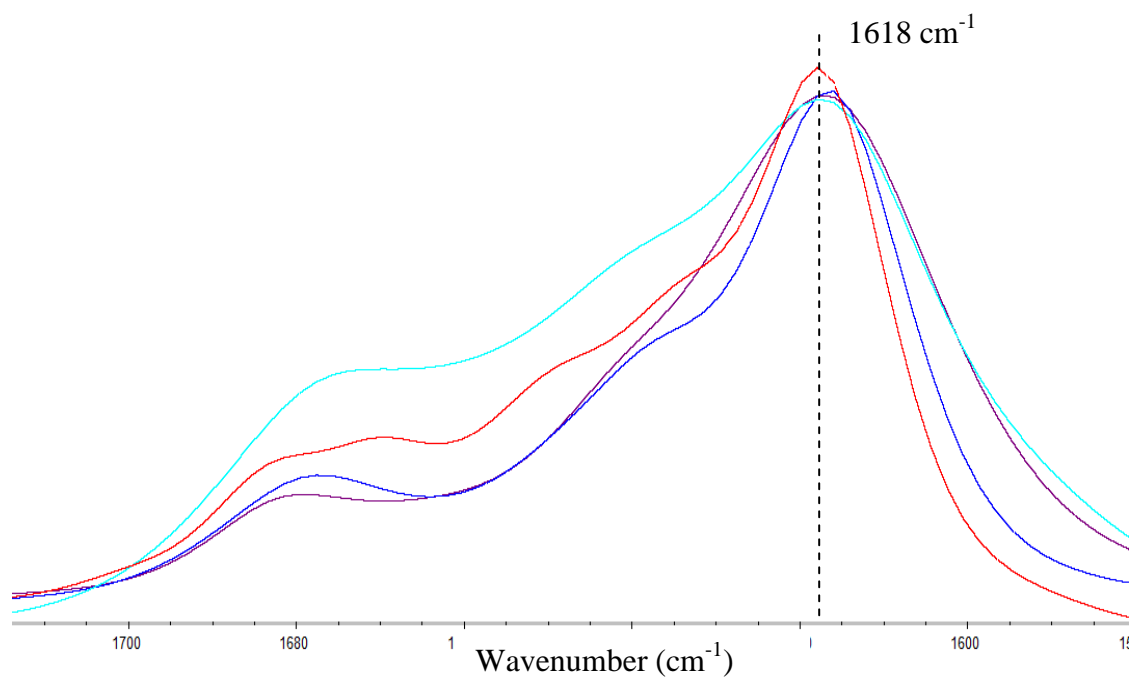


Figure 3.24: Overload IR amide I' regions of 20 mg/ml P₁₁₋₂ in 90% D₂O and 10% HFIP as a function of pD.

3.3.4 Peptide self-assembly in physiological-like solution

3.3.4.1 P₁₁₋₉

It was found that all P₁₁₋₉ solutions (Figure 3.25) prepared in physiological conditions, as described in Table 3.3, resulted in clear self-supporting gels. However, the sample with P₁₁₋₉ in the Tris buffer was a weak gel (Figure 3.25D).

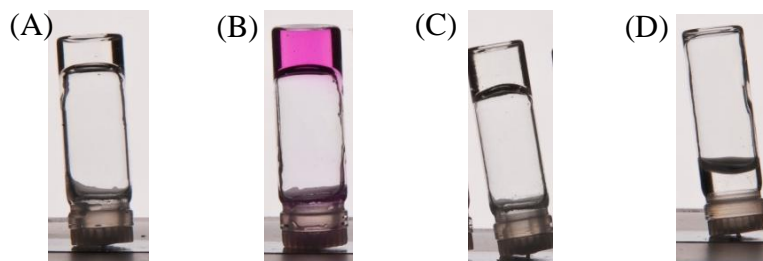


Figure 3.25: Photographs of peptide gels of 20 mg/ml P₁₁₋₉ under different physiological conditions: (A) in DPBS, (B) in DMEM, (C) in physiological-like buffer and (D) in Tris buffer.

3.3.4.1.1 Transmission electron microscopy, TEM

TEM was used to study the morphology of the peptide aggregates in physiological conditions. Figure 3.26 shows that, in all physiological environments, P₁₁₋₉ forms thin fibrils in the presence of ribbon networks. The wide width of the fibrils is 7–9 nm, and the narrow width is 3–4 nm. None of the images in Figure 3.25 show nanotubes.

3.3.4.1.2 Fourier transform infra-red spectroscopy, FTIR

The FTIR spectrum of P₁₁₋₉ (20 mg/ml) in D₂O containing 130 mM NaCl is shown in Figure 3.27. The amide I region of the spectrum was band-fitted; the fitted spectrum is dominated by three peaks for β -sheets located at 1613 cm⁻¹, 1625 cm⁻¹ and 1637 cm⁻¹. There are also peak peaks at 1680 cm⁻¹ and 1686 cm⁻¹, corresponding to the antiparallel β -sheet. The spectrum shows a weak peak at 1646 cm⁻¹, which corresponds to the random coil state. Table 3.7 lists the peak assignments and shows that β -sheet aggregates involve about 57% of the peptides, while random coils constitute about 6%.

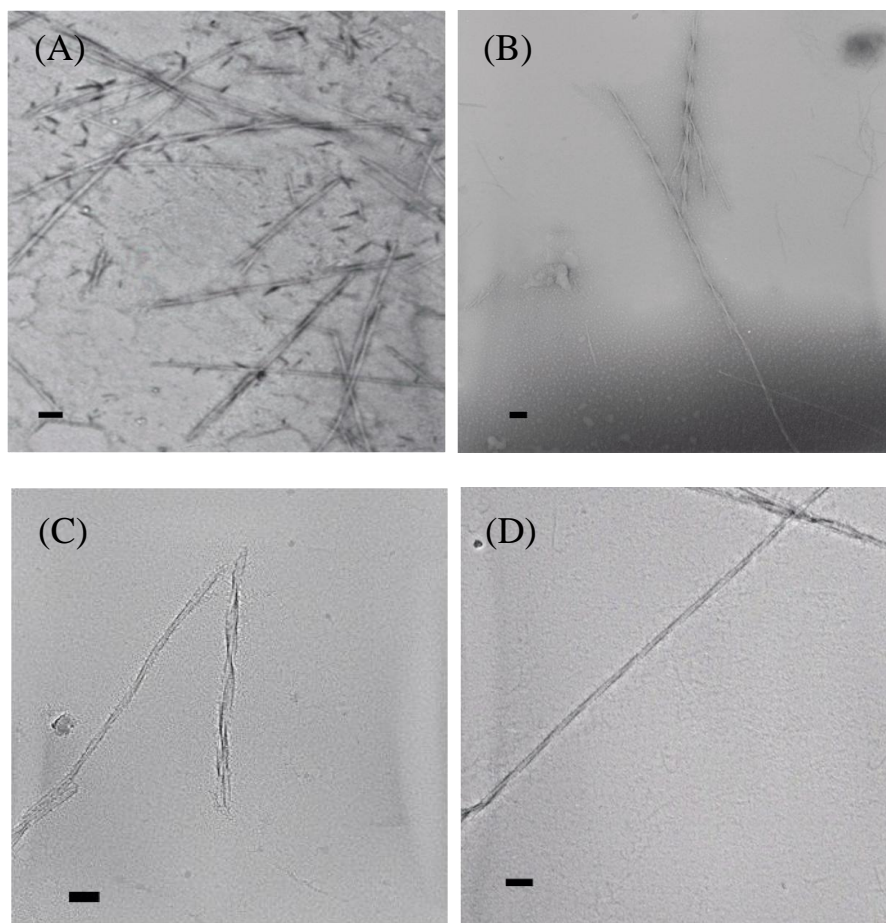


Figure 3.26: TEM images of 20 mg/ml P₁₁₋₉ under different physiological-like conditions: (A) in DPBS, (B) in DMEM, (C) in physiological-like buffer and (D) in Tris buffer.

Scale bar =100 nm.

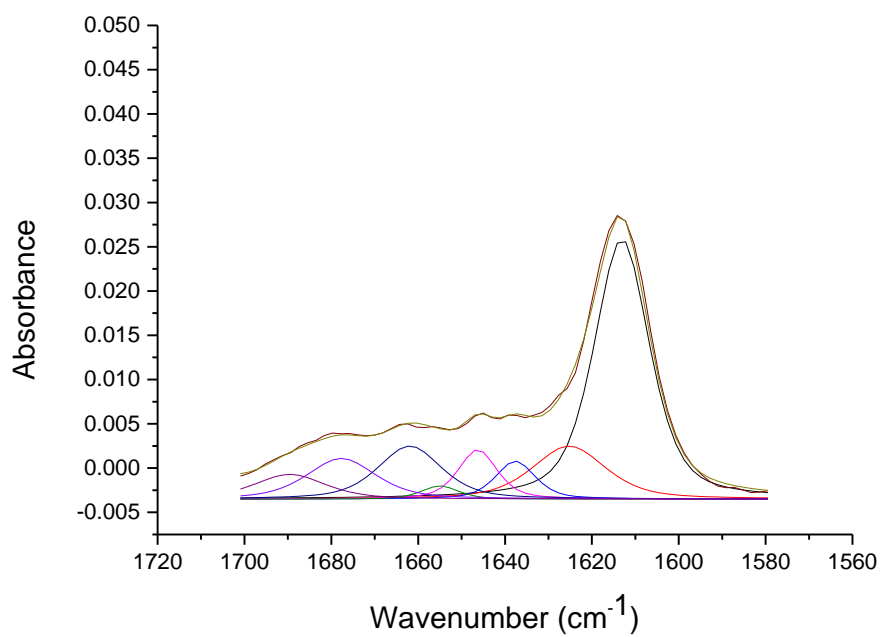


Figure 3.27: Fitted IR amide I' band of 20 mg/ml P₁₁₋₉ in D₂O containing 130 mM NaCl.

Table 3.7: Identifications of peaks in the fitted IR amide I' band of 20 mg/ml P₁₁₋₉ in D₂O containing 130 mM NaCl.

Peak Centre cm ⁻¹	Area	Assignment
1613.009	0.6876	β-sheet
1625.259	0.1332	β-sheet
1637.620	0.1101	β-sheet
1646.311	0.1073	Random coil
1654.970	0.5876	α-helix
1661.952	0.1266	Turn
1680.002	0.1001	β-sheet
1686.587	0.0730	β-sheet

The FTIR spectrum of 20 mg/ml P₁₁₋₉ in D₂O containing 130 mM NaCl and 30 mM triss-HCl was collected (Figure 3.28). The amide I region of the spectrum was band fitted. The β-sheet peaks are located at 1613 cm⁻¹ and 1623 cm⁻¹. The antiparallel β-sheet peak is located at 1681 cm⁻¹. A weak peak is located at 1644 cm⁻¹ corresponding to the random coil state. The individual components of the spectrum are listed in the Table 3.8. The table shows that about 82% of the peptide is β-sheet, whilst about 8% is in the random coil state.

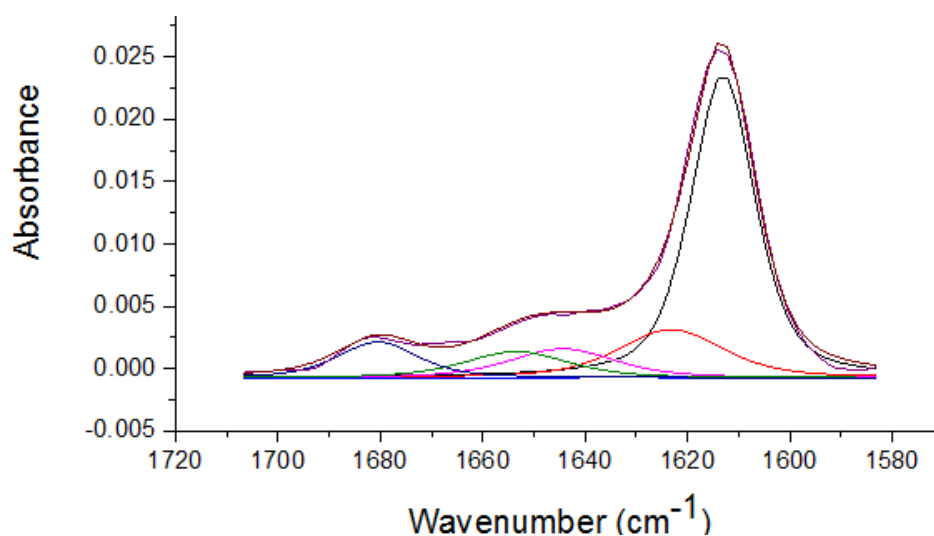


Figure 3.28: Fitted IR amid I' band of 20 mg/ml P₁₁₋₉ in D₂O containing 130 mM NaCl and 30 mM of Tris-HCl.

Table 3.8: Identification of peaks in the IR fitted amide I' band of 20 mg/ml P₁₁-9 in D₂O containing 130 mM NaCl and 30 mM Tris-HCl.

Peak Centre cm ⁻¹	Area	Assignment
1613.110	0.4877	β-sheet
1623.235	0.1251	β-sheet
1644.421	0.0762	Random coil
1654.850	0.0676	α-helix
1681.525	0.0830	β-sheet

3.3.4.2 P₁₁-12

All P₁₁-12 solutions were prepared as described in Table 3.4; they form clear self-supporting gels, as shown in Figure 3.29.

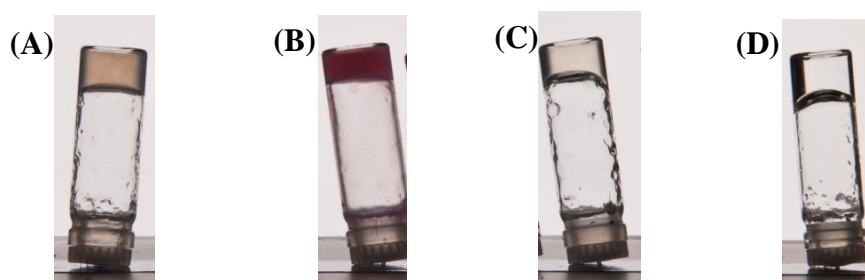


Figure 3.29: Photographs of peptide gels of 20 mg/ml P₁₁-12 under different physiological-like conditions. (A) in DPBS, (B) in DMEM, (C) in physiological-like buffer, (D) in Tris buffer.

3.3.4.2.1 Transmission electron microscopy, TEM

Figure 3.30 shows the morphology of P₁₁-12 self-assembled peptides under different physiological conditions. The figure shows that the structures are all fibrils, and no peptide nanotubes form.

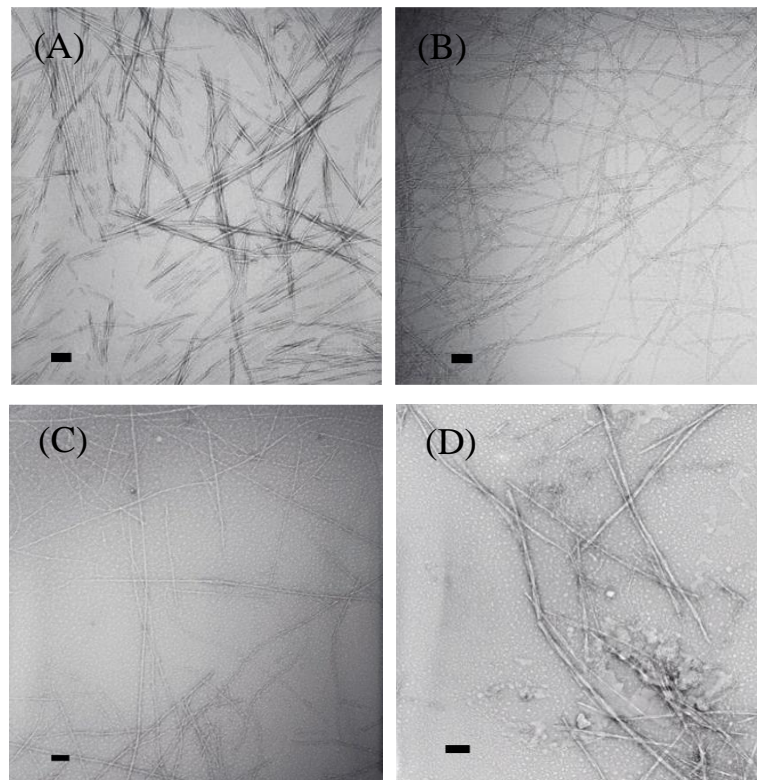


Figure 3.30: TEM images of 20 mg/ml P₁₁₋₁₂ under different physiological-like conditions: (A) in DPBS, (B) in DMEM, (C) in physiological-like buffer and (D) in Tris buffer.

3.3.4.2.2 Fourier transform infra-red spectroscopy, FTIR

FTIR spectra of 20 mg/ml P₁₁₋₁₂ in D₂O containing 130 mM NaCl were collected, as shown in Figure 3.31. The amide I region of the spectrum was band-fitted. Two peaks for β -sheet aggregates appear at 1615 cm⁻¹, 1629 cm⁻¹. From Table 3.9, it was found that about 71% of the peptides form β -sheet aggregates.

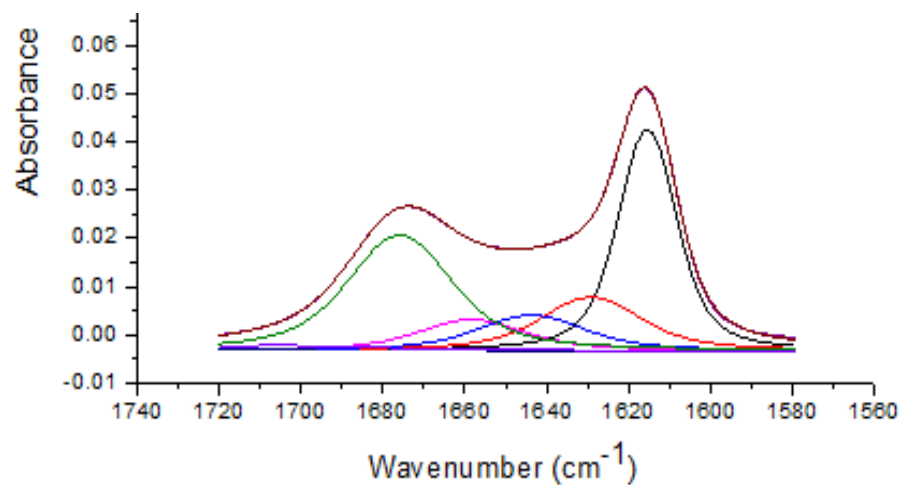


Figure 3.31: Fitted IR amide I' band for 20 mg/ml P₁₁₋₁₂ in D₂O containing 130 mM NaCl.

Table 3.9: Identification of peaks in fitted IR amide I' band of 20 mg/ml P₁₁₋₁₂ in D₂O containing 130 mM NaCl.

Peak Centre cm ⁻¹	Area	Assignment
1615.394	1.0085	β-sheet
1629.152	0.4381	β-sheet
1643.754	0.3118	Helix
1658.370	0.2699	Turn
1675.868	0.9668	TFA

The FTIR spectra of 20 mg/ml P₁₁₋₁₂ in D₂O containing 130 mM NaCl and 30 mM Tris-HCl were also collected (Figure 3.32), and the amide I region of the spectra was band-fitted. Peaks for β-sheets are located at 1615 cm⁻¹, 1629 cm⁻¹ and 1637 cm⁻¹. A weak peak, corresponding to the random coil state, is located at 1645 cm⁻¹. The individual components of the spectrum are identified in Table 3.10. The table shows that about 72 % of the peptides are in β-sheets, while about 6% are in the random coil state.

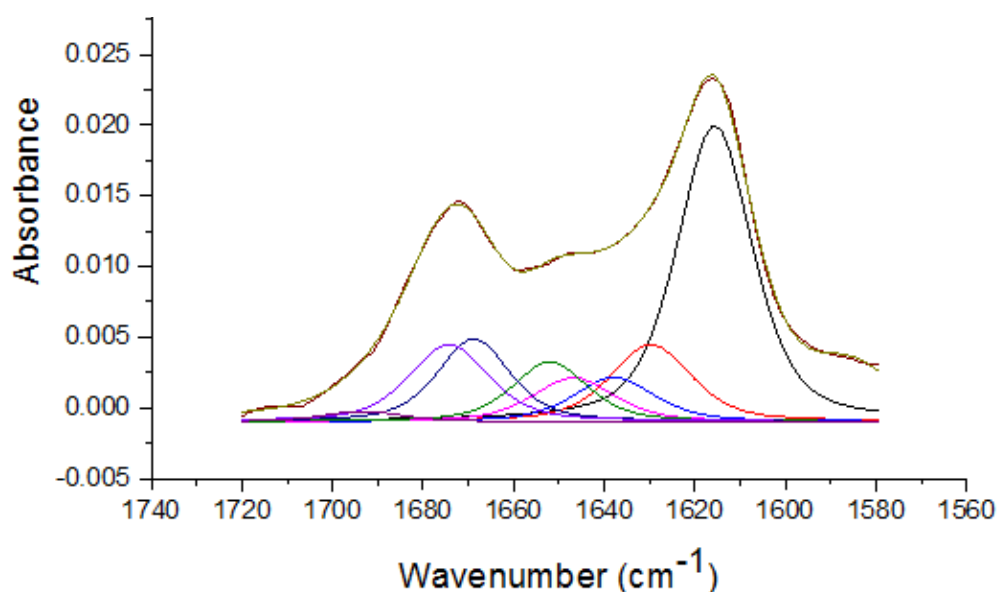


Figure 3.32: Fitted IR amide I' band of 20 mg/ml P₁₁₋₁₂ in 130 mM NaCl and 30 mM of Tris-HCl in D₂O.

Table 3.10: Identification of peaks in fitted amide I' band for 20 mg/ml P₁₁-12 in 130 mM NaCl and 30 mM of Tris-HCl in D₂O.

Peak Centre cm ⁻¹	Area	Assignment
1615.700	0.5010	β-sheet
1629.392	0.1245	β-sheet
1637.246	0.0869	β-sheet
1646.963	0.0646	random coil
1651.479	0.1093	Helix
1668.000	0.0955	Turn
1674.055	0.1976	TFA

3.4 Discussion

3.4.1 Self-assembly of P₁₁-2 in 100% D₂O

It has been previously found that the amphiphilic nature of P₁₁-2 leads to the formation of peptide tapes. A critical concentration is needed to start the self-assembly process. The assembly of peptide molecules into higher structures increases with increasing peptide concentration. This hypothesis is tested in this section. Birefringence was weak at low concentrations and strong at high concentrations, which demonstrates that P₁₁-2 forms high-order aggregates as the peptide concentration increases. TEM images of P₁₁-2 in water showed networks of long polymers covering the grids. At a concentration of 60 mg/ml, fibre-like junctions appear, while at lower concentrations, the structures are fibrils and ribbons. The images support the hypothesis that structural order increases with increasing peptide concentration. This progression matches reports by the Aggeli group [45, 128]. The behaviour of P₁₁-2 in water as a function of peptide concentration is summarized in Figure 3.33

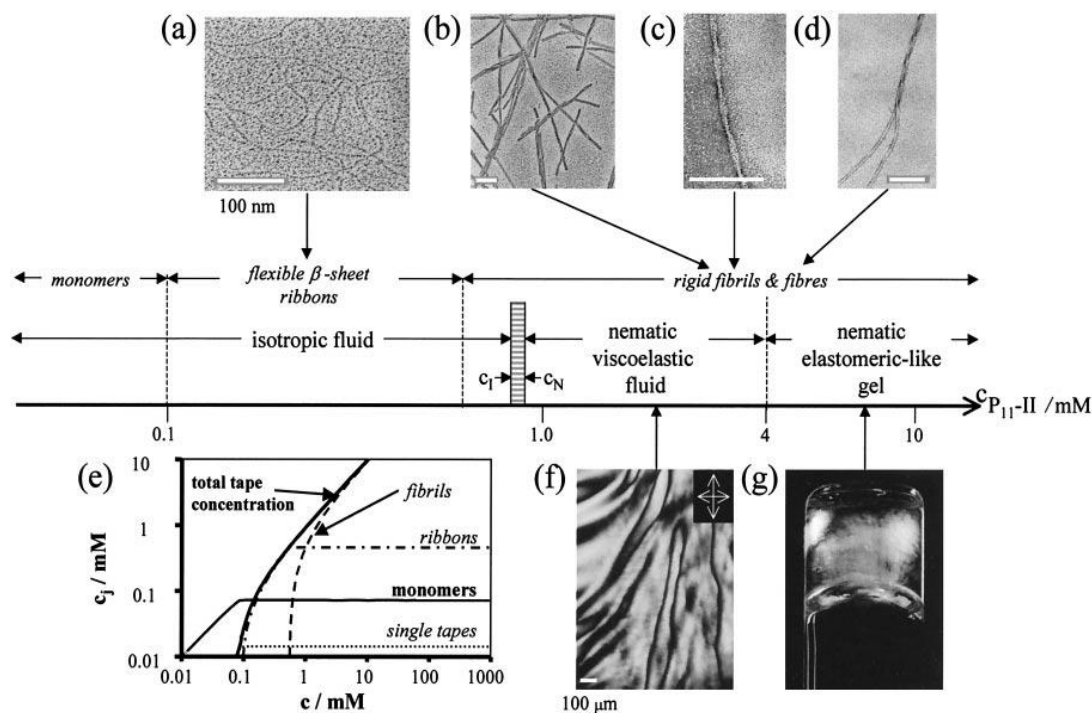


Figure 3.33: Behaviour of P₁₁-2 in water as a function of increasing peptide concentration [44].

3.4.2 Self-assembly of P₁₁-2 in 90% D₂O and 10% HFIP

The gelation of P₁₁-2 in aqueous solutions of HFIP shows the same behaviour as that of the peptide without HFIP. The presence of HFIP does not affect the formation of β -sheets or change critical concentrations. FTIR revealed that the percentage of β -sheet in the aqueous solutions of HFIP was 92%, which is relatively in the same average of the β -sheet portion of the solution peptide without HFIP, which was 89%. The TEM images in Section 3.3.1.1 show that P₁₁-2 in water, without the addition of HFIP, forms nanofibrillar structures. However, the data in Section 3.3.2 show that in the presence of 10% HFIP, P₁₁-2 forms nanotubes rather than fibrils at concentrations of 20 and 40 mg/ml. HFIP is a very strong polar solvent that is considered to be a key material in nanotube formation. HFIP decreases interactions between ribbons by interacting with ribbons faces and preventing them from stacking on top of each other to form nanotube structures, see Figure 3.34. However, nanotubes did not appear at a concentration of 60 mg/ml. This suggests that the nanotubes are metastable structures and only form over a narrow range of concentrations. However, these phenomena have not yet been fully explored [123].

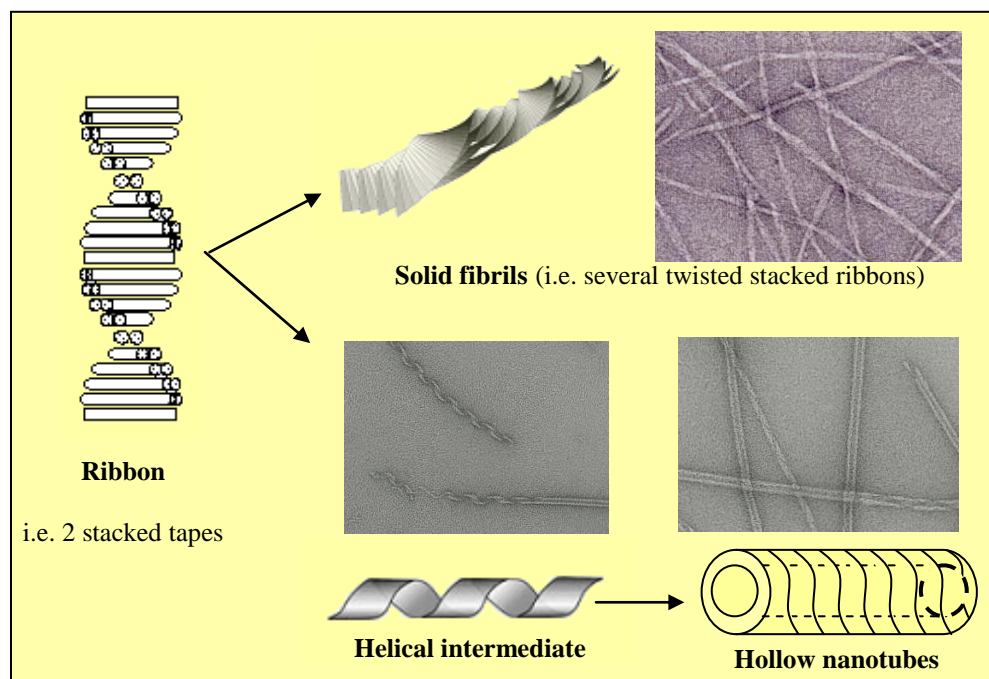


Figure 3.34: Schematic of proposed self-assembly pathways for formation of fibrils and nanotubes starting from ribbons [123].

3.4.3 Self-assembly of P₁₁₋₂ as a function of pD

The investigation on the responsiveness of P₁₁₋₂ to different pD levels demonstrated that peptide self-assembly can be triggered by switching the pH/pD of the solutions. At low pD, P₁₁₋₂ forms a clear nematic gel. At high pD levels of 5.2, 7.3 and 9, P₁₁₋₂ flocculates and forms a cloudy liquid with many gel-like precipitates. These results are consistent with those reported by Aggeli; see Figure 3.35.

The dispersion of self-assembled peptides is stabilized by electrostatic interactions. Amino acids having side chains with $-\text{COOH}$ or $-\text{NH}_2$ terminal groups can be in either a deprotonated or protonated state at pH values below or above their nominal pK values. Thus, electrostatic interactions between neighbouring peptides can be controlled [122]. Based on this fact, P₁₁₋₂ was designed to form a clear nematic gel at low pH. At low pH, arginine is protonated; hence, P₁₁₋₂ molecules have one positive charge (Arg^+) that stabilizes fibrillar dispersion and results in a stable gel. At high pH, the carboxyl group of the glutamic acid side chain is deprotonated (Figure 3.36). As a result, glutamic acids are negatively charged, causing the peptide molecule to have a zero net charge and causing flocculation to occur. Therefore, one unit of net positive or negative charge is required per peptide molecule to stabilize the dispersions of fibrils [122].

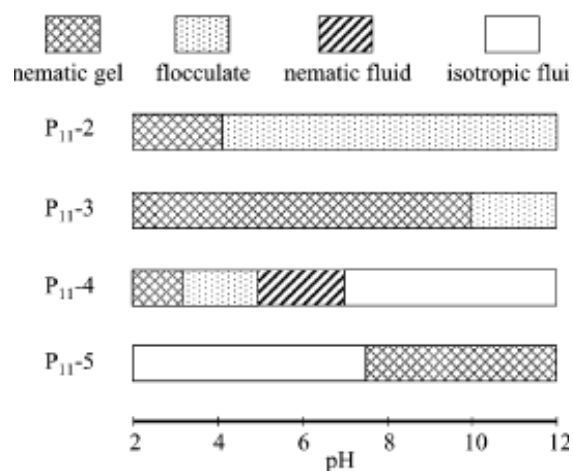
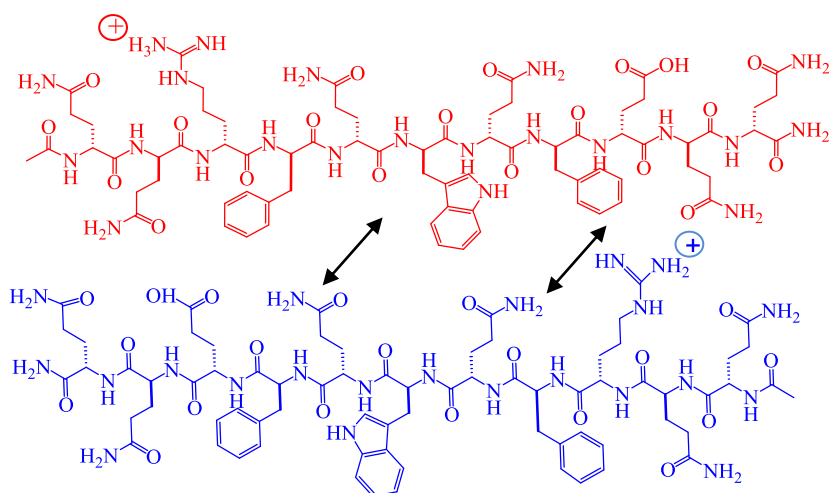


Figure 3.35: Schematic of phase behaviour of P_{11} amino acid residue peptides in aqueous solution as functions of pH. P_{11-2} , P_{11-3} and P_{11-4} at $c = 6.3$ mM, P_{11-5} at $c = 13.1$ mM [122].

(A) $\text{pH} < 5$



(B) $\text{pH} > 5$

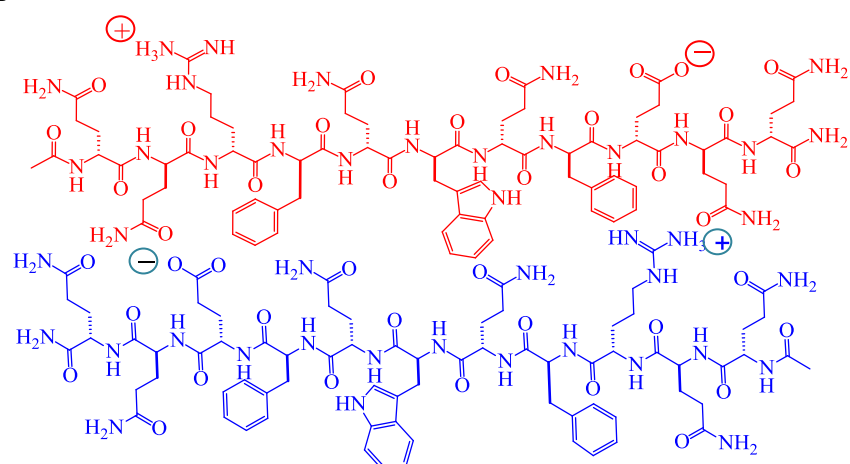


Figure 3.36: Charge distributions on P_{11-2} dimers in an antiparallel β -sheet tapelike substructure: (A) $\text{pH} < 5$ and (B) $\text{pH} > 5$. The repulsion between molecules is indicated by arrows.

TEM images showed that P₁₁₋₂ fibrils at pD = 2.8 are well distributed because of the presence of a +1 charge on each peptide molecule. This net charge allows peptide aggregates to repel one another. At pD = 5, P₁₁₋₂ starts to form bundles of insoluble structures. At pD > 5, where the peptides have a zero net charge, peptide bundles accumulate because of insufficient repulsion between peptide molecules.

FTIR spectra revealed that at pD > 5, P₁₁₋₂ has large peaks centred around the absorption area for β -sheets. These results indicate that β -sheet aggregates were present in those samples, even though they were insoluble solutions. However, the formation of β -sheets is not sufficient to stabilize a gel; stabilisation also requires the presence of a net charge on each peptide molecule.

3.4.4 Peptide self-assembly under physiological-like solutions

Under physiological conditions, the presence of salts screens the electrostatic repulsion between peptide molecules. Therefore, higher number of net charges is required to form a stable gel in physiological conditions. P₁₁₋₉ and P₁₁₋₁₂ were designed to form gels under physiological conditions. P₁₁₋₉ contains three glutamic acids side chain per molecule. In neutral pH, the structure of P₁₁₋₉ allows these peptide molecules to have a net charge of -2. This slight net negative charge allows the peptide molecules to form soluble aggregate structures, and thus gel, rather than precipitate [86]. P₁₁₋₁₂ contains three positively charged side chains; two ornithine and one arginin. The structure of P₁₁₋₁₂ allows these peptide molecules to have a net charge of +2. This slight net positive charge enables the peptide molecules to form soluble aggregate structures and thus form gels rather than precipitates [86].

Similar to self-assembly in water, self-assembly under physiological conditions is a nucleated process by which monomers aggregate into β -sheet tapes. FTIR spectra confirmed that β -sheet conformations formed, However, TEM images showed no nanotubes on the grids; only fibrillar structures appeared. The main difference between the fibrillar structure of P₁₁₋₉ and P₁₁₋₁₂ that P₁₁₋₉ is more twisted than P₁₁₋₁₂. Peptides with positive charge tend to be loosely associated allowing the aggregates to be ascertained, while peptides with negative charge tend to be tightly packed resulting with highly twisted fibrils [86].

3.5 Conclusions

Based on investigations using TEM and FTIR, the peptide P₁₁₋₂ self-assembles into either nanofibrils or nanotubes in water and forms hydrogels. The behaviour of the peptide was studied as a function of P₁₁₋₂ concentration in water. At low concentrations, such as 1 mg/ml, P₁₁₋₂ formed nematic fluids, while at high concentrations, such as 40 and 60 mg/ml, P₁₁₋₂ formed self-supported gels. TEM images showed that P₁₁₋₂ in D₂O self-assembles into nanofibrillar aggregates. Fibrils formed as a result of ribbons interacting with each other via their wide sides, thereby stacking on top of each other. However, in aqueous solutions of 10% HFIP, P₁₁₋₂ self-assembled into tightly packed open-ended nanotubes, predominantly at a concentration of 40 mg/ml. These nanotubes are believed to form as a result of interactions of HFIP with ribbon faces, preventing them from stacking on top of each other and allowing only edge-to-edge interactions of β -sheet ribbons.

Hydrogels were formed by both P₁₁₋₉ and P₁₁₋₁₂ under all physiological conditions tested. FTIR spectra confirmed that they formed β -sheet aggregates, and TEM images showed that the aggregates were fibrils. It could be concluded that the formed nanotubes were metastable. For this reason, the peptides investigated in this chapter will not be used as drug carriers in this project. Other peptides were therefore required, P₁₁₋₈ and P₁₁₋₄ were used, as discussed in subsequent chapters.

Chapter 4

4 Preparation and characterization of self-assembled peptide coated cellulosic fabric

4.1 Introduction

The aim of the previous chapter was to compare peptide nanotubes with peptide nanofibres so as to select one for use as drug carriers. For this purpose, P₁₁-2, P₁₁-9 and P₁₁-12, were investigated. However, the nanotubes formed from these peptides were found to be metastable; therefore, fibrillar structure would be more favourable drug carriers in this project. Consequently, in this chapter, we propose to use peptide P₁₁-4 (CH₃CO-Q-Q-R-F-E-W-E-F-E-Q-Q-NH₂) and P₁₁-8 (CH₃CO-Q-Q-R-F-O-W-O-F-E-Q-Q-NH₂) since they have already been extensively investigated and used for biomedical applications. They are biocompatible, biodegradable, non-toxic to human and murine cells and do not cause an immunogenic response in mice [129, 130]. P₁₁-4 was clinically studied for dental repair application, and it is now in the commercial process at Cridentis ag (Zurich, Switzerland) [129]. In this chapter, the feasibility of manufacturing cellulosic fibre nonwovens coated with P₁₁-4 and P₁₁-8 is studied as a potential route for the preparation of bioactive wound dressings.

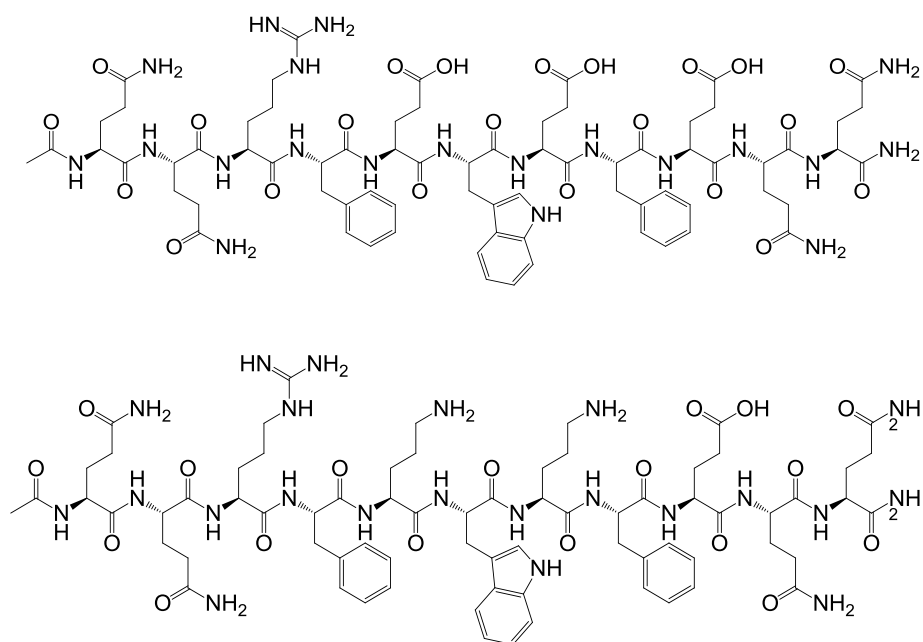


Figure 4.1: Molecular structures of peptide P₁₁₋₄ (top) and peptide P₁₁₋₈ (bottom).

4.1.1 Modified coated dressing for wound care applications

Coating is defined as applying layers of any substance to cover the surface of an object. Coating dressings with a drug is a simple process achieved by dipping the fabric in a drug solution. Drug loading efficiency depends on the nature of the fabric polymer and drug. For instance, a drug with a high affinity for a fabric polymer will readily coat it and form layers on fabric surfaces [3].

Silver ions have been widely used to coat wound dressings due to their broad-spectrum antimicrobial efficacy against fungi, viruses, and bacteria. They are substantially released when the dressing is in contact with wound exudes. Actisorb[®] Plus is an example of a dressing impregnated with silver ions and produced by the Johnson & Johnson Company. It is made from charcoal fabric coated with silver ions. In applications, the charcoal dressing absorbs bacteria from wound exudates, while silver ions are released from the dressing to inactivate bacteria [131]. Inadine[®] is another example of a wound dressing product also produced by Johnson & Johnson. This dressing contains povidone-iodine, which is active against both Gram-positive and Gram-negative bacteria, fungi and protozoa [17].

Applying an antimicrobial coating directly to a dressing without a carrier coating is effective for developing antimicrobial activity; however, the effects of high local

concentrations of drugs could be toxic to cells. Further, the release of drugs immediately after the dressing is applied is another limitation. To circumvent this limitation, researchers are developing modified dressings that incorporate drugs into carrier coatings. For example, the Anghel group has developed a cotton-based wound dressing coated with a hybrid coating composed of magnetic iron oxide nanoparticles and a limonene (natural antiseptic). The anti-biofilm properties of the modified dressing were assessed *in vitro* using two bacterial strains commonly found in infected wounds: *Pseudomonas aeruginosa* and *Staphylococcus aureus*. The dressing exhibited significant anti-adherence and anti-biofilm properties against these two bacterial strains [132].

Antibiotics have been incorporated in several coatings, such as poly (D, L-lactide) (PDLLA), poly (L-lactic acid) (PLLA), polyurethane and polyphosphoester. For example, the surface of orthopaedic implants was coated with PDLLA containing gentamycin. Based on *in vivo* and *in vitro* investigations, the modified implant showed a drastically decreased infection rate compared to systemic gentamycin treatments [133]. rifampicin and fusidic acid were mixed and incorporated into PLLA coatings by Kalicke et al. This hybrid coating was found to be effective in killing *Staphylococcus aureus* infections in a rabbit tibia infection model [134].

This study attempts to develop dressings by incorporating antibiotics into pH-responsive coating. In the presence of infection, the local pH is changed stimulating the coating to release the loaded drug. The fabrics used herein were made from cellulose polymer. Cellulose and its derivatives are widely used in wound dressings due, in part, to their hygroscopic nature, which helps provide an optimal moisture balance in the wound by absorbing exudates from moist wounds and hydrating dry wounds [135, 136]. Cellulose is chemically defined as a polysaccharide polymer consisting of a linear chain of glucose units with the formula $(C_6H_{10}O_5)_n$. Hydroxyl groups on the side of one glucose chain form hydrogen bonds with oxygen atoms on the side of a neighbouring chain, thereby forming strong microfibrils (Figure 4.2). There are many sources of cellulose for industrial use. The most common sources are wood pulp and cotton linters (a by-product in manufacturing cotton yarn). The mechanical properties of cellulose fibres make them a good material for textile fabric production. Regenerated cellulose fibres, such as viscose rayon, are extensively used in the textile industry in numerous different products such as dresses, bed sheets, towels and medical products including wound dressings [137]. The fibres may be incorporated into yarns for manufacturing

medical gauze and into nonwovens as components for modern wound dressings. G.M. Raghavendra *et al* .described the development of Cellulose–silver composites fibers. They impregnated the film with silver nanoparticles by immersion in a reduced silver nitrate solution and reported enhanced antimicrobial activity against *E.coli* [138].

Biely and Cavorsi reported a first study on the effects of cellulose dressings in delivering vancomycin. They evaluated the effects of a cellulose dressing and topical vancomycin on methicillin-resistant *Staphylococcus aureus* (MRSA) and Gram-positive organisms in chronic wounds on 23 patients. They found that the dressing was effective in treating patients with positive results on MRSA and Gram-positive bacteria, reducing the number of patients from 23 to 4. This result suggests that reducing wound bacteria in chronic wounds may help healing [136].

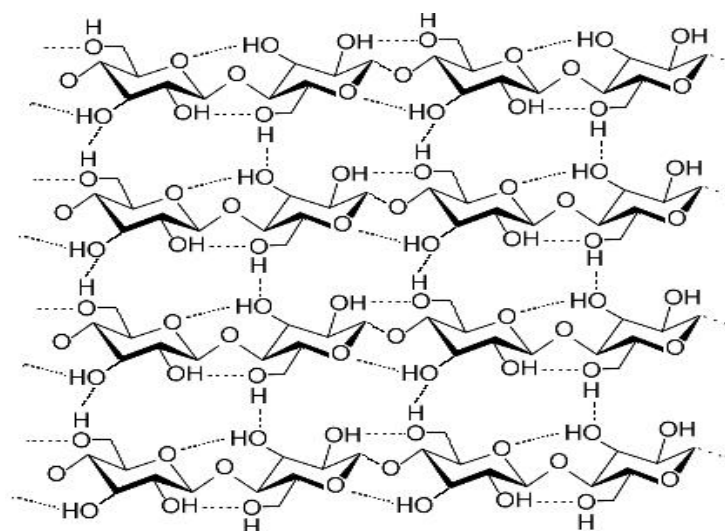


Figure 4.2: Cellulose strand showing hydrogen bonding between chains [139].

Given the properties of P₁₁-4 and P₁₁-8, their utilisation as carriers for bioactive agents in a wound-dressing construct is highly attractive, particularly if a novel approach can be demonstrated for controlling drug delivery. Accordingly, an experimental study was conducted using commercially applicable fabrication techniques to examine the incorporation of P₁₁-4 and P₁₁-8 in a nonwoven wound dressing material. In this study, regenerated cellulose fibres (viscose rayon) were coated with self-assembled peptides as drug carriers. The nonwoven fabrics composed were obtained from the Nonwovens Research Group at the University of Leeds. Peptides were then added by coating fibre surfaces by the full impregnation (dipping) of the fabric samples. Figure 4.3 illustrates

the preparation method. The resultant fabric is a smart pH-stimulus responsive dressing that immediately releases a drug only when triggered by external pH. Specimens were separately coated with P₁₁₋₈ or P₁₁₋₄ peptide fibrils using two concentrations: 2 mg/ml (the concentration at which peptides form ribbons in a viscous solution) and 10 mg/ml (at this concentration, peptides form β -sheets as a gel). The coating process was based upon the peptide self-assembly mechanism triggered by the pH effect.

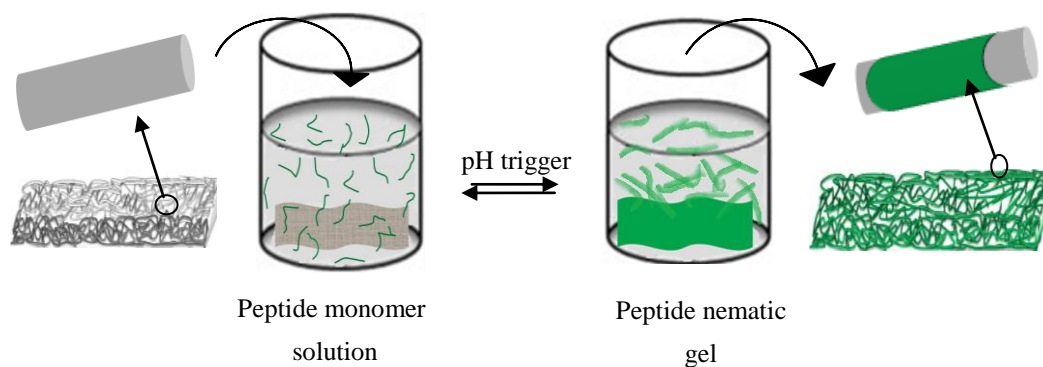


Figure 4.3: Schematic of the dipping method for preparing regenerated cellulose fabric coated with self-assembled peptides. Green = peptide

4.2 Materials and methods

4.2.1 Materials

Regenerative cellulose dressing (100% viscose rayon) was received from Nonwovens Research Group at the University of Leeds. viscose rayon is usually prepared by treating cellulose with sodium hydroxide and carbon disulfide.

4.2.2 Methods

4.2.2.1 Coating of cellulose fabric with P₁₁₋₄

A peptide solution was prepared by adding 10 mg of P₁₁₋₄ to 1 ml of H₂O. Approximately 0.15 mg of fluorescein-tagged P₁₁₋₄ was mixed with the peptide solution. The ratio of tagged to untagged P₁₁₋₄ was 1:60. The solution was vortexed for 30 s. The pH of the solution was measured to be 5.8; at this pH, P₁₁₋₄ flocculated. Drops of 6 μ l of

1 M NaOH were added to form a clear liquid solution at pH 11. Then, 0.5×0.5 cm regenerated cellulose fabric samples were dipped in the monomer solution and left overnight. Drops of 8 μ l of 1 M HCl were added to the solution to decrease the pH to 2.8. At this pH, P₁₁₋₄ molecules self-assembled into β -sheets, forming a gel. The fabric was left in the gel overnight. The fabric was then removed and left overnight to air dry. A control sample of cellulose fabric was prepared using the same method in a solution containing only water.

4.2.2.2 Coating of cellulose fabric with P₁₁₋₈

A peptide solution was prepared by adding 10 mg of P₁₁₋₈ to 1 ml of H₂O. Approximately 0.15 mg of fluorescein-tagged P₁₁₋₄ was mixed with the peptide solution. The ratio of the tagged P₁₁₋₄ to untagged P₁₁₋₈ was 1:60. The solution was vortexed for 30 s. The pH of the solution was measured to be 3.9; at this pH, P₁₁₋₈ molecules are monomers forming a liquid solution. Then, 0.5×0.5 cm-regenerated cellulose fabrics were dipped in the monomer solution and left overnight. Drops of 5 μ l of 1 M NaOH were added to the solution to increase the pH to 10. At this pH, P₁₁₋₈ molecules self-assembled into β -sheets, forming a nematic gel. The fabric was left in the gel overnight. The fabric was then removed and left overnight to air dry. A control sample of uncoated regenerated cellulose fabric was prepared using the same method in a solution containing only water.

4.3. Results

4.3.1 Coating of cellulose fabric with self-assembling peptides

A specimen of cellulose fabric (0.5×0.5 cm) was coated with P₁₁₋₄ fibrils by dipping the fabric in 10 mg/ml of a P₁₁₋₄ solution, see Figure 4.4. Another specimen of cellulose fabric (0.5×0.5 cm) was coated with P₁₁₋₈ fibrils by dipping the fabric in 10 mg/ml of a P₁₁₋₈ solution (Figure 4.5). By the similar method, specimens were coated by P₁₁₋₄ and P₁₁₋₈ at 2 mg/ml (Figures 4.6 and 4.7). In this case, specimens were dipped in viscous solutions rather than gels at 10 mg/ml.

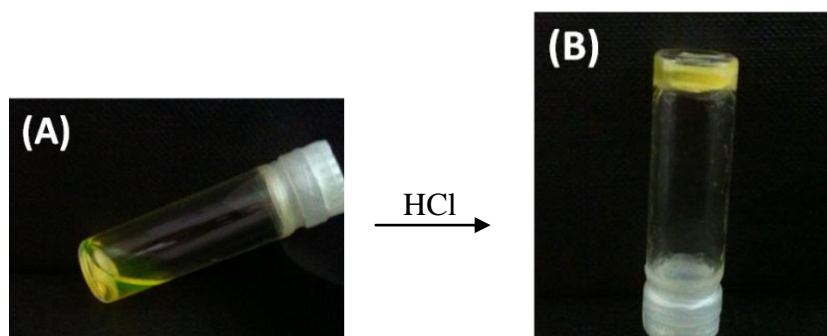


**Figure 4.4: Photograph of cellulose fabrics dipped in P₁₁₋₄ at 10 mg/ml.
(A) at pH 11. (B) at pH 2.8.**

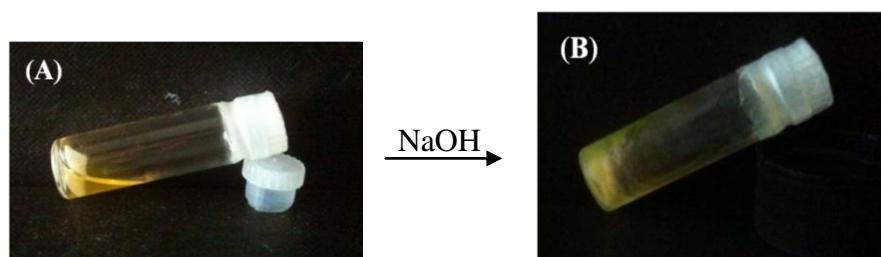


**Figure 4.5: Photograph of cellulose fabrics dipped in P₁₁₋₈ at 10 mg/ml.
(A) at pH 3.9. (B) at pH 10.**

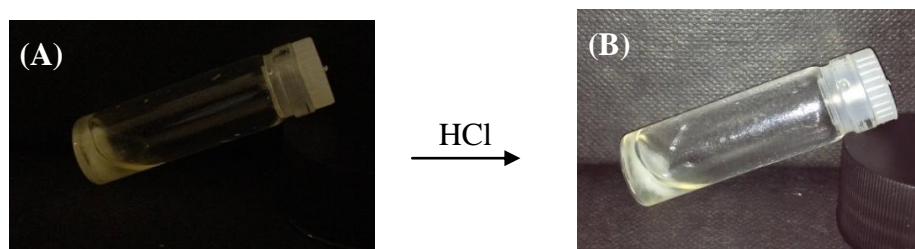


**Figure 4.6: Photograph of cellulose fabrics dipped in P₁₁₋₄ at 2 mg/ml.
(A) at pH 11. (B) at pH 2.8.**

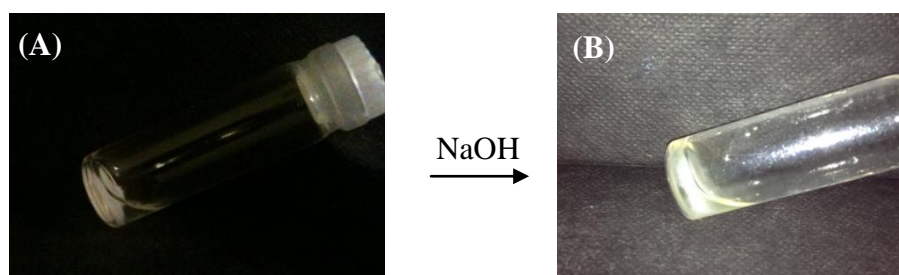


**Figure 4.7: Photograph of cellulose fabrics dipped in P₁₁₋₈ at 2 mg/ml.
(A) at pH 3.9. (B) at pH 10.**

4.3.2 Transmission Electron Microscopy, TEM

TEM was used to inspect the peptide structures in the coatings applied to the fabrics (Figure 4.8). Figure 4.8 (A) reveals the fibrillar structures of P₁₁-4 (10 mg/ml) resulting from the coating. The fibrils have wide diameter range from 8 - 13 nm and small diameters between 2-3 nm. Figure 4.8 (B) reveals P₁₁-8 fibrillar structures of large diameter ranging from 7 - 11 nm and small diameters from 2-3 nm.

4.3.3 Scanning Electron Microscopy, SEM

SEM was employed to compare the morphologies of the peptide coated and uncoated fabrics. In this comparison, samples treated with NaOH and HCl were also included because the coating process requires the addition of acid and base to the solution in which the fabric was dipped. Therefore, it is important to determine how fabric surfaces are affected by low and high pH.

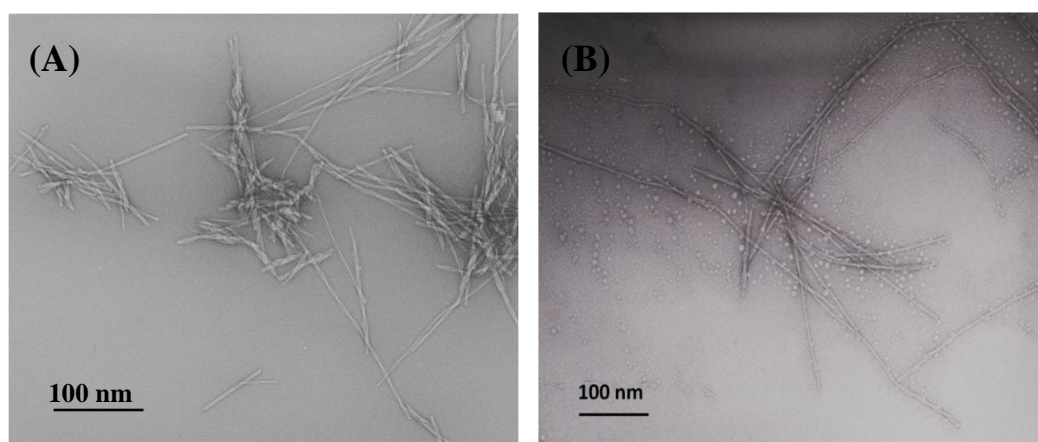


Figure 4.8: TEM micrographs of peptide fibrils. (A) P₁₁-4 in water (10 mg/ml) at pH 2.9. (B) P₁₁-8 in water (10 mg/ml) at pH 10.

4.3.3.1 Cellulose fabric coated with P₁₁-4 (10 mg/ml)

Figure 4.9(A) shows a complex network of flexible cellulose fibres, which is characteristic of mechanically bonded nonwoven fabrics in which fibres are entwined with each other and have looped configurations. The cellulose fibres have

diameters of 15–20 μm . Figure 4.9(B) shows a cellulose sample treated with HCL, and Figure 4.9 (C) shows a specimen coated with P₁₁-4. At low magnification, there is no visible difference between the three samples.

The magnification was further increased, images are shown in Figure 4.10 Image 4.10(A) shows a cellulose sample without any peptide coating, while image 4.10(B) shows an HCl-treated sample. These two images show that, without acid treatment, the surface morphology of cellulose fibres is smooth in Figure 4.10(A), while the sample surface in image 4.10(B) is roughened after HCl treatment. The image 4.10(C) shows cellulose fibres coated with the peptide in which gel has accumulated between cellulose fibres.

Figure 4.11 provides a high-magnification comparison between the details of the surfaces of the control sample, the sample treated with HCl and that coated with P₁₁-4. Image 4.11(B) shows changes in the surface morphology of fibres treated with HCL. These changes are not visible in image 4.11(C) because the peptide gel extends around and between cellulose fibres.

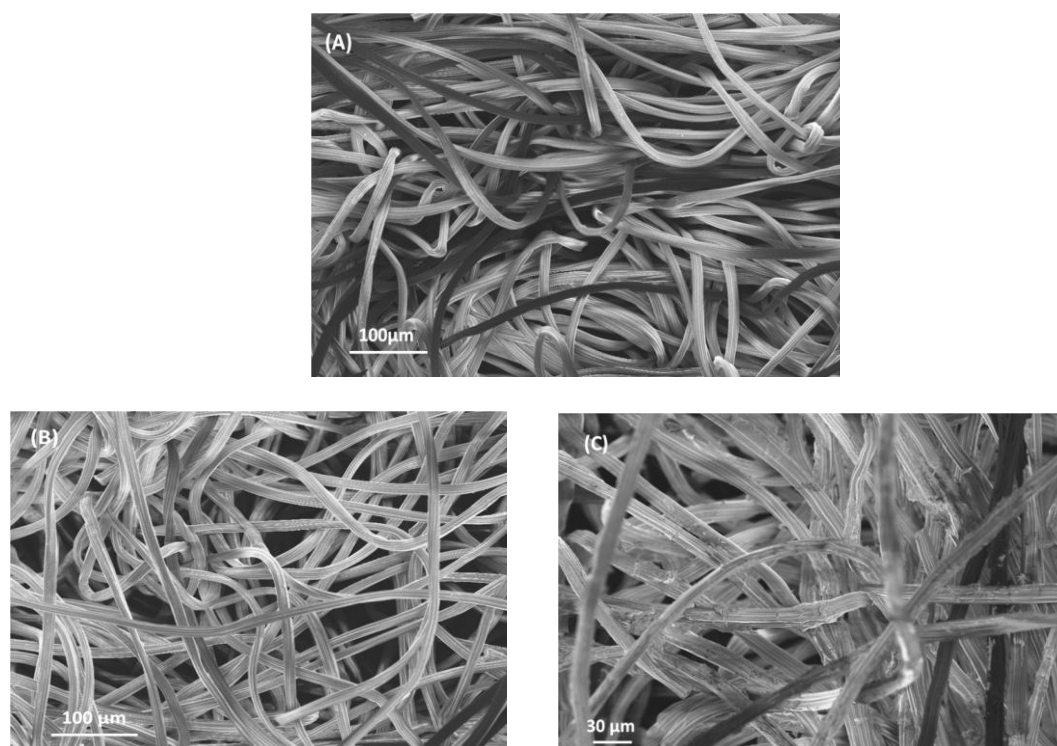


Figure 4.9: SEM micrographs of cellulose fabrics at relatively low magnification. (A) Uncoated cellulose fabric. (B) Cellulose fabric treated with HCl. (C) Cellulose fabric coated with P₁₁-4 (10 mg/ml).

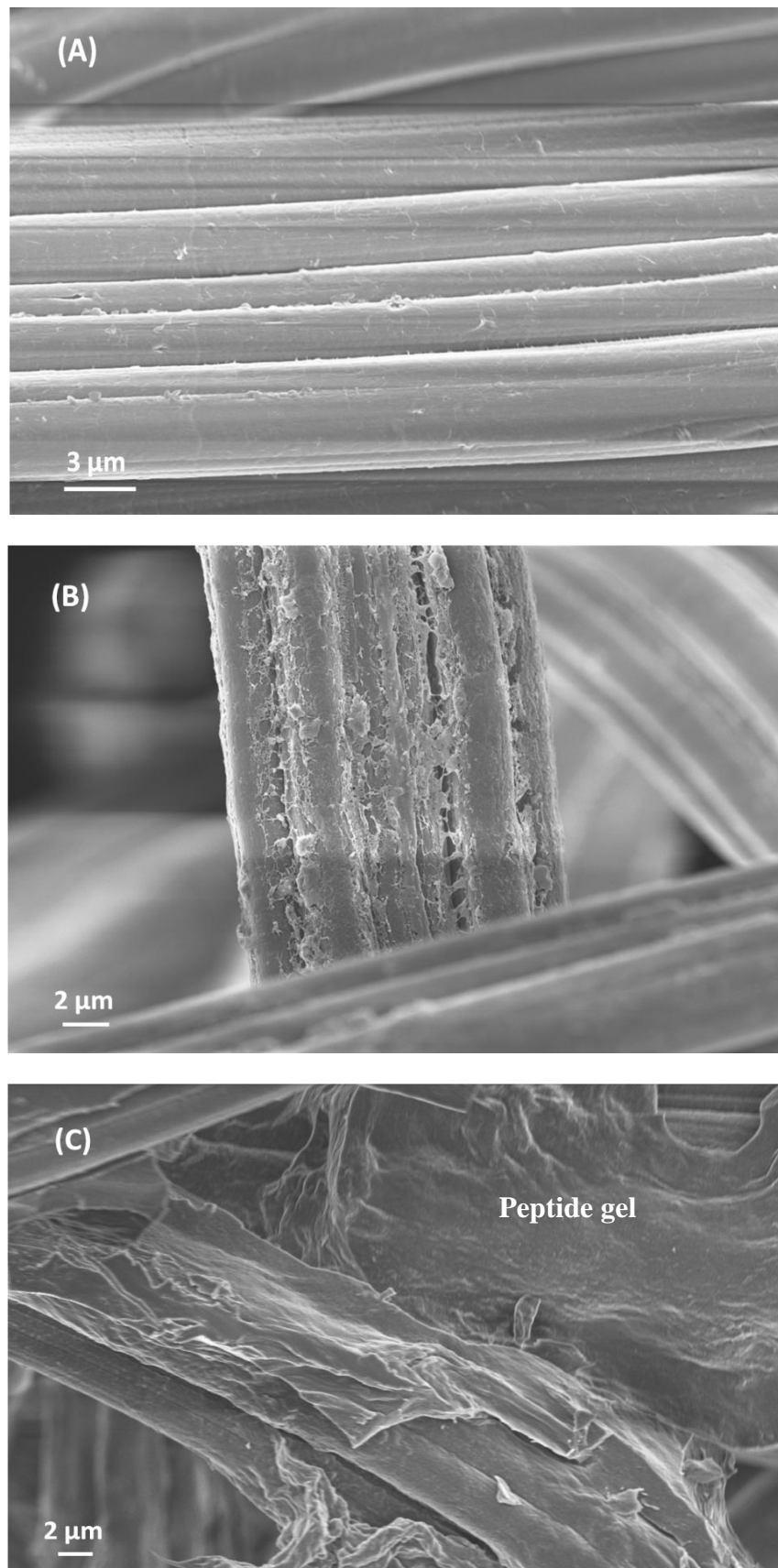


Figure 4.10: SEM micrographs of cellulose fabrics at relatively moderate magnification. (A) Uncoated cellulose fabric. (B) Cellulose fabric treated with HCl. (C) Cellulose fabric coated with P₁₁-4 (10 mg/ml).

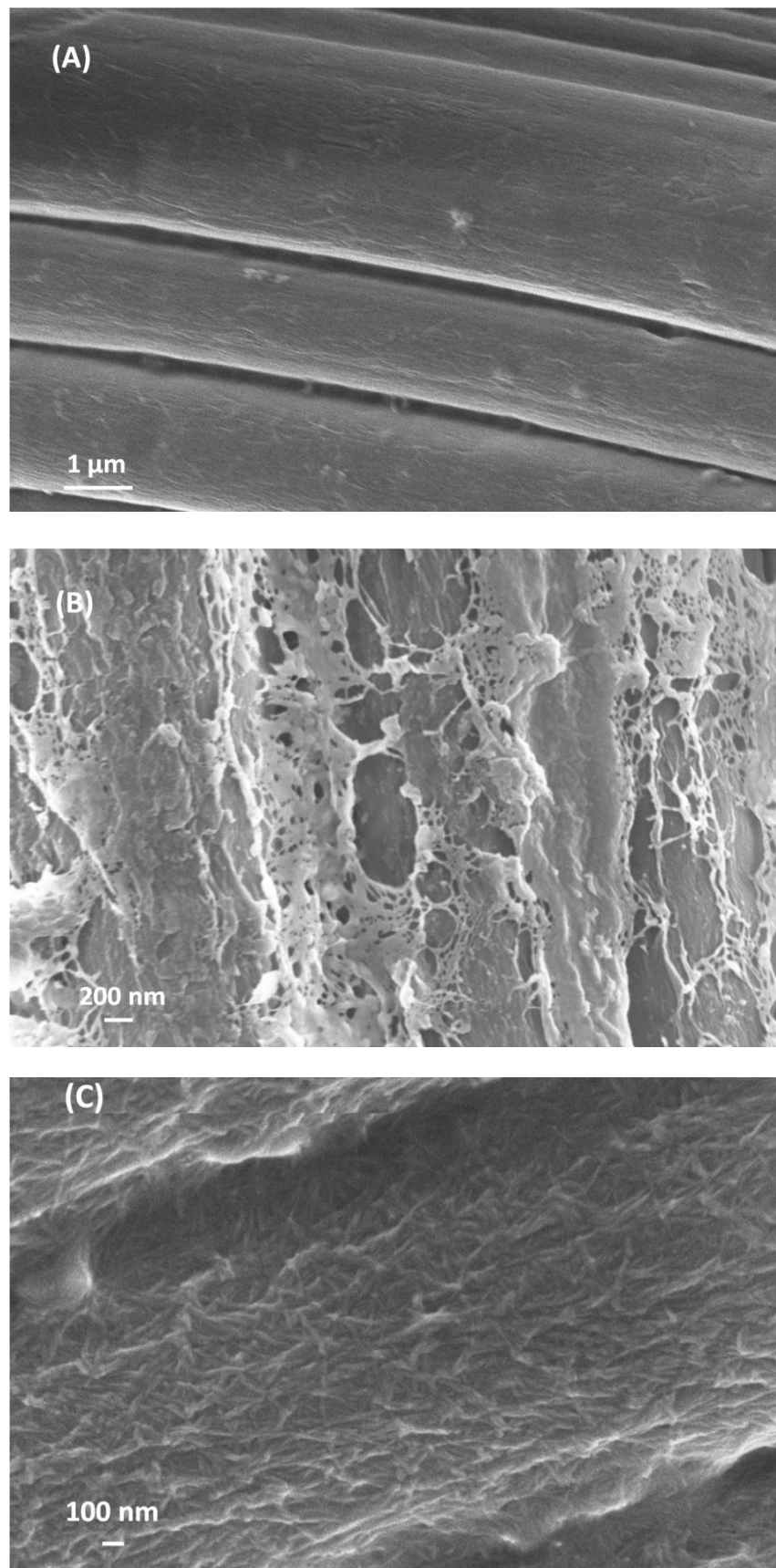


Figure 4.11: SEM micrographs of cellulose fabrics at relatively high magnification. (A) Uncoated cellulose fabric. (B) Cellulose fabric treated with HCl. (C) Cellulose fabric coated with P₁₁-4 (10 mg/ml).

4.3.3.2 Cellulose fabric coated with P₁₁-4 (2 mg/ml)

Figures 4.12, 4.13, and 4.14 show SEM images of cellulose fabric coated with 2 mg/ml of P₁₁-4 at low, medium and high magnification, respectively. These should be compared with Figures 4.9, 4.10 and 4.11 for fibres coated with a high peptide concentration of 10 mg/ml. In general, Figures 4.12–4.14 show that the fabric coated with the low peptide concentration of 2 mg/ml does not have gel accumulations between fibres. The figures show that surfaces are affected by HCl treatment. At high magnification, Figure 4.14(B) shows denatured surfaces that are not visible in Figure 4.14(C) due to the peptide coating.

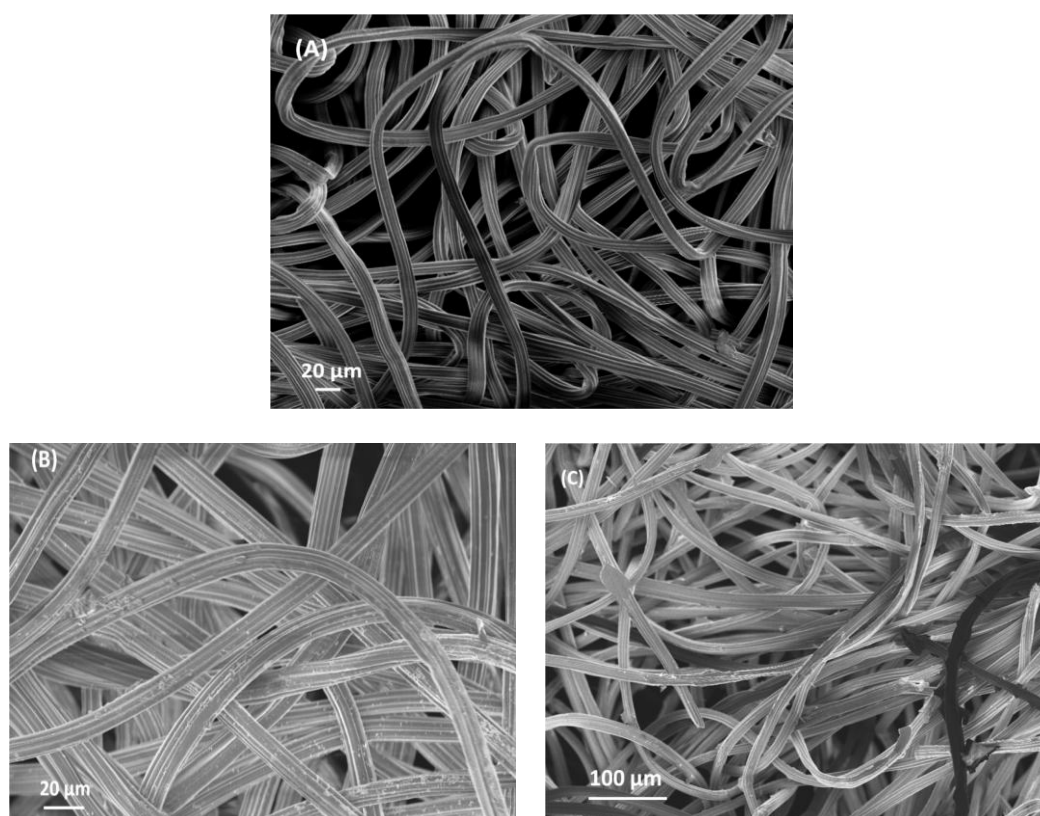


Figure 4.12: SEM micrographs of cellulose fabrics at relatively low magnification. (A) Uncoated cellulose fabric. (B) Cellulose fabric treated with HCl. (C) Cellulose fabric coated with P₁₁-4 (2 mg/ml).

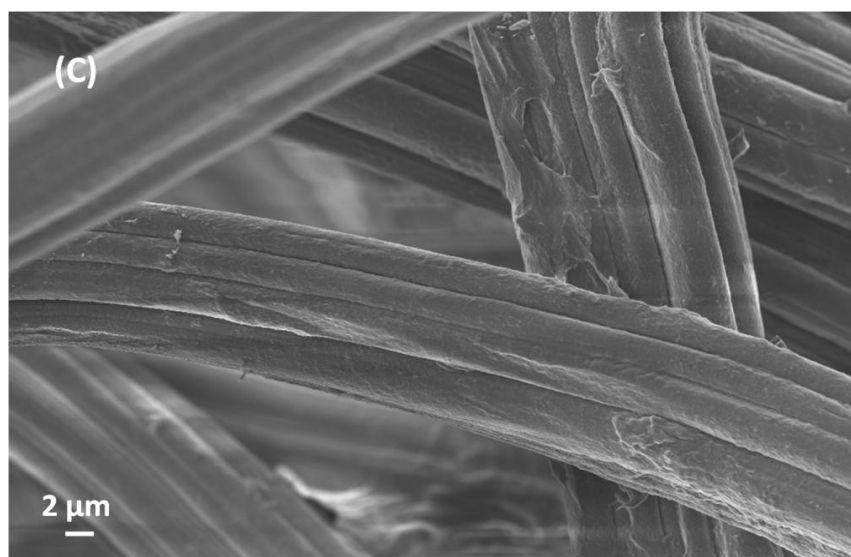
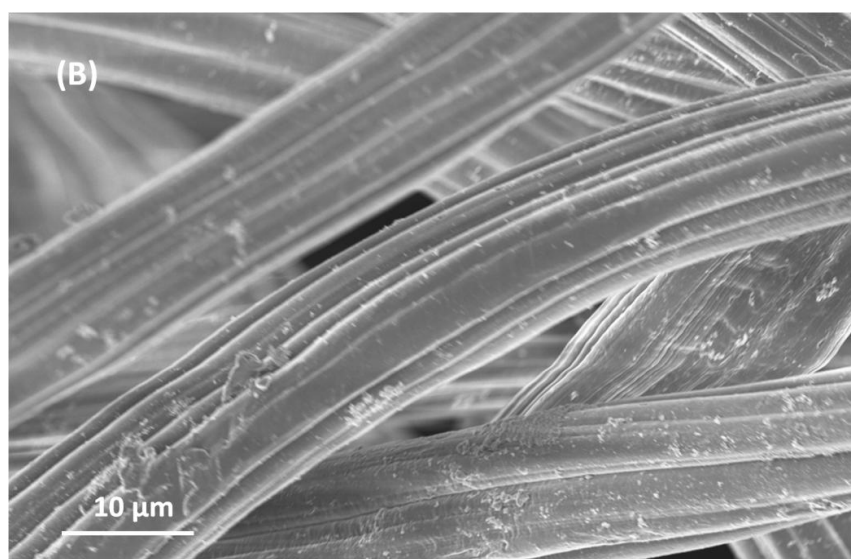
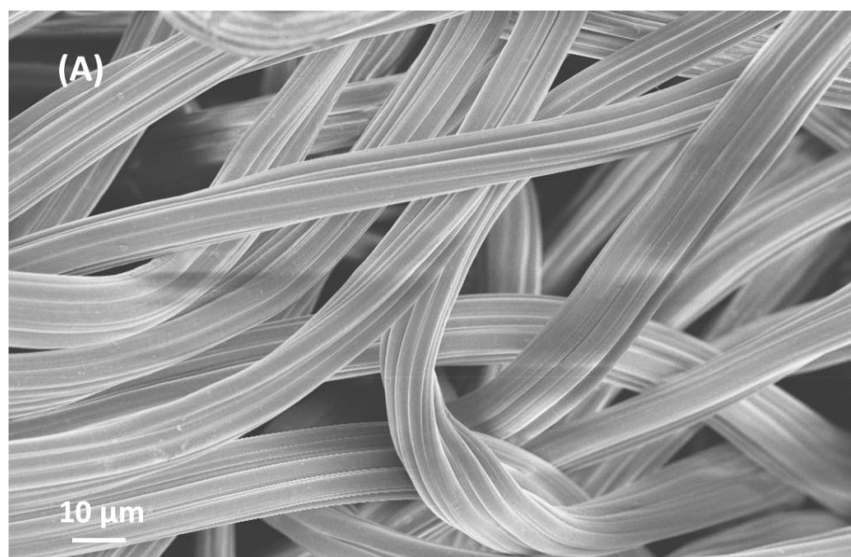


Figure 4.13: SEM micrographs of cellulose fabrics at relatively moderate magnification. (A) Uncoated cellulose fabric. (B) Cellulose fabric treated with HCl. (C) Cellulose fabric coated with P₁₁-4 (2 mg/ml).

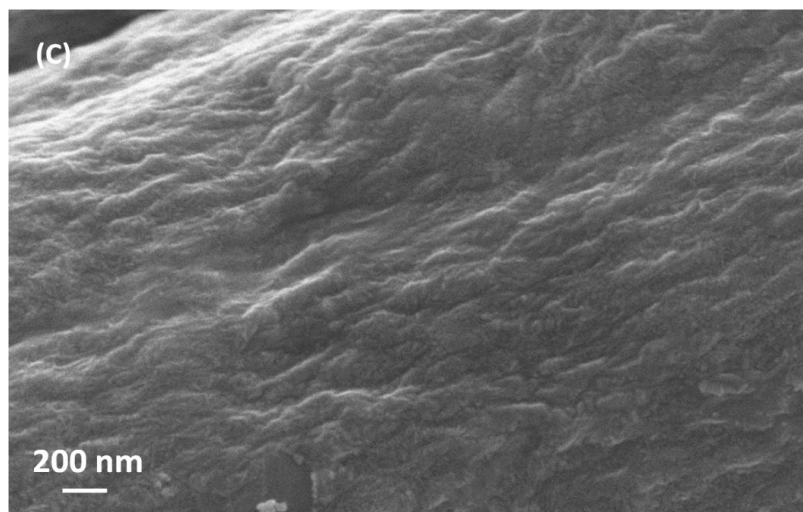
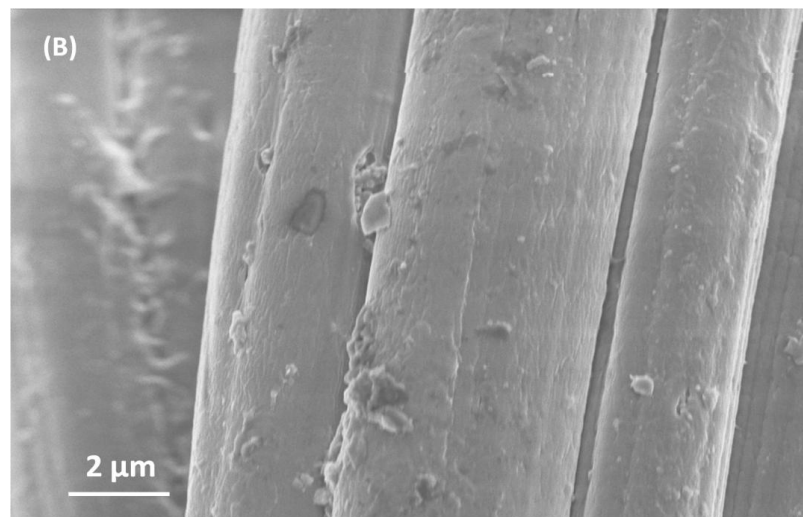
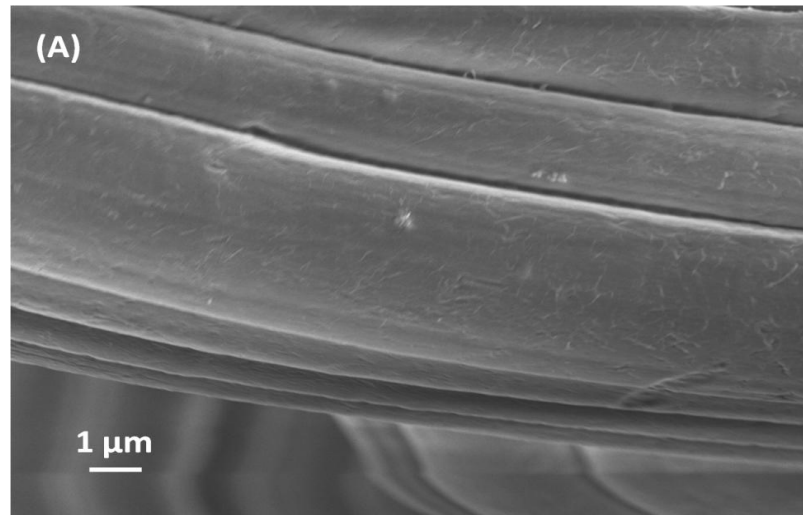


Figure 4.14: SEM micrographs of cellulose fabrics at relatively high magnification. (A) Uncoated cellulose fabric. (B) Cellulose sample treated with HCl. (C) Cellulose sample coated with P₁₁-4 (2 mg/ml).

4.3.3.3 Cellulose fabric coated with P₁₁-8 (10 mg/ml)

As was done with the P₁₁-4 samples coated with P₁₁-8 is compared with uncoated samples. Figure 4.15(B) shows a cellulose sample treated with NaOH that appears to be denatured with the evidence of the presence of random features on the surface. In Figure 4.15(C), the peptide-coated specimen has accumulations of gel at crossover points between fibres. The magnification was further increased in Figure 4.16 and 4.17. Figures 4.16(A) and 4.17(A) show the cellulose sample without any peptide coating, and the characteristic morphology of regenerated cellulose fibres produced by the viscose process is evident. Figures 4.16(B) and 4.17(B) reveal more details of morphological changes in fibres as a result of NaOH treatment, particularly, modifications of the surface structure. These changes cannot be detected in Figures 4.16(C) and 4.17(C) for which the fibres were coated by the peptide gel around and between cellulose fibres.

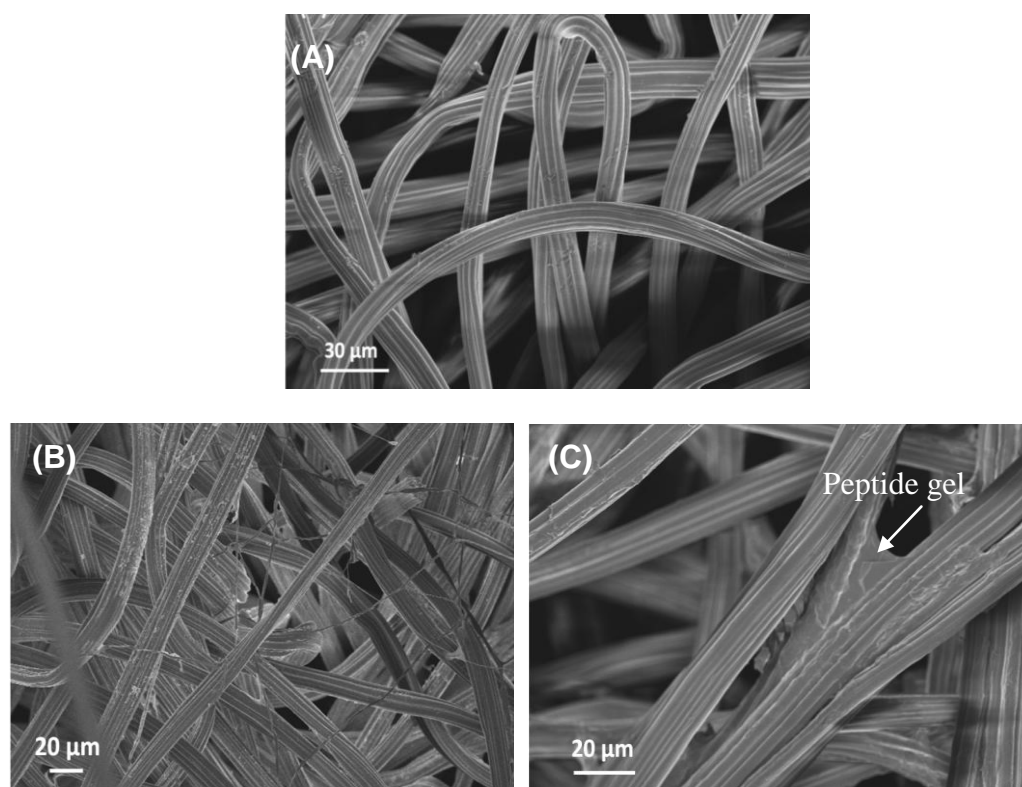


Figure 4.15: SEM micrographs of cellulose fabrics at relatively low magnification . (A) Uncoated cellulose fabric. (B) Cellulose fabric treated with NaOH. (C) Cellulose fabric coated with P₁₁-8 (10 mg/ml).

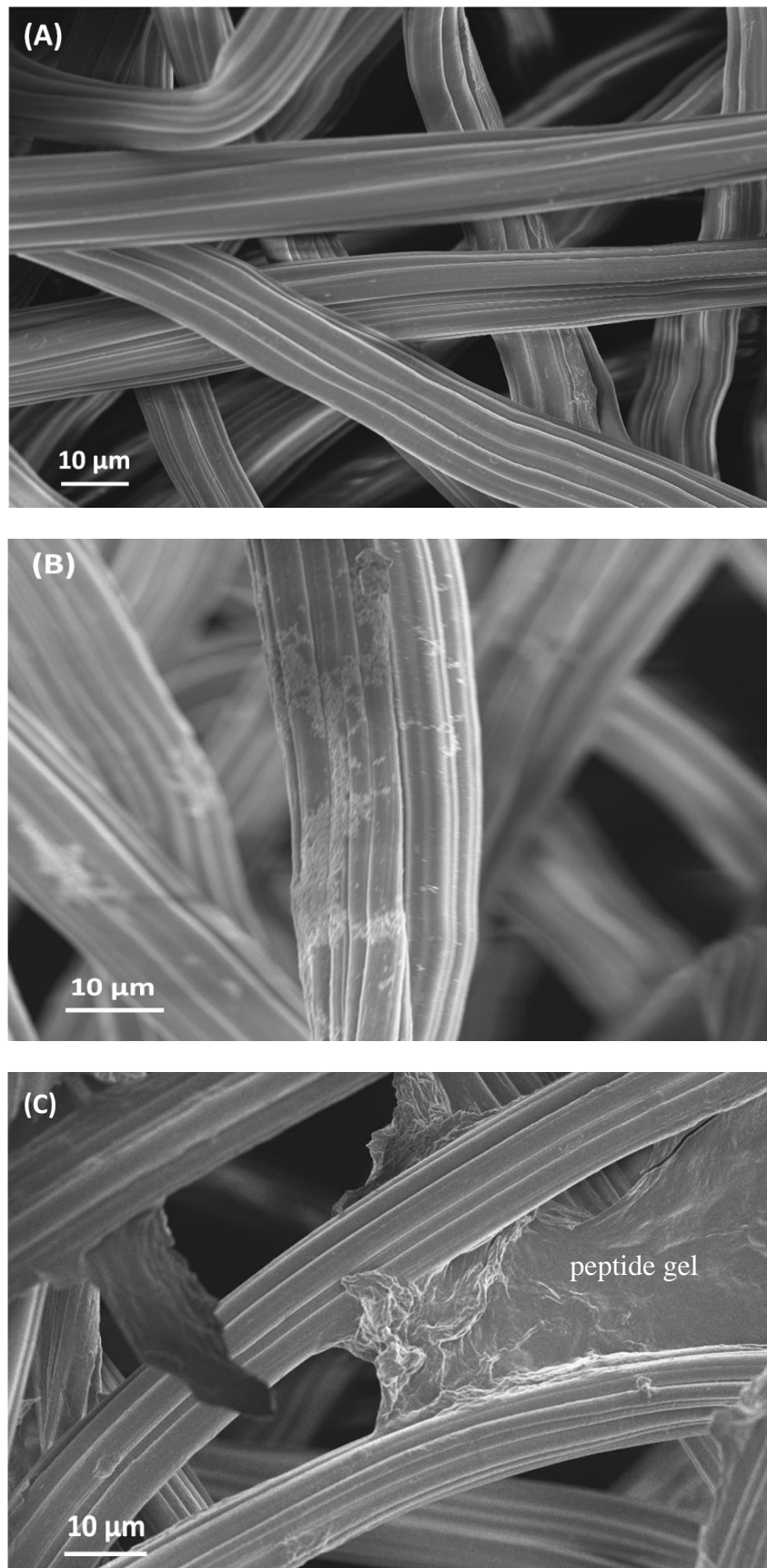


Figure 4.16: SEM micrographs of cellulose fabrics at relatively moderate magnification. (A) Uncoated cellulose fabric. (B) Cellulose fabric treated with NaOH. (C) Cellulose fabric coated with P₁₁-8 (10 mg/ml)

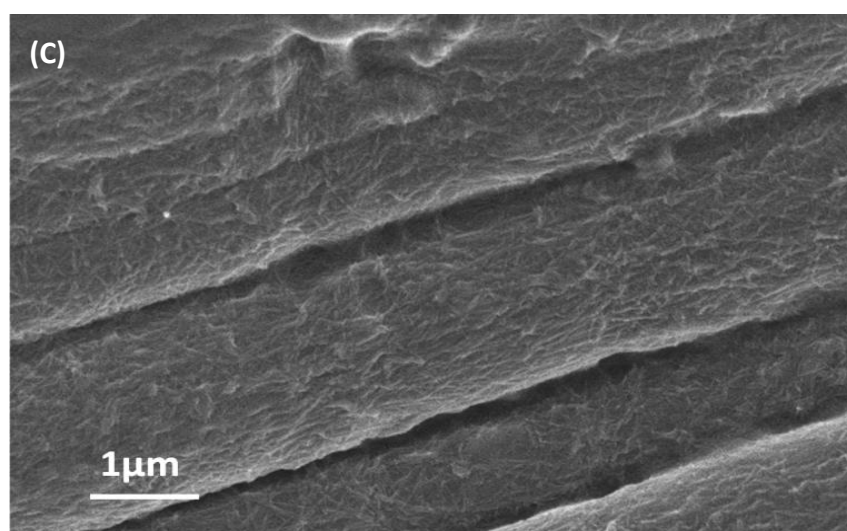
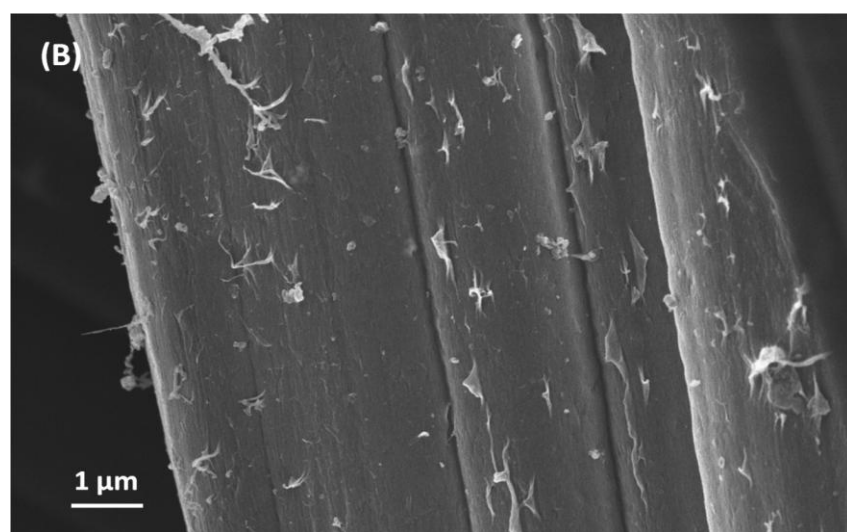
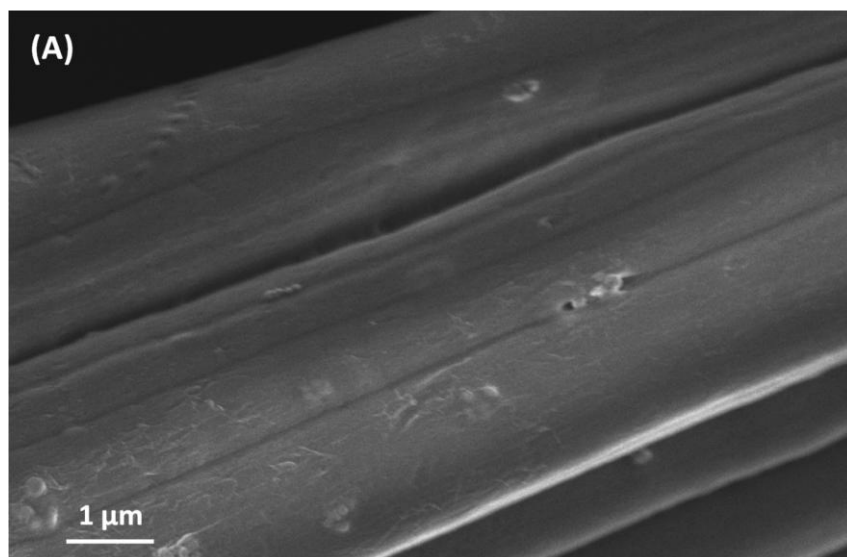


Figure 4.17: SEM micrographs of cellulose fabrics at relatively high magnification. (A) Uncoated cellulose fabric. (B) Cellulose fabric treated with NaOH. (C) Cellulose fabric coated with P₁₁₋₈ (10 mg/ml).

4.3.3.4 Cellulose fabric coated with P₁₁-8 (2 mg/ml)

A P₁₁-8 peptide solution in water at low concentration (2 mg/ml) was prepared to compare the performance with that of the high-concentration peptide solution, as was done with P₁₁-4. Figure 4.18 shows that, at low magnification, differences in the morphological textures of samples could not be readily distinguished. Figures 4.19 and 4.20 show images at higher magnification, and differences such as surface roughening are clear. The modification of cellulose fibre surfaces as a result of NaOH treatment in Figure 4.20(B) is completely hidden in Figure 4.20(C) by the presence of the peptide coating.

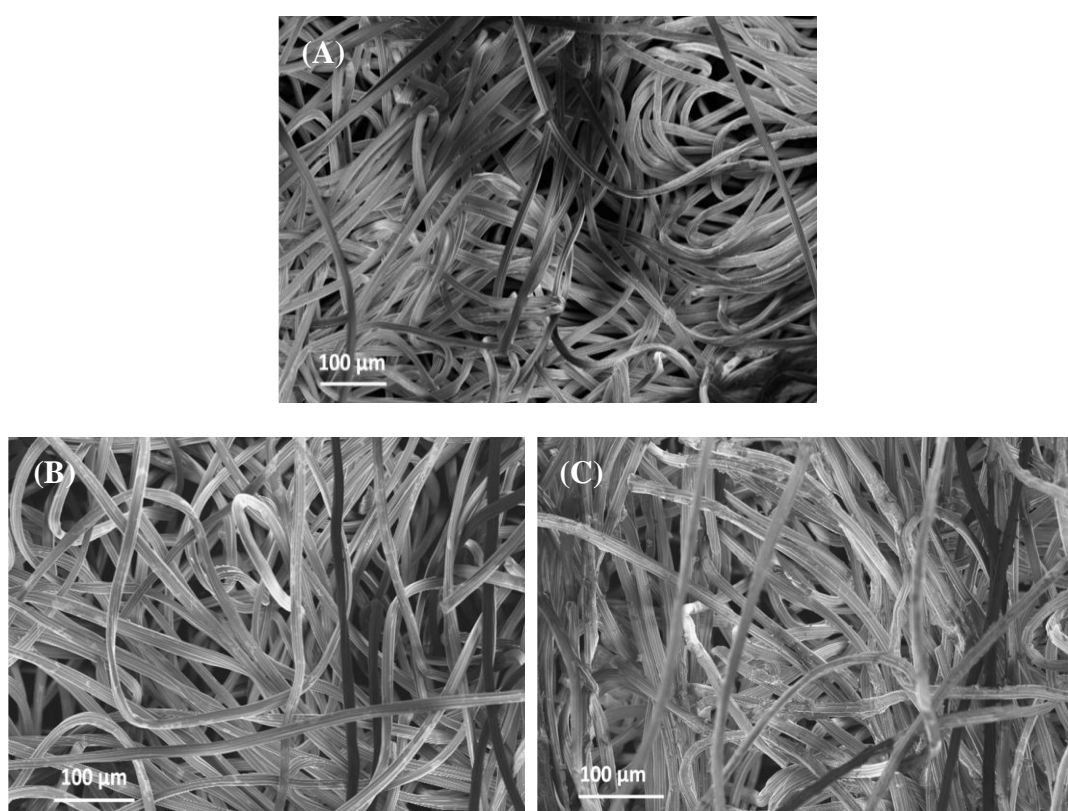


Figure 4.18: SEM micrographs of cellulose fabrics at relatively low magnification. (A) Uncoated cellulose fabric. (B) Cellulose fabric treated with NaOH. (C) Cellulose fabric coated with P₁₁-8 (2 mg/ml).

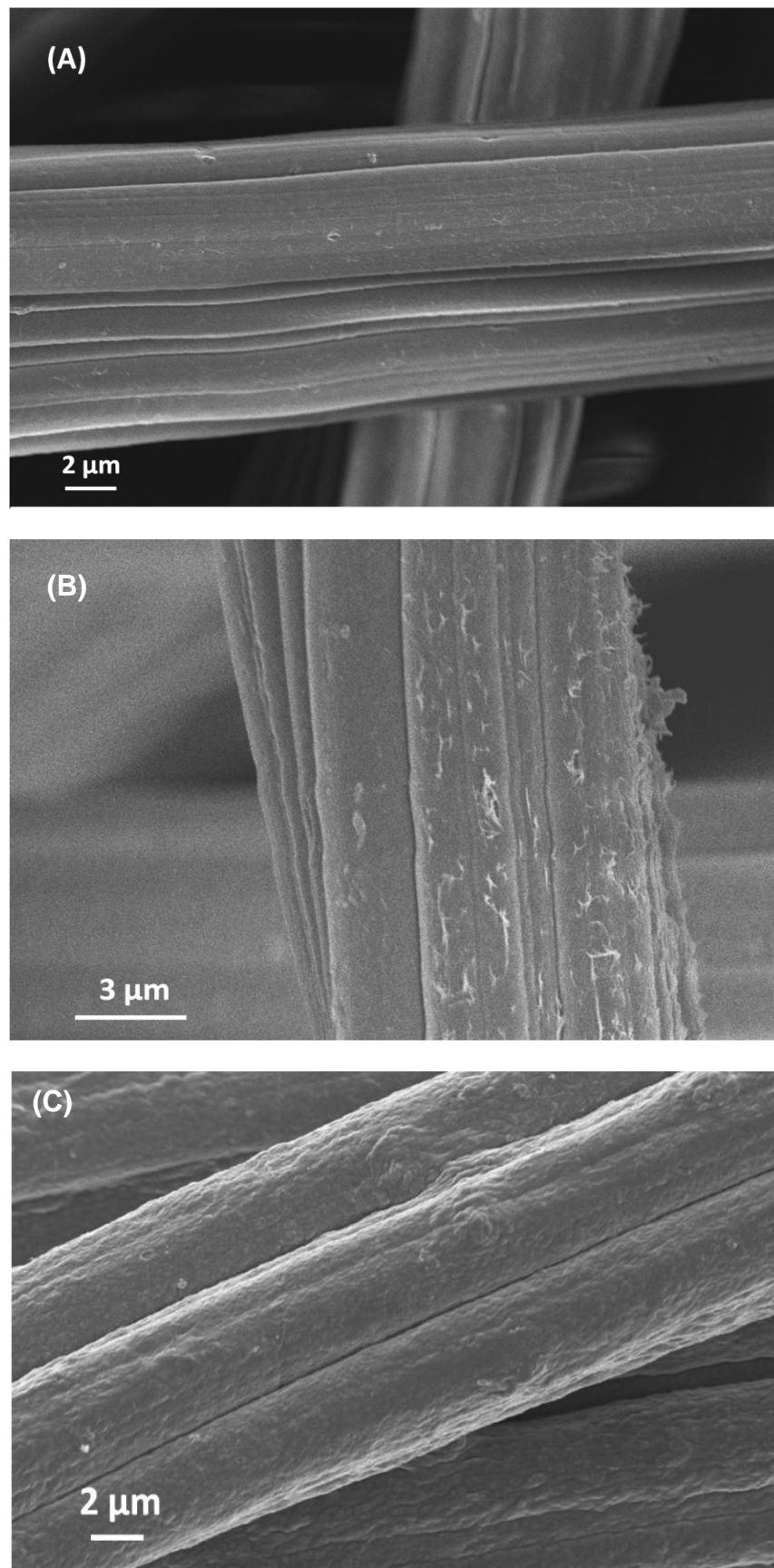


Figure 4.19: SEM micrographs of cellulose fabrics at relatively moderate magnification. (A) Uncoated cellulose fabric. (B) Cellulose fabric treated with NaOH. (C) Cellulose fabric coated with P₁₁-8 (2 mg/ml).

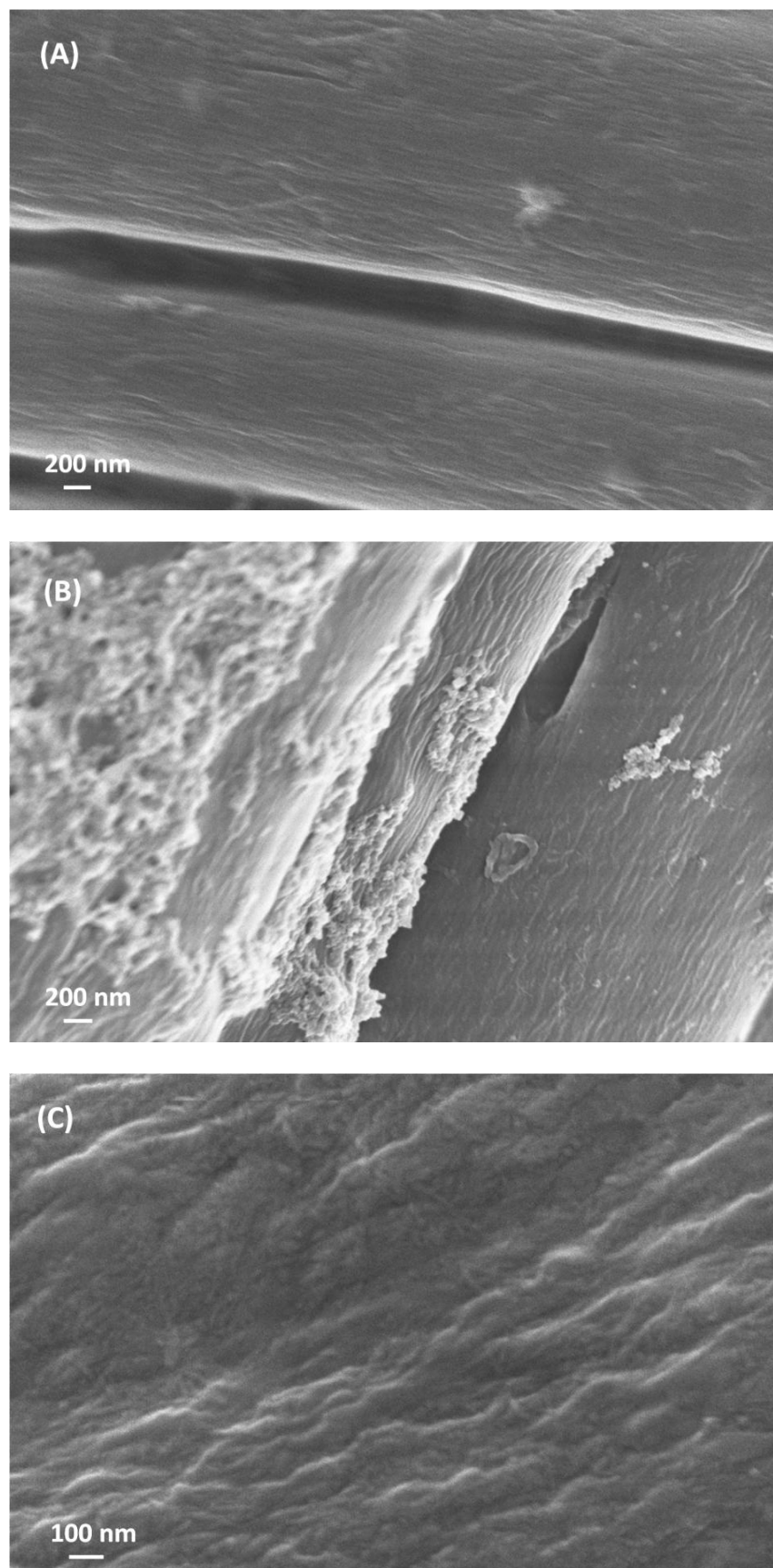


Figure 4.20: SEM micrographs of cellulose fabrics at relatively high. (A) Uncoated cellulose fabric. (B) Cellulose fabric treated with NaOH. (C) Cellulose fabric coated with P₁₁-8 (2 mg/ml).

4.3.4 Confocal Laser scanning microscopy, CLSM

4.3.4.1 Cellulose fabric coated with P₁₁₋₄

CLSM images in Figure 4.21 show that the fabric coated with P₁₁₋₄ is distinctly different from the control fabric and control peptide gel. In Figure 4.21(A), the fabric control sample shows a black background as a result of no fluorescence. In image 4.21(B), the fluorescently tagged peptide gel formed a randomly ordered gel. In images 4.21(C) and 4.21(D), the fluorescently tagged peptide appears to have coated the sample, revealing the underlying fibrous structure of the fabric. The supporting fibrous scaffold provided by the nonwoven fabric, together with the peptide coating, had diameters of 15 to 18 μm .

The widespread fluorescence across the specimen surface in Figure 4.22 shows that cellulose samples dipped in a solution of P₁₁₋₄ at 2 mg/ml were extensively coated with the peptide. However, reduced fluorescence appears at the fibre crossover points compared with that in the samples dipped in P₁₁₋₄ (10 mg/ml) in Figure 4.21. This reflects the reduced gel mass in P₁₁₋₄ at 2 mg/ml as compared with that in P₁₁₋₄ at 10 mg/ml.

4.3.4.2 Cellulose fabric coated with P₁₁₋₈

Figures 4.23 and 4.24 show CLSM images for fabric samples dipped in solutions of P₁₁₋₈ at 10 mg/ml and 2 mg/ml, respectively. Figure 4.23 shows that the 2 mg/ml coating extends over the fibres in the fabric. Just as for P₁₁₋₄, fluorescence in the corners around intersections of the fibres coated with the 2 mg/ml peptide is reduced in comparison with those dipped in P₁₁₋₈ at the higher concentration of 10 mg/ml. Again, this reflects the lower gel mass at the lower concentration.

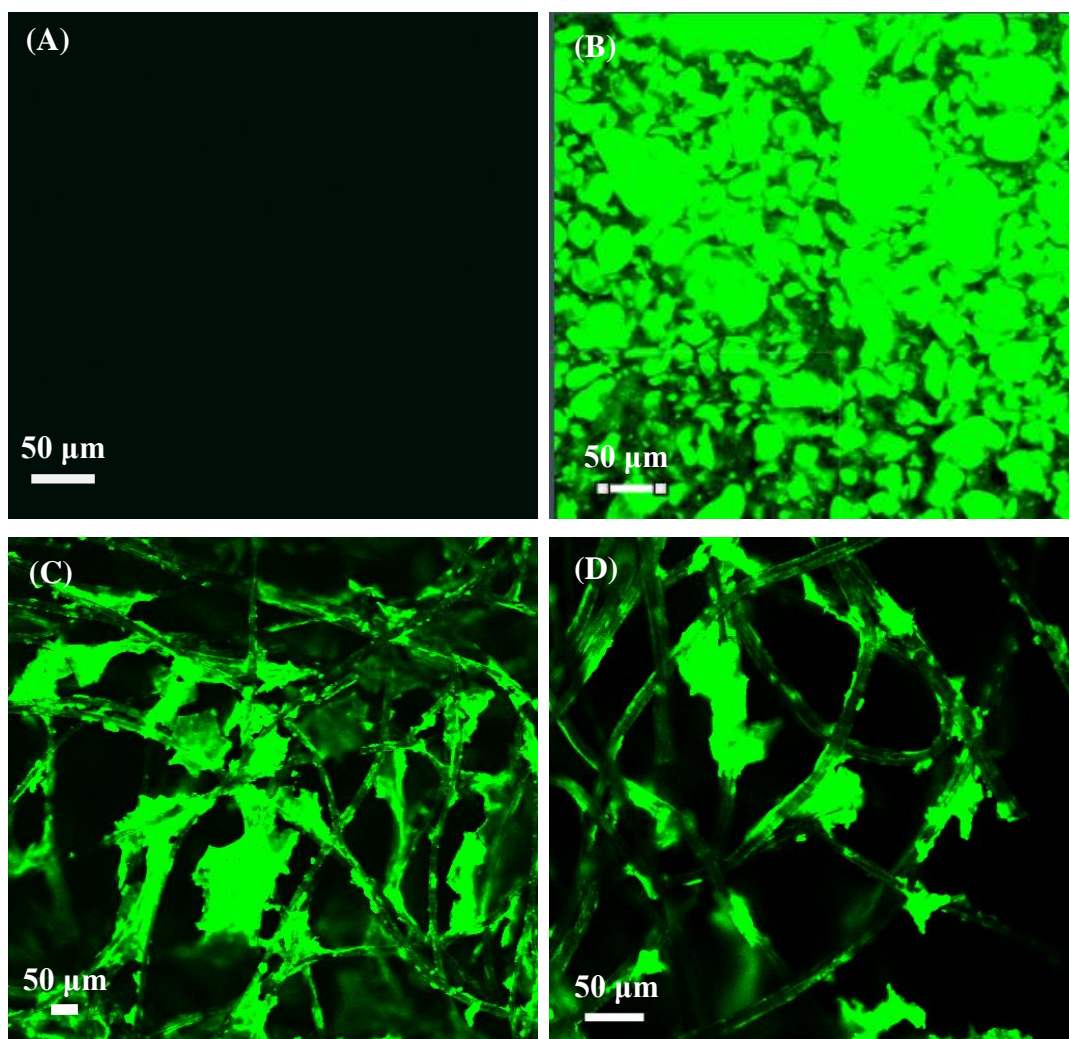


Figure 4.21: CLSM images of cellulose fabrics. (A) Uncoated cellulose fabric. (B) Fluorescently tagged P₁₁-4 peptide gel at 10 mg/ml. (C) Fabric coated with fluorescently tagged peptide P₁₁-4 (10 mg/ml) at 10 X magnification. (D) Same as (C) but at 20 X magnification.

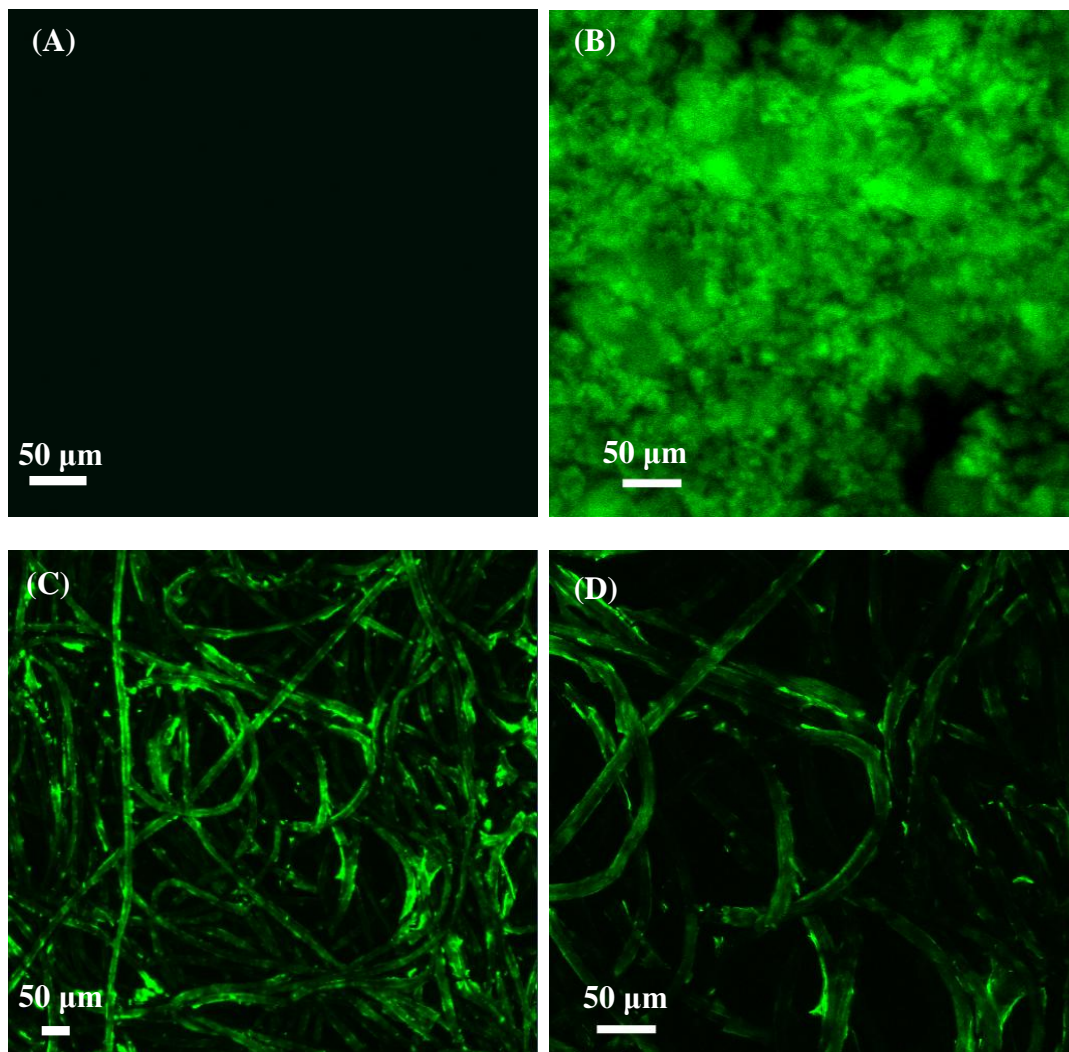


Figure 4.22: CLSM images of cellulose fabrics. (A) Uncoated cellulose fabric. (B) Fluorescently tagged P₁₁₋₄ peptide gel at 2 mg/ml. (C) Fabric coated with fluorescently tagged peptide P₁₁₋₄ (2 mg/ml) at 10 X magnification. (D) Same as (C) but at 20 X magnification.

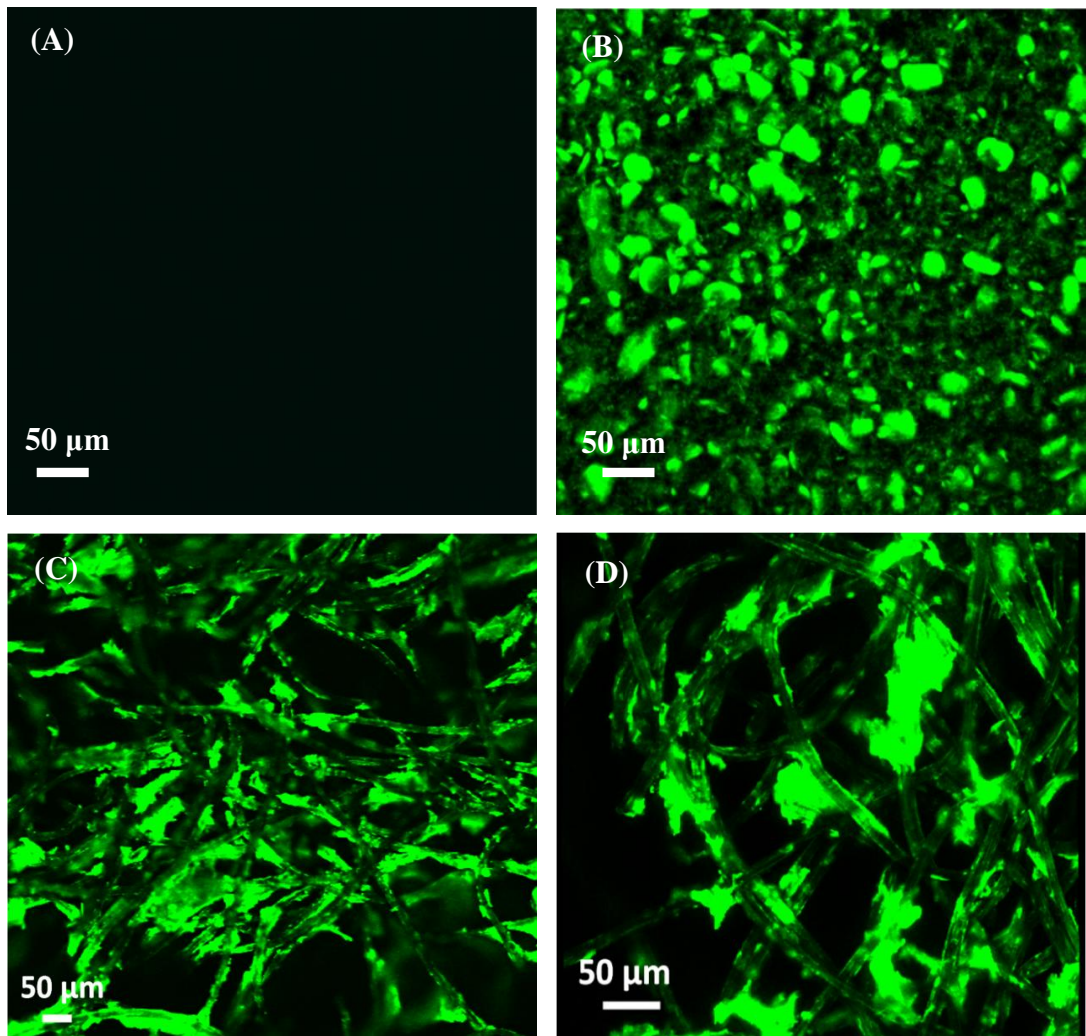


Figure 4.23: CLSM images of cellulose fabrics. (A) Uncoated cellulose fabric. (B) Fluorescently tagged P₁₁₋₈ peptide gel at 10 mg/ml. (C) Fabric coated with fluorescently tagged peptide P₁₁₋₈ (10 mg/ml) at 10 X magnification. (D) Same as (C) but at 20 X magnification.

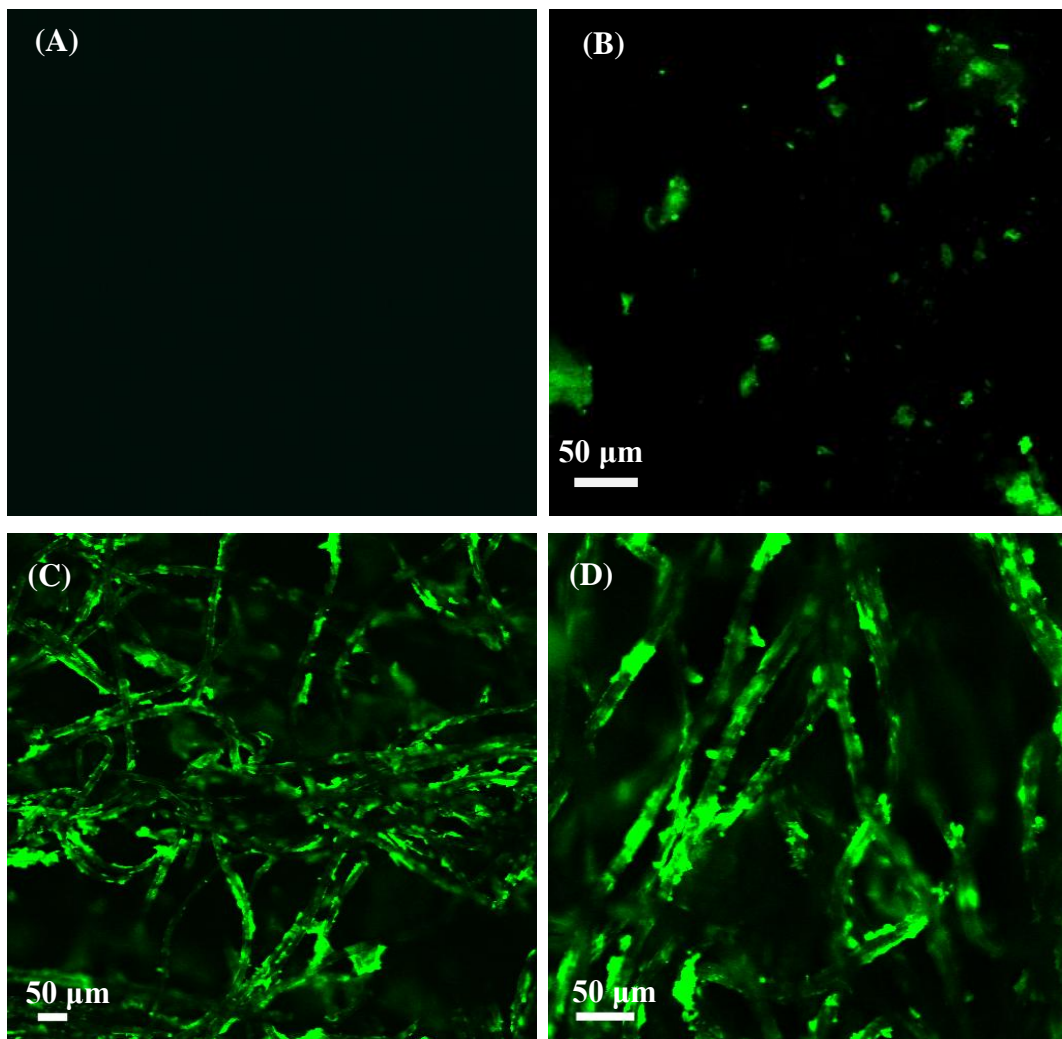


Figure 4.24: CLSM images of cellulose fabrics. (A) Uncoated cellulose fabric. (B) Fluorescently tagged P₁₁-8 peptide gel at 2 mg/ml. (C) Fabric coated with fluorescently tagged peptide P₁₁-8 (2 mg/ml) at 10 X magnification. (D) Same as (C) but at 20 X magnification.

4.3.5 Attenuated Total Reflectance spectroscopy, ATR

ATR-FTIR studies of the samples were performed to investigate the characteristic groups present in the deposited peptide fibrils.

4.3.5.1 Cellulose fabric coated with P₁₁-4 (10 mg/ml)

Figure 4.25 compares the spectra of the blank regenerated cellulose sample and the sample coated with P₁₁-4 (10 mg/ml). The figure shows that cellulose/P₁₁-4 spectrum is dominated by a peak centred at β -sheet region, while the blank cellulose spectrum is shifted to higher wavenumber. The amide I region of the spectra was band-fitted to determine the percentage of β -sheet aggregates (Figure 4.26). The band-fitted spectrum was dominated by β -sheet components located at 1614 cm^{-1} and 1623 cm^{-1} . Table 4.1 identifies the individual peaks in the band-fitted spectrum; from the table, β -sheets represent about 72% of the coating.

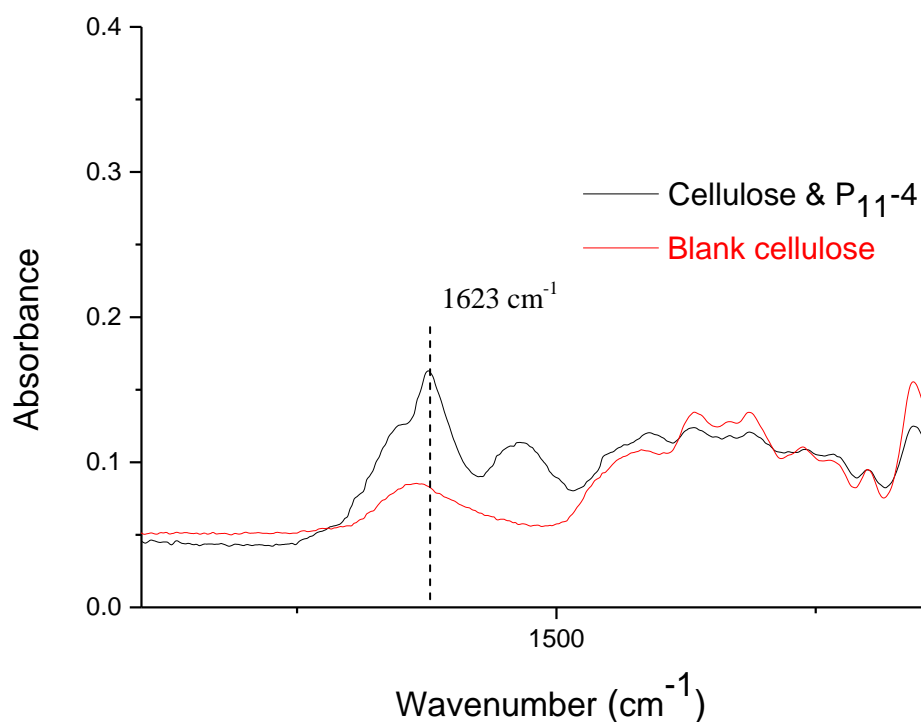


Figure 4.25: IR spectra of a blank cellulose sample (red) and cellulose sample coated with P₁₁-4 (10 mg/ml) (black).

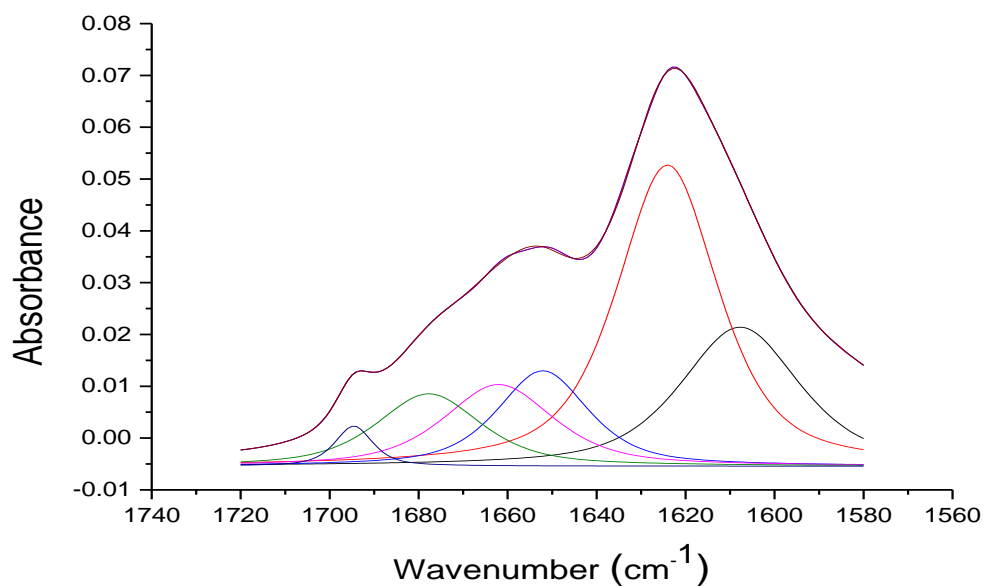


Figure 4.26: Band-fitted IR amide I' band of cellulose fabric coated with P₁₁-4 (10 mg/ml) showing β -sheet conformation.

Table 4.1: Identifications of peaks in the fitted amide I' band of cellulose coated with P₁₁-4 (10 mg/ml).

Peak Centre cm^{-1}	Area	Assignment
1614.207	2.2837	β -sheet
1623.563	4.1776	β -sheet
1650.444	0.9449	α -helix
1661.967	1.0038	Turn
1673.129	1.0632	TFA
1694.444	0.5037	Turn

4.3.5.2 Cellulose fabric coated with P₁₁-4 (2 mg/ml)

Figure 4.27 compares the spectrum of an uncoated sample with that of a sample coated with P₁₁-4 (2 mg/ml). Similar to above, the spectrum of the sample coated with peptide

is centred at β -sheet region, while the uncoated one is shifted. The amide I region was band fitted, as shown in Figure 4.28, and the band-fitted spectrum is dominated by a large absorption peak located at 1625 cm^{-1} , which corresponds to peptides with the β -sheet conformation. Table 4.2 identifies the individual peaks in the band-fitted spectrum; from this table, the β -sheets represent about 46.9% of the coating.

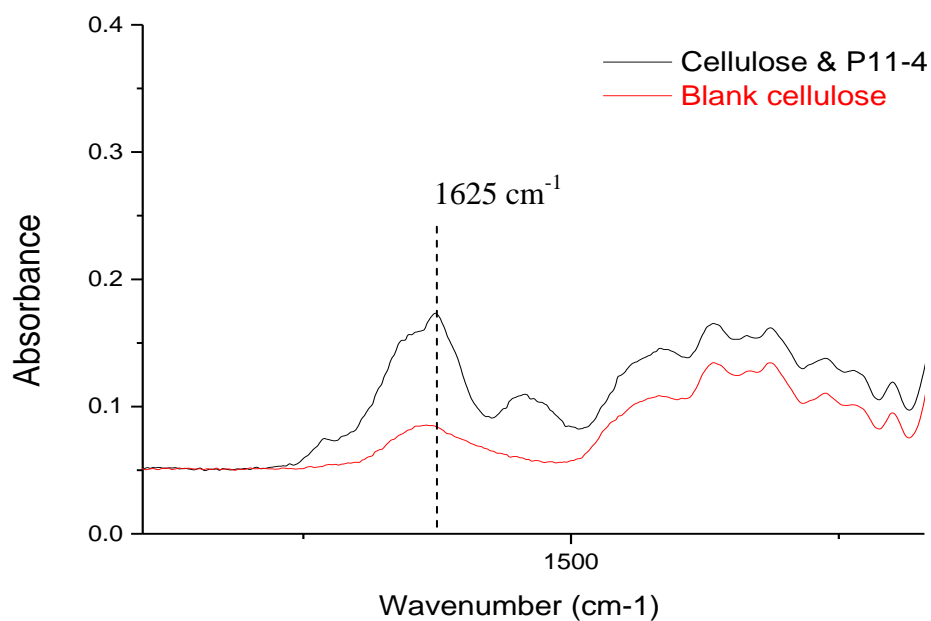


Figure 4.27: IR spectrum of blank cellulose sample (red) and cellulose sample coated with P₁₁-4 (2 mg/ml) (black).

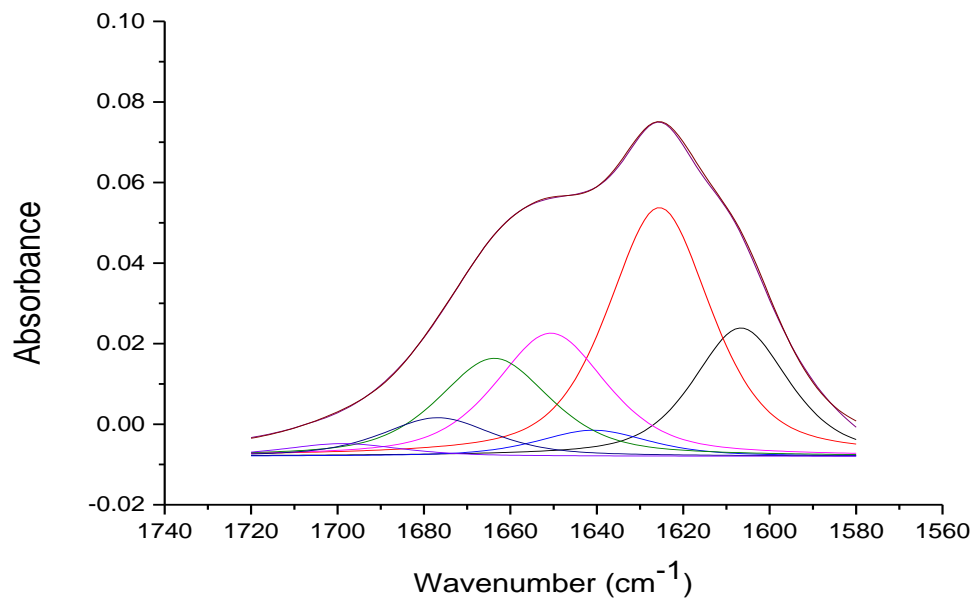


Figure 4.28: Fitted IR amide I' band of cellulose fabric coated with P₁₁-4 (2 mg/ml) with the β -sheet conformation.

Table 4.2: Identifications of peaks found in fitted amide I' band of cellulose coated with P₁₁-4 (2 mg/ml).

Peak Centre cm^{-1}	Area	Assignment
1606.667	1.1124	arginine side chain
1625.524	2.3382	β -sheet
1640.816	0.2639	random coil
1650.632	1.2473	α -helix
1663.727	0.9980	Turn
1676.824	0.3880	TFA
1697.784	0.1358	Turn

4.3.5.3 Cellulose fabric coated with P₁₁-8 (10 mg/ml)

Figure 4.29 compares the spectra of the blank regenerated cellulose sample and the sample coated with P₁₁-8 (10 mg/ml). To enable the calculation of the percentage of

β -sheets in the sample, the amide I region of the spectra was band fitted, as shown in Figure 4.30. The band-fitted spectrum shows a large peak centred at 1621 cm^{-1} , which corresponds to β -sheet aggregates, plus another peak centred at 1634 cm^{-1} . The fitted spectra also show two weak peaks located at 1681 cm^{-1} and 1692 cm^{-1} ; these correspond to anti-parallel β -sheets. Table 4.3 identifies the individual peaks in the band-fitted spectrum; from this table, β -sheets represent about 65.3% of the coating.

4.3.5.4 Cellulose fabric coated with P₁₁-8 (2 mg/ml)

Figure 4.31 shows the spectra of an uncoated sample and a sample coated with P₁₁-8 (2 mg/ml), and Figure 4.32 shows the band-fitted spectra. The figure shows a large absorption band at 1623 cm^{-1} , which correspond to β -sheet aggregates. Table 4.3 identifies the individual peaks in the band-fitted spectra, showing that the percentage of β -sheets in the coating was 47%.

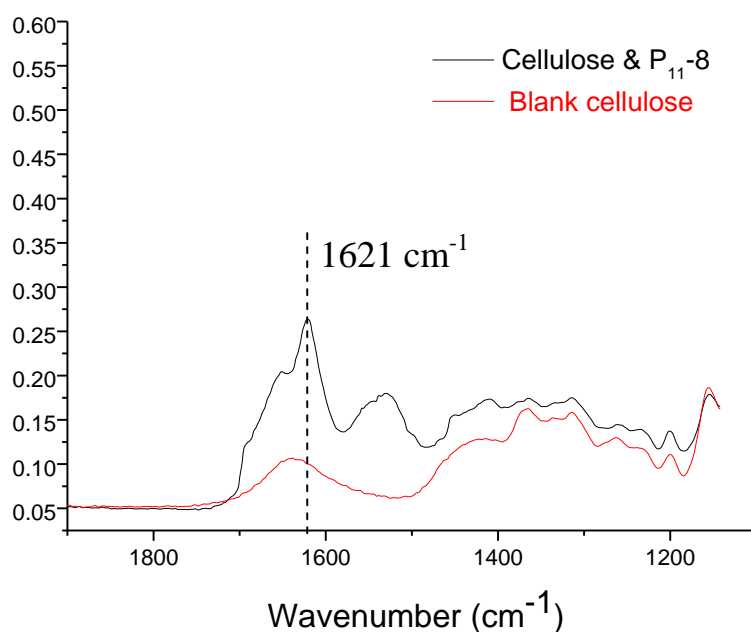


Figure 4.29: IR spectra of blank cellulose sample (red) and cellulose sample coated with P₁₁-8 (10 mg/ml) (black).

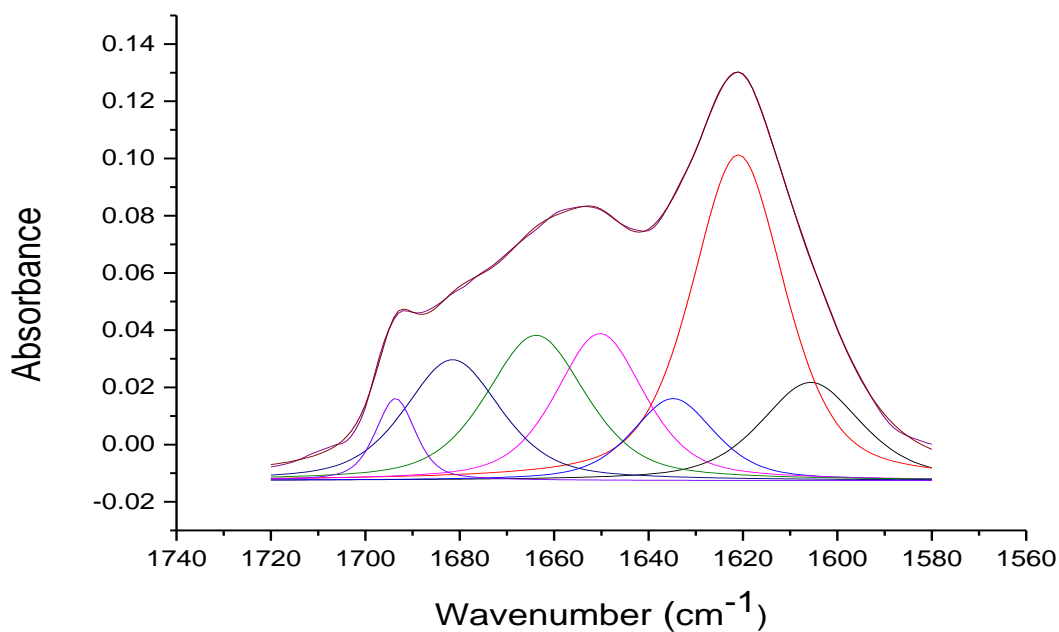


Figure 4.30: Fitted IR amide I' band of cellulose coated with P₁₁-8 (10 mg/ml) showing β -sheet conformation.

Table 4.3: Identification of peaks found in fitted amide I' band of cellulose coated with P₁₁-8 (10 mg/ml).

Peak Centre cm^{-1}	Area	Assignment
1605.650	1.14091	Arginine side chain
1621.000	3.5072	β -sheet
1634.790	0.7869	β -sheet
1650.289	1.5105	α -helix
1663.824	1.6757	Turn
1681.510	1.3389	β -sheet
1692.618	0.3793	β -sheet

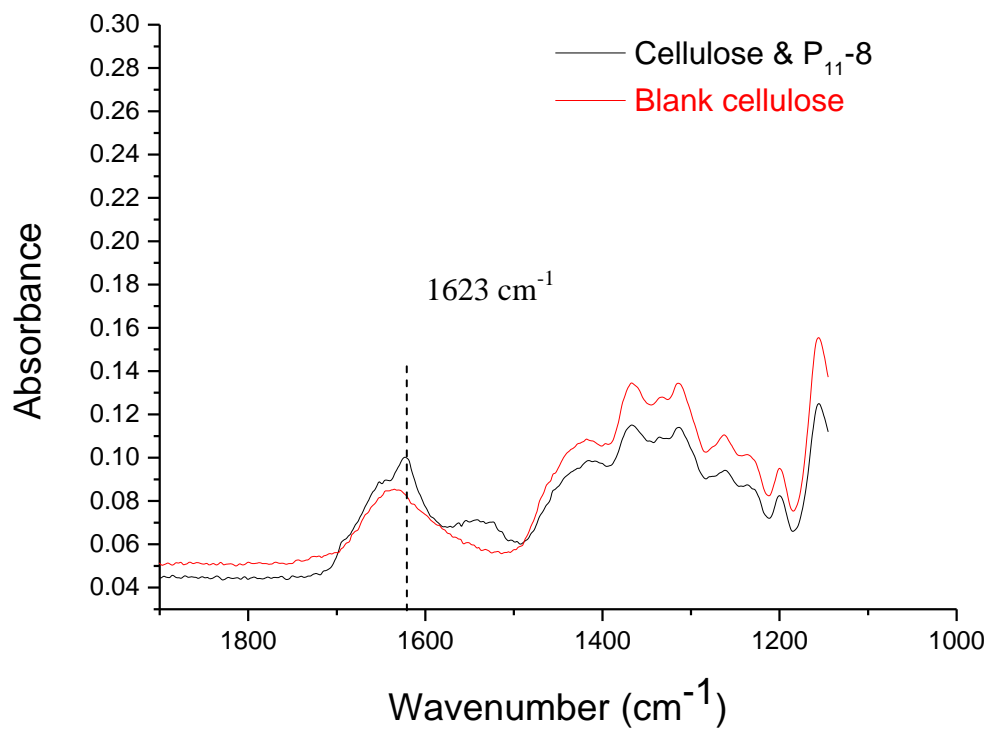


Figure 4.31: IR spectra of blank cellulose sample and cellulose sample coated with P_{11-8} (2 mg/ml).

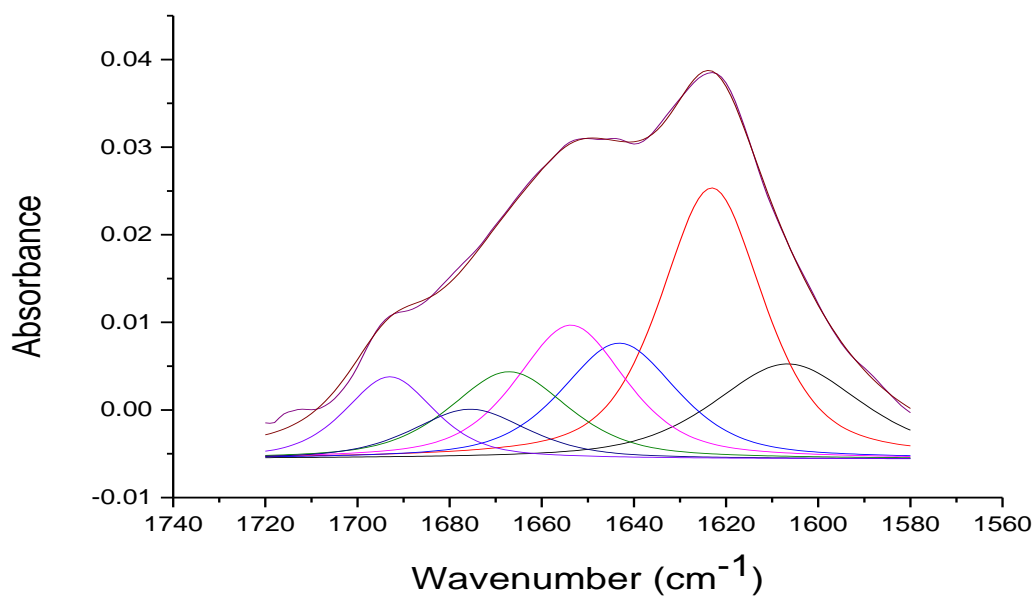


Figure 4.32: Fitted IR amide I' band of cellulose/ P_{11-8} (2 mg/ml) showing β -sheet conformation.

Table 4.4: Identification of peaks found in fitted amide I' band of cellulose coated with P₁₁-8 (2 mg/ml).

Peak Centre cm ⁻¹	Area	Assignment
1606.646	0.5561	arginine side chain
1623.095	1.1006	β-sheet
1643.194	0.5288	Random coil
1653.686	0.5788	α-helix
1667.109	0.4072	Turn
1674.535	0.2265	TFA
1694.000	0.2852	Turn

4.4 Discussion

The integration of peptides with cellulose fibres in the form of a coated nonwoven wound dressing is a novel approach that has not been previously reported. In this study, mechanically bonded nonwoven dressings, which are commonly utilised in wound care, containing regenerated cellulose fibres (viscose rayon) were coated with peptide fibrils that were prepared at two different concentrations.

4.4.1 Fabrics coated with P₁₁-4

It was found that fabrics were successfully coated with either of the two self-assembled peptides: P₁₁-4 and P₁₁-8. The peptide P₁₁-4 forms nematic gels at low pH and monomeric fluids at high pH, and it has glutamic acid on side chains 5, 7 and 9. At pH 9–12, all glutamic acid molecules are protonated, giving the peptide molecule a net charge of -2. This net charge causes repulsion between peptide monomers and results in a monomer fluid. At pH < 3, the P₁₁-4 molecule has a net charge of +1 at position 3 on the arginine side chain and forms a self-supporting gel (Figure 4.33). Based on this

behaviour, cellulose fibres coated with P₁₁₋₄ were readily produced by first dipping the fabric in a monomer solution of P₁₁₋₄ at a high pH of 10. Then, the pH of the solution was decreased, which decreases repulsions between peptide monomers and enables the formation of peptide tapes that then cover fibre surfaces within the fabric. Figure 4.34 shows the behaviour of P₁₁₋₄ as a function of pH, which was applied to coat the fabric at low pH.

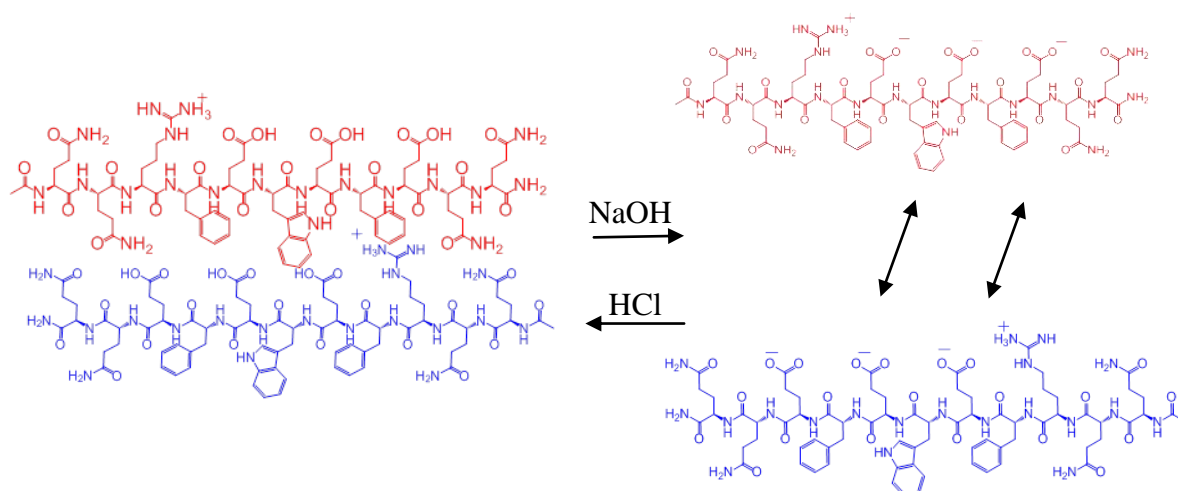


Figure 4.33: Structural changes in P₁₁₋₄ nanotapes in response to changes in pH.

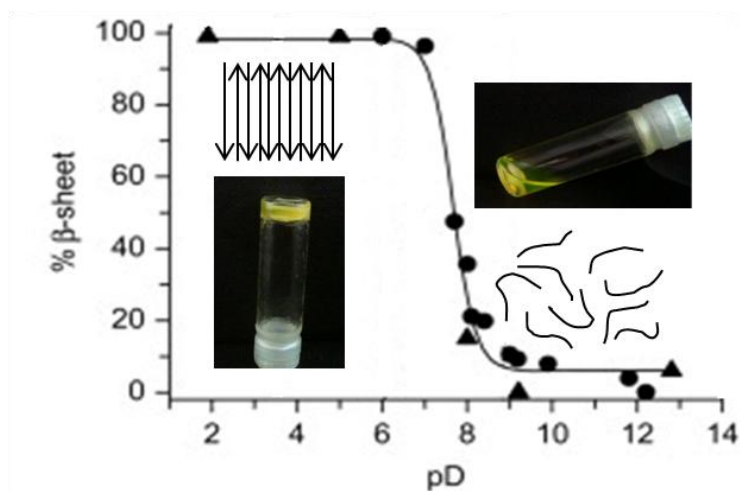


Figure 4.34: pH-dependant behaviour of P₁₁₋₄ nanotapes • is the percentage of β-sheet by FTIR and ▲ by NMR. Adopted from Aggeli 2007 [86].

4.4.2 Fabrics coated with P₁₁₋₈

Compared with P₁₁₋₄, the peptide P₁₁₋₈ is designed to have the opposite switching behaviour. It forms monomeric peptide solutions at low pH and self-assembles into β -sheet fibrils at high pH [86]. This behaviour is driven by the primary structure of P₁₁₋₈. P₁₁₋₈ has an arginine side chain at position 3, ornithine side chains at positions 5 and 6 and a glutamic acid side chain at position 9. The charges of the arginine and ornithine side chains are positive in solutions with pH below their pK_a values of 12.5 and 10.8 respectively. As a result, at $6 > \text{pH} > 3$, P₁₁₋₈ forms a clear isotropic fluid due to the +2 net charge per peptide (Figure 4.35). At $10.3 > \text{pH} > 6$, self-assembly occurs because the ornithine side chains are deprotonated; this decreases repulsions between peptides molecules and a gel forms [8]. Based on this behaviour, cellulose fibres coated with P₁₁₋₈ were readily produced by first dipping the fabric in a monomer solution of P₁₁₋₈ at a low pH of ~ 3 . Then, the pH of the solution was increased, which decreases repulsions between peptide monomers and enables the formation of peptide tapes that then cover the fibre surfaces (Figure 4.36).

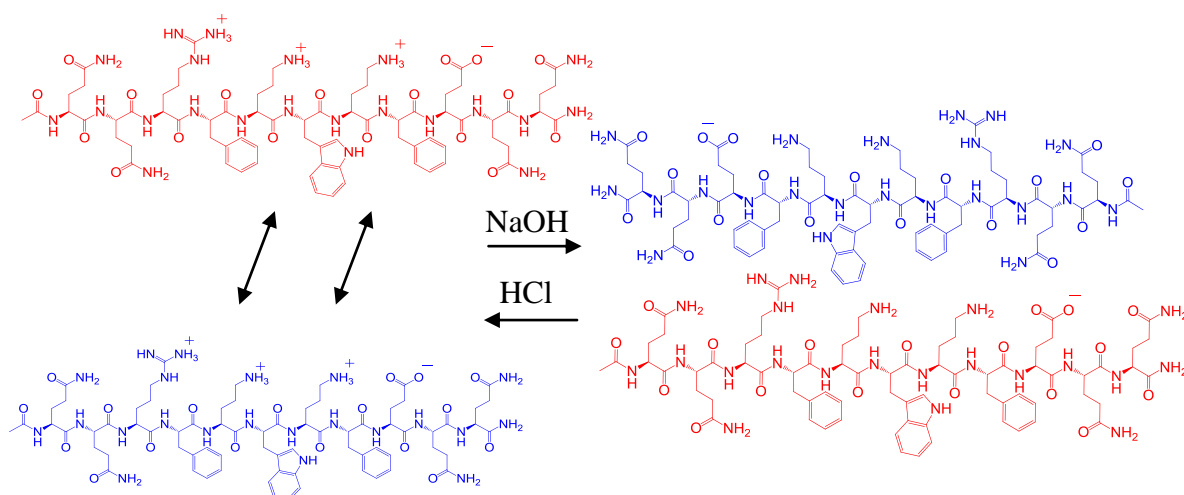


Figure 4.35: Structural changes in P₁₁₋₈ nanotapes in response to changes in pH.

4.4.3 Characterization of samples coated with self-assembled peptides

The tendency to coat a fabric depends on the nature of the fabric material and coating substance. The fabrics used here were made from cellulose polymer, which contains many hydrogen bonds in its strands. Therefore, it was feasible to coat cellulose fibres with peptides fibrils because peptides also have hydrogen bonds in their structures. The feasibility of coating cellulose fabric with peptides was investigated by complementary characterization techniques: SEM, CLSM and FTIR. All these techniques demonstrated that fabric samples were successfully coated with the peptides.

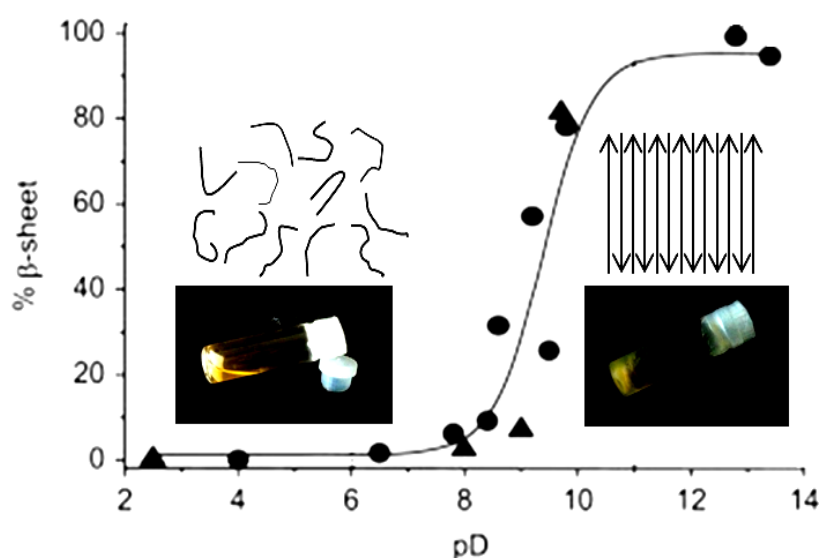


Figure 4.36: pH-dependant behaviour of P₁₁₋₈ nanotapes ● is the percentage of β -sheet by FTIR and ▲ by NMR. Adopted from Aggeli 2007 [86].

We used SEM to explore differences between three types of samples: control samples, coated samples and samples treated with an acid or base. At low magnification, SEM images did not show any differences between the three samples. However, at high magnification, SEM images revealed clear differences in cellulose fibre morphology. In samples coated with peptides at a concentration of 10 mg/ml, massive accumulation of bulk gel was trapped between specimen fibres; this accumulation did not appear in specimens coated with peptide at a low concentration of 2 mg/ml. At high concentrations, differences in surface details were clear. The fabric sample treated with NaOH exhibited surface roughening. Many authors have reported the effects of NaOH on cellulosic fabrics by hydrolysis process, including Wang [140]. Wang showed that NaOH can dissolve cellulose tissue over a narrow range. These defective surfaces were

not visible in SEM images of the coated samples because the peptide fibrils that covered fabric surfaces concealed the denaturation [31]. Also, the addition of HCl caused surface roughening, which indicates that cellulosic fabrics hydrolyzed [141, 142].

CLSM confirmed the presence of fluorescently tagged peptides in coatings that covered the underlying cellulose fibres. The technique showed that, at a high concentration of 10 mg/ml, heavy accumulation of peptide gel formed between fibre surfaces. At 2 mg/ml, the fibres were extensively coated without accumulation of excess gel; these observations confirm those by SEM. FTIR demonstrated that the higher concentration of peptides forms a higher percentage of β -sheets. High percentages of β -sheets could provide higher capacities for uploading drug molecules. Therefore, for drug-release applications, high peptide concentrations are favourable.

4.5 Conclusions

It is expected that, owing to their flexibility and versatility, composite medical fabrics will continue to have a significant impact in many medical applications. In addition, their low production costs, together with the ease and options for surface modifications, make them attractive alternatives to current drug delivery devices. In this chapter, cellulosic fabrics were coated with pH-responsive peptides. SEM, CLSM and FTIR were used to evaluate the coated dressings. The two main findings from those characterization techniques are as follows: (a) peptides can readily be applied as coatings on cellulosic dressings, and (b) FTIR results showed that fabric samples immersed in a higher concentration of peptides produced coatings that contain a higher proportion of β -sheet peptides.

Chapter 5

5 Antimicrobial activity of self-assembled peptide-coated cellulosic fabric against *Staphylococcus epidermidis*

5.1 Introduction

The previous chapter described the successful coating of cellulosic fabrics with P₁₁-4 and P₁₁-8 fibrils. This chapter considers the feasibility of incorporating antibiotics into the peptide fibril coating. Vancomycin and levofloxacin were selected for this purpose, because they are commonly used to treat *Staphylococcus epidermidis* (*SE*) infections. The release of these bacteria from fibril coatings was determined using agar diffusion assay.

SE

SE is a Gram-positive bacterium present in the normal flora of the skin. The spherical cells arrange into grape-like clusters and form creamy/white colonies approximately 1–2 mm in diameter after overnight incubation on an agar plate. The optimal pH for its activity is 6–8 [143, 144].

The main source of *SE* infection is the skin, and *SE* is the most frequently isolated microorganism in the clinical microbiology laboratory, particularly from patients with hospital-acquired infections. *SE* is not normally pathogenic; however, under some conditions it converts from a commensal organism to a pathogen. Newborns, elderly and people with a compromised immune system are at a risk of *SE* infection. Patients with foreign bodies such as catheters or implants are at a high risk of *SE* contamination. Devices such as implants cause infection by introducing *SE* from the skin or mucous membranes into the implantation site. Bacteria that colonize the implant form biofilms, which comprise multiple layers of cell clusters that are embedded in amorphous

5.1.1 Bacterial resistance to antibiotics

Bacterial resistance occurs when an antibiotic loses its ability to kill bacteria or control their growth, the bacteria survive and continue causing harm. The genetic and biochemical mechanisms of antibiotic resistance have been investigated. Resistance to antibiotics can be classified as intrinsic or acquired. Intrinsic resistance is the ability of bacteria to resist the activity of antibiotics through their inherent structure. For example, *Pseudomonas aeruginosa* has low membrane permeability, which is the reason for its innate resistance to several antimicrobials. Acquired resistance occurs when microorganism transform from susceptible to resistant. Susceptible bacteria can acquire resistance by different mechanisms. Some bacteria become resistant to antibiotics through a mechanism known as efflux. Efflux pumps are channels that export antibiotics from the cell. Antibacterial agents enter bacteria through channels termed as porins. The agents are pumped back out the bacteria by efflux pumps. By pumping out antibacterial agents, intracellular accumulation of the agents is prevented and their lethal activity is inhibited. Acquiring changes that prevent drug binding to antimicrobial target sites is a common mechanism of resistance. Target site changes often result from the spontaneous mutation of genes on the bacterial chromosome or from the acquisition of antimicrobial resistance genes from other bacteria. Antibiotic inactivation is another common resistance mechanism. Some bacteria release enzymes that inactivate drugs by hydrolysis or by modification (group transfer or redox mechanisms). Several antibiotics possess chemical bonds that are susceptible to hydrolysis and whose integrity is central to biological activity. When these vulnerable bonds are cleaved, antibiotic activity is destroyed [147-149].

Infectious diseases caused by microbes that have become resistant to antibiotics are an increasing public health problem. Wound infections, malaria, gonorrhoea, tuberculosis, pneumonia and septicaemia are examples of diseases that have become harder to treat with antibiotics. Sever health consequences can arise from resistant bacteria, such as prolonged infections, increased recovery times, increased hospital stays and increases in health care costs. More toxic medications are often needed to cure infection and these medications cause higher mortality rates. There are several reasons why antibiotic resistance is increasing, including increased use of antibiotics, improper use of antibiotics and poor hygiene practices [150].

This chapter describes the incorporation of antibiotics within peptide fibrils before coating the fabrics (Figure 5.2). The addition of antibiotics molecule to the peptide solution was tested to determine whether they interfere with the formation of β -sheet or not. The cellulosic fabrics were coated with the fibril-encapsulated antibiotics to develop a pH-responsive dressing, which was then assessed for the ability to inhibit the growth of *SE*. Hopefully, this dressing could be clinically applied on infected wounds in the future to release the drug when required and reduce the problem of bacterial resistance to antibiotics in wound care (Figure 5.3).

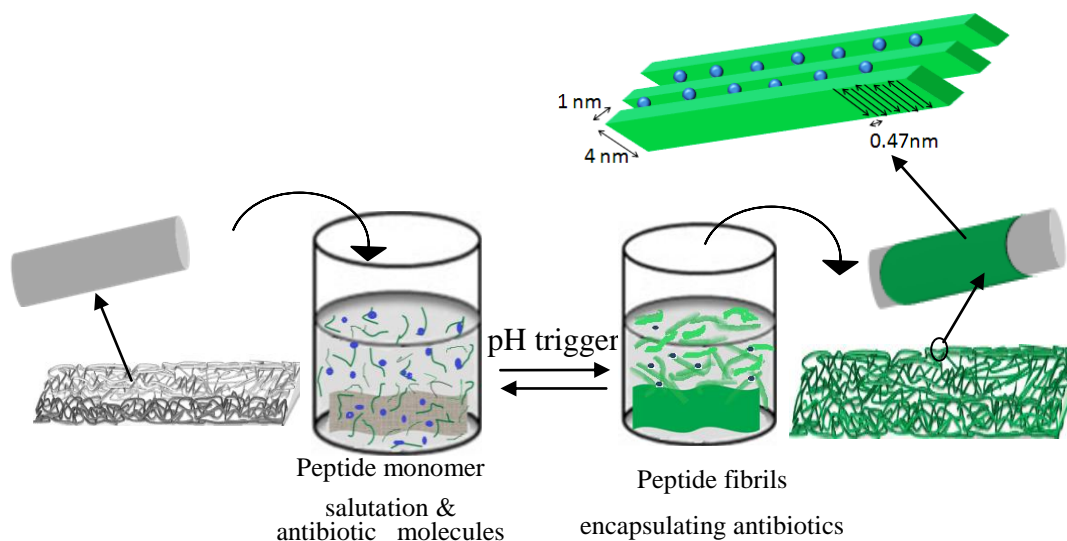


Figure 5.2: Development of cellulosic fabrics coated with peptide fibril-encapsulated antibiotics. Blue is antibiotic, green is peptide.

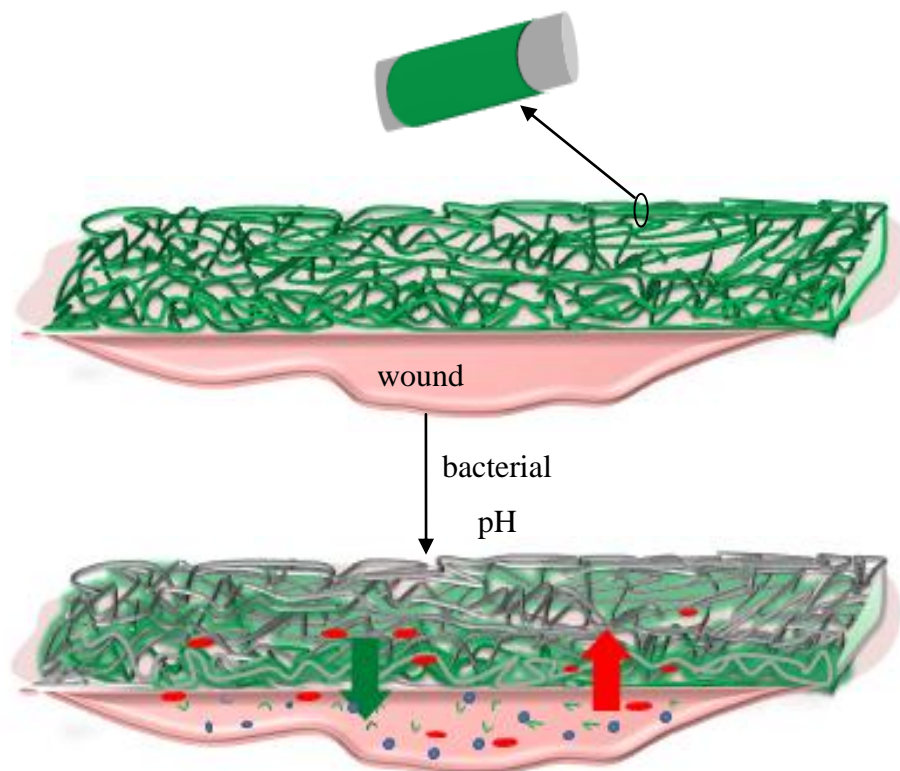


Figure 5.3: Switchable drug release from the pH-responsive dressing stimulated by bacterial-induced changes of pH. Red is bacteria. Green is peptide. Blue is antibiotic.

5.2 Materials and method

5.2.1 Materials

Antibiotics

Vancomycin (1449.3 g/mol) and Levofloxacin (361.368 g/mol) was purchased from Sigma Aldrich.

SE

SE strain NCTC-13360 was purchased from The National Collection of Type Cultures (NCTC). Muller–Hinton agar, nutrient agar and nutrient broth were purchased from Sigma Aldrich.

5.2.2 Methods

5.2.2.1 Development of an antimicrobial dressing

5.2.2.1.1 Antibiotic encapsulation into P₁₁₋₄

The peptide solution was prepared by adding 10 mg of P₁₁₋₄ into 1 ml of D₂O, vortexing for 30 s and adding approximately 0.15 mg fluoro P₁₁₋₄ to the solution. The pD of the solution was 5.8 and caused P₁₁₋₄ to flocculate. NaOD (1 M) was added (3 μ l drops) to clarify the solution (pD 11), and a piece of 0.5 \times 0.5 cm cellulose fibre was dipped into the monomer solution, which was incubated overnight. DCI (1 M) was added dropwise (6 μ l drops) to the solution to decrease the pD to 2.9, which induced P₁₁₋₄ molecules to self-assemble into β -sheets. The fabric was trapped inside the gel overnight. The fabric was then removed and air-dried overnight. A control sample of cellulose fabric was prepared in water using the same method.

5.2.2.1.2 Antibiotic encapsulation into P₁₁₋₈

The peptide solution was prepared by adding 10 mg of P₁₁₋₈ into 1 ml of D₂O followed by vortexing for 30 s. Approximately 0.15 mg of fluoro-P₁₁₋₄ was added (pD 3.9) to form P₁₁₋₈ monomers. A piece of 0.5 \times 0.5 cm cellulose fibre was dipped in the monomer solution and left overnight. NaOD (1 M) was added (4 μ l drops) to increase the pD to 10 and induce the self-assembly of P₁₁₋₈ into β -sheets that subsequently form a nematic gel. The fabric was trapped inside the gel overnight, removed and air-dried overnight. A control sample of cellulose fabric was prepared in water using the same method.

5.2.2.2 Isolation of single colonies

SE was collected as freeze-dried beads. One bead was added to each of the three types of culture medium and incubated at 37 °C for 24 h. Reconstituted bacterial broth was used to subculture the bacteria on agar plates. The inoculating loop was heated to red hot in a blue Bunsen flame and cooled before streaking. A loopful was collected from the bacterial broth culture and immediately streaked gently across the plate. The streaking pattern is shown in Figure 5.4.

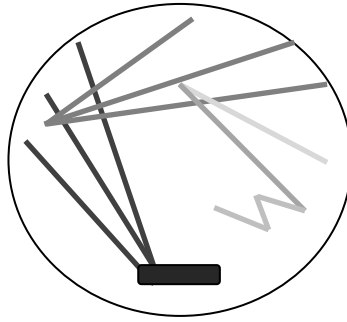


Figure 5.4: Streaking pattern.

5.2.2.3 Gram staining

A single well-isolated colony of *SE* was collected and mixed with a single loop of sterile deionised water on a glass slide (a sterilized loop was used to collect the suspension). The bacterial suspension was heat-fixed to the slide by passing it a few times through a blue Bunsen flame. The slide was flooded with oxalate crystal violet and rinsed with running tap water after 1 min. The slide was flooded with iodine solution, and it was rinsed with running tap water after 1 min. The slide was decolorized by flooding it with acetone for 5 s and washed with running water. The slide was then washed with carbol fuchsin for a few seconds and then rinsed with running water. The sample was viewed using a visible light microscope.

5.2.2.4 Disk diffusion assay

An overnight broth culture was diluted to 0.5 McFarland and standard turbidity, which is equivalent to approximately 1.50×10^8 cells/ml. The turbidity of the suspension was determined using a spectrophotometer, and the absorbance was adjusted to 0.08 at 625 nm. A sterile swab was used to collect the bacteria, and excess liquid was removed by gently pressing the swab against the inside of the tube. The swab was streaked across a Mueller–Hinton agar (4 mm deep) plate, rotated 90° and streaked again in one direction. This procedure was repeated three times. The plates were allowed to dry for approximately 5 min. The coated fabrics (0.5 cm in diameter) were placed on the plates (three samples for each dressing). The plates were incubated at 37 °C for 24 h, and the diameters (mm) of the zones of growth inhibition were recorded.

5.3 Results

5.3.1 Effect of antibiotics on peptide self-assembly

Before starting the coating process, the incorporation of antibiotics within peptide fibrils was investigated to determine whether the antibiotics molecules influenced peptide self-assembly and gel formation. Solutions of peptide monomers (10 mg/ml) were mixed with 0.1 mg of antibiotic, and gelation was triggered by changing the pH. Self-supporting gels were formed in all samples, suggesting that the antibiotics did not inhibit peptide self-assembly (Appendix B).

5.3.1.1 Transmission electron microscopy, TEM

Solutions of P₁₁-8 and P₁₁-4 gels containing antibiotics were viewed using TEM (Figure 5.5). Control P₁₁-4 formed fibrils a few microns long, approximately 13–18 nm and 10–14 nm at their widest and narrowest points, respectively. Their helical pitch was 190–240 nm. In P₁₁-4-containing antibiotics, there was no significant difference in the fibril dimensions or morphology compared with the samples without antibiotics. P₁₁-4-containing vancomycin or levofloxacin formed fibrils up to 12–19 nm and 14–18 nm wide, respectively.

Control P₁₁-8 formed fibrils 12–16 nm wide, which formed rope-like structures approximately 24–30 nm wide. P₁₁-8 containing antibiotics formed fibrous structures (14–17 mm long) that were not significantly different compared with the control. These observations indicate that the antibiotics did not interfere with peptide self-assembly.

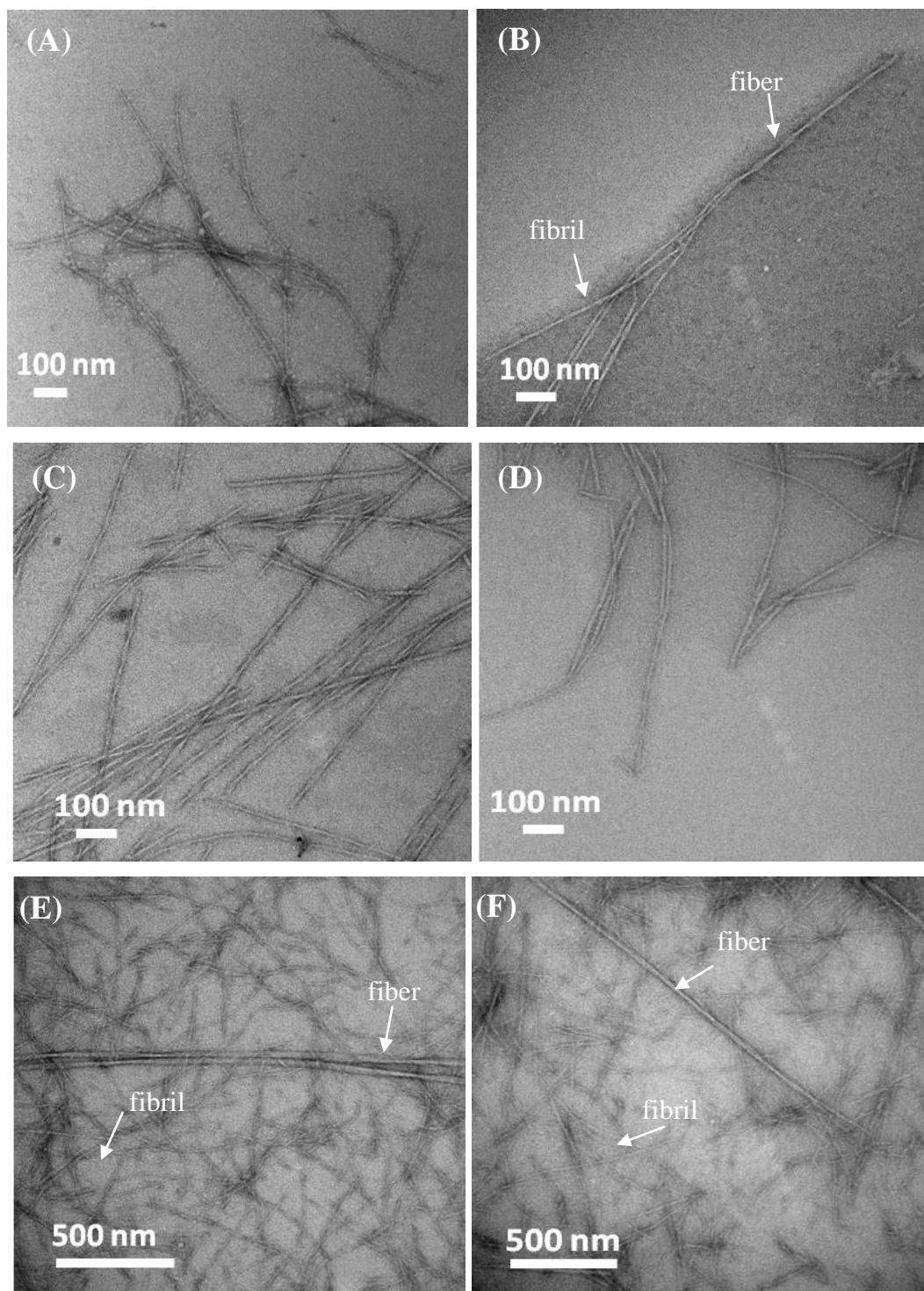


Figure 5.5: TEM images of peptides fibrils encapsulating antibiotics (A) Control P₁₁-4, (B) control P₁₁-8 (C) P₁₁-4/vancomycin (D) P₁₁-4/levofloxacin (E) P₁₁-8/vancomycin (F) P₁₁-8/levofloxacin.

5.3.2 Coating cellulosic fabrics with fibril-encapsulated antibiotics

After TEM confirmed that antibiotics did not affect the formation of peptide fibrils, the incorporated antibiotics into peptide fibrils were used to coat cellulosic fabrics to

develop smart dressings that respond to *SE*-induced changes in pH. The coating process is shown in Figures 5.6 and 5.7.

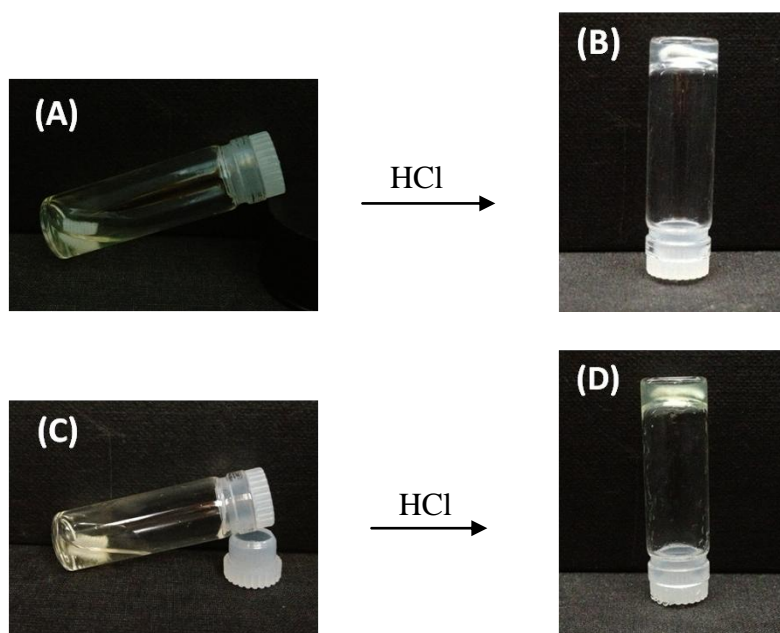


Figure 5.6: Development of fabric coated with P₁₁₋₄ encapsulated antibiotics. (A) P₁₁₋₄ fluid solution containing vancomycin. (B) P₁₁₋₄ gel containing vancomycin. (C) P₁₁₋₄ fluid solution containing levofloxacin. (D) P₁₁₋₄ gel containing levofloxacin.

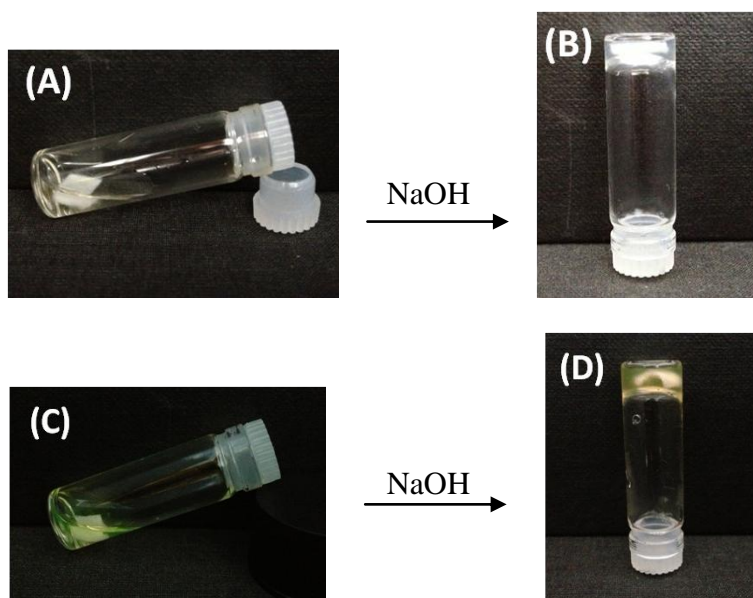


Figure 5.7: Development of fabric coated with P₁₁₋₈ encapsulated antibiotics. (A) P₁₁₋₈ fluid solution containing vancomycin, (B) P₁₁₋₈ gel containing vancomycin, (C) P₁₁₋₈ fluid solution containing levofloxacin, (D) P₁₁₋₈ gel containing levofloxacin.

5.3.2.1 Scanning electron microscopy, SEM

SEM images revealed the details of the surfaces of the coated fabrics prepared in this chapter (with antibiotics). These samples were compared with coated samples prepared in the previous chapter (without antibiotics) to demonstrate if the addition of antibiotics affected the coating process.

The surfaces of the fabrics impregnated with vancomycin or levofloxacin solution are shown in Figure 5.8 (A) and (B), respectively. Their surfaces are smooth and resemble those of control samples shown in the previous chapter (Figures 4.13, 4.16, 4.19 and 4.22). Figures (C) and (D) show the distributions of peptide P₁₁₋₄ fibrils containing vancomycin and levofloxacin, respectively. Images (E) and (F) show the distribution of peptide P₁₁₋₈ fibrils containing vancomycin and levofloxacin, respectively. The images reveal that the morphologies of the network of antibiotic-encapsulated fibrils are similar to those of the coated samples shown in the previous chapter. These comparisons indicate that the peptide fibrils were successfully coated with antibiotics.

5.3.2.2 Confocal laser scanning microscopy, CLSM

Confocal microscopy was used in the previous chapter to investigate the presence of the peptide fibril layers on the fibres of the fabric. In this chapter, CLSM was applied again to investigate the presence of antibiotic-containing peptide fibrils on the surface of the fabric. Figure 5.9 presents the layers on top of the fabrics is consistent with that acquired in the previous chapter.

The results of using both techniques, SEM and CLSM, indicate that the addition of antibiotics to the peptide coating solution did not change the affinity of peptide fibrils for the surface of the fabric.

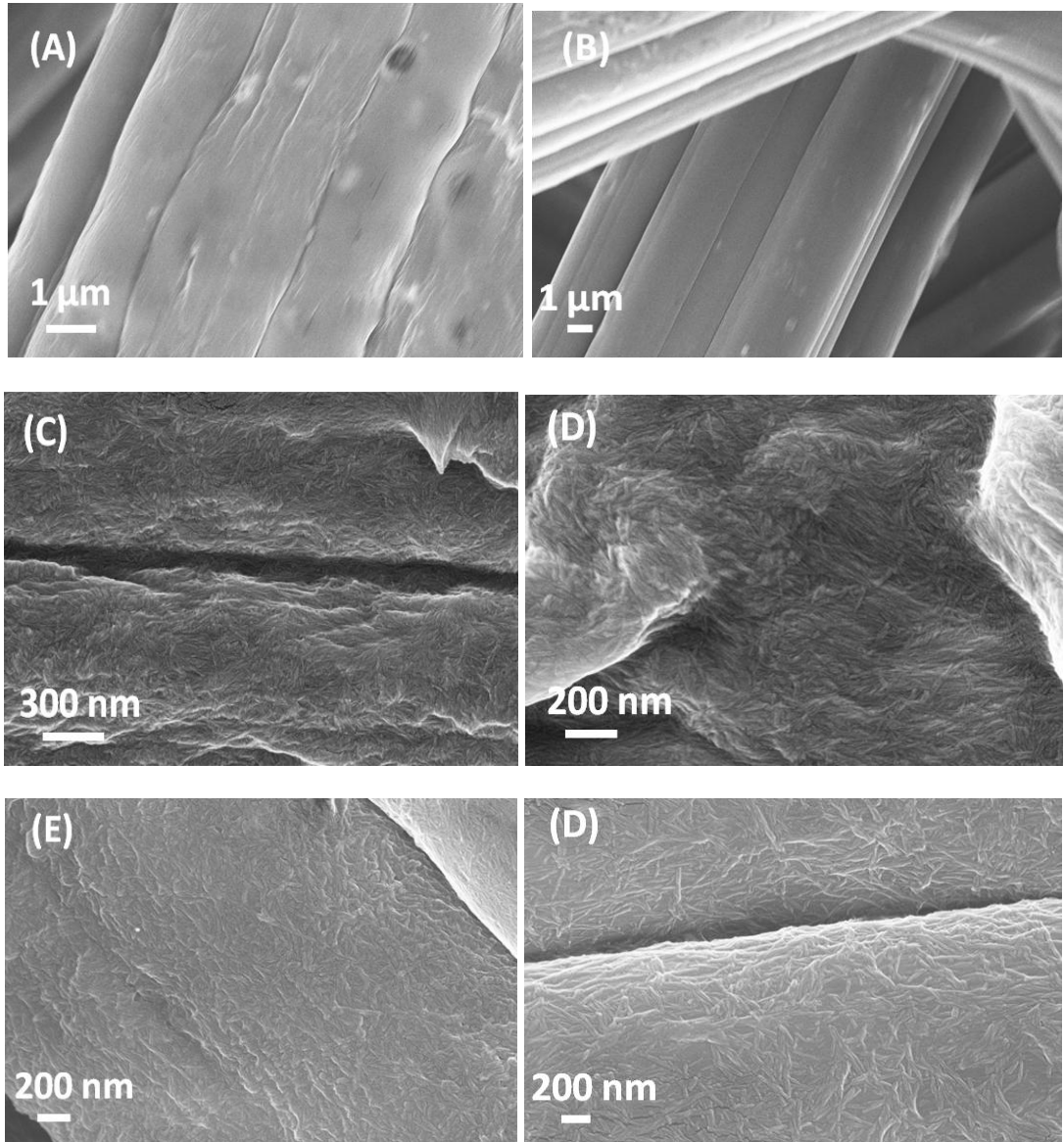


Figure 5.8: SEM images of dressings coated with peptide fibrils containing antibiotics. (A) Control sample of cellulose fabric with vancomycin, (B) cellulose and levofloxacin, (C) cellulose fabric coated with P₁₁-4/vancomycin, (D) cellulosic fabric coated with P₁₁-4/levofloxacin, (E) cellulose fabric coated with P₁₁-8/vancomycin, (F) cellulose and P₁₁-8/levofloxacin.

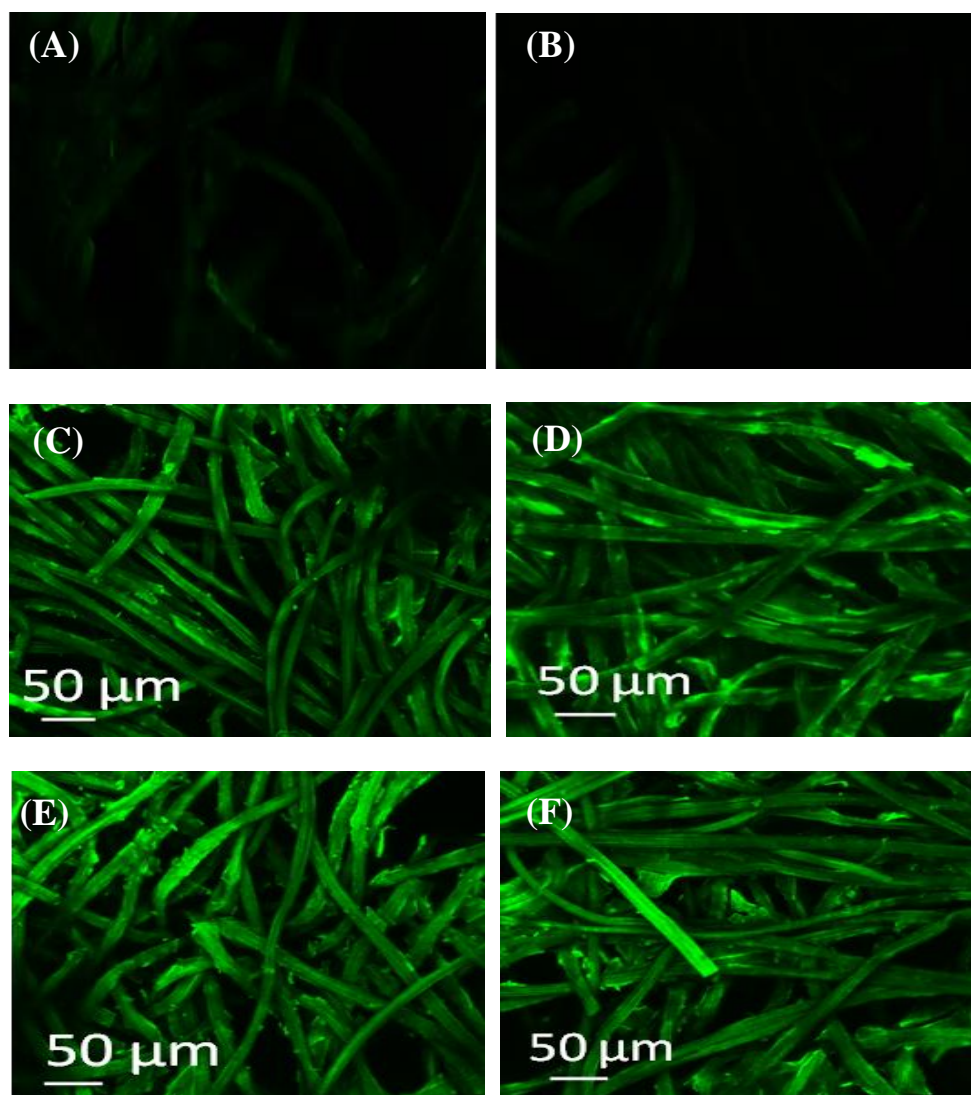


Figure 5.9: CLSM images of dressings coated with peptide fibrils and antibiotics. (A) Control, (B) P₁₁-4/vancomycin, (C) P₁₁-4/levofloxacin, (D) control, (E) P₁₁-8/vancomycin, (F) P₁₁-8/levofloxacin

5.3.2.3 Attenuated total reflectance spectroscopy, ATR-IR

Figures 5.10 shows the overlaid spectra of samples coated with 10 mg/ml P₁₁-4 gel containing 0.1 mg antibiotic. Figure 5.11 shows the overlaid spectra of samples coated with 10 mg/ml P₁₁-8 gel containing 0.1 mg antibiotic. Both figures show that all spectra of samples containing antibiotics remained unshifted from β -sheet region.

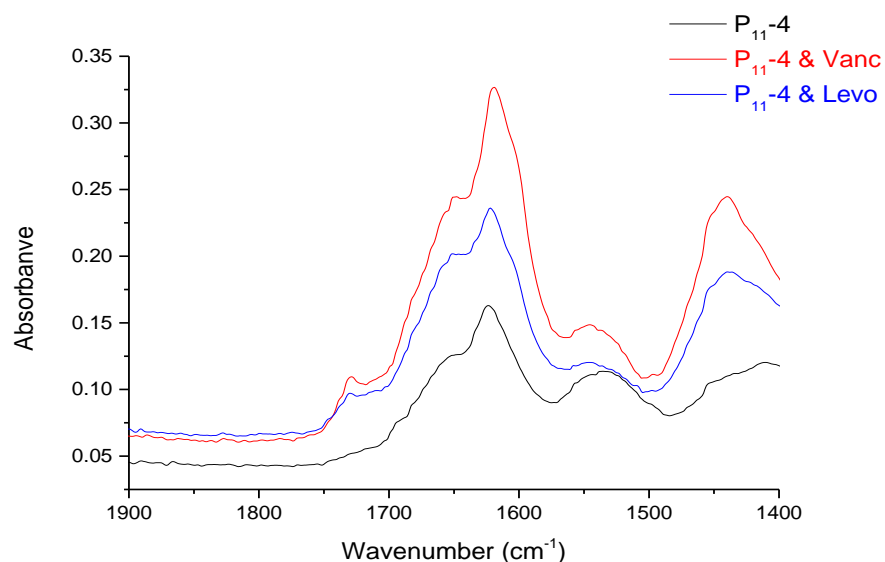


Figure 5.10: IR spectra of a cellulose sample coated with P₁₁-4 peptide fibrils, cellulosic fabric coated with P₁₁-4/vancomycin and fabric coated with P₁₁-4/levofloxacin.

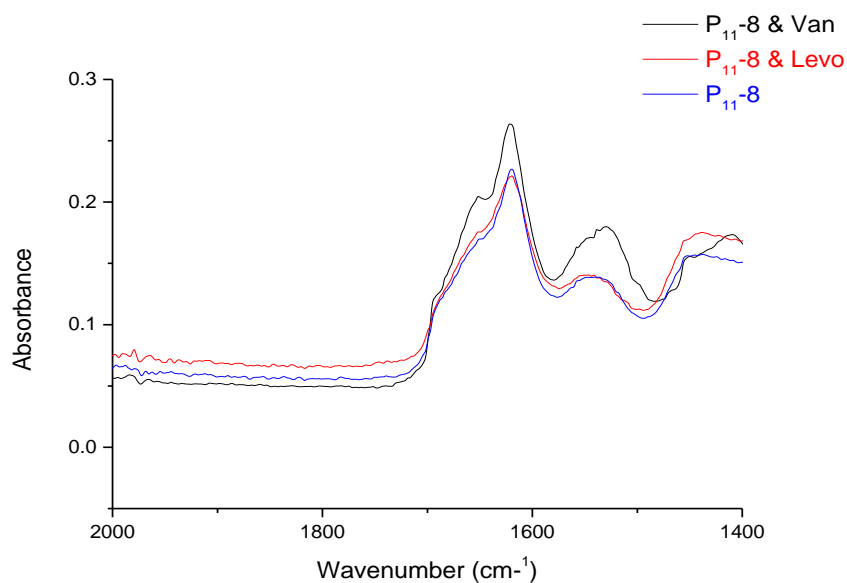


Figure 5.11: IR spectra of a cellulose sample coated with P₁₁-8 peptide fibrils, cellulosic fabric coated with P₁₁-8/vancomycin and fabric coated with P₁₁-8/levofloxacin.

5.3.3 Antimicrobial activity of the coated fabrics

All characterisation techniques proved that antibiotics were successfully incorporated into the peptide coating. Subsequently, the effect of the coated fabric on the growth of *SE* was determined.

5.3.3.1 Identification of *SE*

To confirm the identity of *SE*, cultures were incubated at 37 °C overnight. The cream-coloured flat colonies with regular edges are shown in Figure 5.12A. A single colony was collected using a sterilised loop for gram staining. The figure shows Gram-positive cocci in grape-like clusters (Figure 5.12B). pH of the *SE* colonies was determined by applying strips of pH paper to the cultured plates. The starting pH was 7, increased to 8 after 24 h, and increased to 9 after 5 days (Figure 5.13).

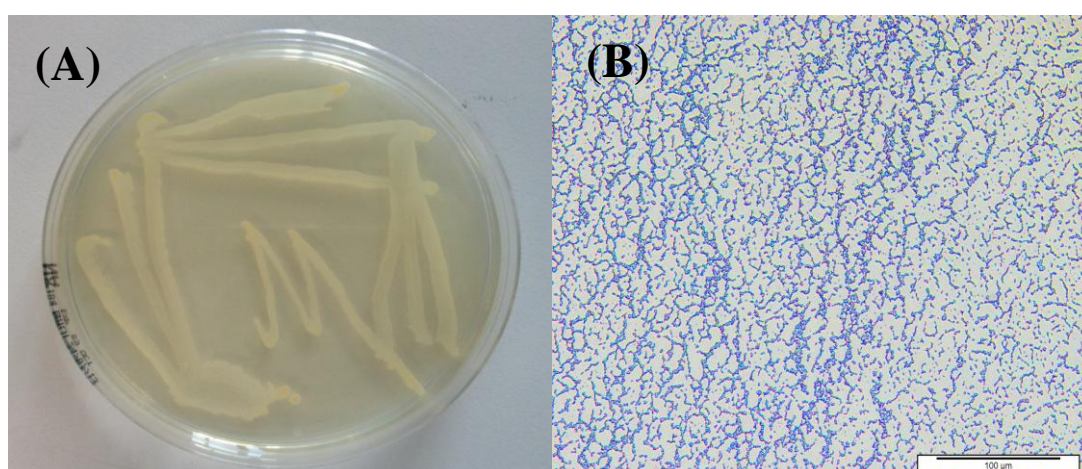


Figure 5.12: Identification of *SE*. (A) MHA plate displaying typical colony morphology, the creamy colour of *SE*. (B) Gram stain of a single colony, grape-like clusters of Gram-positive cocci.

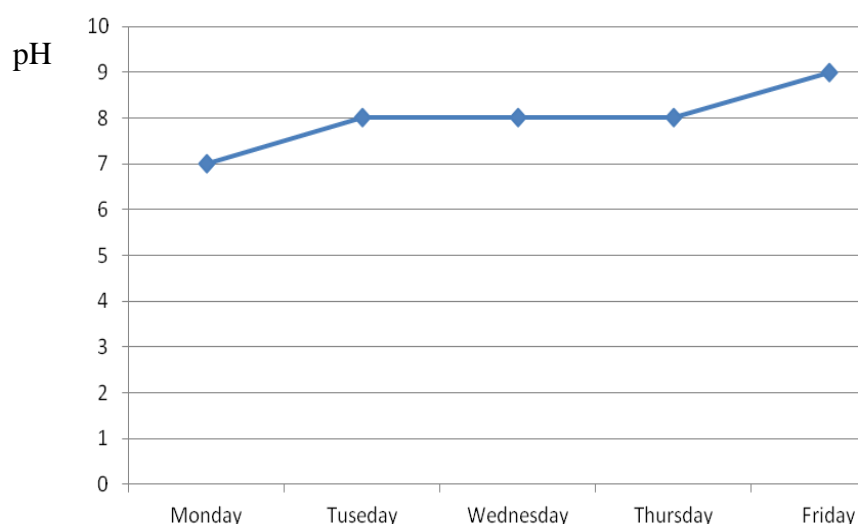


Figure 5.13: Measurement of the pH of an *SE* culture.

5.3.3.2 Effect of bacterial pH on peptide self-assembly

Before investigating the release of antibiotics from the peptide fibrils, the effect of bacterial pH on peptide fibrils before encapsulating them with antibiotics was determined. Because the pH of *SE* cultures is the external trigger that disassembles peptide fibrils, peptide gels were deposited on *SE* cultures, and the P₁₁₋₄ and P₁₁₋₈ gels were observed after overnight incubation.

Figures 5.14, 5.15 and 5.16 show the effects of bacterial pH on the self-assembly of solutions of 30, 20 and 10 mg/ml P₁₁₋₄, respectively. The figures compare plates containing peptide gels deposited on plates with and without bacteria. The figures show that all P₁₁₋₄ gels were completely dissolved, indicating that P₁₁₋₄ gels were triggered by the bacterial pH and that the β -sheet structure of fibrils disassembled into monomers.

Figures from 5.17 to 5.19 show the effect of bacterial pH on P₁₁₋₈ gels at concentrations 30, 20, 10 mg/ml. It is clear from the images that part of P₁₁₋₈ remained gel in the middle of the deposited area of the gel and part was dissolved in the surrounding edge, suggesting that P₁₁₋₈ was partially disassembled by bacterial pH.

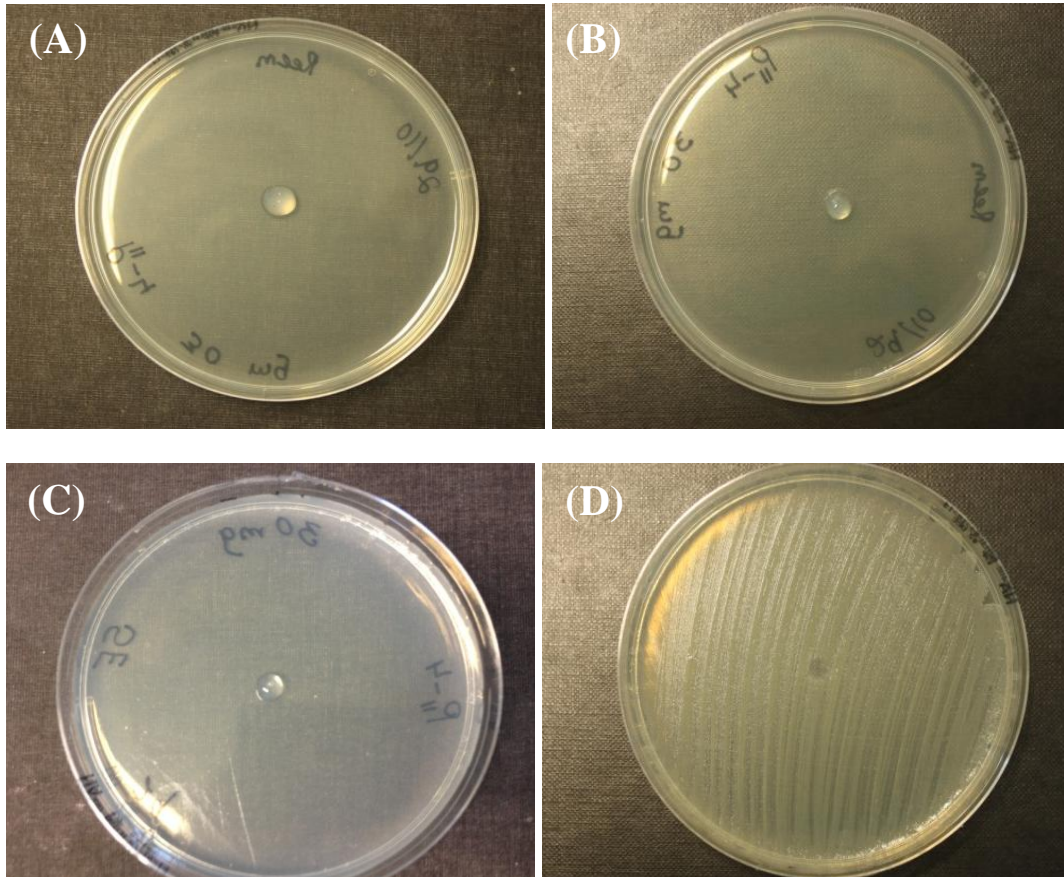


Figure 5.14: Effect of bacteria on the 30 mg/ml P₁₁-4gel. (A) Blank agar immediately after applying the P₁₁-4 gel, (B) blank agar one day after applying the P₁₁-4 gel, (C) agar with the SE culture immediately after applying the P₁₁-4 gel, (D) agar with the P₁₁-4 and SE culture after one day.

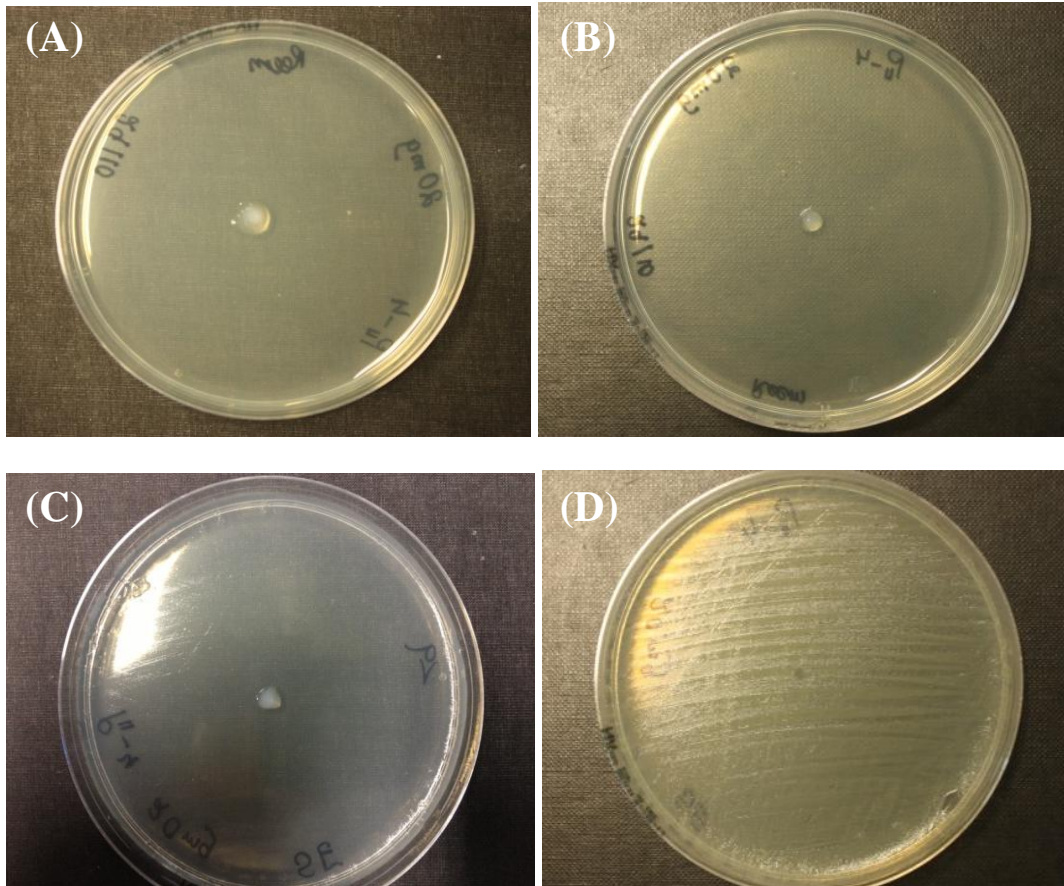


Figure 5.15: Effect of bacteria on the 20 mg/ml the P₁₁-4 gel. (A) Blank agar immediately after applying the P₁₁-4 gel on agar, (B) blank agar one day after applying the P₁₁-4 gel, (C) agar with the SE culture immediately after applying the P₁₁-4 gel, (D) agar with the P₁₁-4 gel with the SE culture after one day

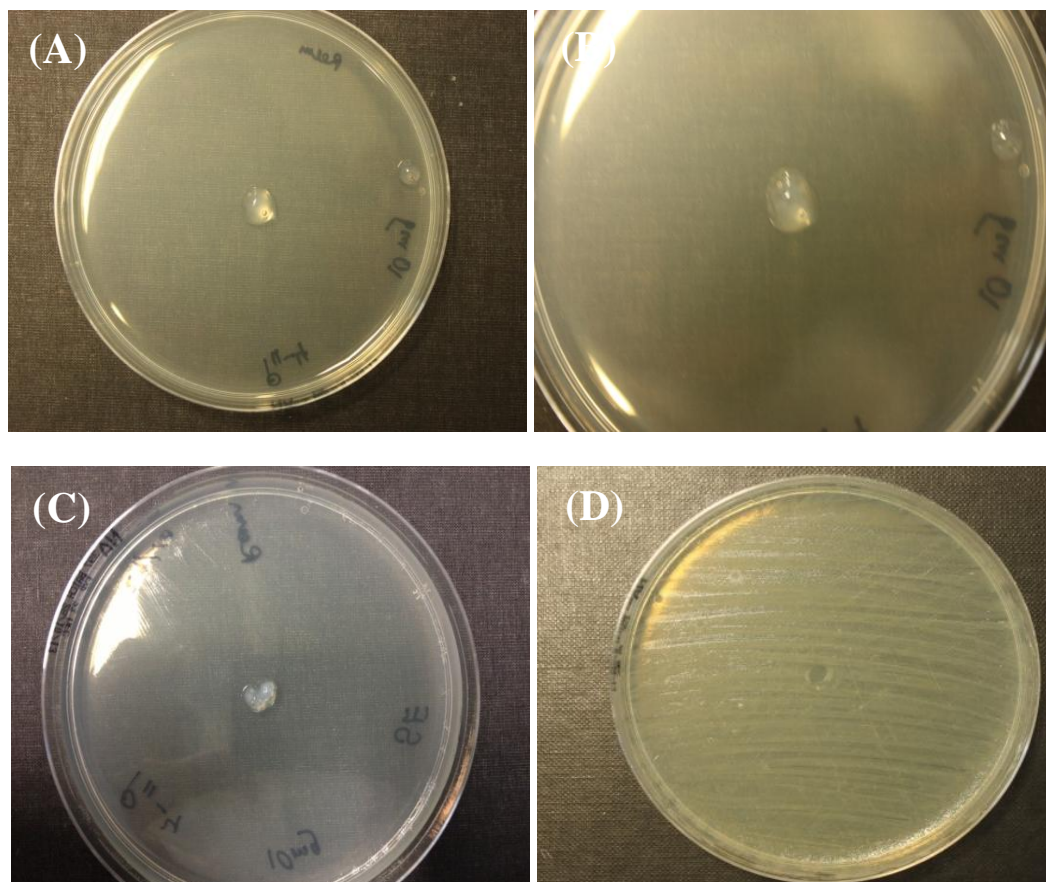


Figure 5.16: The effect of bacteria on the 10 mg/ml P₁₁₋₄ gel. (A) Blank agar immediately after applying the P₁₁₋₄ gel, (B) blank agar with the P₁₁₋₄ gel after one day, (C) agar with the *SE* culture immediately after applying the P₁₁₋₄ gel, (D) agar with the P₁₁₋₄ gel and the *SE* culture after one day.

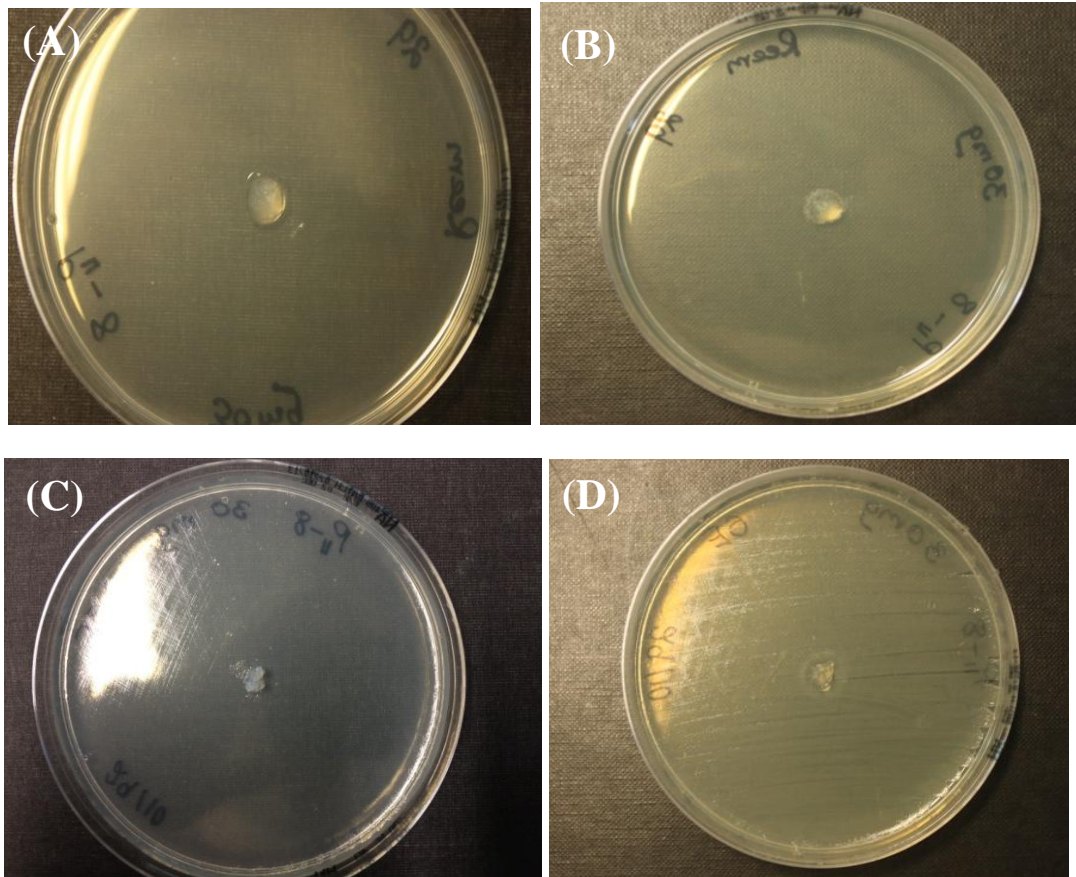


Figure 5.17: Effect of bacteria on the 30 mg/ml P₁₁-8 gel. (A) Blank agar immediately after applying the P₁₁-8 gel, (B) blank agar with the P₁₁-8 gel after one day, (C) agar with the *SE* culture immediately after applying the P₁₁-8 gel, (D) agar with the *SE* culture and the P₁₁-4 gel after one day.

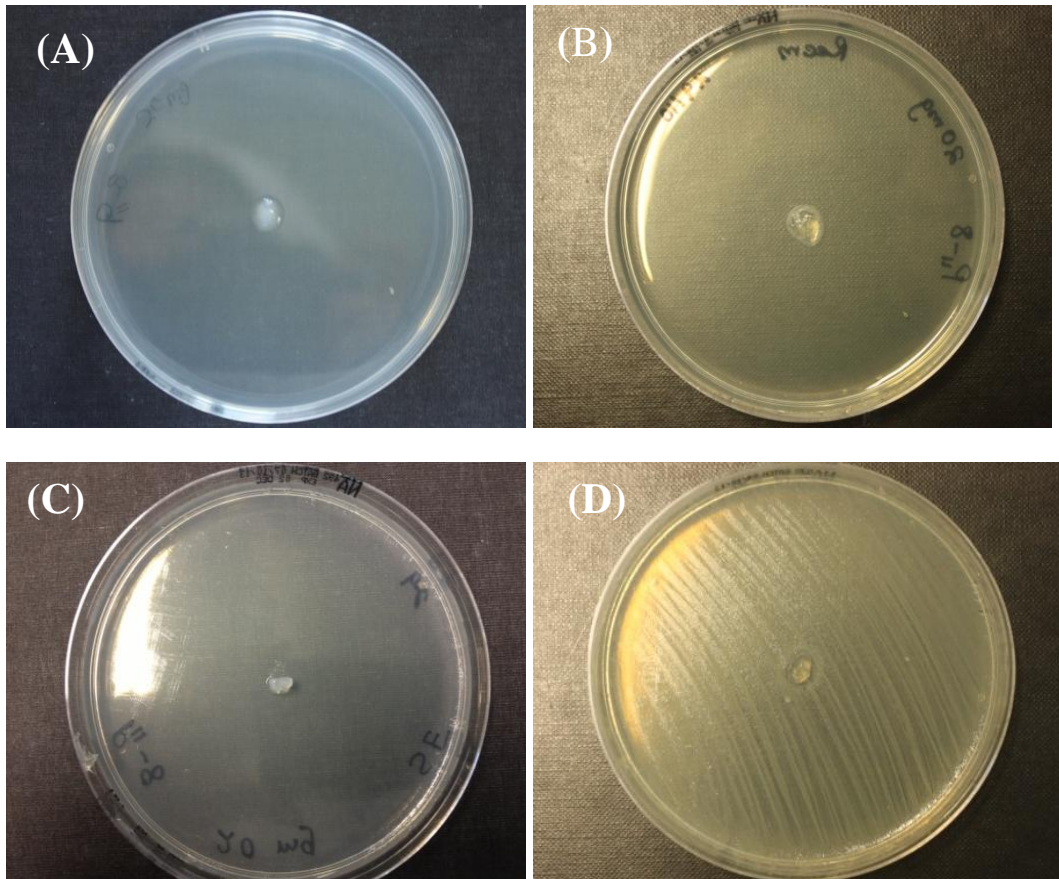


Figure 5.18: Effect of bacteria on the 20 mg/ml P₁₁-8 gel at (A) blank agar immediately after applying the P₁₁-8 gel, (B) blank agar with the P₁₁-8 gel after one day, (C) agar with the *SE* culture immediately after applying the P₁₁-8 gel, (D) agar with the *SE* culture with the P₁₁-8 gel after one day.

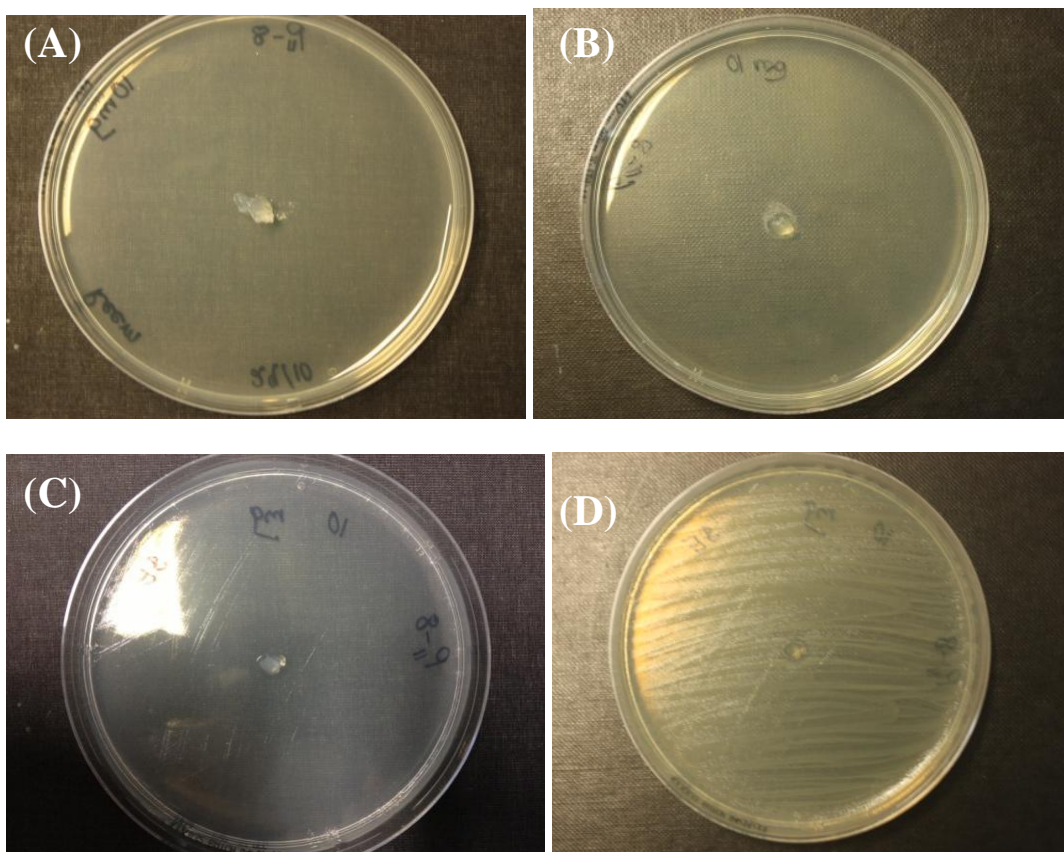


Figure 5.19: Effect of bacteria on the 10 mg/ml P₁₁₋₈ gel. (A) Blank agar immediately after applying the P₁₁₋₈ gel, (B) blank agar with the P₁₁₋₈ gel after one day, (C) agar with the *SE* culture immediately after applying the P₁₁₋₈ gel, (D) agar with the *SE* culture and P₁₁₋₈ gel after one day.

5.3.3.3 Drug release study

The Kirby–Bauer (KB) antibiotic test or disk diffusion test is commonly used to test bacterial susceptibility to antibiotics, which is indicated by a clear zone of growth inhibition surrounding an antibiotic disk. The diameter (mm) of the zone of inhibition indicates the degree of susceptibility. The bigger the diameter of the inhibition zone, the more susceptible is the microorganism to the antimicrobial agent [149].

The KB test was applied here to assess drug release and determine the pH-responsiveness of the modified coated dressing. The test was performed by applying an approximately 10^8 CFU/ml to the surface of a Mueller–Hinton agar plate. Coated dressings with a diameter of 0.5 cm were placed on the inoculated agar surface. Before investigating the zone of inhibition surrounding the dressings coated with the fibril/antibiotic complex, the zone of inhibition was measured around dressings coated with the fibrils only. Samples without antibiotics did not generate zones of inhibition, indicating that the growth of *SE* was not susceptible to the peptide fibrils (Figure 5.20).

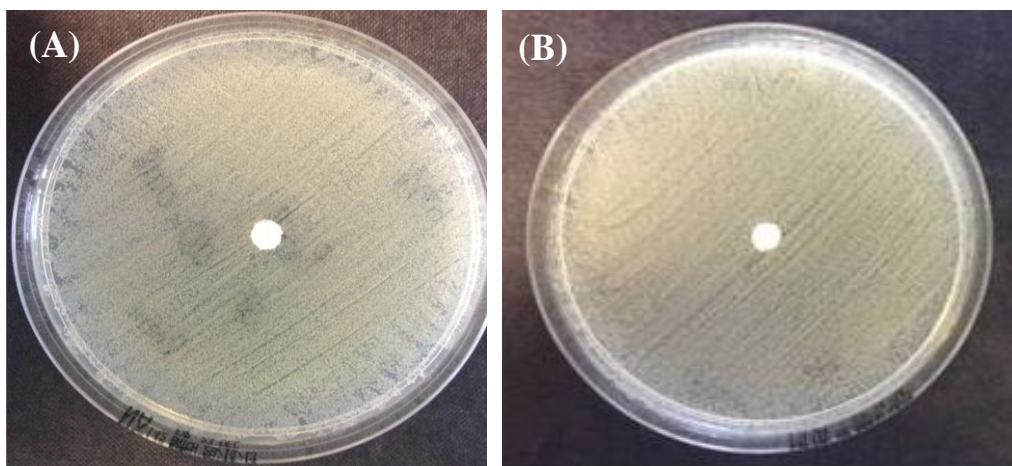


Figure 5.20: Disk diffusion test of control samples. (A) Control P₁₁-4, (B) Control P₁₁-8.

5.3.3.4.1 Vancomycin release

Figures 5.21–5.23 show P₁₁-8 and P₁₁-4-encapsulated vancomycin. The antibiotics were used at high MICs (16, 32 and 64 μg) to produce clearly visible zones of inhibition. The results demonstrated that both encapsulated antibiotics were effective. However, antibiotics encapsulated by P₁₁-4 showed greater activity compared with antibiotics encapsulated by P₁₁-8. Compared with controls, P₁₁-4-encapsulated vancomycin produced very slight decrease of the zone of inhibition, indicating that the majority of the drug molecules were released. For drugs encapsulated by P₁₁-8 fibrils, there were significant decreases in the diameters of the zones of inhibition, suggesting that antibiotics were trapped in the fibrils. There was no increase in the diameters of the zones of inhibition after 48 h. The experiments were done in triplicate, and the average of inhibition zones diameters is shown in Figure 5.24.

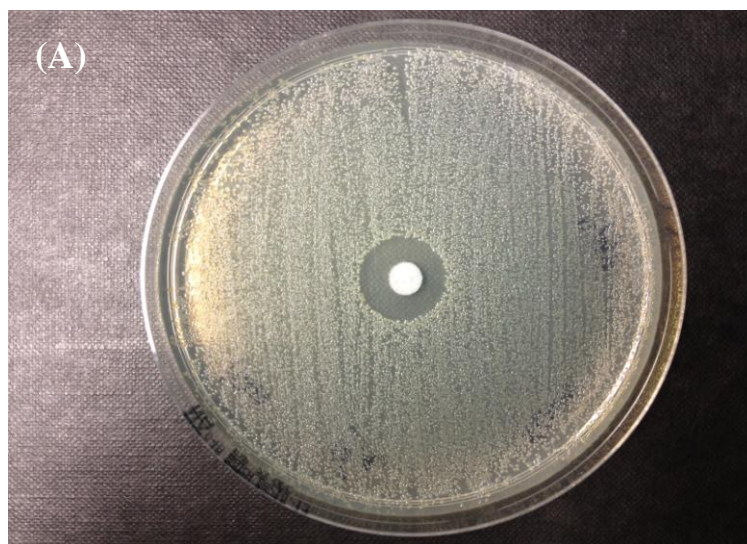


Figure 5.21: Disk diffusion test of vancomycin (16 $\mu\text{g/ml}$) released from peptide fibrils. (A) Fabric containing vancomycin, (B) fabric containing P₁₁-4-encapsulated vancomycin, (C) fabric containing P₁₁-8-encapsulated vancomycin

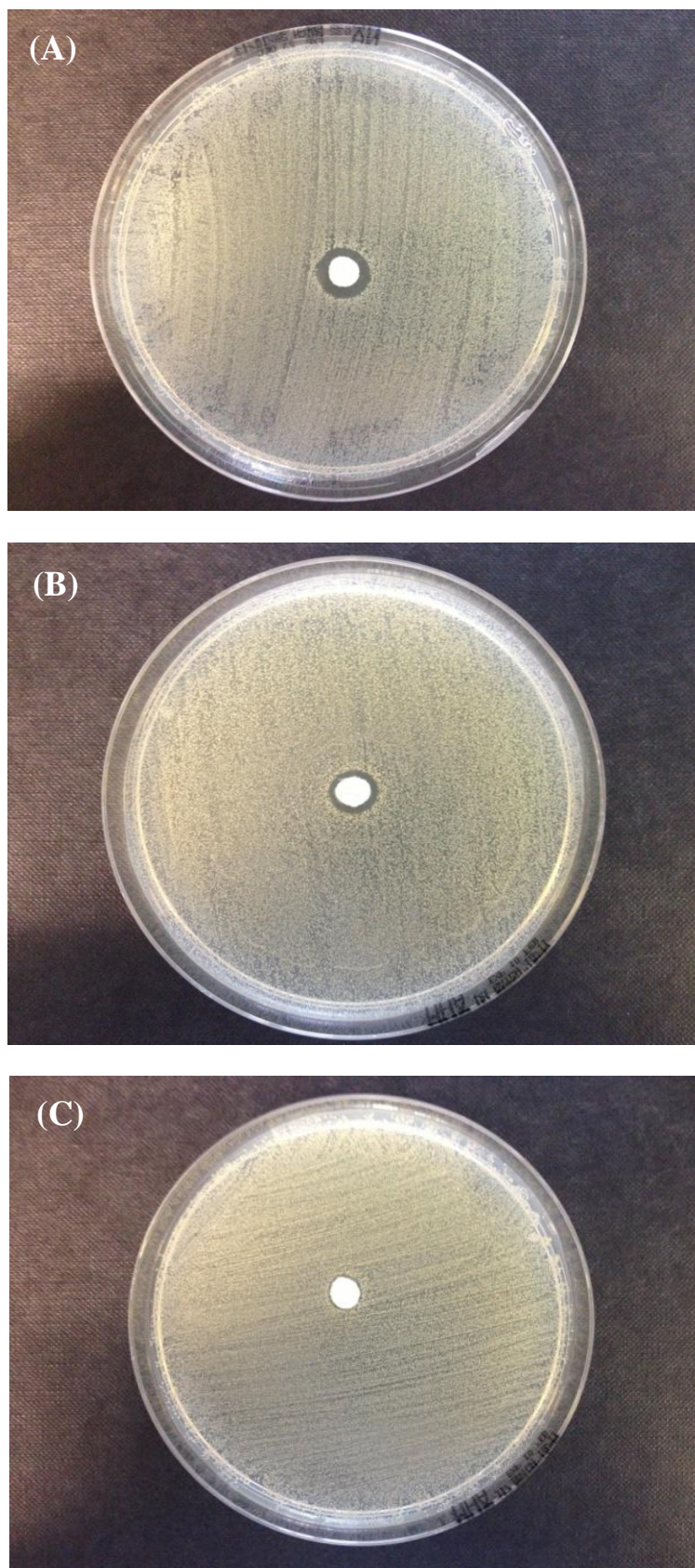


Figure 5.22: Disk diffusion test of the release of vancomycin (32 $\mu\text{g/ml}$) from peptide fibrils. (A) Fabric containing vancomycin, (B) fabric containing P_{11-4} -encapsulated vancomycin, (C) fabric containing P_{11-8} -encapsulated vancomycin.

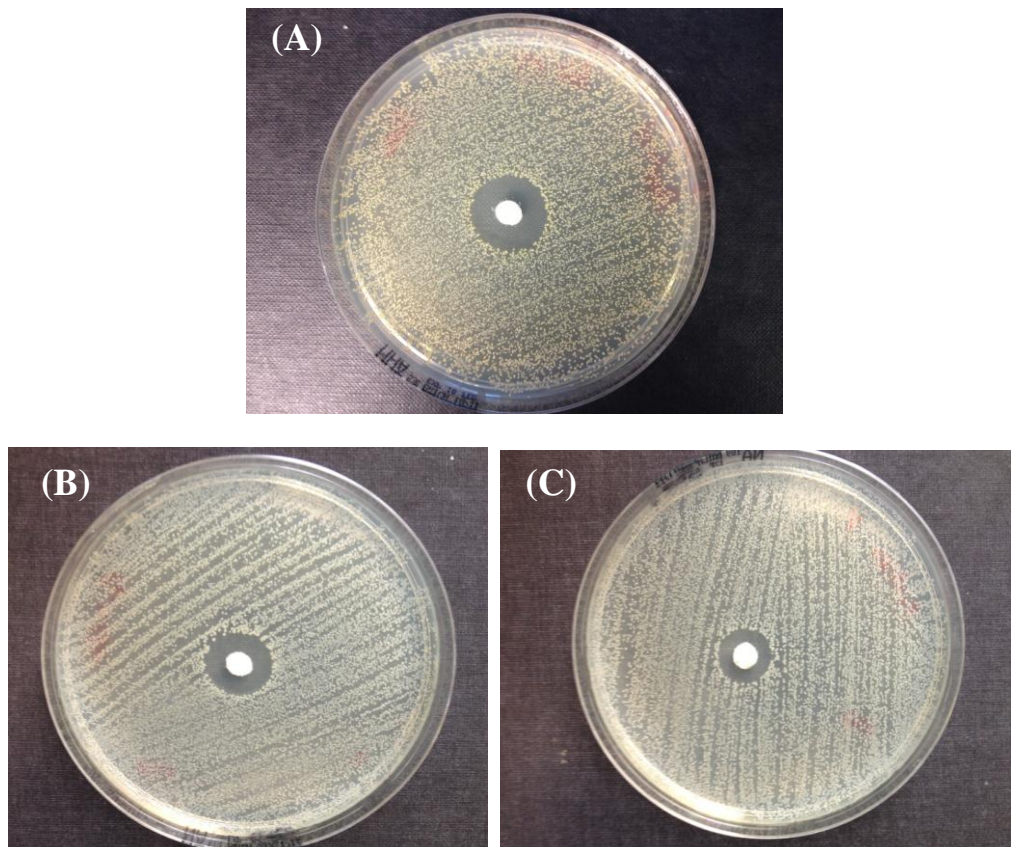


Figure 5.23: Disk diffusion test of the release of vancomycin (64 µg/ml) from peptide fibrils. (A) Fabric containing vancomycin, (B) fabric containing P₁₁₋₄-encapsulated vancomycin, (C) fabric containing P₁₁₋₈-encapsulated vancomycin.

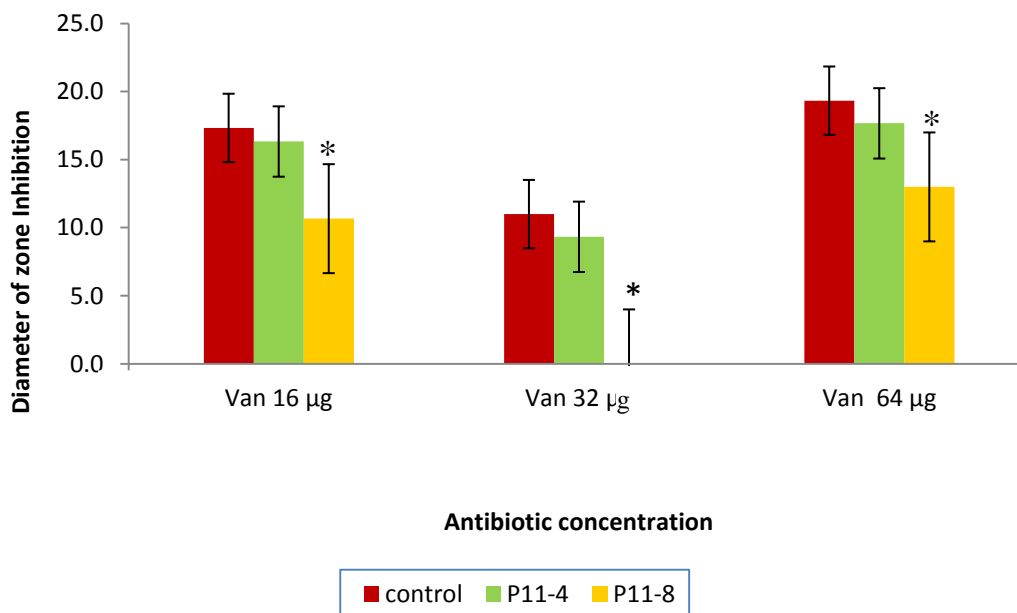


Figure 5.24: Average of inhibition zones diameters in the disk diffusion assay of vancomycin. Data is expressed as the mean (n=3) ± 95% confidence intervals. Data was analysed by one way ANOVA followed by calculation of the minimum significant difference by the post-hoc T test (p < 0.05). * = significant difference compared to the control sample.

5.3.3.4.1 Levofloxacin release

The results for dressing coated with encapsulated levofloxacin were similar to those described above for vancomycin. The diameter of the zone of inhibition in the presence of levofloxacin-encapsulated within P₁₁-4 was larger than that of P₁₁-8, indicating that *SE* is more susceptible to P₁₁-4-encapsulated levofloxacin than those encapsulated within P₁₁-8. There was no significant difference in the results after 48 h (Figures 25-27). Again, the experiments were done in triplicate, and the average of inhibition zones diameters is shown in Figure 5.28.

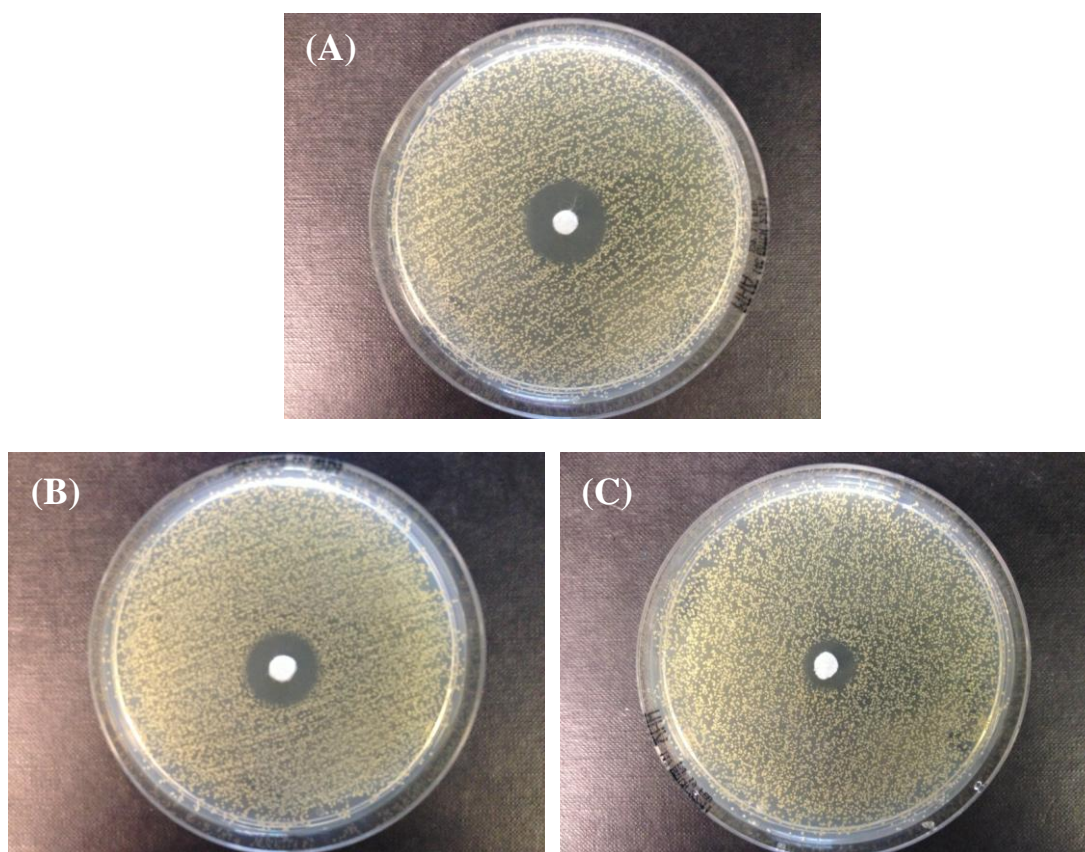


Figure 5.25: Disk diffusion test for the release of levofloxacin (16 µg/ml) from peptide fibrils. (A) Fabric containing levofloxacin, (B) fabric containing levofloxacin encapsulated into P₁₁-4, (C) fabric containing levofloxacin encapsulated into P₁₁-8

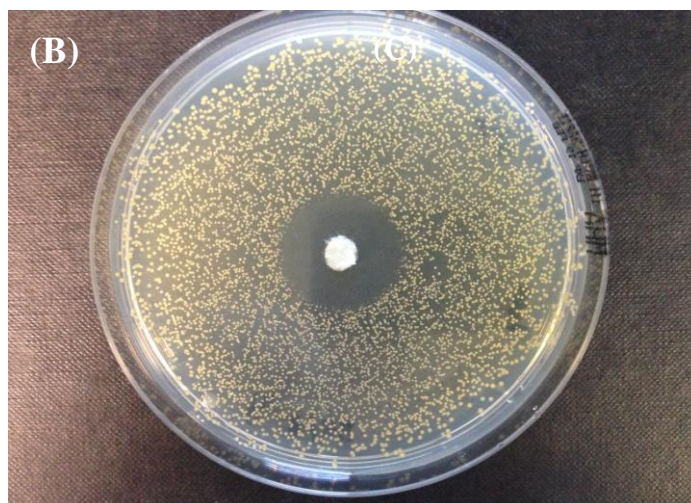


Figure 5.26: Disk diffusion assay of the release of levofloxacin (32 $\mu\text{g/ml}$) from peptide fibrils. (A) Fabric containing levofloxacin, (B) fabric containing levofloxacin encapsulated into P₁₁-4, (C) fabric containing levofloxacin encapsulated into P₁₁-8.

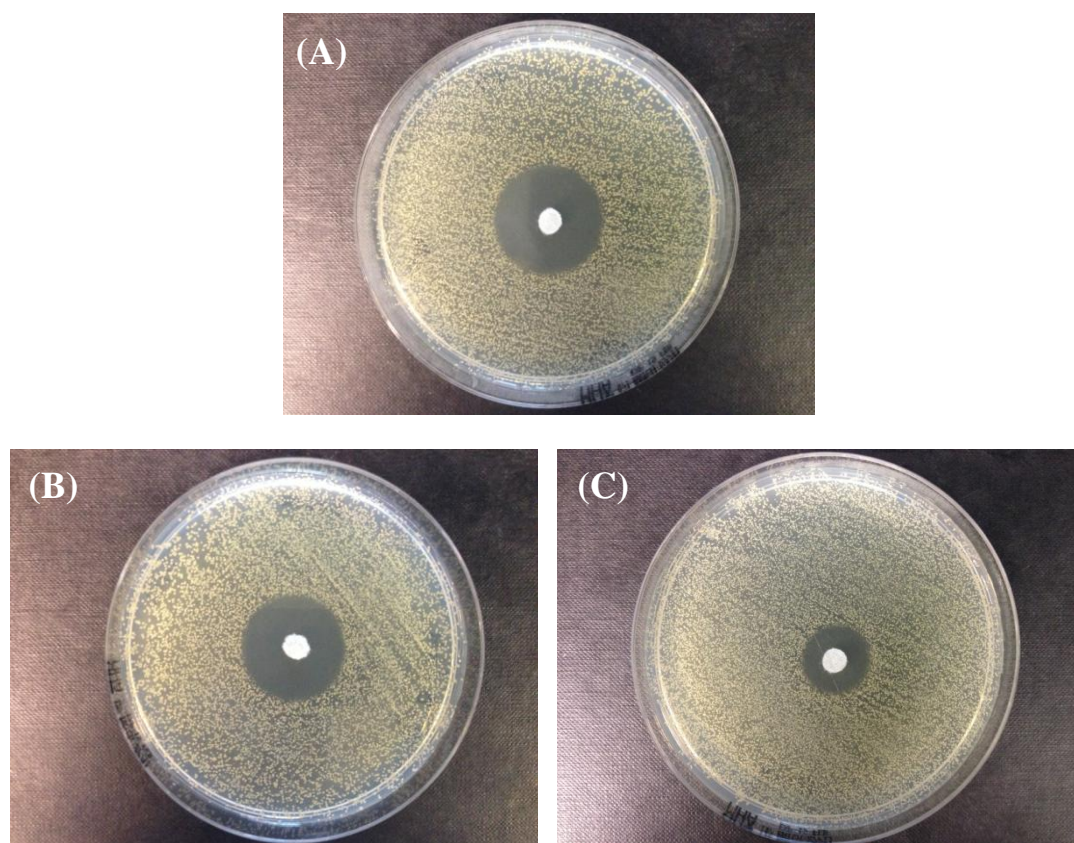


Figure 5.27: Disc diffusion assay of the release of levofloxacin (64 mg/ml) from peptide fibrils. (A) Fabric containing levofloxacin, (B) fabric containing levofloxacin encapsulated into P₁₁₋₄, (C) fabric containing levofloxacin encapsulated into P₁₁₋₈.

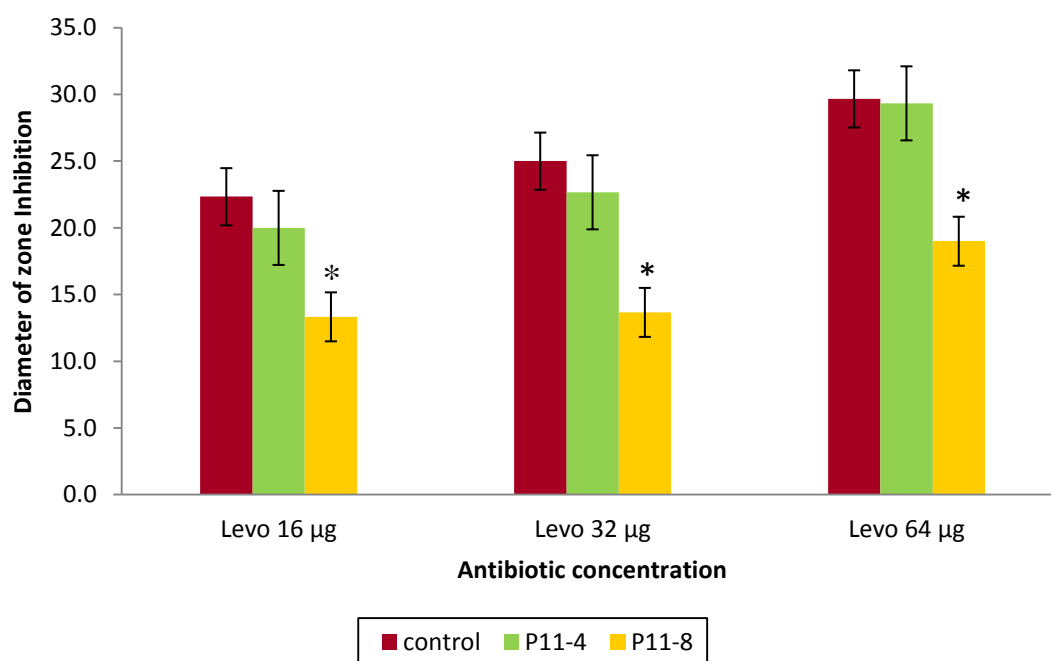


Figure 5.28: Average of inhibition zones diameters in the disk diffusion assay of levofloxacin. Data is expressed as the mean (n=3) ± 95% confidence intervals. Data was analysed by one way ANOVA followed by calculation of the minimum significant difference by the post-hoc T test ($p < 0.05$). * = significant difference compared to the control sample.

5.4 Discussion

The purpose of this study was to evaluate the effectiveness of antibiotics incorporated into peptide fibrils. The modified coated dressings containing antibiotics were characterized using SEM, TEM, CLSM and FTIR. Inhibition of bacterial growth by the dressings was analysed using agar diffusion methods. In these assays, a clear zone surrounding the antibiotic-impregnated material indicates inhibition of bacterial growth.

TEM analyses demonstrated that the addition of vancomycin or levofloxacin did not alter the morphology of peptide fibrils likely because the concentrations of antibiotics are low, while peptides concentrations were in vast excess. Therefore, when the peptide monomers were stimulated to aggregate in the presence of the antibiotics, they were encapsulated into the peptide gel. The analyses using visible-light microscopy, SEM and CLSM presented in the previous chapter show that the appearance of the peptide coatings was unchanged in the presence of antibiotics, indicating that the antibiotics did not alter the affinity of peptide for cellulosic fabrics.

SE was selected for this study because it is present in the common microflora of human skin. If the skin is injured, the wound is vulnerable to infection with *SE* [150]. The *SE* strain used in this study was identified by Gram staining method. Gram staining is a method used to differentiate bacteria into two groups, Gram-negative and gram-positive. Gram positive bacteria are characterised with violet stain, while gram negative bacteria are characterised with pink stain. The reason of Gram-staining bacteria is that some bacterial culture may become contaminated during preparation. Therefore, it was necessary to ensure that they were the pure culture prior using. Here in, the Gram-stain results, cell morphology and colony shape and colour were sufficient to conclude that the *SE* colonies were pure.

After verifying the purity of the *SE* isolate, the pH of the culture was measured for five days using pH indicator strips because pH of the *SE* culture provides the external trigger that disaggregates the peptide gel. Subsequently, the effect of pH on peptide self-assembly was investigated. The P₁₁₋₄ gels that were formed at 10, 20 and 30 mg/ml were completely dissolved. P₁₁₋₄ is monomeric in solution at alkaline pH. It forms a self-supporting gel at $\text{pH} \leq 3$ and flocculates at $\text{pH} > 3$ due to the charged peptides. When the pH is further increased, glutamic acid residues are increasingly deprotonated, and the β -sheet is converted to monomers due to the net negative charge of the peptide.

At pH 8–9, P₁₁₋₄ fibrils are completely converted to monomers (Figure 5.29). Therefore, P₁₁₋₄ gels were completely dissolved at the alkaline pH of *SE*. The gels formed by P₁₁₋₈ at concentrations of 10, 20 and 30 mg/ml were partially converted to monomeric liquids because P₁₁₋₈ at $6 < \text{pH} < 10.3$ forms a biphasic solution containing gel particles and clear fluid (Figure 5.30). The biphasic solution of P₁₁₋₈ is clearly shown in a vial in Appendix C.

After determining the responsiveness of the peptide fibrils to *SE*, the fibrils were applied as antibiotic carriers to coat the cellulosic dressing, and their release of antibiotics was determined using a disk diffusion assay. Overall, the inhibition zone diameters resulted in significant differences between antibiotics loaded into P₁₁₋₄ and those loaded into P₁₁₋₈. Larger zones of inhibition were observed with the samples treated by P₁₁₋₄/drugs. P₁₁₋₄/antibiotics shows zone inhibition diameters relatively similar to the control samples with very slight decrease. As indicated above, P₁₁₋₄ is completely monomer in alkaline pH. As a result, the majority of antibiotic molecules were released from the dressings. On the other hand, in the case of P₁₁₋₈/antibiotics, the zone inhibition diameters were clearly smaller than P₁₁₋₄/antibiotics. The reason was that P₁₁₋₈ is biphasic solution at the alkaline pH of *SE*. Thereby, molecules were released from the liquid phase and other molecules were entrapped within the gel phase. As the drug molecules were released from the fibrils that indicate that the interaction between the fibrils and the drug molecules is non-covalent interaction. The release schematic is described in Figures 5.31 and 5.32.

It is important to notice in this investigation that the effectiveness of vancomycin at the concentration of 32 μg were dropped (comparing to 16, and 64 μg) against *SE* either with the addition of peptides to vancomycin or not. The test were repeated to make sure this finding was not due to some faults in the experiment, but it comes up with the same result. There is no clear and definite explanation, however, some researches, suggested that, staphylococci could be developed some kind of resistant against vancomycin at concentration of 32 μg [151, 152].

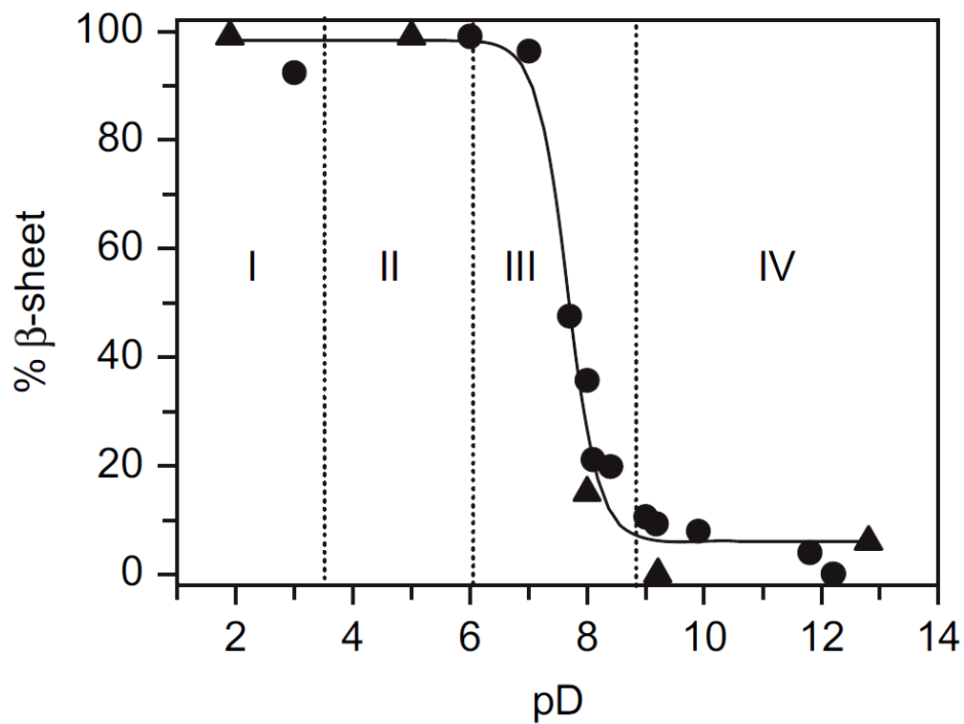


Figure 5.29: β -Sheet percentage of P_{11-4} • as determined by FTIR and \blacktriangle by NMR. I: nematic gel, II: flocculate, III: nematic fluid, IV: isotropic fluid [86].

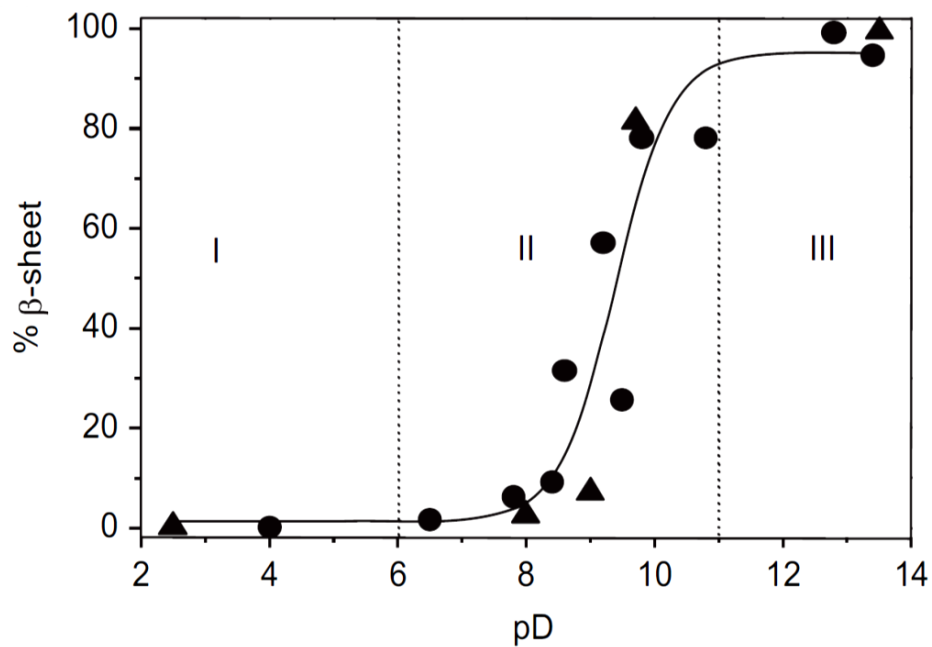


Figure 5.30: β -Sheet percentage of P_{11-8} • as determined by FTIR and \blacktriangle by NMR. I: isotropic fluid, II: biphasic solution, III: nematic gel [86].

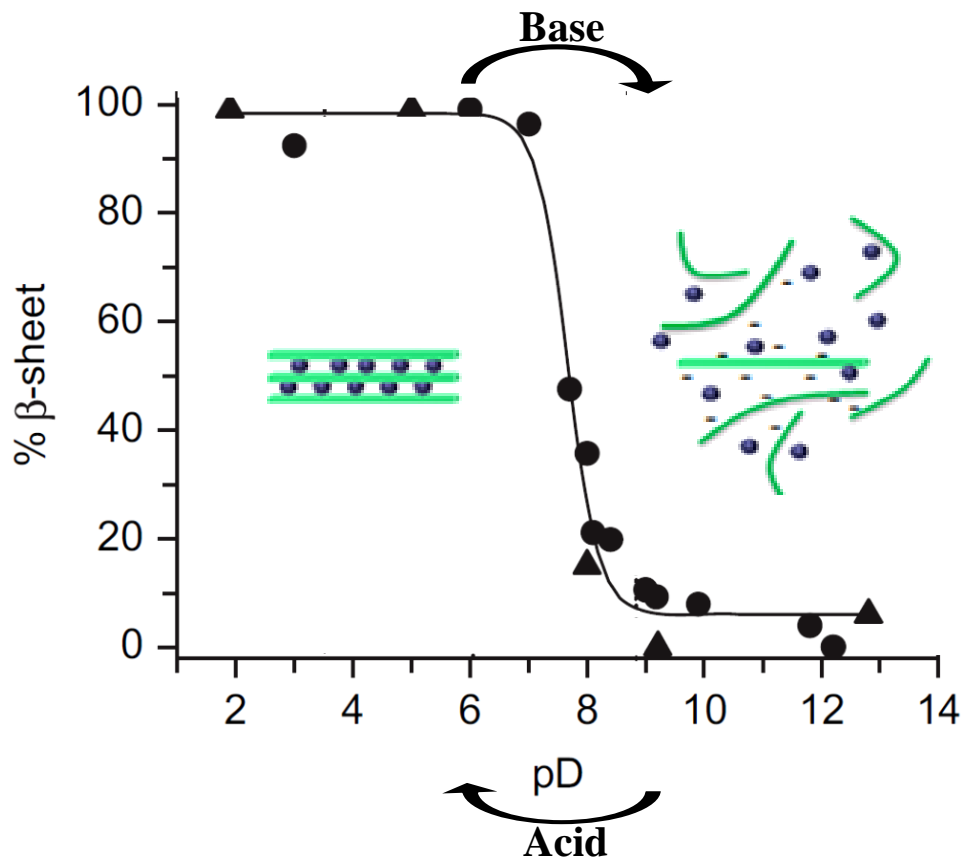


Figure 5.31: The hypothesis of the therapeutic release from P₁₁₋₄ fibrils. Green is peptide, blue is antibiotic.

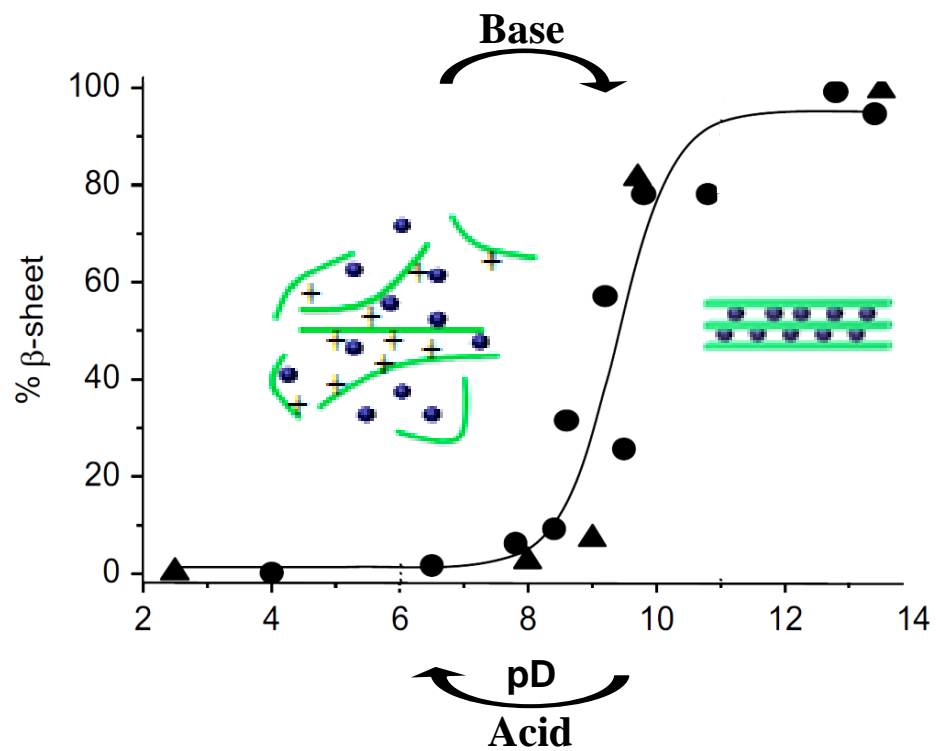


Figure 5.32: The hypothesis of the therapeutic release from P₁₁₋₈ fibrils. Green is peptide, blue is antibiotic.

5.5 Conclusions

pH-sensitive dressing were prepared by impregnating fabrics in peptide solutions, P₁₁-8 and P₁₁-4 solutions separately, containing antibiotics. The feasibility of coating fabrics with peptides/antibiotics complex was investigated with complementary microscopic and spectroscopic techniques. The effectiveness of the dressings were *in vitro* investigated by testing the dressings against *Staphylococcus epidermis*. The results showed that the dressings were stimulated by the pH of the bacteria and released the loaded drugs. However, the results also showed that the antibacterial activity of the fabrics modified with P₁₁-4 was higher compared with those modified with P₁₁-8.

Chapter 6

6 Fabrication and characterization of polycaprolactone peptide-enriched fabrics

6.1 Introduction

In chapter 4, self-assembled peptides were applied to coat the outer surface of the fabrics to serve as drug carriers for wound care applications. In this chapter, the electrospinning technique was applied to incorporate self-assembled peptides within the texture of the fabrics for biomedical applications.

6.1.1 Introduction to electrospinning

Electrospun nanofibers are increasingly being used in a broad range of applications. They are defined as ultra-fine elongated thread-like solid fibres with very small diameters having average diameters ranging from 100 nm to 5 μm [153]. Electrospinning is one of the most promising techniques to fabricate nanofibers. The fundamental theory of electrospinning goes back to 80 years when Formhals produced fibres from a polymer solution using an electrostatic force. In early 1900s, Renker and co-workers have revived the interest in this technology and popularised the name of electrospinning. Between 1934 to 1944, he published a number of patents describing the experimental setup of electrospinning [154]. They have demonstrated the possibility to fabricate nanofibres from a wide range of organic polymers [155]. Recently, within the past 10 years, attention to the electrospinning technique has increased dramatically due to the increased interest in nanoscale properties [156]. The number of Publications on this promising technique is rocketing as shown in Figure 6.1.

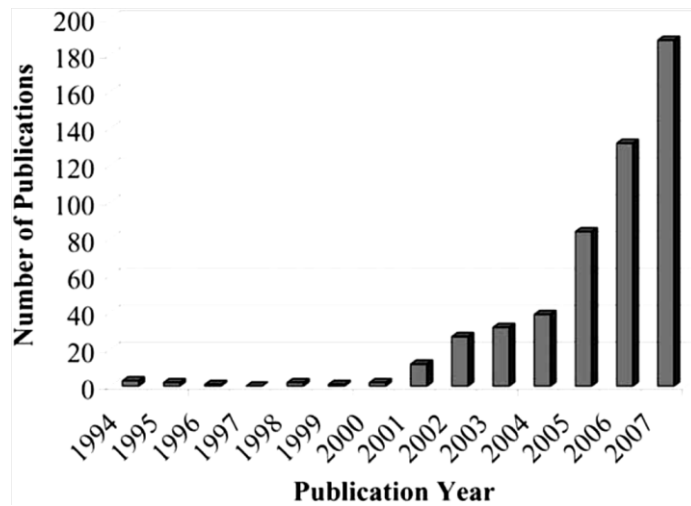


Figure 6.1: Publications on electrospinning [157].

The electrospinning setup simply consists of a syringe pump fed with polymer solution, a high voltage source, and a collector (Figure 6.2). The syringe is connected towards the collector. The syringe is filled with polymer solution. An electrical charge is induced to the polymer solution by high electrical field. When the induced electrical force overcomes the solution surface tension force, a charged jet of the solution is travels to the collector [158]. Before collecting, the solvent jet is stretched and the solvent is evaporated forming solid nanofibres in the collector [159].

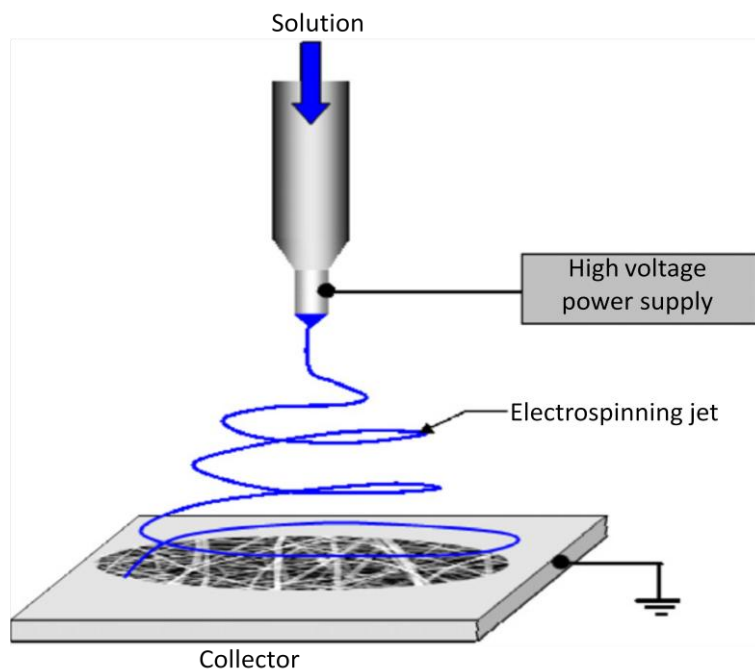


Figure 6.2: Electrospinning equipment [160].

Electrospun fibres exhibit outstanding functional quality. They have large surface area per unit mass, small pore size, high length/diameter ratio, flexible surface with superior mechanical performance, and tuneable surface morphology [161]. It is a cheap process and the most straightforward way to produce nanofibres [162]. They are excellent materials for a variety of applications including reinforced fibres, support for enzymes, fuel cells, photonic sensors, medicine, pharmacy, filtration, tissue engendering, catalyst support, drug delivery system and wound dressings [162].

In the field of drug delivery systems, recent experiments have successfully proved that certain drugs can be incorporated and released from electrospun nanofibres such as antibiotics and anticancer agents [163]. The large surface/volume ratio allows antibacterial drugs to be retained within the structure. The first work using electrospun fibres as drug carriers was reported by Kenawy *et al.* They fabricated fibres from poly (lactic acid) (PLA), poly (ethylene-co-vinyl acetate) (PEVA) and 50/50 PLA/ PEVA blend. The fibres encapsulated tetracycline hydrochloride as a drug model. The release profile of the fibres was compared with commercially available Actisite[®] (Alza Corporation, Palo Alto, CA). The results suggest that encapsulated electrospun matrices may significantly impact on the drug controlled release technology [164].

Bolgen *et al.* examined the potential function of antibiotic embedded electrospun polycaprolactone PCL to prevent abdominal adhesions after abdominal surgeries. Usually, after abdominal surgeries, adhesions developed in the peritoneal cavity as pathological fibrotic bands at the surgery site. The risk of adhesions development can be increased by certain bacteria. For this investigation, Bolgen *et al.* have made defects in the peritoneum abdominal walls in a rat model. They embedded the commercial antibiotic (Biteral[®]) into an electrospun PCL membrane (Figure 6.3). They slowly dropped the drug solution to be absorbed by the electrospun nonwoven membrane sample, and they fixed it in the rat abdominal wall to cover the injured site. The authors found that the abdominal adhesions were reduced and the healing process was accelerated [165].

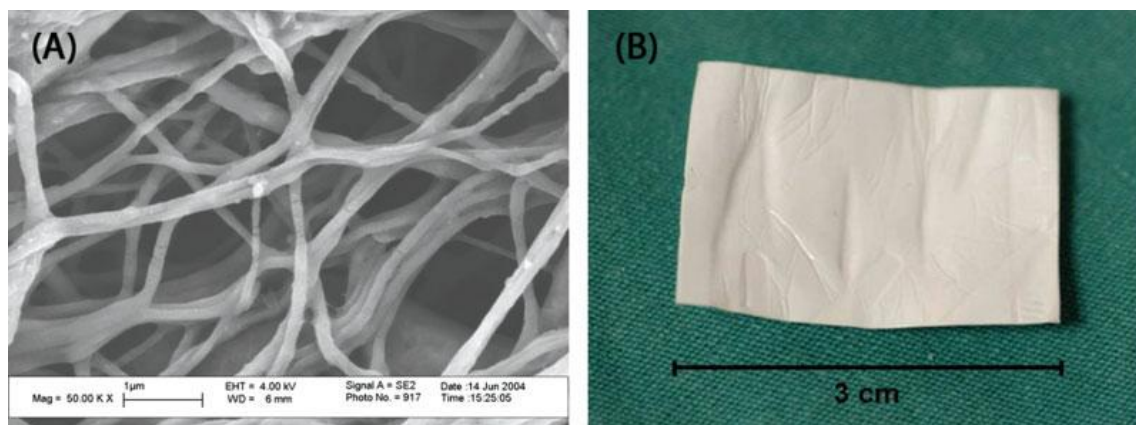


Figure 6.3: An electrospun PCL membrane made by Bolgen *et al.* A) SEM micrograph. B) an optical micrograph [165].

Kim *et al.* examined electrospun PLGA and PLGA/PEG-b-PLA/PLA mats embedded with the hydrophilic antibiotic (Mefoxin[®]). The loading process was different than the method used by Bolgen *et al.* They dissolved the antibiotic and the polymers before electrospinning. The authors examined the morphology of the loaded fibre with unloaded one. They found that the drug affected the morphology of the electrospun fibre. They observed that the sample without drug has a bead-and-string morphology, while the sample with 5 wt% has a fibrous structure. By using NMR and UV-vis, they have found that the structure of the drug was not affected by the electrospinning process, indicating that the antibiotic retained its bioactivity. They demonstrated that PLGA and PLGA/PEG-b-PLA/PLA mats containing 5 wt% antibiotics inhibited greater than 90% of *Staphylococcus aureus* growth. Thus, the authors concluded that antibiotic loaded electrospun mats can effectively reduce infections [166].

Xu *et al.* incorporated BCNU anticancer into electrospun PEG-PLLA (Figure 6.4). The polymer and the drug were dissolved and electrospun. They examined the effect of anticancer drug loaded electrospun fibres on the growth of rat Glioma C6 cells [167]. They observed that loaded PEG-PLLA mats with BCNU exhibited anticancer activity over a period of 72 hr, while the free BCNU began to lose its activity after 48 hrs [167].

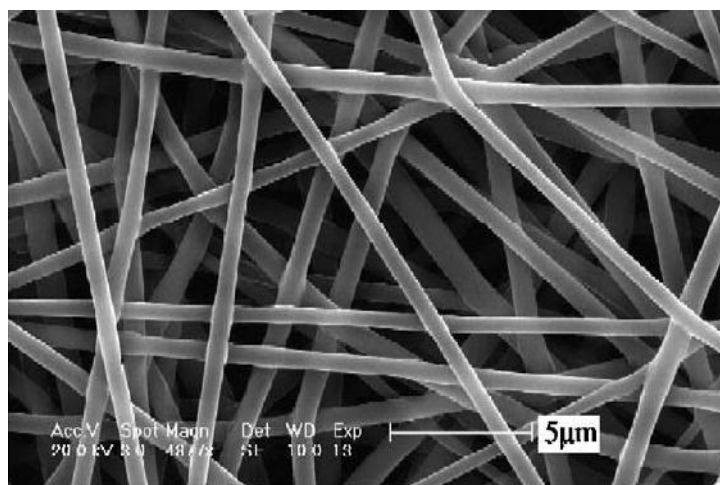


Figure 6.4: ESEM photographs of BCNU/PEG–PLLA fibres containing 10% wt of BCNU [167].

E. Luong-Van *et al.* fabricated heparin-loaded polycaprolactone fiber for the treatment of vascular injury. The fiber was successfully prepared by electrospinning and heparin remained homogenous in the spinning solution. They hypothesized that heparin release could be controlled over 14 days. The released heparin retained biological functionality, indicating that the fabricated electrospun fiber is a promising candidate for the drug delivery applications [168].

The study on electrospun-fibre for wound dressing application is still limited; however, there are a few papers published for this application. It is demonstrated that electrospun nanofibres are excellent candidates to be applied as a wound dressing. They show controlled liquid evaporation and oxygen permeability [162]. Their pore sizes are usually in the range of 500 to 1000 nm which is small enough to prevent bacteria from penetration. Large surface area of to volume ration of electrospun fibres makes them extremely efficient for fluid absorption and dermal delivery [157]. Chong fabricated a composite wound dressing from a semi-permeable barrier and a scaffold filter layer for the skin cells. Tegaderm polyurethane TG was electrospun and employed as a semi-permeable barrier. Then, PCL was electrospun onto the surface of the TG to form a TG-nanofibre (TG-NF) composite. TG-NF was employed as a suitable host substrate for human dermal fibroblast [157]. Another example of wound dressing was made from electrospun gelatine with superabsorbent Norsocryl XFS and bentonite. This formed dressing was applied to acute hemostasis and used to treat chronic ulcers.

The combination of self-assembled peptides and electrospun polymers has so far seen very limited numbers of applications. R. Danesin *et al.* have designed PCL fibres

containing self-assembling peptide fibres to support the adhesion and growth of h-osteoblast. They prepared five different mats: EAK/PCL, DAK/PCL, EabuK/PCL, EYK/PCL, and RGD-EAK/PCL (Figure 6.5). They added the self-assembled peptides to PCL solution before the electrospinning process. They have found using FTIR and XPS that the secondary structure of the self-assembled peptides is not affected during electrospinning. They found that the designed membranes were able to enhance h-osteoblast adhesion to maintain osteoblast [169].

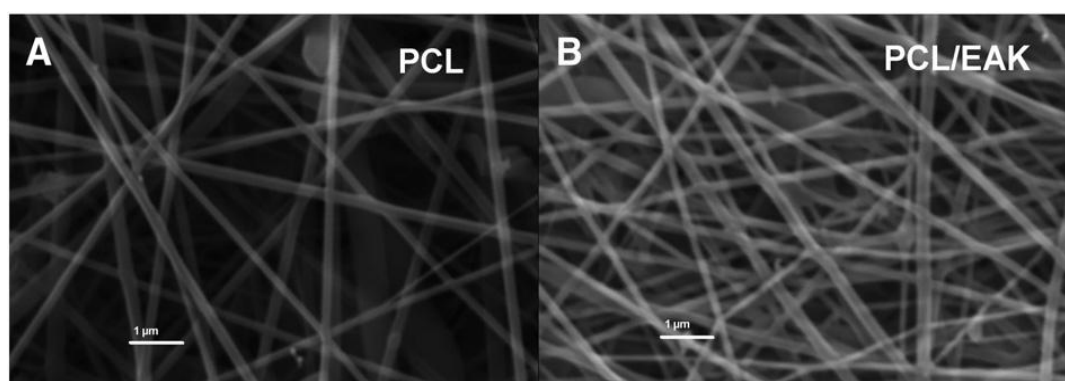


Figure 6.5: SEM images of electrospun scaffolds. (A) PCL scaffold; (B) PCL-EAK scaffold [169].

P. Brun *et al.* designed hybrid scaffolds made by electrospinning polyethylene oxide, PEO, in combination with self-assembling peptides to promote bone regeneration in bone defects. Solutions were prepared by dissolving PEO in H₂O and sodium phosphate at pH 7.4. Each self-assembling peptide (EAK, RGD-EAK, RGD-EAK_{sc}, EabuK, EYK, and DAK) were added to each solution and stirred to obtain a homogeneous mixture. The solutions were electrospun to an aluminium collector screen (Figure 6.6). The calcium assay data confirmed that the hybrid materials are more appealing to promote growth and differentiation of human osteoblasts [170].

The goal of this chapter is to combine the advantages of electrospun polycaprolactone with the advantages of self-assembled peptides using electrospinning to fabricate novel hybrid material to be used in biomedical application (Figure 6.7). PCL is FDA approved polymer [171, 172]. It is a hydrophobic, semicrystalline biodegradable polyester belongs to polyhydroxy acids family [170]. It has shown great potential in tissue engineering and drug delivery [157, 163, 173]. In tissue engineering point of view, it is an ideal material to biologically mimic extra cellular matrix (ECM) [169, 174].

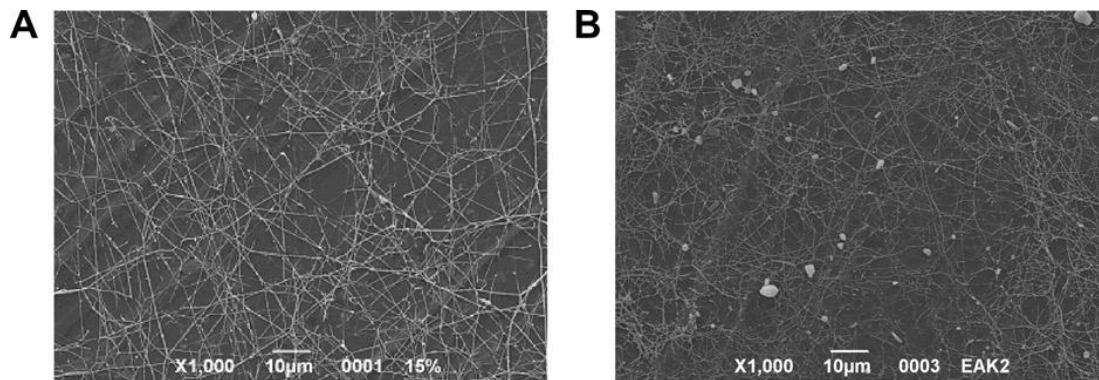


Figure 6.6: SEM images SEM images of electrospun scaffolds (A) PEO scaffold; (B) PEO with 0.059% (w/v) EAK [170].

They showed enhanced cell adhesion, migration, proliferation, cellular differentiation [169, 175]. In the field of drug delivery, due to its slow degradation rate, it is a good candidate for long-term drug delivery application [153, 176, 177]. It is widely fabricated using electrospinning technique [178]. However, electrospinning is not a simple one-step top-down process to produce fibres. The architecture of the fabricated fibers is affected by variety of parameters: 1) system parameters such as molecular weight, solution properties (viscosity, conductivity, surface tension) and 2) process parameters such as flow rate, concentration, distance between tip to collector, temperature, and applied voltage) [177, 179]. The study in this chapter is accomplished by investigating the effect of electrospinning parameter on PCL/peptide fabrics.

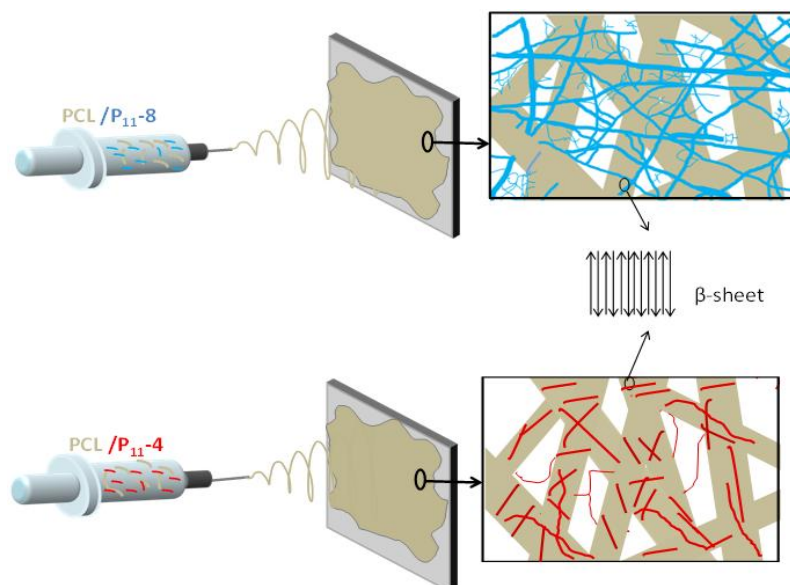


Figure 6.7: Schematic illustrates the hypothesis of the PCL/peptide fibres preparation. Gray; PCL. Blue; P₁₁-4. Red P₁₁-8.

6.2 Materials and methods

6.2.1 Materials

PCL pellets (molecular Formula $(C_6H_{10}O_2)_n$ and Molecular weight 50.000) was purchased from Sigma Aldrich.

6.2.2 Methods

6.2.2.1 Solutions for electrospinning

Solutions were prepared at a concentration of 6% w/w by dissolving 375 mg of PCL in 10 ml of HFIP. About 200 mg of each peptide were added to each solution. A control solution (6% wt/wt) of PCL in HFIP was also prepared. The solutions were then stored for 24 hours time and were ready to electrospin after obtaining a homogenous mixture.

6.2.2.2 Electrospinning process

During the electrospinning, the solution was pumped from a 5 ml syringe through a 20 gauge stainless steel nozzle (Sigma Aldrich), and connected to a dual head syringe pump (KDS-200 CE) operating at a feed rate of 1 ml/min. A copper electrode supplying the current and voltage was attached to the syringe needle at its base. Electrospinning was performed inside a fume cupboard with continuous suction to remove the floating fibres. At first step, Three different voltage values of 15, 20, and 25 kV were used at the same distance between the spinning surface and collector counter (16 cm) and normal conditions ($22 \pm 1^\circ\text{C}$, RH = 38%). In the second phase these three experiments were repeated in the same atmospheric condition with two other distances (18, and 20 cm), and finally all 9 performed experiments were repeated on the other atmospheric condition of $50 \pm 1^\circ\text{C}$, RH = 38%. In all 18 experiments, fibres were collected on an aluminium foil sheet (6 x 6 cm). The parameters settings were summarized in Table 6.1.

Table 6.1: Electrospinning parameters.

Voltage Temp Distance	$V_1= 15$ kV $T_1(\text{room temp}/ T_2 50^\circ\text{C})$	$V_2= 20$ kV $T_1(\text{room temp})/T_2 50^\circ\text{C}$	$V_3= 25$ kV $T_1 (\text{room temp})/T_2 50^\circ\text{C}$
$D_1= 16$ cm	Sample 1= $D_1V_1T_1$ Sample 2= $D_1V_1T_2$	Sample 3= $D_1V_2T_1$ Sample 4= $D_1V_2T_2$	Sample 5= $D_1V_3T_1$ Sample 6= $D_1V_3T_2$
$D_2= 18$ cm	Sample 7= $D_2V_1T_1$ Sample 8= $D_2V_1T_2$	Sample 9= $D_2V_2T_1$ Sample 10= $D_2V_2T_2$	Sample 11= $D_2V_3T_1$ Sample 12= $D_2V_3T_2$
$D_3= 20$ cm	Sample 13= $D_3V_1T_1$ Sample 14= $D_3V_1T_2$	Sample 15= $D_3V_2T_1$ Sample 16= $D_3V_2T_2$	Sample 17= $D_3V_3T_1$ Sample 18= $D_3V_3T_2$

6.3 Results

Before applying microscopy and spectroscopy to characterize the morphology and the chemical composition of the fabricated samples, the surface wettability of the fabricated 100% PCL was simply tested by depositing a drop of deionized water on the surface. See Appendix D.

6.3.1 Scanning electron microscope, SEM

SEM images of all electrospun fibers were obtained. The images indicate that there are morphological differences between samples with peptide and without peptide. In general, all fibers, with peptide and without peptide have circular cross-sectional shape. Uniform nanofibres were obtained from control PCL. Mostly, the fiber diameters were between 600 and 850 nm. The fibres of PCL/P₁₁-4 samples have diameters in the range of 350 to 750 nm. However, In the case of PCL/P₁₁-8, in each sample two ranges of diameter were observed, one has fiber diameters between 280 and 600 nm, and the other has fiber diameter range of 30 – 70 nm.

6.3.1.1 100% PCL

6.3.1.1.1 The effect of distance

Fibres that fabricated when the distance was varied from 18 to 20 cm and the applied voltage was 25 kV at room temperature are presented in Figure 6.8. Figure 6.8 (A and B) exhibit fibres were collected at distance of 18 cm. The fibres diameters are in the range of 624-898 nm. Figure 6.8 (C and D) show fibres were collected at distance of 20 cm. The fibre diameters range decreased to 450-580 nm. From this result, varying the distance between the tip and the collector significantly impacts the fibres diameters.

6.3.1.1.2 The effect of temperature

Figure 6.9 (A and B) shows samples were made at room temperature, the applied voltage was 25 kV, and were collected at a distance of 16 cm from the needle. The fibres diameters are in the range of 668-3317 nm. Figure 6.9 (C and D) presents fibres were made at 50 °C. The fibers diameters are in the range of 589-896 nm, which is smaller than the fibers made at room temperature.

6.3.1.1.3 The effect of applied voltage

To evaluate the diameters as a function of voltage, the other two parameters should be constant. The distance was 18 cm and the process was done at room temperature. Figure 6.10 (A and B) show samples were fabricated when the applied voltage was 15 kV. The fibers diameters are in the range of 576-970 nm. Figures 6.10 (C and D) shows samples were made when the applied voltage was 20 kV. The fibers' diameters are in the range of 2501-2867 nm, which is wider than the diameters of the fibers when they were made using an applied voltage of 15 kV. The measurements with the rest samples are listed in Appendix E.

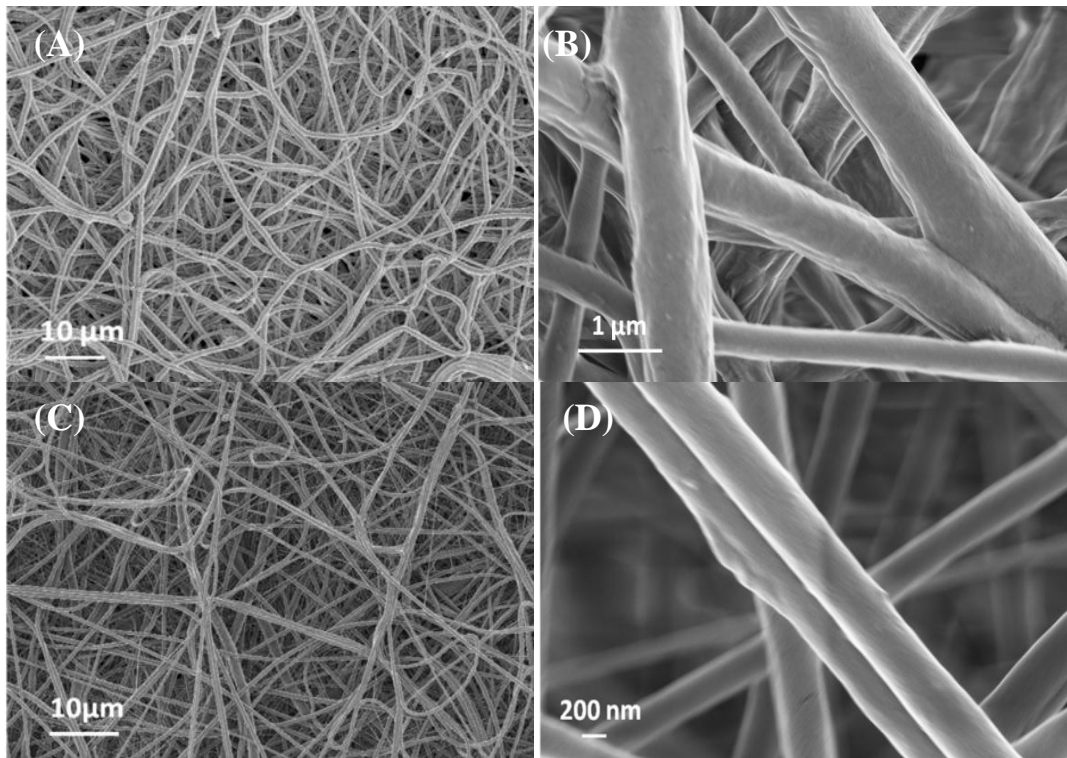


Figure 6.8: Effect of distance on 100% PCL fibre' diameters. (A) tip to collector = 18 cm; Mag 2.36 KX. (B) tip to collector =18 cm; Mag 49.14 KX. (C) tip to collector = 20 cm; Mag 2.9 KX .(D) tip to collector = 20 cm; Mag 63.63 KX (voltage= 25 kV; at room Temp).

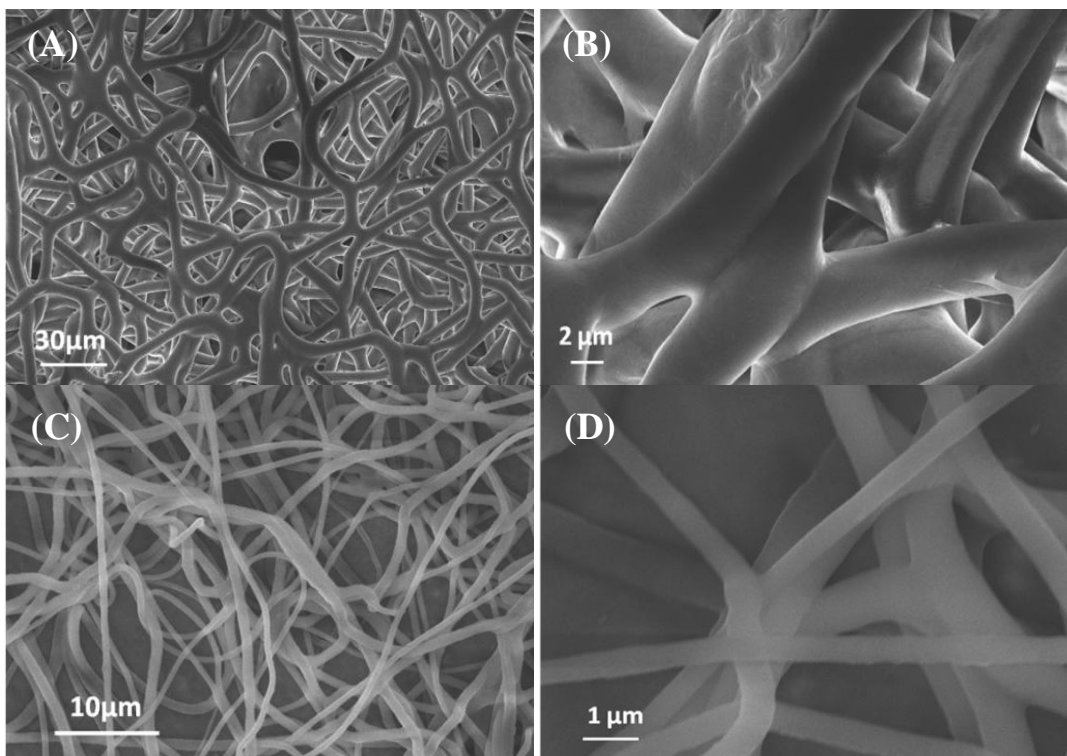


Figure 6.9: Effect of temperature on 100% PCL fibre' diameters. (A) room temp; Mag 4.5 KX. (B) room temp; Mag 27.14 KX. (C) 50 °C; Mag 3.8 KX. (D) 50 °C; Mag 83.63 KX (voltage = 25 kV; distance =16).

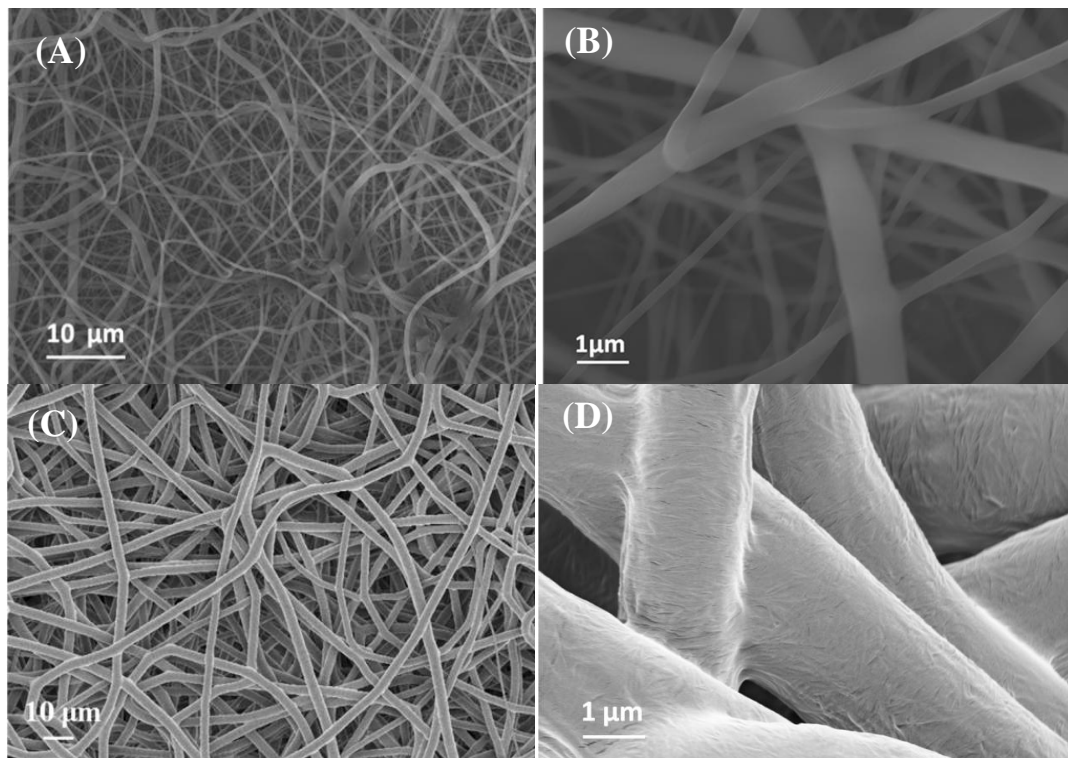


Figure 6.10: Effect of voltage on 100% PCL fibre' diameters. (A) V=15 kV; Mag 2.36 KX. (B) V =15 kV; Mag 49.14 KX. (C) V = 20 kV; Mag 2.9 KX. (D) V = 20 kV; Mag 63.63 KX (room temp; distance=18).

6.3.1.2 PCL/P₁₁₋₄

6.3.1.2.1 The effect of distance

The morphologies of PCL fabrics containing 35% of P₁₁₋₄ were also investigated. Fibres were fabricated with tip to collector distances of 16, 18, and 20 cm. The applied voltage was 15 kV at room temperature. Figures 6.11 (A) and 6 (B) exhibit fibres were collected at distance of 16 cm. The fibres diameters are in the range of 202-541 nm. Figures 6.11 (C) and (D) show fibres were collected at distance of 18 cm. The fibre diameters range decreased to 280-430 nm.

6.3.1.2.2 The effect of temperature

Figures 6.12 (A) and 6.12 (B) present samples were prepared with the applied voltage of 20 kV, and were collected from a distance of 18 cm. The figures show fibres with diameters range between 480-650. Figures 6.12 (C) and 6.12 (D) show samples were made at 50 °C. The fibres in those figures decreased to the range of 365-594 nm.

6.3.1.2.3 The effect of applied voltage

To investigate the effect of voltage, temperature and distance will be constant. Distance to collector is 16 cm and temperature is 50 °C. Figure 6.13 shows the samples' morphology as a function of voltage of 15, 20, and 25 kV. From the figure, there was a slight decreased in the average of the fibre's diameters with increasing voltage from 15kV to 20 kV. The diameter was increased when higher voltage was applied to 25 KV. The measurements of the rest samples are listed in Appendix F.

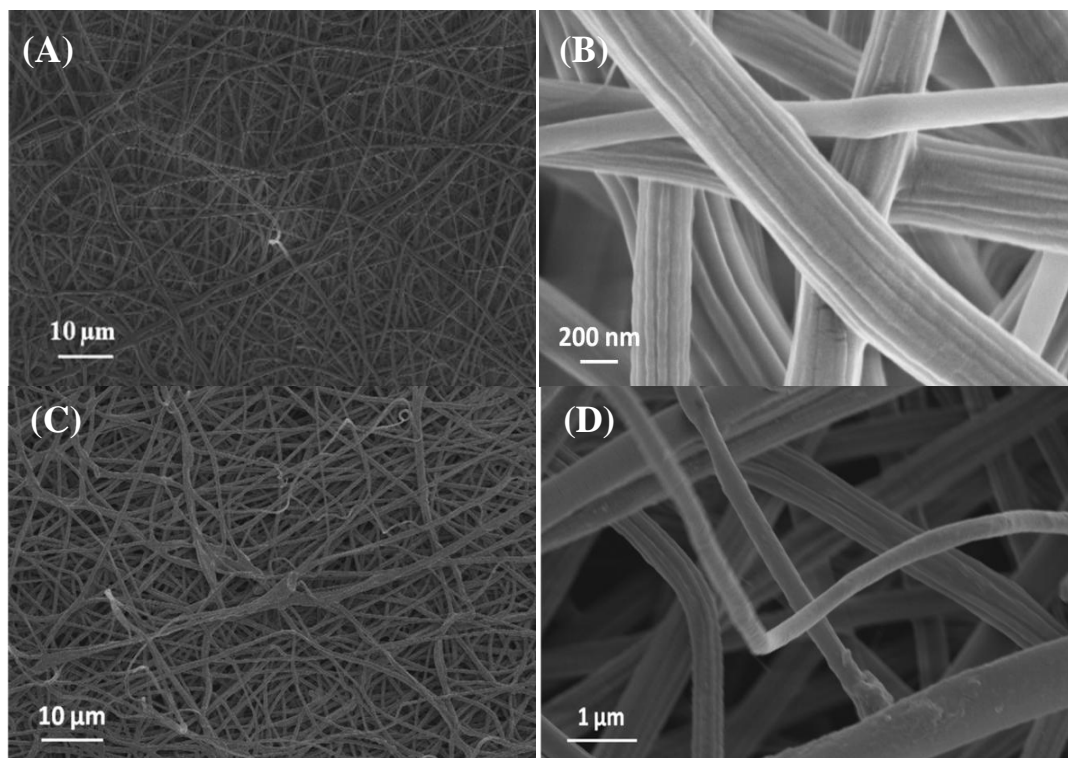


Figure 6.11: Effect of distance on PCL/P₁₁-4 fibbers' diameters. (A) tip to collector =16 cm; Mag 2.02 KX. (B) tip to collector = 16 cm; Mag 100.00 KX. (C) tip to collector = 18 cm; Mag 3.06 KX. (D) tip to collector = 18 cm; Mag 40.32 KX (V =15 kV; room temp).

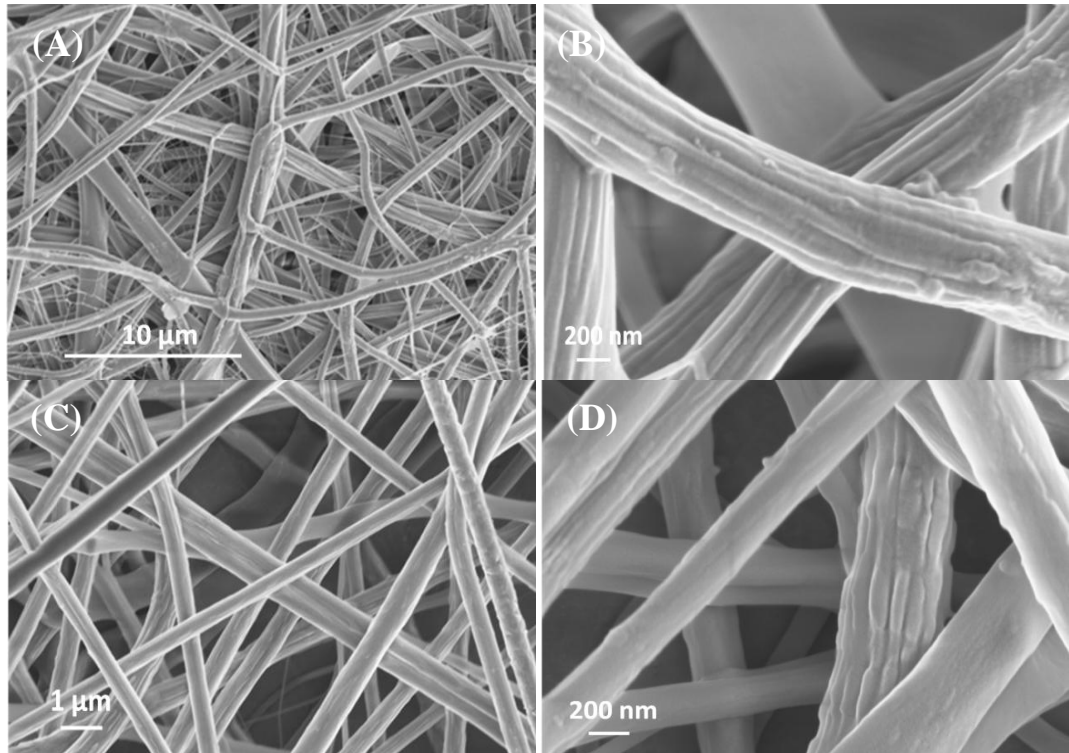


Figure 6.12: : Effect of temperature on PCL/P₁₁₋₄ fibres' diameters. (A) room temp; Mag 6.61 KX. A2) at room temp; Mag 111.71 KX. (C) at 50 °C; Mag 3.8 KX. B2) 50 °C; Mag 83.63 KX (voltage = 20 kV; tip to collector distance = 20).

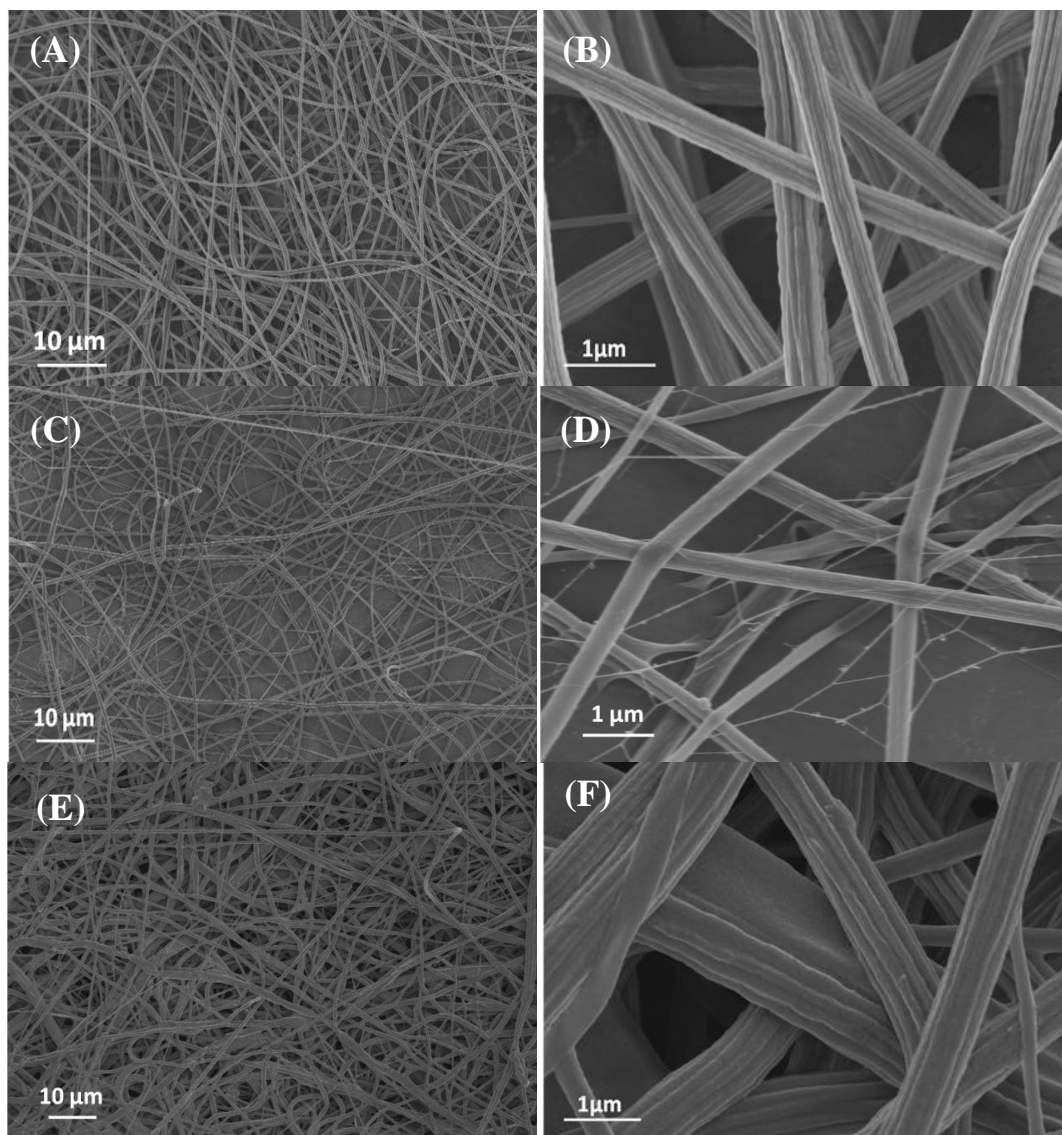


Figure 6.13: Effect of voltage on PCL/P₁₁-4 fibre' diameters. (A) 15 kV; Mag 2.36 KX. (B) 15 kV; Mag 1.9 KX. (C) 20 kV; Mag 1.9 KX. (D) 20 kV; Mag 57.63. (E) 25 kV; Mag 43.82. (F) 25 kV;

6.3.1.3 PCL/P₁₁-8

6.3.1.3.1 The effect of distance

Fibres of PCL containing 35% of P₁₁-8 were fabricated with tip to collector distances of 16, 18, and 20 cm. The applied voltage was 25 kV at room temperature. Figures 6.14 (A) and (B) exhibit fibres were collected at distance of 16 cm. The fibres diameters are in the range of 300-471 nm. Figures (C) and (D) show fibres were collected at distance of 18 cm. The fibre diameters range decreased to 200-300 nm. Figures (E) and (F) show fibres were collected at distance of 20 cm. Further decrease in the fibres diameters were observed with the presence of fibres less than 100 nm. Again as presented above, varying the distance between the tip and the collector appreciably impacts the fibre diameters.

6.3.1.3.2 The effect of temperature

Figures 6.15 (A) and (B) present samples were made using the applied voltage of 20 kV, and were collected from a distance of 18 cm. The figures show fibres with diameters range between 197-291 nm and thin fibres with diameters range from 50 to 80 nm. Figure 6.15 (C) and (D) show samples were made at 50 °C. The fibres in those figures decreased to the range of 156-276 nm with the presence of very thin fibres.

6.3.1.3.3 The effect of applied voltage

In this section, temperature and distance are constant; distance to collector is 16 cm and temperature is 50 °C. Figure 6.16 shows the samples' morphology as a function of voltage: 15, 20, and 25 kV. From the figure, there was a slight decrease in the average of the fibre's diameters with increasing voltage from 15 kV to 20 kV. When higher voltage was applied to 25 KV, opposite behaviour was observed. The diameters were clearly increased to the average of 1200 nm. The measurements of the rest samples are listed in Appendix G.

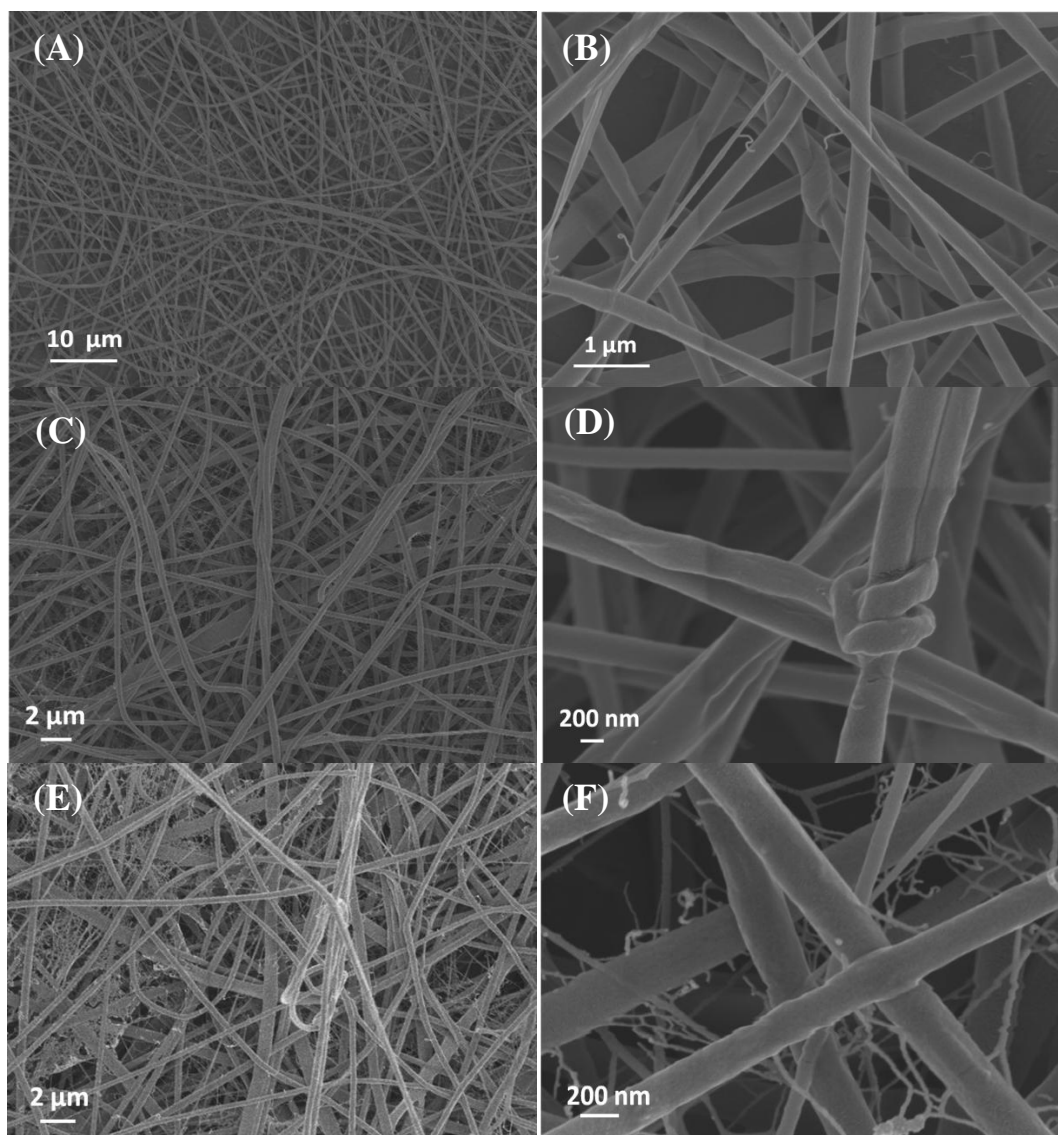


Figure 6.14: Effect of distance on PCL/P₁₁-8 fibbers' diameters. (A) tip to collector = 16 cm; Mag 3.55 KX. (B) tip to collector =16 cm; Mag 43.14 KX. (C) tip to collector = 18 cm; Mag 6.36 KX. (D) tip to collector = 18 cm; Mag 73.63 KX. (E) tip to collector = 20 cm; Mag 8.75 KX. (F) tip to collector = 20 cm; Mag 143 KX (voltage= 25 kV; at room Temp).

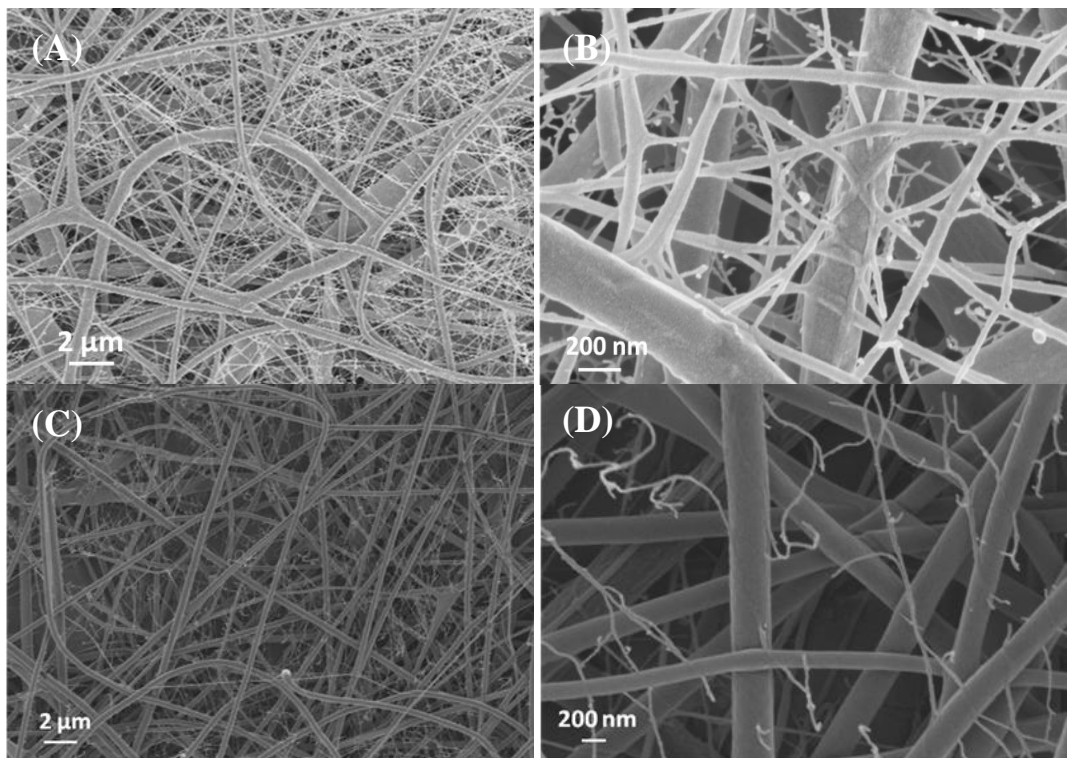


Figure 6.151: Effect of temperature on PCL/P₁₁-8 fibres' diameters. (A) room temp; Mag 6.61 KX. (B) at room temp; Mag 111.71 KX. (C) at 50 °C; Mag 3.8 KX . (D) 50 °C; Mag 83.63 KX (voltage = 20 kV; tip to collector distance = 18 cm).

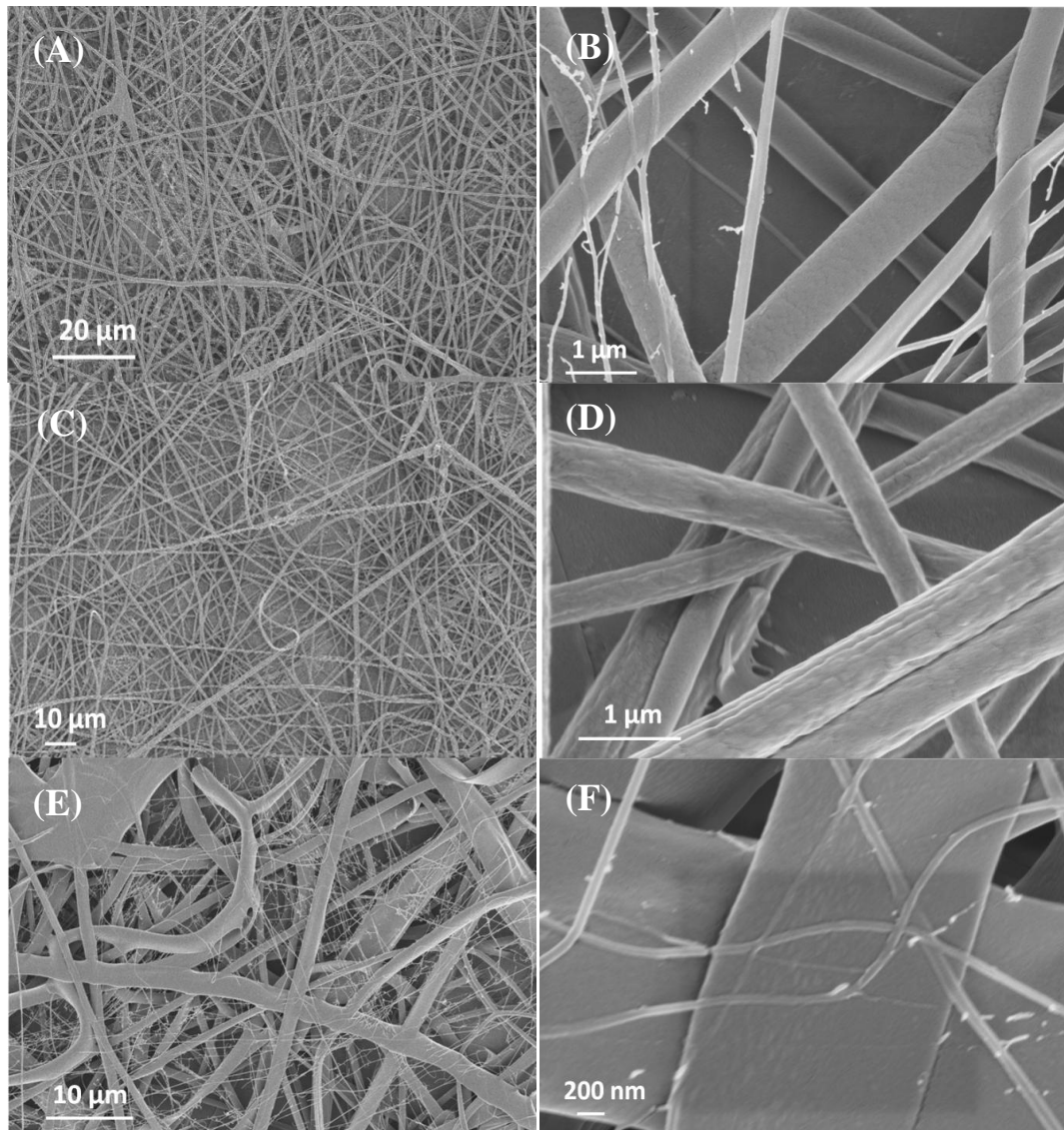


Figure 6.16: Effect of voltage on PCL/P₁₁-8 fibre' diameters. (A) 15 kV; Mag 2.36 KX. (A) 15 kV; Mag 57.14 KX. (C) 20 kV; Mag 1.9 KX . (D) 20 kV; Mag 57.63 KX. (E) 25 kV; Mag . (F) 25 kV; Mag (Temp= 50 °C; distance = 16).

6.3.2 Confocal laser scanning microscope, CLSM

To investigate the peptides distribution in the fibres, they were fluorescently labelled and viewed by confocal microscopy. Figure 6.17 provides CLSM micrographs of the electrospun samples. The figure gives no fluorescence background emitted from the fabric without peptide. In contrast, it shows green fluorescence emitted from PCL/P₁₁-8 and PCL/P₁₁-4 compositions. In those treated samples, the individual fibres are clearly visible. Thus further supports the conclusion that peptides are homogenously distributed along their entire length. One sample from each type of fabric (%100 PCL, PCL/P₁₁-4,

PCL/P₁₁-8) is presented in the Figure 6.17, also, all samples prepared at different electrospinning parameters showed the same results.

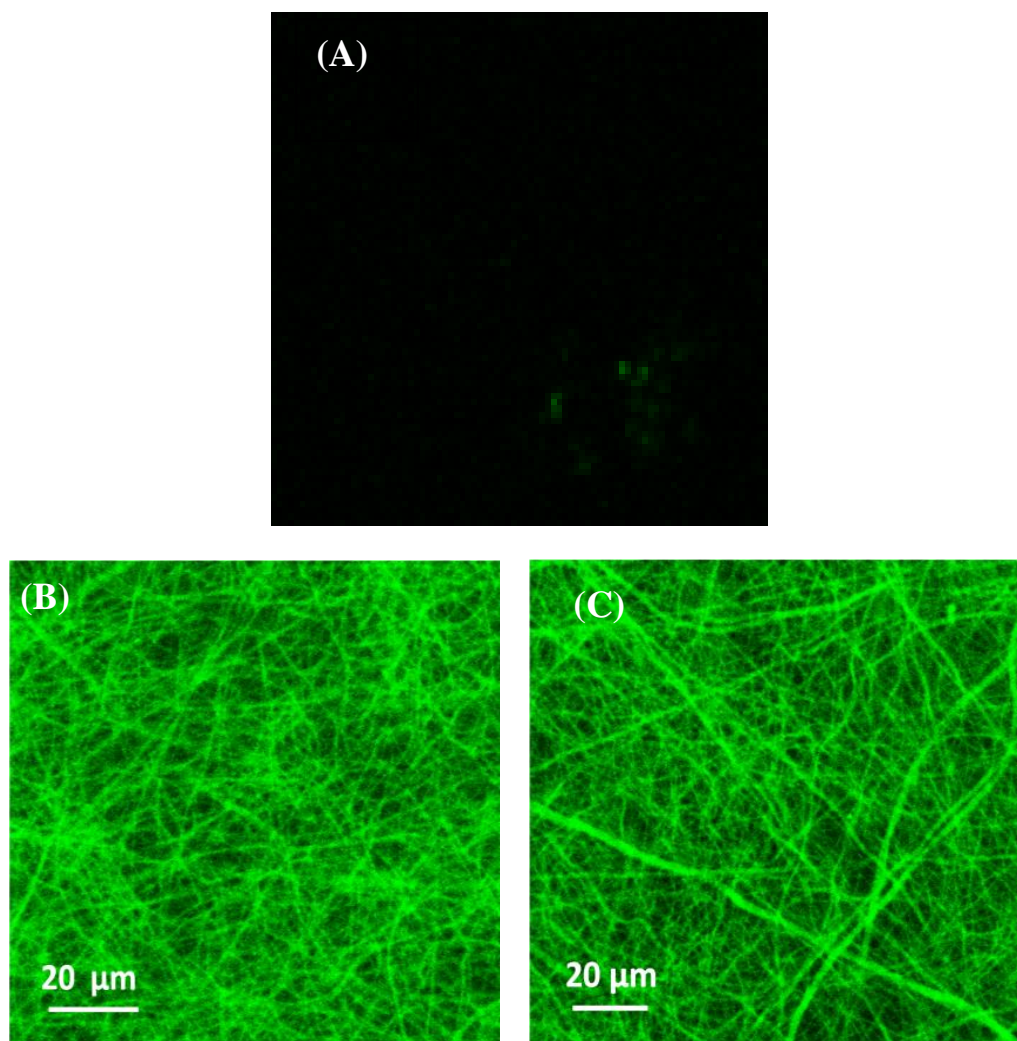


Figure 6.17: Visualization of fluorescence-labelled P₁₁-4 in PCL fibres.

6.3.3 Energy-dispersive X-ray spectroscopy, EDX

EDX spectrometer is used in conjunction with SEM to examine the fibre's chemical composition. The EDX spectra of PCL fibres with and without peptides are shown in Figure 6.18. The presence of nitrogen peaks are observed in PCL/P₁₁-8 and PCL/P₁₁-4 spectra. The nitrogen peaks in the EDX spectra are attributed to peptide molecules which indicate the successful incorporation of peptides in those fibres. A nitrogen peak is not appeared in control PCL spectrum because peptides are not added to this

sample. Table 6.2 summarizes the quantitative results of the chemical elements in the samples.

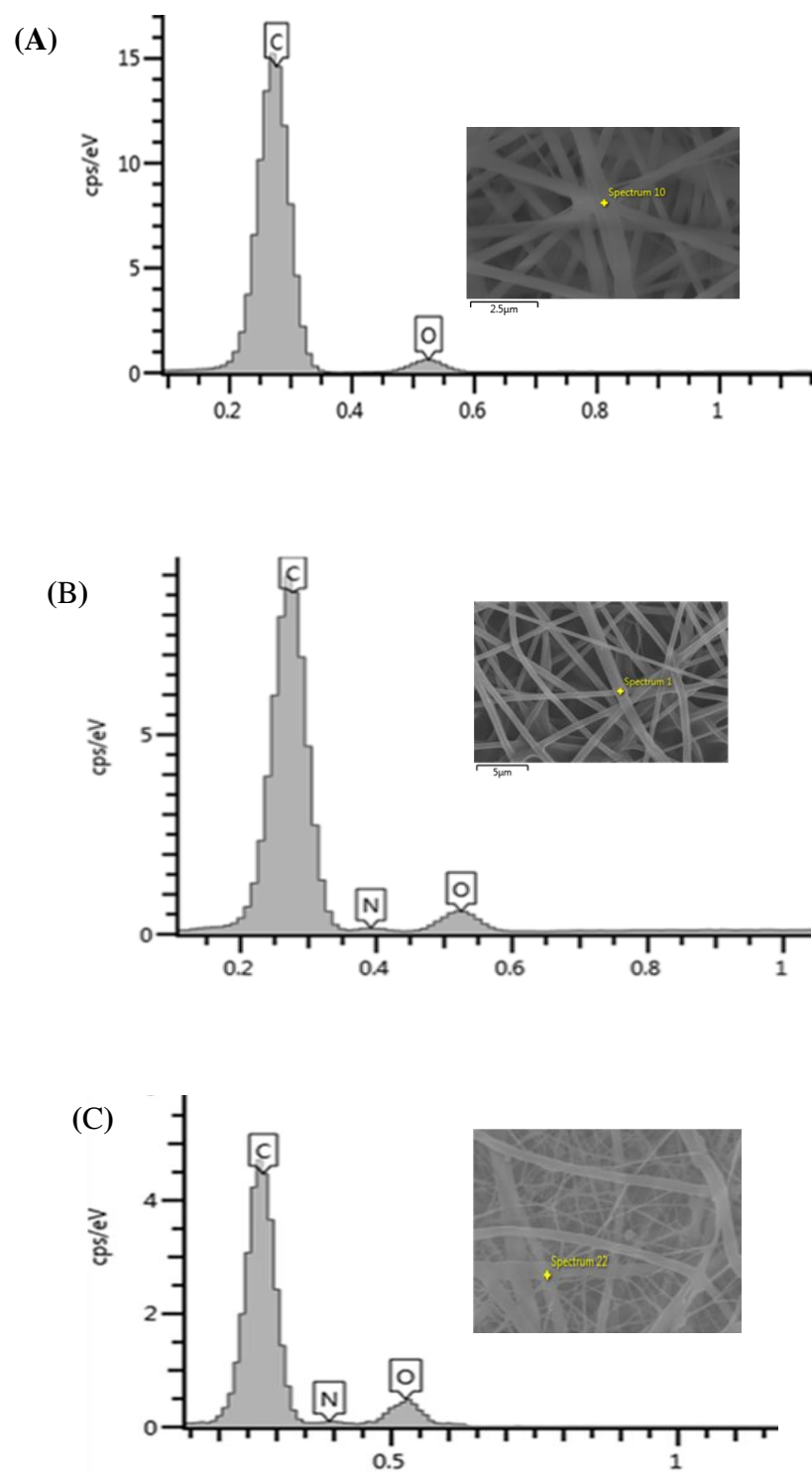


Figure 6.18: EDX spectra of electrospun fibres. (A) Control PCL. (B) PCL/P₁₁-4.

(C) PCL/P₁₁-8.

Table 6.2: The chemical elements in the electrospun fibres by SEM/EDX.

Sample	C %	N %	O %
PCL	91.8 ± 3.6	0.0	8.2 ± 3.7
PCL/P ₁₁ -8	70.4 ± 13.1	19.3 ± 2.9	10.3 ± 6.6
PCL/P ₁₁ -4	78.5 ± 13.7	10.4 ± 3.9	11.1 ± 4.2

6.3.4 X-ray photoelectron spectrometer, XPS

The surface chemistry of the samples was analyzed by X-ray photoelectron spectroscopy. Figure 6.19 displays the absorption of C_{1s} at 285.0 eV and O_{1s} at 531.0 eV in 100% PCL. In the peptides enriched samples, in addition to C_{1s} and O_{1s}, there is an absorption peak of N_{1s} at 420 eV (Figure 6.20). The presence of nitrogen peaks in the spectra indicates that there is an amount of peptides laying on the surface of the treated samples. The intensity of nitrogen peak in PCL/P₁₁-8 sample is higher than PCL/P₁₁-4 due to the higher number of nitrogen in P₁₁-8. The quantitative results are summarized in Table 6.3.

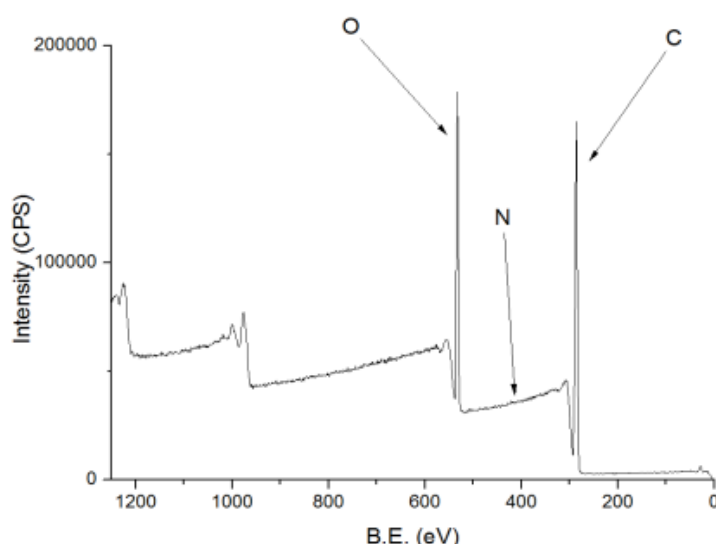


Figure 6.19: XPS spectra of the electrospun samples of 100% PCL.

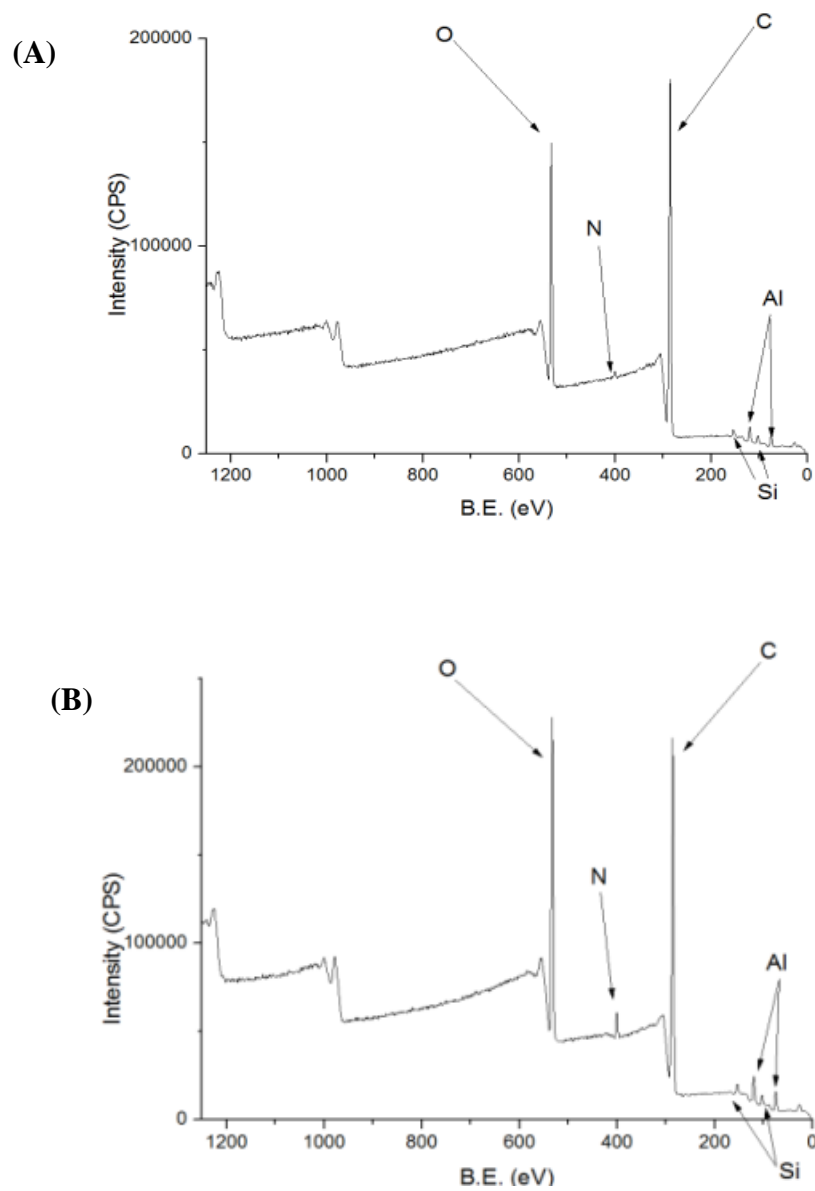


Figure 6.20: XPS spectra of the electrospun samples (B) PCL/P₁₁-4. (C) PCL/P₁₁-8.

Table 6.3: The chemical elements in the electrospun fibres by XPS.

Sample	C %	N %	O %
PCL	79.0	0.0	21.0
PCL/P ₁₁ -8	81.5	2.0	16.5
PCL/P ₁₁ -4	80.9	0.6	18.5

6.3.5 Attenuated total reflectance spectroscopy, ATR

ATR was applied to investigate the mixture of PCL and peptides before and after electrospinning. The spectra are shown in Figure 6.21. Before electrospinning, the spectra displays carbonyl C=O stretching mode of PCL which is appeared at 1730 cm^{-1} in all three overlaid samples in Figure 6.21 (A). The figure shows no β -sheet conformation in the solution before electrospinning. After electrospinning, changes were observed. New small feature is added to the PCL/P₁₁-8 spectrum near to the PCL carbonyl stretching area. This new peak is located in the amide I region around 1625 cm^{-1} , see Figure 6.21 (B). Peptides spectra were subtracted from PCL spectrum to determine the conformation of the peptide incorporated into the PCL fibres (Figure 6.21 C). PCL/P₁₁-8 has a strong absorption peak at 1625 cm^{-1} corresponding to its high β -sheet contents. About 85% of the peptide present in PCL/P₁₁-8 is in the β -sheet conformation. PCL/P₁₁-4 has a strong absorption peak centred at 1655 cm^{-1} indicating the high content of random coil. About 70% of the peptide in PCL/P₁₁-4 is at random coil conformation, while β -sheet is 30%.

6.3.6 The effect of the electrode charge on fabric morphology

The results shown by SEM have opened some more questions. What are these thin fibres? Why they do appear in PCL/P₁₁-8 more than PCL/P₁₁-4? and what is the difference in the chemical compositions between thin and thick fibres?

In an attempt to find the reason of the presence of small network fibres in PCL/P₁₁-8 fabric, electrode polarity was swapped. All previous samples described above were pumped from a syringe that connected to a positive electrode. Figure 6.22 shows the morphology of samples were pumped from a syringe that connected to a negative electrode. Image (A) and (B) shows low and high magnification images of PCL/P₁₁-4 fabric which ejected from negative connected syringe. The images show no difference between them and samples ejected from positive electrode. Also PCL/P₁₁-8 solution when was pumped from syringe connected to negative electrode showed no significant different morphology than sample prepared from syringe connected to positive electrode. Still the fabrics have two different networks of fibres.

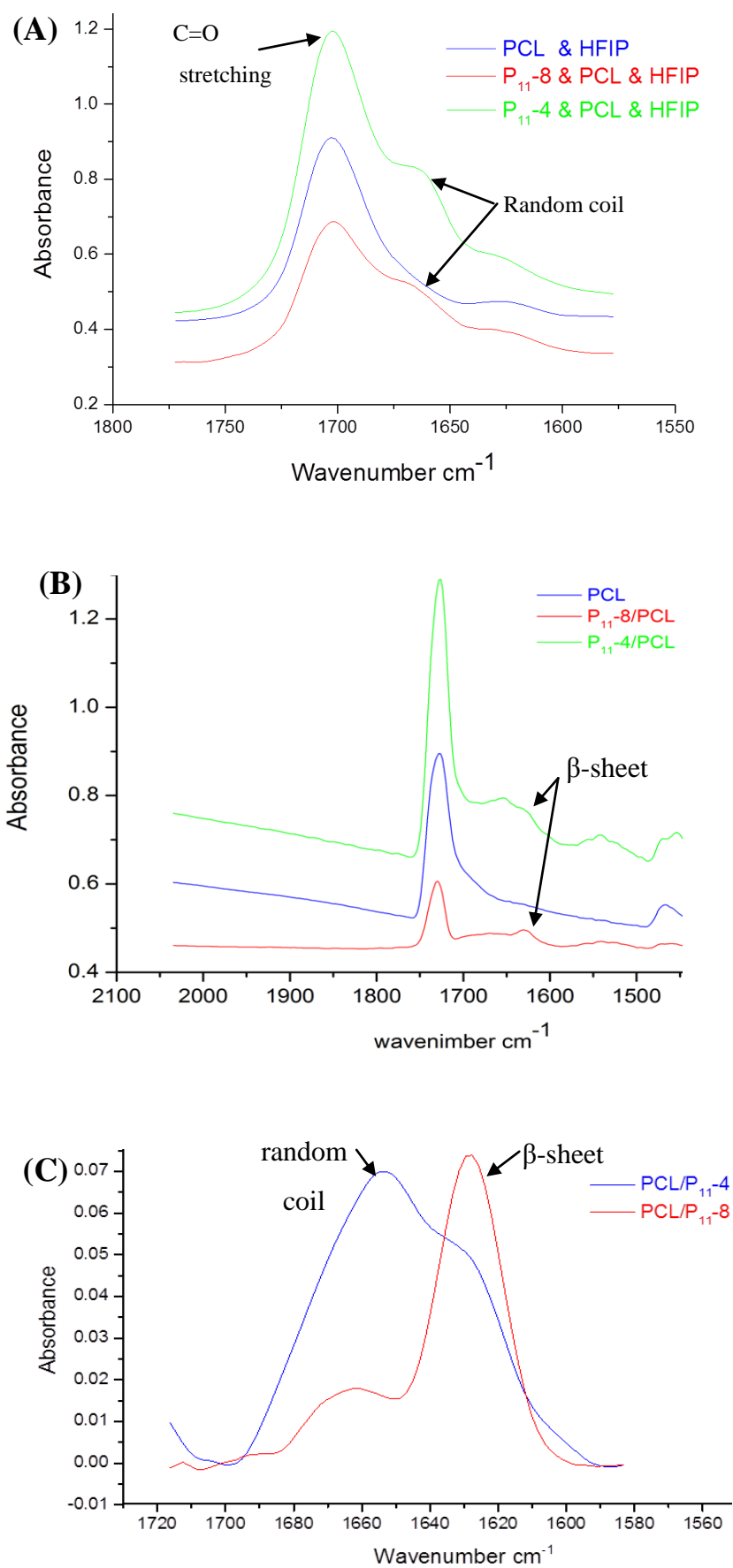


Figure 6.21: IR spectra of electrospun fabric. (A) before electrospinning. (B) after electrospinning. (C) overlaid band fitted of amide I for PCL/P₁₁-8 and PCL/P₁₁-4.

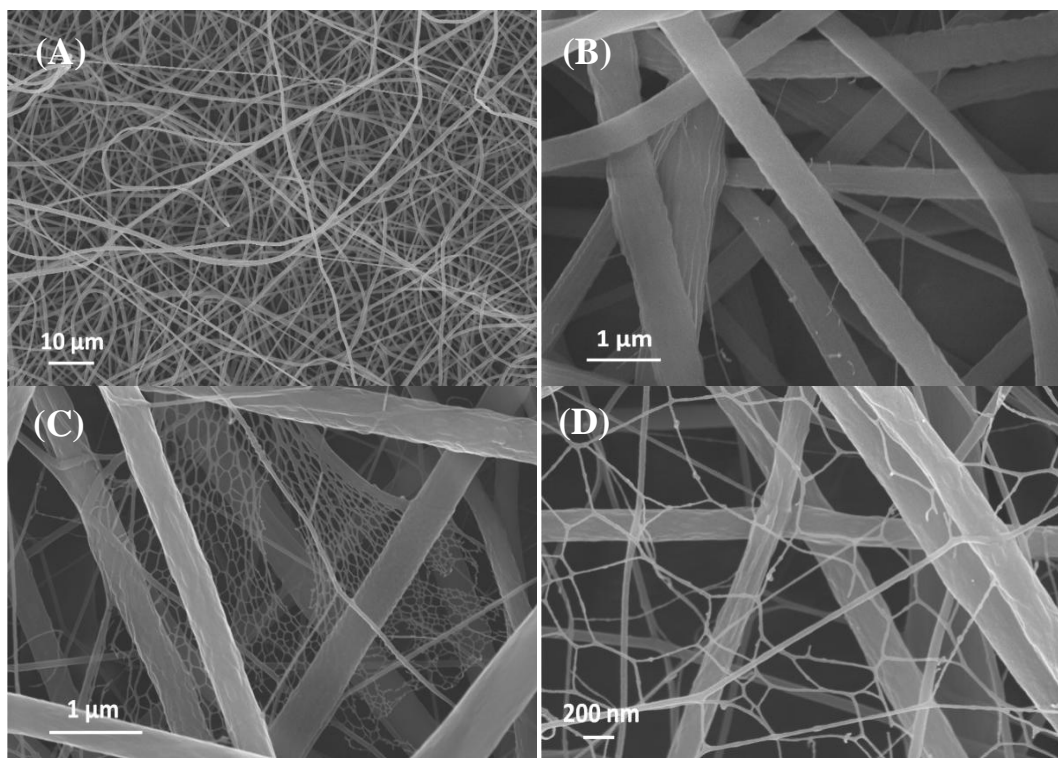


Figure 6.22: SEM images of electrospun fibres. (A) and (B) low and high magnification of PCL/P₁₁₋₄. (C) and (D) low and high magnification of PCL/P₁₁₋₈.

6.3.7 The effect of peptide concentration on fabric morphology

Another experiment was done to find the reason of the presence of thin fibres in PCL/P₁₁₋₈ fabric. PCL/P₁₁₋₈ fabric was again fabricated but with high P₁₁₋₈ concentration. P₁₁₋₈ concentration was increased to double the concentration of the samples in the previous experiments. From Figure 6.23, it is clear that there is a large increase in the number of thin fibres in the fabric.

6.3.7.1 Transmission electron microscopy, TEM

PCL/P₁₁₋₈ sample was viewed by EDX/TEM in order to investigate the different in the chemical composition between thin and thick fibres. Figure 6.24 shows TEM image of PCL/P₁₁₋₈. Figure 6.25 shows the EDX spectra of PCL/P₁₁₋₈.

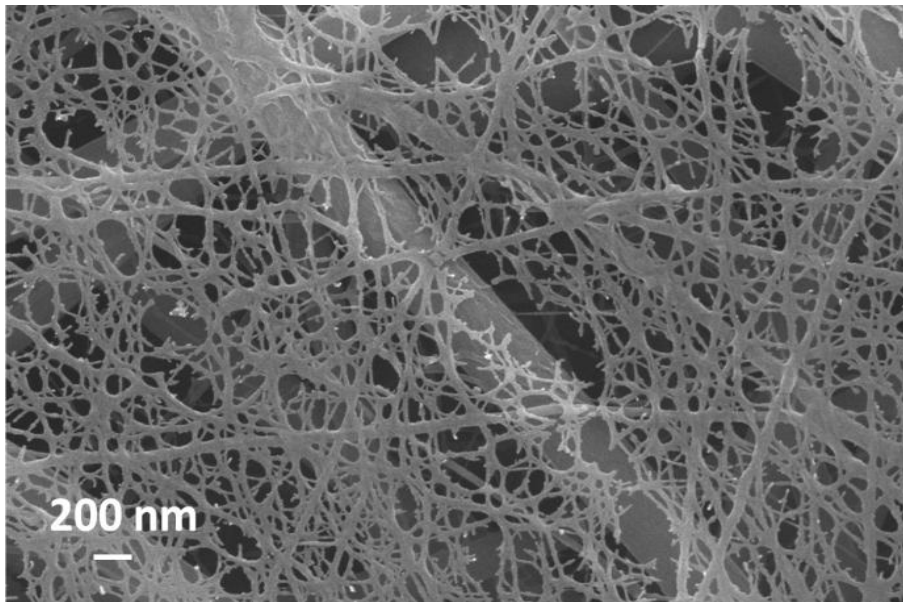
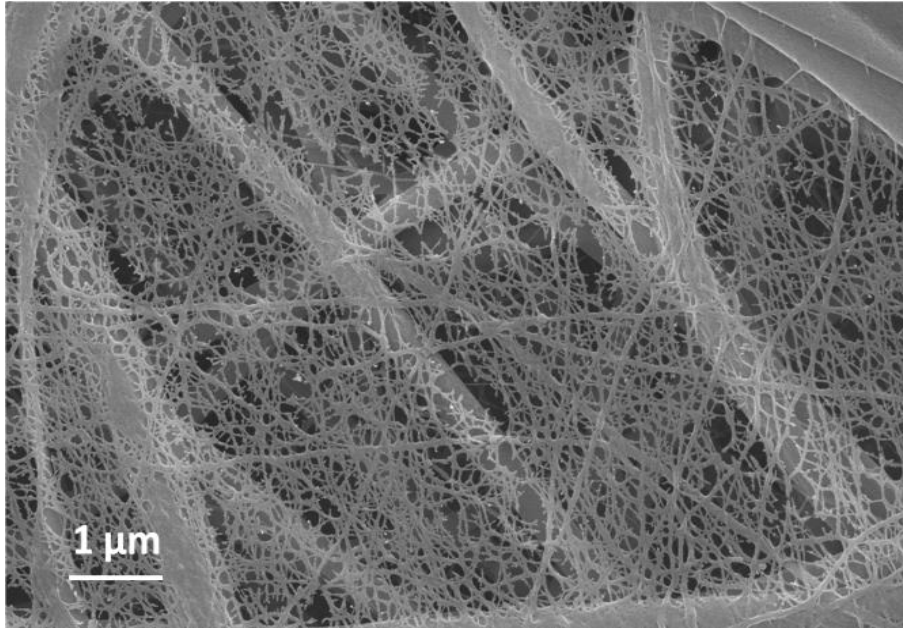


Figure 6.23: SEM images of PCL/P₁₁₋₈ with high concentration of P₁₁₋₈.

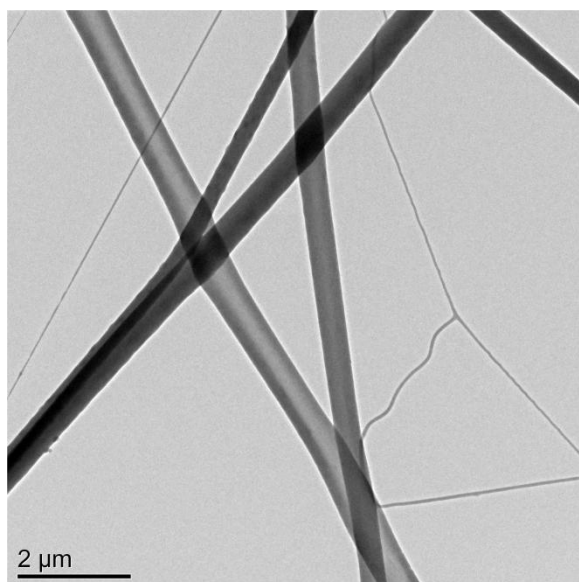


Figure 6. 24: TEM image of PCL/P₁₁-8 showing thick and thin fibres.

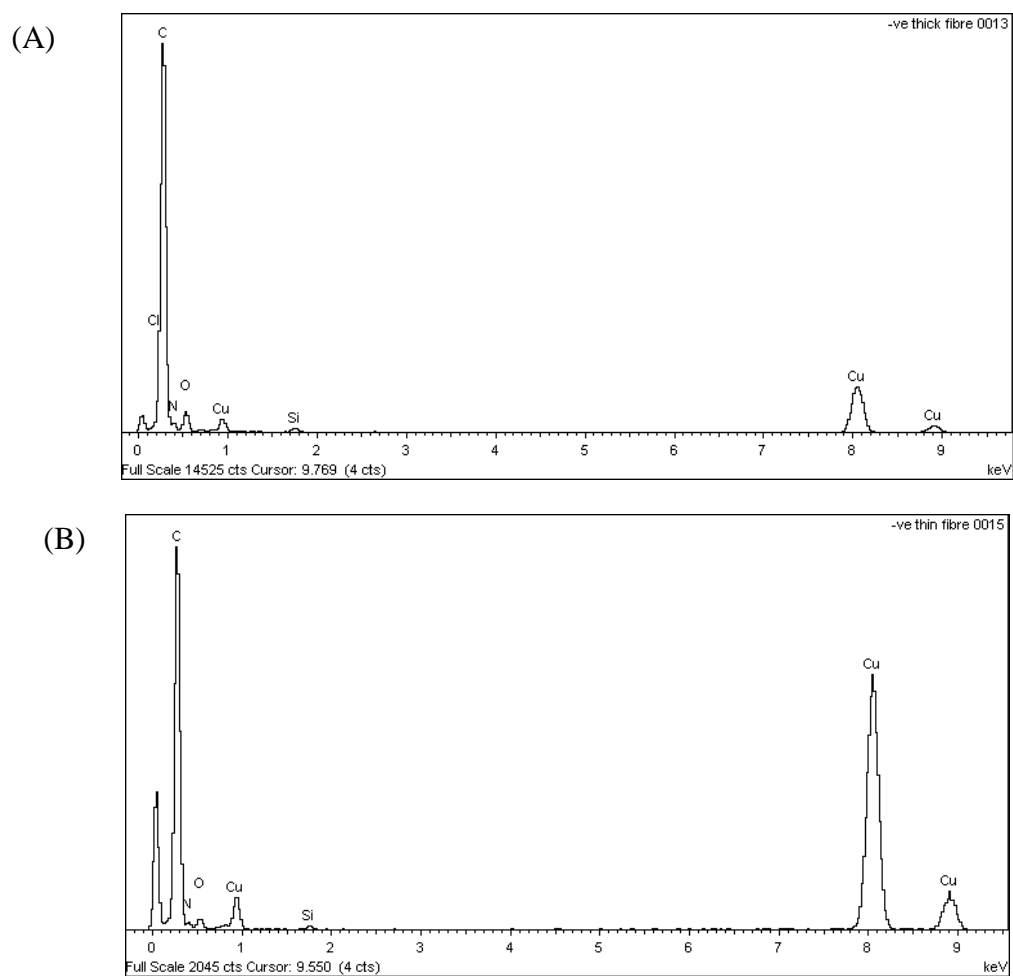


Figure 6.25: The EDX spectrum of PCL/P₁₁-8. (A) thick. (B) thin fibre.

6.4 Discussion

The goal of this chapter was to design a composition of peptide-enriched electrospun materials for biomedical application. This new fabricated materials were characterized using several tools.

From SEM results, it is observed that the average of fibres diameters was slightly decreased with the addition of peptide compared to fibres without peptide. The presence of charged molecules in the spinning solution increases the charge density on the surface of the ejected polymer jet. When the solution travels through the electric field, greater elongation and thinning force are imposed due to enhanced conductivity. As a result, fibres with smaller diameter are fabricated [168, 170]. In agreement with this result, the same effect has been seen by many authors. Zang *et al.* have shown that poly(vinyl alcohol) fibre diameters were decreased from 214 ± 19 nm to 159 ± 21 nm when NaCl concentration was increased from 0.05 to 0.2% [180]. J.Zeng *et al.* have concluded from their investigation that the addition of anions or cations to the electrospinning solution increases the electrospinning conductivity causing a decrease in the fibre diameter [181].

Electrospinning parameters have significant effect on the fibres' diameter. Distance is an effective parameter in the electrospinning process. The diameters were observed to decrease with increasing distance. The reason could be that longer travelling distance gives the polymer solution more time to be elongated. As a result, smaller diameters are fabricated. This conclusion is consistent with work of Doshi and Reneker. They examined the effects of various processing parameters on PEO fibre morphology. They found that the fibre diameter decreased with increasing distance [163]. In other work done by, Jaeger *et al.* they also found that longer distance decreases the fibre diameters of PEO/water system [163].

The fibres diameters were observed to be decreased with increasing temperature. This result is in agreement with a work made by Mit-Uppatham *et al.* They found that increasing the temperature yielded with smaller polyamide-6 fibres. They attributed this result to the decrease in the polymer viscosity at high temperature and to the increase in the evaporation rate of the solvent (HFIP) [182].

The voltage was found to have two opposing effects on the fibers diameters. In our results, there was an increase in the fibres diameter upon increasing the applied electric voltage, but on the opposite way, there was also a decrease in some fibers' diameters. Voltage can either increase the diameter or decrease it, so the effect of the electric voltage is ambiguous. At the end, it could be concluded that it is difficult to isolate the effect of the electrospinning parameters since they are interrelated.

CLSM revealed that the peptide distribution was homogenous during eletrospinning. ATR proved that peptides were self-assembled during electrospinning. Before electrospinning, when the solvent is present, peptides are below the critical concentration to self-assemble. During electrospinning, the solvent is rabidly evaporated and the peptide self-assembly process is started. However, ATR also showed that PCL/P₁₁-8 nanofibres have more β -sheet conformation than PCL/P₁₁-4 fabrics.

At the end of this chapter, some experiments were done to investigate the reason of the presence of thin fibres in PCL/P₁₁-8 more than PCL/P₁₁-4. The elecrosinning polarity was swapped and the result showed no difference in the fabric morphology. Then, the concentration of P₁₁-8 was increased in the fabric PCL/P₁₁-8 and the result showed that thin fibres were increased. This result indicates that P₁₁-8 causes thin fibres formation. Then, PCL/P₁₁-8 was viewed by TEM/EDX to investigate the chemical composition in the two different networks of fibres. TEM/EDX showed no difference in the chemical composition between the two networks; thick and thin fibres.

Chapter 7

7 Conclusions and future work

7.1 Conclusions

The controlled delivery of antibacterial agents to the wound site is favorable, particularly when systemic delivery could cause organ damage due to toxicity caused by the preferred agents. A limitation associated with using drug releasing dressings is the immediate release of the drug when the dressing is applied even before the bacteria is arrested. The overall aim of this study was to develop a 'smart' wound dressing that able to release the antibacterial agents only in the presence of bacteria. This work had four major findings.

In chapter 3, the behaviour of three candidates of β -sheet forming peptides was examined in aqueous solutions and physiological-like conditions. The peptides were analysed using analytical techniques (FTIR and TEM) to determine their behaviour at the molecular & nanoscale. It was shown that P₁₁-2 self-assemble into nanofibrils in water, and into nanotubes in the aqueous solution of HFIP in a narrow range. In physiological conditions, it was found that the P₁₁-9 and P₁₁-12 follow a hierarchical self-assembly process similar to that in pure water and form fibrils. Peptide nanotube was not seen in physiological condition and the conclusion was that peptide nanotubes appear in limited range.

In chapter 4, the feasibility of coating cellulosic fabrics with peptides was investigated. The dressings were evaluated using SEM, CLSM and FTIR. It was shown that peptides can readily form a self-assembled coating around the cellulosic fabrics.

In chapter 5, preliminary work for designing a simple pH-sensitive dressing were prepared by impregnating fabrics in peptide solutions, P₁₁-8 and P₁₁-4 solutions

separately, containing antibiotics. The effectiveness of the dressings were *in vitro* investigated against *Staphylococcus epidermis*. The study has demonstrated that a peptides/antibiotics system can be used for controlling bacterial growth. The results showed that the peptides were stimulated by the pH of the bacteria and the loaded drugs were released. However, the results also showed that the antibacterial activity of the fabrics modified with P₁₁-4 was higher than those modified with P₁₁-8. The partial release of the drug from P₁₁-8 demonstrated that if the peptide is in a monomer state, the drug is liberated and released, while if the peptide is gel the drug is entrapped.

In chapter 6, 100% PCL and PCL/peptide nanofibres have been successfully electrospun. The presence of self-assembling peptides in the nanofibres produced was confirmed by FTIR and CLSM analysis. For PCL/P₁₁-4 solution, uniform fibres were observed. For the blend of PCL/ P₁₁-8, two ranges of fibre diameter were observed in SEM images; fibres in the range of more than 100 nano-meters diameter, with average diameter of 380-600 nano-meters and fibres in the range of less than 100 nano-meters with the average fibre diameter of 30-70 nano-meters. It was suggested that the networks of small fibres could be peptides, which have been self-assembled to fibres, as they seem to be emerged from the main structure. Electrospinning parameters of voltage and tip-to-collector distance as well as the temperature of electrospinning environment were found to be the key factors that controlled the morphology of the nano-fibres.

7.2 Future work

The main aim of this thesis has been met. However, there are several areas of this thesis that can be expanded at a future stage.

It has been shown that P₁₁-2 form well defined nanotubes in the presence of HFIP. Further studies are required in order to fully understand the mechanism for nanotube formation. This could be achieved by X-ray diffraction, TEM, FTIR and NMR.

The work in chapter 5 presented a first step in the development of P₁₁ sequence of peptide incorporating drugs for controlled release applications. Further work should be focus on understanding the interaction between peptides and drug molecules. In this chapter, we demonstrated that dressings coated with peptide/drug have released the antibiotics in response to changes in pH induced by bacterial growth. This is a promising result for preventing infections caused by the implantation of medical devices.

Further studies could be done to optimise this methodology to treat infections caused by other bacterial species. Also, the experiments done here could be repeated with other peptides that form strong self-supporting gel at the pH of *SE* to determine if there is leakage of the drug from the peptide fibrils.

In fact, exudating wounds contain salts. It has been shown, within Aggeli group, that salt affects the peptide self-assembly. Therefore, the drug release should be investigated in a wound model.

In chapter 6, well ordered nanostructures have already been successfully formed from self-assembling peptides into PCL nanofibres, however, their potential as wound dressings and drug-releasing textiles has not yet been investigated. Therefore, future studies can be carried out to evaluate their ability to combine the triggered release property with the slow kinetic release for long-term use.

8. References

1. Anand, S.C., et al., *Medical textiles and biomaterials for healthcare*. 2005: Cambridge, England.
2. Horrocks, A.R. and S.C. Anand, *Handbook of technical textiles*. 2000: England.
3. Bartels, V., *Handbook of medical textiles*. 2011: England.
4. Rajendran, S. and S. Anand, *Contribution of textiles to medical and healthcare products and developing innovative medical devices*. Indian Journal of Fibre and Textile Research, 2006. 31(1): p. 215-229.
5. Bressan, E., et al., *Biopolymers for hard and soft engineered tissues: application in odontoiatric and plastic surgery field*. Polymers, 2011. 3(1): p. 509-526.
6. Kinoshita, Y. and H. Maeda, *Recent Developments of Functional Scaffolds for Craniomaxillofacial Bone Tissue Engineering Applications*. The Scientific World Journal, 2013.
7. Fujita, M., et al., *Proliferation and differentiation of rat bone marrow stromal cells on poly (glycolic acid)-collagen sponge*. Tissue Engineering, 2005. 11(9-10): p. 1346-1355.
8. Anand, S.C., et al., *Medical and healthcare textiles*. 2010: Elsevier.
9. Mueller, W.F., *The Origins of the Basic Inventions Underlying Du Pont*, in *The rate and direction of inventive activity: Economic and social factors*. 1962, NBER. p. 323-358.
10. Teebken, O.E. and A. Haverich, *Tissue engineering of small diameter vascular grafts*. European journal of vascular and endovascular surgery, 2002. 23(6): p. 475-485.
11. Thomas, L.V., V. Lekshmi, and P.D. Nair, *Tissue engineered vascular grafts—Preclinical aspects*. International Journal of Cardiology, 2013. 167(4): p. 1091-1100.
12. Hasan, A., et al., *Electrospun scaffolds for tissue engineering of vascular grafts*. Acta biomaterialia, 2014. 10(1): p. 11-25.
13. Zhong, W., *An introduction to healthcare and medical textiles*. 2013: DEStech Publications, Inc.
14. Kist, C., et al., *Comparative study of intraperitoneal adhesions associated with the use of meshes of polypropylene and polypropylene coated with omega-3 fatty acid*. Revista do Colégio Brasileiro de Cirurgiões, 2012. 39(3): p. 201-206.

15. Sivoilella, S., et al., *Nanostructured Guidance for Peripheral Nerve Injuries: A Review with a Perspective in the Oral and Maxillofacial Area*. International Journal of Mmolecular Sciences, 2014. 15(2): p. 3088-3117.
16. Masaeli, E., et al., *Fabrication, characterization and cellular compatibility of poly (hydroxy alkanooate) composite nanofibrous scaffolds for nerve tissue engineering*. PloS one, 2013. 8(2): p. e57157.
17. Van Langenhove, L., *Smart textiles for medicine and healthcare: materials, systems and applications*. 2007. USA.
18. Ten Breteler, M., V. Nierstrasz, and M. Warmoeskerken, *Textile slowrelease systems with medical applications*. AUTEX Research Journal, 2002. 2(4): p. 175-189.
19. Boateng, J.S., et al., *Wound healing dressings and drug delivery systems: a review*. Journal of Pharmaceutical Sciences, 2008. 97(8): p. 2892-2923.
20. Kim, G.H., et al., *Wound Dressings for Wound Healing and Drug Delivery*. Tissue Engineering and Regenerative Medicine, 2011. 8(1): p. 1-7.
21. Flanagan, M. and D.J. Marks-Maran, *Wound management*. 1997: Churchill Livingstone London.
22. Adderley, U.J., *Managing wound exudate and promoting healing*. British Journal of Community Nursing, 2010. 15: p. S15-S18.
23. Hunt, T.K., H. Hopf, and Z. Hussain, *Physiology of wound healing*. Advances in Skin & Wound Care, 2000. 13(2 Suppl): p. 6.
24. Hunt, T.K., *The physiology of wound healing*. Annals of Emergency Medicine, 1988. 17(12): p. 1265-1273.
25. Russell, L., *Understanding physiology of wound healing and how dressings help*. British Journal of Nursing (Mark Allen Publishing), 2000. 9(1): p. 10-20.
26. Menaker, L., *Biologic Basis of Wound Healing*. 1975, Hagerstown, Md.: Medical Dept. Harper & Row, New York.
27. Thomas K. Hunt, M.D., *Wound healing and wound infection : theory and surgical practice*. 1980, Appleton-Century-Crofts, New York.
28. Bowler, P., B. Duerden, and D. Armstrong, *Wound icrobiology and associated approaches to wound management*. Clinical microbiology reviews, 2001. 14(2): p. 244-269.
29. Grzybowski, J., et al., *New anti-infective collagen dressing containing antibiotics*. Journal of Biomedical Materials Research, 1997. 36(2): p. 163-166.

30. Gupta, B., *Textile-based smart wound dressings*. Indian Journal of Fibre & Textile Research, 2010. 35: p. 174-187.
31. Shah, F., *Development of a novel wound dressing material*. 2002: Leeds. PhD Thesis, University of Leeds.
32. Moody, A., *Use of a hydrogel dressing for management of a painful leg ulcer*. Wound Care, 2006.
33. Jones, A. and D. Vaughan, *Hydrogel dressings in the management of a variety of wound types: A review*. Journal of Orthopaedic Nursing, 2005. 9: p. S1-S11.
34. Sussman, G. and C. Weller, *Wound dressings update*. Journal of Pharmacy Practice and Research, 2006. 36(4): p. 318.
35. Woodings, C., *Regenerated Cellulose fibres*. 2001, UK.
36. Loke, W.K., et al., *Wound dressing with sustained anti-microbial capability*. Journal of Biomedical Materials Research, 2000. 53(1): p. 8-17.
37. Costache, M.C., et al., *Polymer-xerogel composites for controlled release wound dressings*. Biomaterials, 2010. 31(24): p. 6336-6343.
38. Elliott, W.H., et al., *Biochemistry and molecular biology*. 1997: Oxford University Press Oxford.
39. Kessel, A. and N. Ben-Tal, *Introduction to proteins: structure, function, and motion*. 2012: CRC Press.
40. H.Lodish., *Molecular cell biology*. 2000, New York.
41. Brown, W.H., M.K. Campbell, and S.O. Farrell, *Introduction to organic and biochemistry*. 2008: Cengage Learning. Canada.
42. Ulijn, R.V. and A.M. Smith, *Designing peptide based nanomaterials*. Chemical Society Reviews, 2008. 37(4): p. 664-675.
43. Nyrkova, I.A., et al., *Fibril stability in solutions of twisted beta-sheet peptides: a new kind of micellization in chiral systems*. European Physical Journal B, 2000. 17(3): p. 481-497.
44. Aggeli, A., et al., *Hierarchical self-assembly of chiral rod-like molecules as a model for peptide beta-sheet tapes, ribbons, fibrils, and fibers*. Proceedings of the National Academy of Sciences of the United States of America, 2001. 98(21): p. 11857-11862.
45. Davies, R.P.W., et al., *Self-assembling beta-sheet tape forming peptides*. Supramolecular Chemistry, 2006. 18(5): p. 435-443.

46. Cui, H., M.J. Webber, and S.I. Stupp, *Self-assembly of peptide amphiphiles: From molecules to nanostructures to biomaterials*. Peptide Science, 2010. 94(1): p. 1-18.
47. Ghadiri, M.R., Self-assembled nanoscale tubular ensembles. *Advanced Materials*, 1995. 7(7): p. 675-677.
48. Hartgerink, J.D., T.D. Clark, and M.R. Ghadiri, *Peptide nanotubes and beyond*. *Chemistry-a European Journal*, 1998. 4(8): p. 1367-1372.
49. Kohli, P. and C.R. Martin, *Smart nanotubes for biotechnology*. *Current Pharmaceutical Biotechnology*, 2005. 6(1): p. 35-47.
50. Hartgerink, J.D., et al., *Self-assembling peptide nanotubes*. *Journal of the American Chemical Society*, 1996. 118(1): p. 43-50.
51. Banerjee, A. and A. Yadav, *Self-assembling cyclic systems as drug carriers*. *Applied Nanoscience*, 2013. 3(6): p. 515-528.
52. Reches, M. and E. Gazit, *Molecular self-assembly of peptide nanostructures: mechanism of association and potential uses*. *Current Nanoscience*, 2006. 2(2): p. 105-111.
53. Gazit, E., *Self-assembled peptide nanostructures: the design of molecular building blocks and their technological utilization*. *Chemical Society Reviews*, 2007. 36(8): p. 1263.
54. Gorbitz, C.H., *The structure of nanotubes formed by diphenylalanine, the core recognition motif of Alzheimer's beta-amyloid polypeptide*. *Chemical Communications*, 2006(22): p. 2332-2334.
55. Gorbitz, C.H., *The structure of nanotubes formed by diphenylalanine, the core recognition motif of Alzheimer's -amyloid polypeptide*. *Chemical Communications.*, 2006(22): p. 2332-2334.
56. Scanlon, S. and A. Aggeli, *Self-assembling peptide nanotubes*. *Nano Today*, 2008. 3(3-4): p. 22-30.
57. Maji, S.K., et al., *Amyloid as a depot for the formulation of long-acting drugs*. *PLoS biology*, 2008. 6(2): p. e17.
58. Mankar, S., et al., *Nanomaterials: amyloids reflect their brighter side*. *Nano Reviews*, 2011. p:1-12.
59. Larsen, T.H., et al., *Sequence-Dependent Gelation Kinetics of beta-Hairpin Peptide Hydrogels*. *Macromolecules*, 2009. 42(21): p. 8443-8450.

60. Yucel, T., et al., *Direct observation of early-time hydrogelation in -hairpin peptide self-assembly*. *Macromolecules*, 2008. 41(15): p. 5763-5772.
61. Schneider, J.P., et al., *Responsive hydrogels from the intramolecular folding and self-assembly of a designed peptide*. *Journal of the American Chemical Society*, 2002. 124(50): p. 15030-15037.
62. Branco, M.C., et al., *Macromolecular diffusion and release from self-assembled β -hairpin peptide hydrogels*. *Biomaterials*, 2009. 30(7): p. 1339-1347.
63. Dreher, S.M., et al., *Bulk Material Properties of Beta-Bulge Peptide Hydrogels For Tissue Engineering*. *The FASEB Journal*, 2008. 22: p. 1005
64. Haines-Butterick, L.A., et al., *In vitro assessment of the pro-inflammatory potential of β -hairpin peptide hydrogels*. *Biomaterials*, 2008. 29(31): p. 4164-4169.
65. Altunbas, A., et al., *Encapsulation of curcumin in self-assembling peptide hydrogels as injectable drug delivery vehicles*. *Biomaterials*, 2011. 32(25): p. 5906-5914.
66. Fernández-Carneado, J., et al., *Amphipathic peptides and drug delivery*. *Peptide Science*, 2004. 76(2): p. 196-203.
67. Zhang, S.G., et al., *Design of nanostructured biological materials through self-assembly of peptides and proteins*. *Current Opinion in Chemical Biology*, 2002. 6(6): p. 865-871.
68. Zhao, X., *Design of self-assembling surfactant-like peptides and their applications*. *Current Opinion in Colloid & Interface Science*, 2009. 14(5): p. 340-348.
69. Vauthey, S., et al., *Molecular self-assembly of surfactant-like peptides to form nanotubes and nanovesicles*. *Proceedings of the National Academy of Sciences of the United States of America*, 2002. 99(8): p. 5355- 5360.
70. Santoso, S., et al., *Self-assembly of surfactant-like peptides with variable glycine tails to form nanotubes and nanovesicles*. *Nano Letters*, 2002. 2(7): p. 687-691.
71. Hamley, I., *Self-assembly of amphiphilic peptides*. *Soft Matter*, 2011. 7(9): p. 4122-4138.
72. Hartgerink, J.D., E. Beniash, and S.I. Stupp, *Self-assembly and mineralization of peptide-amphiphile nanofibers*. *Science*, 2001, 294: p. 1684-1688.
73. Hartgerink, J.D., E. Beniash, and S.I. Stupp, *Peptide-amphiphile nanofibers: a versatile scaffold for the preparation of self-assembling materials*. *Proceedings*

- of the National Academy of Sciences of the United States of America, 2002. 99(8): p. 5133-5138.
74. Cui, H.G., M.J. Webber, and S.I. Stupp, *Self-Assembly of Peptide Amphiphiles: From Molecules to Nanostructures to Biomaterials*. Biopolymers, 2009. 94(1): p. 1-18.
 75. Chen, J.-X., et al., *Construction of surfactant-like tetra-tail amphiphilic peptide with RGD ligand for encapsulation of porphyrin for photodynamic therapy*. Biomaterials, 2011. 32(6): p. 1678-1684.
 76. Accardo, A., et al., *Nanostructures by self-assembling peptide amphiphile as potential selective drug carriers*. Peptide Science, 2007. 88(2): p. 115-121.
 77. Zhang, S., *Fabrication of novel biomaterials through molecular self-assembly*. Nature Biotechnology, 2003. 21(10): p. 1171-1178.
 78. D'Auria, G., et al., *Self assembling properties of ionic complementary peptides*. Journal of Peptide Science, 2009. 15(3): p. 210-219.
 79. Chen, P., *Self-assembly of ionic-complementary peptides: a physicochemical viewpoint*. Colloids and Surfaces A: Physicochemical and Engineering Aspects, 2005. 261(1-3): p. 3-24.
 80. Boothroyd, S., A. Saiani, and A.F. Miller. *Formation of Mixed Ionic Complementary Peptide Fibrils*. 2008. Wiley Online Library.
 81. D'Auria, G., et al., *Self-assembling properties of ionic-complementary peptides*. Journal of Peptide Science, 2009. 15(3): p. 210-219.
 82. Hong, Y., et al., *Effect of amino acid sequence and pH on nanofiber formation of self-assembling peptides EAK16-II and EAK16-IV*. Biomacromolecules, 2003. 4(5): p. 1433-1442.
 83. Dzwolak, W. and V. Smirnovas, *A conformational [alpha]-helix to [beta]-sheet transition accompanies racemic self-assembly of polylysine: an FT-IR spectroscopic study*. Biophysical chemistry, 2005. 115(1): p. 49-54.
 84. Aggeli, A., et al., *Self-assembling peptide polyelectrolyte P-sheet complexes form nematic hydrogels*. Angew. Chem. Int. Ed, 2003. 42: p. 5603-5606.
 85. Maude, S., et al., *Peptide synthesis and self-assembly*, in *Peptide-Based Materials*. 2012, Springer. p. 27-69.
 86. Carrick, L.M., et al., *Effect of ionic strength on the self-assembly, morphology and gelation of pH responsive beta-sheet tape-forming peptides*. Tetrahedron, 2007. 63(31): p. 7457-7467.

87. Ryu, J. and C.B. Park, *High stability of self-assembled peptide nanowires against thermal, chemical, and proteolytic attacks*. Biotechnology and Bioengineering, 2010. 105(2): p. 221-230.
88. Lakshmanan, A., S. Zhang, and C.A. Hauser, *Short self-assembling peptides as building blocks for modern nanodevices*. Trends in Biotechnology, 2012. 30(3): p. 155-165.
89. Clark, T.D., L.K. Buehler, and M.R. Ghadiri, *Self-assembling cyclic β 3-peptide nanotubes as artificial transmembrane ion channels*. Journal of the American Chemical Society, 1998. 120(4): p. 651-656.
90. Fernandez-Lopez, S., et al., *Antibacterial agents based on the cyclic D, L- α -peptide architecture*. Nature, 2001. 412(6845): p. 452-455.
91. Zhang, S., F. Gelain, and X. Zhao. *Designer self-assembling peptide nanofiber scaffolds for 3D tissue cell cultures*. in *Seminars in cancer biology*. 2005.
92. R sler, A., G.W.M. Vandermeulen, and H.A. Klok, *Advanced drug delivery devices via self-assembly of amphiphilic block copolymers*. Advanced Drug Delivery Reviews, 2001. 53(1): p. 95-108.
93. Dobson, K., *Nanomedicine for Targeted Drug Delivery*. Journal of Materials Chemistry, 2009. 19(6294-6307).
94. Lindsey, J.S., *Self-assembly in synthetic routes to molecular devices. Biological principles and chemical perspectives: a review*. New Jurna of Chemistry, 1991. 15: p. 153–180.
95. Champness, P.E., *Electron diffraction in the transmission electron microscope*. 2001: BIOS Scientific Publishers, Oxford.
96. Williams, D.B., *Transmission electron microscopy : a textbook for materials science*. 1996, New York, Plenum Press, London.
97. Swift, J.A., *Electron microscopes*. 1970, Kogan Page, London.
98. Brydson, R.M. and C. Hammond, *Generic methodologies for nanotechnology: characterization*. Nanoscale Science and Technology, 2005: p. 56-129.
99. Goodhew, P.J., *Electron microscopy and analysis*. 2nd ed. 1988, Taylor & Francis, London.
100. Humphreys, P.J.G.a.F.J., *Scanning electron microscopy and x-ray microanalysis*. 3rd ed. 2003, London: Kluwer Academic/Plenum Publishers, New York.
101. Goldstein, J.I., *Scanning electron microscopy and x-ray microanalysis*. 3rd ed. 2003, London: Kluwer Academic/Plenum Publishers, New York.

102. Joshi, M., A. Bhattacharyya, and S. Wazed, *Characterization techniques for nanotechnology applications in textiles*. Indian Journal of Fiber and Textile Research, 2008. 33: p. 304-317.
103. http://en.wikipedia.org/wiki/Scanning_electron_microscope. [cited assessed 2010, 3 March.
104. Holme, D.J., *Analytical Biochemistry*. 3rd ed. 1998, Harlow: Longman.
105. Cohen, J., *Introduction to Fourier transform spectroscopy*. 1986, Gaithersburg, MD Springfield, Dept. of Commerce National Bureau of Standards ; National Technical Information Service distributor VA: U.S.
106. Hollas, J.M., *Basic atomic and molecular spectroscopy*. 2002, Cambridge: Royal Society of Chemistry.
107. Pavia, D.L., *Introduction to spectroscopy : a guide for students of organic chemistry*. 3rd ed. 2001, Harcourt College Publishers, Fort Worth, Tex.
108. Duckett, S., *Foundations of spectroscopy*. 2000, Oxford: Oxford University Press.
109. http://en.wikipedia.org/wiki/File:FTIR_Interferometer.png. [cited 2011 23 December].
110. Valenti, L., et al., *IR study of TFA unpurified synthetic peptides in aqueous solution. TFA removal and band assignment*. Analytical Biochemistry, 2011.
111. Fersht, A., *Enzyme structure and mechanism*. 1977, New York ; Reading: W. H. Freeman.
112. Jackson, M. and H.H. Mantsch, *The use and misuse of FTIR spectroscopy in the determination of protein structure*. Critical Reviews in Biochemistry and Molecular Biology, 1995. 30(2): p. 95-120.
113. Gunzler, H., Hans Gremlic, *IR spectroscopy : an introduction*. 2002, Weinheim ; Cambridge: Wiley-VCH.
114. http://en.wikipedia.org/wiki/File:ATR_path-en.svg. [cited 2013 23 September].
115. Herman, B., *Fluorescence microscopy*. 2nd ed. 1998, Oxford: BIOS Scientific in association with the Royal Microscopical Society.
116. Hibbs, A.R., *Confocal microscopy for biologists*. 2004, New York ; London: Kluwer Academic/Plenum.
117. Jan slavik, *Fluorescence microscopy and fluorescent probes*. 1996, New York: Plenum Press.

118. Rost, F.W.D., *Fluorescence microscopy*. 1992, Cambridge: Cambridge University Press.
119. Claxton, N.S., T.J. Fellers, and M.W. Davidson, *Laser scanning confocal microscopy*. Olympus. Available online at <http://www.olympusconfocal.com/theory/LSCMIntro.pdf>, 2006.
120. Chen, G., *Nanotube-Based Controlled Drug Delivery*. Pharmaceut Anal Acta, 2012. 3: p. e136.
121. Hilder, T.A. and J.M. Hill. *Encapsulation of the anticancer drug cisplatin into nanotubes*. in *Nanoscience and Nanotechnology, 2008. ICONN 2008. International Conference on*. 2008. IEEE.
122. Aggeli, A., et al., *pH as a trigger of peptide beta-sheet self-assembly and reversible switching between nematic and isotropic phases*. Journal of the American Chemical Society, 2003. 125(32): p. 9619-9628.
123. Scanlon, S., *Nanostructured Porous Materials Based on Designed Self-Assembling Biopolymers*, PhD Thesis, School of Chemistry,. 2006, University of Leeds,.
124. Felton, S.H., *Self-assembling β -sheet peptide networks as smart scaffolds for tissue engineering*. 2005, PhD thesis, School of chemistry. University of Leeds.
125. Kre el, A. and W. Bal, *A formula for correlating pKa values determined in D2O and H2O*. Journal of inorganic biochemistry, 2004. 98(1): p. 161-166.
126. Maude, S., et al., *De novo designed positively charged tape-forming peptides: self-assembly and gelation in physiological solutions and their evaluation as 3D matrices for cell growth*. Soft Matter, 2011. 7(18): p. 8085-8099.
127. Knapman, T.W., A. Aggeli, and A.E. Ashcroft, *Critical concentrations of β -sheet peptide self-assembly quantified directly by nanoelectrospray ionization mass spectrometry*. Rapid Communications in Mass Spectrometry, 2008. 22(10): p. 1611-1614.
128. Fishwick, C.W., et al., *Structures of helical β -tapes and twisted ribbons: the role of side-chain interactions on twist and bend behavior*. Nano letters, 2003. 3(11): p. 1475-1479.
129. Maude, S., E. Ingham, and A. Aggeli, *Biomimetic self-assembling peptides as scaffolds for soft tissue engineering*. Nanomedicine, 2013. 8(5): p. 823-847.
130. D.E.Miles, *Self-assembling peptide/glycosaminoglycan hydrogels for spinal therapies*. University of leeds 2012.

131. Kerihuel, J.C., *Charcoal combined with silver for the treatment of chronic wounds*. Wounds UK, 2009. 5(3): p. 87-93.
132. Anghel, I., et al., *Modified wound dressing with phyto-nanostructured coating to prevent staphylococcal and pseudomonal biofilm development*. Nanoscale research letters, 2012. 7(1): p. 1-8.
133. Källicke, T., et al., *Effect on infection resistance of a local antiseptic and antibiotic coating on osteosynthesis implants: an in vitro and in vivo study*. Journal of orthopaedic research, 2006. 24(8): p. 1622-1640.
134. Knetsch, M.L. and L.H. Koole, *New strategies in the development of antimicrobial coatings: the example of increasing usage of silver and silver nanoparticles*. Polymers, 2011. 3(1): p. 340-366.
135. Ahamed, M. and T. Sastry, *Wound dressing application of chitosan based bioactive compounds*. International Journal of Pharmacy & Life Sciences, 2011. 2(8).
136. Albaugh, K., S. Biely, and J. Cavorsi, *The Effect of a Cellulose Dressing and Topical Vancomycin on Methicillin-resistant Staphylococcus aureus (MRSA) and Gram-positive Organisms in Chronic Wounds: A Case Series*. Ostomy/wound management, 2013. 59(5): p. 34-44.
137. Nevell, T.P. and S.H. Zeronian, *Cellulose chemistry and its application*. 1985: E. Horwood; Halsted Press; John Wiley.
138. Raghavendra, G.M., et al., *Cellulose–polymer–Ag nanocomposite fibers for antibacterial fabrics/skin scaffolds*. Carbohydrate polymers, 2013. 93(2): p. 553-560.
139. http://en.wikipedia.org/wiki/File:Cellulose_strand.svg. [cited 2013 21 May].
140. Wang, Y., *Cellulose fiber dissolution in sodium hydroxide solution at low temperature: Dissolution kinetics and solubility improvement*. 2008: ProQuest.
141. Siqueira, G., J. Bras, and A. Dufresne, *Cellulosic bionanocomposites: a review of preparation, properties and applications*. Polymers, 2010. 2(4): p. 728-765.
142. Hon, D.N.-S. and N. Shiraishi, *Wood and Cellulosic Chemistry, Revised, and Expanded*. 2000: CRC Press.
143. Sloot, N., et al., *Purification and characterisation of elastase from Staphylococcus epidermidis*. Journal of medical microbiology, 1992. 37(3): p. 201-205.
144. Inglis, T.J., *Microbiology and infection*. 1996: Churchill Livingstone.

145. Fischetti, V.A., et al., *Gram-positive pathogens*. 2006: ASM Press. 146. Salter, C.J., R.C. Mitchell, and A.F. Drake, infrared spectroscopy studies of vancomycin and its unteractions with *N-acetyl-D-ALA-D-ALA and N,N'-diacetyl-LLYS-D-ALA-D-ALA*. *Journal of the Chemical Society-Perkin Transactions 2*, 1995(12): p. 2203-2211.
146. Salter, C.J., R.C. Mitchell, and A.F. Drake, *INFRARED SPECTROSCOPIC STUDIES OF VANCOMYCIN AND ITS INTERACTIONS WITH N-ACETYL-D-ALA-D-ALA AND N,N'-DIACETYL-L-LYS-D-ALA-D-ALA*. *Journal of the Chemical Society-Perkin Transactions 2*, 1995(12): p. 2203-2211.
147. <http://en.wikipedia.org/wiki/File:Vancomycin.svg>. [cited 2008 17 October].
148. <http://en.wikipedia.org/wiki/Levofloxacin>. [cited 2009 16 June].
149. Malmborg, A.-S., *Assay of Antibiotics with Agar Diffusion Technique*, in *Laboratory Aspects of Infections*. 1976, Springer. p. 115-124.
150. Cogen, A.L., et al., *Staphylococcus epidermidis antimicrobial δ -toxin (phenol-soluble modulín- γ) cooperates with host antimicrobial peptides to kill group A Streptococcus*. *PLoS One*, 2010. 5(1): p. e8557.
151. Pace, J.L., M.E. Rupp, and R.G. Finch, *Biofilms, infection, and antimicrobial therapy*. 2005: CRC Press.
152. Gomes, F., et al., *Evaluation of antimicrobial activity of certain combinations of antibiotics against in vitro Staphylococcus epidermidis biofilms*. *The Indian journal of medical research*, 2012. 135(4): p. 542.
153. Jeun, J.P., Y.M. Lim, and Y.C. Nho, *Study on morphology of electrospun poly(caprolactone) nanofiber*. *Journal of Industrial and Engineering Chemistry*, 2005. 11(4): p. 573-578.
154. Huang, Z.M., et al., *A review on polymer nanofibers by electrospinning and their applications in nanocomposites*. *Composites Science and Technology*, 2003. 63(15): p. 2223-2253.
155. Tucker, N., et al., *The History of the Science and Technology of Electrospinning from 1600 to 1995*. *Journal of Engineered Fibers and Fabrics*, 2012. 7: p. 63-73.
156. Pham, Q.P., U. Sharma, and A.G. Mikos, *Electrospinning of polymeric nanofibers for tissue engineering applications: a review*. *Tissue engineering*, 2006. 12(5): p. 1197-1211.
157. Lu, P. and B. Ding, *Applications of electrospun fibers*. *Recent patents on nanotechnology*, 2008. 2(3): p. 169-182.

158. Doshi, J. and D.H. Reneker, *Electrospinning process and applications of electrospun fibers*. Journal of electrostatics, 1995. 35(2): p. 151-160.
159. Wang, H.S., G.D. Fu, and X.S. Li, *Functional polymeric nanofibers from electrospinning*. Recent patents on nanotechnology, 2009. 3(1): p. 21-31.
160. Teo, W. and S. Ramakrishna, *A review on electrospinning design and nanofibre assemblies*. Nanotechnology, 2006. 17: p. R89.
161. Cui, W., Y. Zhou, and J. Chang, *Electrospun nanofibrous materials for tissue engineering and drug delivery*. Science and Technology of Advanced Materials, 2010. **11**(1).
162. Ji-Huan He, Y.L., Lu-Feng Mo, Yu-Qin Wan and Lan Xu, *Electrospun nanofibres and their applications*. 2008, Shawbury: iSmithers.
163. Sill, T.J. and H.A. Von Recum, *Electrospinning: applications in drug delivery and tissue engineering*. Biomaterials, 2008. 29(13): p. 1989-2006.
164. Yu, D.-G., et al., *Electrospun nanofiber-based drug delivery systems*. Health, 2009. **1**(2): p. 67-75.
165. BÄ¶llgen, N., et al., *In vivo performance of antibiotic embedded electrospun PCL membranes for prevention of abdominal adhesions*. Journal of Biomedical Materials Research Part B: Applied Biomaterials, 2007. 81(2): p. 530-543.
166. Kim, K., et al., *Incorporation and controlled release of a hydrophilic antibiotic using poly(lactide-co-glycolide)-based electrospun nanofibrous scaffolds*. Journal of Controlled Release, 2004. 98(1): p. 47-56.
167. Xu, X., et al., *BCNU-loaded PEG-PLLA ultrafine fibers and their in vitro antitumor activity against Glioma C6 cells*. Journal of controlled release, 2006. 114(3): p. 307-316.
168. Luong-Van, E., et al., *Controlled release of heparin from poly (caprolactone) electrospun fibers*. Biomaterials, 2006. 27(9): p. 2042-2050.
169. Danesin, R., et al., *Self-assembling peptide-enriched electrospun polycaprolactone scaffolds promote the *h*-osteoblast adhesion and modulate differentiation-associated gene expression*. Bone, 2012.
170. Brun, P., et al., *Electrospun scaffolds of self-assembling peptides with poly (ethylene oxide) for bone tissue engineering*. Acta Biomaterialia, 2011. 7(6): p. 2526-2532.
171. Reed, C.R., et al., *Composite Tissue Engineering on Polycaprolactone Nanofiber Scaffolds*. Annals of Plastic Surgery, 2009. 62(5): p. 505-512.

172. Rutkowska, A., et al., *Biodegradation of modified poly(epsilon-caprolactone) in different environments*. Polish Journal of Environmental Studies, 2002. 11(4): p. 413-420.
173. Goh, Y.-F., I. Shakir, and R. Hussain, *Electrospun fibers for tissue engineering, drug delivery, and wound dressing*. Journal of Materials Science, 2013. 48(8): p. 3027-3054.
174. Iucci, G., et al., *Biomimetic Peptide-Enriched Electrospun Polymers: A Photoelectron and Infrared Spectroscopy Study*. Journal of Applied Polymer Science, 2011. 122(6): p. 3574-3582.
175. Ma, Z.W., et al., *Grafting of gelatin on electrospun poly(caprolactone) nanofibers to improve endothelial cell spreading and proliferation and to control cell orientation*. Tissue Engineering, 2005. 11(7-8): p. 1149-1158.
176. Zahedi, P., et al., *A review on wound dressings with an emphasis on electrospun nanofibrous polymeric bandages*. Polymers for Advanced Technologies, 2010. 21(2): p. 77-95.
177. Kenawy, E.-R., et al., *Processing of polymer nanofibers through electrospinning as drug delivery systems*. Materials Chemistry and Physics, 2009. 113(1): p. 296-302.
178. Sinha, V., et al., *Poly-epsilon-caprolactone microspheres and nanospheres: an overview*. International Journal of Pharmaceutics, 2004. 278(1): p. 1-23.
179. Yu, D.-G., et al., *Electrospun nanofiber-based drug delivery systems*. Health (1949-4998), 2009. 1(2).
180. Zhang, C., et al., *Study on morphology of electrospun poly (vinyl alcohol) mats*. European Polymer Journal, 2005. 41(3): p. 423-432.
181. Zeng, J., et al., *Biodegradable electrospun fibers for drug delivery*. Journal of Controlled Release, 2003. 92(3): p. 227-231.
182. Mit uppatham, C., M. Nithitanakul, and P. Supaphol, *Ultrafine Electrospun Polyamide• 6 Fibers: Effect of Solution Conditions on Morphology and Average Fiber Diameter*. Macromolecular Chemistry and Physics, 2004. 205(17): p. 2327-2338.

Appendix

A. Peptide content

P₁₁-2

Table A1: Data for P₁₁-2, batch CF064650.

HPLC (purity)	97.3 %
In house UV	99.2 %
In house elemental analysis	C 50.8%, H 5.8 %, N 16.9 %

P₁₁-4

Table A2: Data for P₁₁-4, batch: CF10141A

HPLC (purity)	97.3 %
In house UV	99.2 %
In house elemental analysis	C 51.8%, H 6.2 %, N 16.9 %

P₁₁-8

Table A.3: Data for P₁₁-8, Batch: HF34148A

HPLC (purity)	96.3 %
In house UV	80.2 %
In house elemental analysis	C 47.1 %, H 5.6 %, N 15.3 %

P₁₁-9

Table A.4: Data for P₁₁-9, batch CF08380D

HPLC (purity)	98.2%
In house UV	89 %
In house elemental analysis	C 51.4%, H 6.0%, N 14.7%

P₁₁-12

Table A.5: Data for P₁₁-12 AW09357b

HPLC (purity)	96.2%
In house UV	82.1 %
In house elemental analysis	C 45.8%, H 5.5%, N 13.8%

B. Effect of antibiotics on peptide self-assembly

Figure A.2 shows that the addition of the antibiotics, vancomycin and levofloxacin, do not interfere with the self-assembly and the gel formation of P₁₁-4 and P₁₁-8.



Figure B: The effect of antibiotics on peptide self-assembly. From Left; P₁₁-8/vancomycin, P₁₁-8 Levofloxacin, P₁₁-4/vancomycin, P₁₁-4/Levofloxacin.

C. The effect of alkaline pH of P₁₁-8 and P₁₁-4

The figure below shows that P₁₁-4 is monomer solution at pH 8, while P₁₁-8 is biphasic solution containing gel on top of the vial and monomer fluid in the bottom.



Figure C: Solutions of peptides at pH 8. Left; P₁₁-4. Right: P₁₁-8

D. Surface wettability

The evaluation of the hydrophobicity of the material surface is an important basic experiment for gathering information about the surface properties. Drops of pure water were separately deposited on the fibres' surfaces.

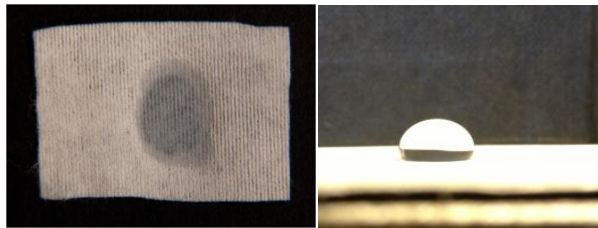


Figure D: Photographs showing the surface characteristic of PCL and cellulose fabrics. Left: a drop of deionized water on cellulosic fabrics. Right; a drop of water on 100% PCL.

E. The effect of elect spinning parameters on 100% PCL

Sample	Distance(cm)	Voltage (V)	Temperature	Diameter range (nm)	Average diameter(nm)
1	16	15	Room temp	972-1079	1025
2	16	15	50°C	868-1249	1058
3	16	20	Room temp	504-879	642
4	16	20	50°C	668-3317	1992
5	16	25	Room temp	589-896	742
6	16	25	50°C	658-1174	916
7	18	15	Room temp	576-970	773
8	18	15	50°C	795-802	798
9	18	20	Room temp	2501-2867	2684
10	18	20	50°C	302-647	475
11	18	25	Room temp	624-898	761
12	18	25	50°C	406-562	484
13	20	15	Room temp	611-1161	886
14	20	15	50°C	931-953	941
15	20	20	Room temp	512-632	572
16	20	20	50°C	442-983	712
17	20	25	Room temp	390-409	400
18	20	25	50°C	365-624	494

F. The effect of elect spinning parameters on PCL/P₁₁-4

Sample	Distance(cm)	Voltage (V)	Temperature	Diameter range (nm)	Average diameter(nm)
1	16	15	Room temp	202-541	371
2	16	15	50°C	382-960	671
3	16	20	Room temp	360-596	478
4	16	20	50°C	444-750	597
5	16	25	Room temp	522-701	611
6	16	25	50°C	491-710	600
7	18	15	Room temp	280-430	355
8	18	15	50°C	505-1030	767
9	18	20	Room temp	480-650	565
10	18	20	50°C	265-494	379
11	18	25	Room temp	483-707	645
12	18	25	50°C	350-624	487
13	20	15	Room temp	367-334	350
14	20	15	50°C	113-612	362
15	20	20	Room temp	318-399	358
16	20	20	50°C	437-520	478
17	20	25	Room temp	430-664	547
18	20	25	50°C	588-998	793

G. The effect of electrspinning parameter on PCL/P₁₁-8

Sample	Distance(cm)	Voltage (V)	Temperature	Diameter range (nm)	Average diameter(nm)
1	16	15	Room temp	200-371	285
2	16	15	50°C	355-480	417
3	16	20	Room temp	204-1300	752
4	16	20	50°C	326-444	385
5	16	25	Room temp	240-332	286
6	16	25	50°C	1700-2008	1854
7	18	15	Room temp	190-319	254
8	18	15	50°C	420-633	316
9	18	20	Room temp	260-275	267
10	18	20	50°C	156-276	216
11	18	25	Room temp	197-291	244
12	18	25	50°C	211-539	480
13	20	15	Room temp	181-245	163
14	20	15	50°C	340-411	375
15	20	20	Room temp	233-853	543
16	20	20	50°C	293-313	303
17	20	25	Room temp	595-633	614
18	20	25	50°C	492-1300	896

